

UNCLASSIFIED

AD 436114

DEFENSE DOCUMENTATION CENTER

FOR

SCIENTIFIC AND TECHNICAL INFORMATION

CAMERON STATION, ALEXANDRIA, VIRGINIA



UNCLASSIFIED

NOTICE: When government or other drawings, specifications or other data are used for any purpose other than in connection with a definitely related government procurement operation, the U. S. Government thereby incurs no responsibility, nor any obligation whatsoever; and the fact that the Government may have formulated, furnished, or in any way supplied the said drawings, specifications, or other data is not to be regarded by implication or otherwise as in any manner licensing the holder or any other person or corporation, or conveying any rights or permission to manufacture, use or sell any patented invention that may in any way be related thereto.

64-12

ASD-TDR-63-764  
VOLUME I

436114

**A PROGRAM TO DETERMINE HIGH  
BLAST-INDUCED AIRLOADS AND STRUCTURAL  
RESPONSE OF LIFTING SURFACES**

TECHNICAL DOCUMENTARY REPORT No. ASD-TDR-63-764, VOL. I

MARCH 1964

AF FLIGHT DYNAMICS LABORATORY  
AERONAUTICAL SYSTEMS DIVISION  
AIR FORCE SYSTEMS COMMAND  
WRIGHT-PATTERSON AIR FORCE BASE, OHIO

Project No. 1350, Task No. 135002

(Prepared under Contract No. AF 33(616)-7099 by  
Aircraft Armaments, Inc., Cockeysville, Maryland;  
R. L. Jarvis, J. J. Kasper, R. R. Mills, Jr., and I. O. Wolf, Authors)

## NOTICES

When Government drawings, specifications, or other data are used for any purpose other than in connection with a definitely related Government procurement operation, the United States Government thereby incurs no responsibility nor any obligation whatsoever; and the fact that the Government may have formulated, furnished, or in any way supplied the said drawings, specifications, or other data, is not to be regarded by implication or otherwise as in any manner licensing the holder or any other person or corporation, or conveying any rights or permission to manufacture, use, or sell any patented invention that may in any way be related thereto.

Qualified requesters may obtain copies of this report from the Defense Documentation Center (DDC), (formerly ASTIA), Cameron Station, Bldg. 5, 5010 Duke Street, Alexandria 4, Virginia.

Items and materials used in the study, or called out in the report by trade name or specifically identified with a manufacturer, were not originated for use in this specific study or for applications necessary to this study. Therefore, the failure of any one of the items or materials to meet the requirements of the study is no reflection on the quality of a manufacturer's product. No criticism of any item or material is implied or intended, nor is any endorsement of any item or material by the USAF implied or intended.

Copies of this report should not be returned to the Aeronautical Systems Division unless return is required by security considerations, contractual obligations, or notice on a specific document.

This report has been released to the Office of Technical Services, U.S. Department of Commerce, Washington 25, D. C., in stock quantities for sale to the general public.



#### FOREWORD

This report was prepared under Air Force Contract No. AF33(616)-7099, Project No. 1350, Task No. 135002, for the AF Flight Dynamics Laboratory, Aeronautical Systems Division, Wright-Patterson Air Force Base, Ohio. Captain J. S. Garner was project engineer, in charge of the program. Mr. W. L. Black of AAI was engineer in charge of the development and design work. Test support was provided by the AFFTC Track Branch, Edwards Air Force Base, California, the Ballistic Research Laboratory of Aberdeen Proving Grounds, Maryland and the NASA Shock Tube Facility at Wallops Island, Virginia. Work was started in April 1960. Field testing began in September 1960 and ended in August 1961. Data reduction and analysis was completed in March 1963. The correlation program is still in process.

This report is issued as ASD-TDR-63-764 from the original document prepared by AAI as ER-2983.

Acknowledgement is made of the assistance provided by Dr. N. P. Hobbs and E. S. Criscione of Avidyne Research, Inc. and Dr. E. A. Witmer, Dr. J. R. Ruetenik and R. D'Amato of the Aeroelasticity and Structures Research Lab., Massachusetts Institute of Technology.

# ABSTRACT

High blast induced airloads and the structural response of lifting surfaces are investigated for determining aircraft vulnerability and safety. Of major interest is the case where the primary structure of the lifting surface undergoes deformations of an inelastic nature. Structural response prediction methods, for completely elastic response conditions, are well documented and quite reliable. However, the methods of evaluating the structural response must be extended into the inelastic region and verified through the use of experimentally collected data.

The Ballistics Research Laboratory (BRL) and the Aeronautical Systems Division (ASD) jointly conducted a program to obtain airloads and structural response data.

BRL photographically recorded the structural response of F-84 horizontal stabilizers mounted on a rocket sled and exposed to a high explosive blast.

ASD utilized the rocket sled for three tests using instrumented airfoil specimens but as a result of problems encountered in the sledborne instrumentation system, subsequent substitution of the NASA Ground Blast Apparatus at Wallops Island yielded airloads data. Six tests were conducted at NASA. The value of the data is limited because of inherent facility limitations, significant ones being the short duration of the shock tunnel flow and the small amount of explosives which can be used.

The planform of the ASD airfoil specimens is similar in configuration to the B-47 and/or B-52. This planform is used because of the interest in aircraft of this type involving the flight Mach numbers in the order of 0.8.

The ASD airfoil specimens consist of one airload specimen and three structural specimens. The airloads airfoil specimen is used in the collection of airloads data in order to permit investigations of aerodynamic phenomena at large peak-induced angles of attack while maintaining relatively

small airfoil motion. The structural specimens have been designed according to current design practice in order to investigate the failure modes and postfailure behavior of typical wing structures.

The airfoil specimens are designed to fail at a particular station to eliminate any problems which may occur in random failure.

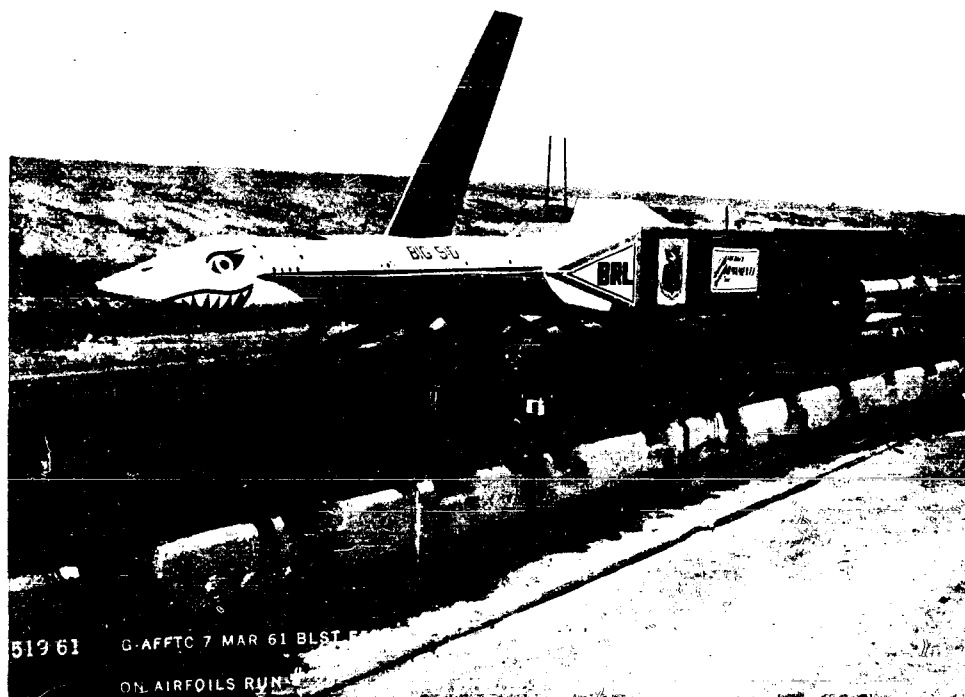
Laboratory tests are performed to determine natural frequencies and elastic behavior. A structural specimen is then tested to destruction to determine the applied moment rotation characteristics in the postfailure region up to a peak angle of rotation of at least 50 degrees.

The experimental data obtained will be used for correlation with theoretical prediction methods and, later, for the refinement of the theoretical methods.

This technical documentary report has been reviewed and is approved.



W. A. Sloan, Jr.  
Colonel, USAF  
Chief, Structures Division  
AF Flight Dynamics Laboratory



AIRLOADS RESEARCH SLED  
(Frontispiece I)



RESEARCH SLED ENTERING BLAST AREA  
(Frontispiece II)

## TABLE OF CONTENTS

### VOLUME I

	<u>Page</u>
1.0 INTRODUCTION	1
2.0 SLED VEHICLE DESIGN	4
2.1 GENERAL DESCRIPTION	4
2.2 DESIGN	8
2.2.1 DESIGN CRITERIA	8
2.2.1.1 PERFORMANCE CHARACTERISTICS	8
2.2.1.2 LOADING CONDITIONS	8
2.2.2 STRUCTURAL ANALYSIS	10
2.2.3 WEIGHT SUMMARY	54
2.3 AERODYNAMICS	55
2.3.1 AERODYNAMIC DRAG	55
2.3.2 BLAST SLED PERFORMANCE CHARACTERISTICS	63
2.3.3 BLAST WAVE LOADING ON SLED BODY STRUCTURE	70
2.3.4 EFFECT OF SLED MOTION ON BLAST WAVE PARAMETERS	81
2.3.5 PRESSURE DISTRIBUTIONS AND CHOKING EFFECTS	87
3.0 AIRFOIL SPECIMEN	96
3.1 DESCRIPTION	96
3.1.1 AIRLOAD SPECIMEN	96
3.1.2 STRUCTURAL SPECIMEN	98
3.2 PRELIMINARY DESIGN	107
3.2.1 AIRLOADS	107
3.2.2 DYNAMIC RESPONSE	116
3.2.3 AIRLOAD SPECIMEN	120
3.2.4 STRUCTURAL SPECIMEN	136
3.3 FINAL DESIGN	195
3.3.1 AIRLOAD SPECIMEN	195
3.3.2 STRUCTURAL SPECIMEN	195

TABLE OF CONTENTS (cont'd)

	<u>Page</u>
4.0 SPECIMEN LABORATORY TESTS	209
4.1 AIRLOAD SPECIMEN	209
4.1.1 DYNAMIC TESTS	209
4.1.2 INFLUENCE COEFFICIENT TEST	225
4.1.3 CALIBRATION OF ELASTIC STRAIN GAGES	236
4.2 STRUCTURAL SPECIMEN	247
4.2.1 DYNAMIC TESTS	247
4.2.2 STATIC TESTS	265
4.2.3 DESTRUCTION TESTS	286
5.0 SLED INSTRUMENTATION	314
5.1 DESCRIPTION OF INSTRUMENTATION	314
5.1.1 LOCATION AND TYPES OF TRANSDUCERS	314
5.1.2 RECORDING EQUIPMENT	317
5.1.3 PHOTOGRAPHIC EQUIPMENT	318
5.1.4 TIME CORRELATION	320
5.2 SYSTEM RESPONSE CHARACTERISTICS	320
5.2.1 ACCELEROMETERS	320
5.2.2 STRAIN GAGES	321
5.2.3 PRESSURE TRANSDUCERS	321
5.3 ESTIMATED ACCURACY	324
5.3.1 ACCELERATION	324
5.3.2 PRESSURE	325
5.3.3 TORSION AND BENDING MOMENT	326
5.3.4 SLED VELOCITY ERROR	329
6.0 FIELD TEST PROGRAM	331
6.1 TEST OBJECTIVES	331
6.2 GENERAL DESCRIPTION	331

TABLE OF CONTENTS (cont'd)

	<u>Page</u>
6.2.1 PHASE I - EDWARDS AIR FORCE BASE SLED TESTS	331
6.2.2 PHASE II - WALLOPS ISLAND SHOCK TUBE TESTS	352
6.2.3 RECOMMENDATIONS	363
7.0 SUMMARY	
7.1 SLED	365
7.2 TEST SPECIMENS	365
7.3 INSTRUMENTATION	365
7.4 TEST DATA	367
7.5 "BIG SEA" PROBLEMS	367
APPENDIX A - JANAF Post-Failure Response Program and Results	369
A.1 INTRODUCTION	369
A.2 THE COMPUTER PROGRAM	369
A.3 RESULTS	371
A.4 CONCLUSIONS	374
REFERENCES	377



# LIST OF ILLUSTRATIONS

<u>Figure No.</u>	<u>Title</u>	<u>Page</u>
2.1.1	Test Sled - Three View Drawing	5
2.2.1	Slipper Loads for Mission No. 30	53
2.3.1	Drag Coefficient for Nose Cone	58
2.3.2	Drag Coefficient for Transition Section	59
2.3.3	Drag Coefficient for Slipper Legs	60
2.3.4	Main Body Base Drag	61
2.3.5	Overall Drag Coefficients for Different Sled Configurations	62
2.3.6	Performance Characteristics for ASD Sled with F-84 Tail and Mount	67
2.3.7	Performance Characteristics for ASD Sled with Airload Specimen 6L	68
2.3.8	Performance Characteristics for ASD Sled with Structural Specimen 6R	69
2.3.9	Blast Wave Parameters for Mission No. 30	76
2.3.10	Air Blast Loading on Closed Rectangular Structure	77
2.3.11	Air Blast Loading on Closed Cylindrical Structure	78
2.3.12	Comparison of Pressure Forces Acting on Rectangular and Cylindrical Structures	79
2.3.13	Air Blast Loading on Closed Cylindrical Structure	80
2.3.14	Geometrical Relationship Between Blast Origin and Track	83
2.3.15	Sled Trajectory Versus Time Diagram	84
2.3.16	Effect of Moving Sled on Positive Phase Duration Mission 1 and 2	86
2.3.17	Effect of Moving Sled on Positive Duration of Mission No. 3.	86

LIST OF ILLUSTRATIONS (cont'd)

<u>Figure No.</u>	<u>Title</u>	<u>Page</u>
2.3.18	Average Pressures on Sled Surfaces at Mach. 1.5, 12 Inches of Water in Trough	94
2.3.19	Average Pressures on Sled Surfaces at Mach 1.2, No Water in Trough	95
3.1.1	6L Airload Model	97
3.1.2	Shear Connector	98
3.1.3	Airload Specimen Installed	99
3.1.4	6R Structural Model	100
3.1.5	Typical Section Outside of Failure Bay	101
3.1.6	Section Through Breakline	104
3.1.7	Root Support for Structural Model 6R	106
3.2.1	Lift Time Curve for ASD Models	115
3.2.2	Dynamic Overstress Factor for Single Degree of Freedom System and Exponential Loadings	118
3.2.3	Time of Maximum Response for Blast Induced Loadings with Exponential Decay Rate	119
3.2.4	Airload Specimen Preliminary Mass and Moment of Inertia Distribution	121
3.2.5	The Maximum Applied Bending Moment and the Resisting Yield Moment for the Airload Specimen	129
3.2.6	Assumed Stress Distribution on Shear Connector	131
3.2.7	Bearing Load Diagram	132
3.2.8	Load Capacity of Shear Connectors for Airload Specimen	134
3.2.9	The Maximum Applied Shear Force and the Yield Shear Capacity Along the Split Plane of the Airload Specimen	135
3.2.10	Structural Specimen - First Preliminary Trial	138
3.2.11	Moment of Inertia of Structural Specimen Normal to the 50% Chord-First Preliminary Trial	141

LIST OF ILLUSTRATIONS (cont'd)

<u>Figure No.</u>	<u>Title</u>	<u>Page</u>
3.2.12	Spanwise Mass Distribution of Structural Specimen - First Preliminary Trial	142
3.2.13	Bending Moment Capacity and Distribution at Failure Load for Structural Specimen - First Preliminary Trial	145
3.2.14	Effective Width of Compression Skin 7075-T6	153
3.2.15	Effective Width of Compression Flange 2024-T3	154
3.2.16	Stress Strain Curve 7075-T6	155
3.2.17	Stress Strain Curve 2024-T3	156
3.2.18	Effective Breakline Section at Peak Load	159
3.2.19	Moment Rotation Curve for Strongback	169
3.2.20	Relative Rotation of Ribs Adjacent to Break Station as a Function of the Moment at the Break Line	172
3.2.21	Relative Rotation of Ribs Adjacent to Break Station as a Function of Moment at Break Line	173
3.2.22	Moment of Inertia of Structural Specimen Normal to the 50% Chord-Second Preliminary Trial	174
3.2.23	Spanwise Mass Distribution of Structural Specimen - Second Preliminary Trial	175
3.2.24	Flutter Model	177
3.2.25	Three Quarter Semi-Span Section	179
3.2.26	Torsional Mass Moment of Inertia for Structural Specimen-Second Preliminary Trial	180
3.2.27	Torsional Stiffness of Structural Wing-Second Preliminary Trial	181
3.2.28	Torsional Mass Model	182
3.2.29	Critical Flutter Speed for the Structural Wing	186
3.2.30	Lumped Mass Distribution for Idealized Structural Specimen - Second Preliminary Trial	188
3.2.31	Bending Vibration Modes - Structural Specimen - Second Preliminary Trial	191

LIST OF ILLUSTRATIONS (cont'd)

<u>Figure No.</u>	<u>Title</u>	<u>Page</u>
3.2.32	Idealized Lumped Mass Distribution for Structural Specimen	193
3.2.33	Idealized Structural Elements of 6R Model	194
3.3.1	Chordwise Center of Gravity Location of Structural Specimen Measured Normal to 50% Chord Line - Final	196
3.3.2	Spanwise Mass Distribution of Structural Specimen - Final	197
3.3.3	Torsional Mass Moment of Inertia of Structural Specimen about 50% Chordline - Final	198
3.3.4	Moment of Inertia of Structural Specimen Normal to the 50% Chordline - Final	199
3.3.5	Bending Moment Strength and Distribution at Failure Load for Structural Specimen - Final	202
3.3.6	Lumped Mass Distribution for Idealized Structural Specimen - Final	205
3.3.7	Bending Vibration Modes for Structural Specimen - Final	208
4.1.1	Shaker Arrangement for Model 6L	210
4.1.2	Tension Pad Locations for Influence Coefficient Test and Probe Point Locations for Dynamic Test - Airload Specimen	211
4.1.3	Frequency Response Curve for Airload Specimen	213
4.1.4	Structural Damping Coefficient Airload Specimen $f_n = 25.8$ CPS	214
4.1.5	Structural Damping Coefficient Airload Specimen $f_n = 43.8$ CPS	215
4.1.6	Structural Damping Coefficient Airload Specimen $f_n = 97.0$ CPS	216
4.1.7	First Mode $f_n = 25.8$ CPS	220
4.1.8	Second Mode $f_n = 43.8$ CPS	221
4.1.9	Third Mode $f_n = 97.0$ CPS	222
4.1.10	Fourth Mode $f_n = 206$ CPS	223

# LIST OF ILLUSTRATIONS (cont'd)

<u>Figure No.</u>	<u>Title</u>	<u>Page</u>
4.1.11	Fifth Mode $f_n = 250$ CPS	224
4.1.12	Test Fixture	226
4.1.13	Static Test Set Up for Model 6L	227
4.1.14	Load Deflection Plot Showing Hysteresis - Airload Specimen	228
4.1.15	Sign Convention for Loading of Wing Models	238
4.1.16	Airload Specimen - Strain Gage Locations	239
4.1.17	Bending Moment at Strain Gage Locations Normal to 50% Chordline vs. Bridge Output	244
4.1.18	Bending Moment at Strain Gage Locations Normal to 50% Chordline vs. Bridge Output	245
4.1.19	Indicated Strain vs. Load Simulated by Resistance of 22.22 <sup>k</sup> , 23.1 <sup>k</sup> , 22 <sup>k</sup> , 43 <sup>k</sup> , 50 <sup>k</sup> , and 100 <sup>k</sup> OHMS.	246
4.2.1	Electrodynamic Shaker and Monitoring Probe Arrangement for Model 6R	248
4.2.2	Tension Pad Locations for Influence Coefficient Test and Probe Point Locations for Dynamic Tests	249
4.2.3	Frequency Response Curve for Structural Specimen	251
4.2.4	Structural Damping Coefficient - Structural Specimen $f_n = 29.0$ CPS	252
4.2.5	Structural Damping Coefficient - Structural Specimen $f_n = 112$ CPS	253
4.2.6	Structural Damping Coefficient - Structural Specimen $f_n = 192$ CPS	254
4.2.7	First Bending Mode $f_n = 29.0$ CPS	257
4.2.8	Second Bending Mode $f_n = 112$ CPS	258
4.2.9	Third Bending Mode $f_n = 275$ CPS	259
4.2.10	First Torsion Mode $f_n = 192$ CPS	260
4.2.11	Second Torsion Mode $f_n = 390$ CPS	261
4.2.12	Node Line Location for $f_n = 29.0$ CPS Model (6R)	262

LIST OF ILLUSTRATIONS (cont'd)

<u>FIGURE NO.</u>	<u>TITLE</u>	<u>PAGE</u>
4.2.13	Node Line Location for $f_n = 112$ CPS Model (6R)	262
4.2.14	Node Line Location for $f_n = 275$ CPS Model (6R)	263
4.2.15	Node Line Location for $f_n = 192$ CPS Model (6R)	263
4.2.16	Node Line Location for $f_n = 390$ CPS Model (6R)	264
4.2.17	Dillon Force Gage	267
4.2.18	Static Test Set Up for Model 6R	267
4.2.19	Load Deflection Plot Showing Hysteresis - Structural Specimen	268
4.2.20	Plan View Location of Strain Gages	277
4.2.21	Typical Location of Elastic, Bending and Torsion Strain Gages	279
4.2.22	Bending Moment - Strain Relationship for Elastic Bridge $M_2$ Made Up of Strain Gages 5R, 7R, 5L, 7L	284
4.2.23	Indicated Strain for Bridges $M_1$ , $T_1$ , and $T_2$ vs. Load Simulated by Resistances of $20^k$ , $40^k$ , $100^k$ , $350^k$ , and $700^k$ OHMS.	285
4.2.24	Destruction Test Set Up for Model 6R	287
4.2.25	Dial Gage Frame for Measuring Post-Elastic Rotation of Model 6R	287
4.2.26	Initial Failure of Model 6R	306
4.2.27	Broken Model 6R	306
4.2.28	Collapsed Compression Buckle of Model 6R	307
4.2.29	Deformed Internal Structure of Model 6R	308
4.2.30	Deformed Internal Structure of Model 6R	308
4.2.31	Postfailure Moment Rotation Curve at the Breakline	309
4.2.32	Postfailure Bending Moment Bridge No. 1	310
4.2.33	Postfailure Bending Moment Bridge No. 2	311
4.2.34	Postfailure Bending Moment Bridge No. 3	312
4.2.35	Postfailure Bending Moment Bridge No. 4	313

LIST OF ILLUSTRATIONS (cont'd)

<u>Figure No.</u>	<u>Title</u>	<u>Page</u>
5.1.1	Instrumentation Installation - Airload Specimen	315
5.1.2	Sledborne Camera Coverage	318
5.1.3	Ground Mounted Camera Coverage	319
6.2.1.1	BRL Specimen	333
6.2.1.2	ASD Specimen	334
6.2.1.3	Part of the Recording Equipment Mounted in the Sled	335
6.2.1.4	The H.E. Charge and Blast Line Instrumentation	336
6.2.1.5	Typical Test Showing the Sled Vehicle Entering the Blast Area	337
6.2.2.1	Wallops Island Test Facility - General Arrangement	354
6.2.2.2	Rake Installation - Wallops Island Shock Tube	355
6.2.2.3	Explosive Emplacement - Wallops Island Shock Tube	356
6.2.2.4	Shock Tube Diaphragm Before Test - Wallops Island Shock Tube	357
6.2.2.5	Shock Tube Diaphragm After Test - Wallops Island Shock Tube	358
6.2.2.6	Specimen Instrumentation Components - Wallops Island Shock Tube	359
A.1	Preliminary Static Post-Failure Curves for Structural Model Design JANAF Program	375
A.2	Aerodynamic Procedures	376

# LIST OF TABLES

<u>Table No.</u>	<u>Title</u>	<u>Page</u>
2.2.1	Summary of Margins of Safety	52
2.2.2	Weight Summary	54
2.3.1	Overall Drag Coefficients of Basic Sled	57
2.3.2	Blast Characteristics of Mission #30	74
2.3.3	Blast Characteristics for ASD Missions	82
2.3.4	Sled Surface Pressure and Mach No. Function	90
3.2.1	Field Tests on ASD Wing Models	108
3.2.2	Lift Data Mission No. 1	112
3.2.3	Lift Data Mission No. 2 and 3	114
3.2.4	Ultimate Bending Moment at Breakline for Local Failure Mode	160
3.2.5	Fundamental Torsional Frequency	183
3.2.6	Summary of Lumped Masses and Elastic Coefficients	189
3.2.7	Orthogonality of Modes for Structural Specimen	190
3.3.1	Summary of Lumped Masses and Elastic Coefficients for Structural Specimen - Final	206
3.3.2	Orthogonality of Modes for Structural Specimen- Final	207
4.1.1	Frequency Survey Data For Airload Specimen	212
4.1.2	Mode Shape Data at Resonant Frequencies - 6L	217
4.1.3	Reduced Load Deflection Data Taken During Influence Coefficient Test	229
4.1.4	Summary of Influence Coefficients - Airload Specimen 6L	235
4.1.5	Strain Gage Number and Location in Bridge	240
4.1.6	Load Strain Data for Airload Specimen	241
4.1.7	Bending Moment Arm	243
4.2.1	Frequency Survey Data	250
4.2.2	Mode Shape Data at Resonant Frequencies - Structural Specimen 6R	255



LIST OF TABLES

<u>Table No.</u>	<u>Title</u>	<u>Page</u>
4.2.3	Reduced Load Deflection Data Taken During Influence Coefficient Test	269
4.2.4	Summary of Influence Coefficients - Structural Model 6R	275
4.2.5	Strain Gage Number and Location in Bridge	280
4.2.6	Load Strain Data	281
4.2.7	Summary of Bending and Torsion Lever Arms	283
4.2.8	Load, Moment, Rotation, and Strain	294
6.2.1	Run Conditions for Phase I Field Test Program	338
6.2.2	Wallops Island Test Conditions	360

# LIST OF SYMBOLS

A	Area
a	Local acoustical velocity; subscript "actual"
ALL.	Allowable
av.	Average
b	Width of section; subscript "bending"
C	Velocity of sound
C <sub>D</sub>	Drag Coefficient
C <sub>L</sub>	Lift Coefficient
C <sub>L</sub> $\alpha$	Slope of lift coefficient vs. angle of attack curve - 1/RAD.
cr	Subscript "critical"
C.G.	Center of gravity
D	Diameter; drag force
D <sub>p</sub> <sup>+</sup>	Time of positive pressure duration
d	Depth of section; subscript "duration"; exponential decay coefficient
D.L.F.	Dynamic load factor
D.O.F.	Dynamic overstress factor
E	Modulus of elasticity
e	Subscript "equivalent"; strain
F	Allowable stress
F <sub>b</sub>	Allowable bending stress
F <sub>bru</sub>	Allowable ultimate bearing stress
F <sub>bry</sub>	Allowable yield bearing stress
F <sub>c</sub>	Allowable compressive stress
F <sub>s</sub>	Allowable shearing stress
F <sub>sy</sub>	Allowable shearing yield stress
F <sub>tu</sub>	Allowable Ultimate tensile stress
F <sub>ty</sub>	Allowable Yield tensile stress
f	Internal (or calculated) stress

LIST OF SYMBOLS (cont'd)

$f_b$	Internal (or calculated) primary bending stress
$f_{br}$	Internal (or calculated) bearing stress
$f_c$	Internal (or calculated) compressive stress
$f_N$	Natural frequency
$f_s$	Internal (or calculated) shear stress
ft	Feet
g	Gravitational acceleration; structural damping coefficient
H	Horizontal force
i	Incident
I	Moment of inertia
$l_{sp}$	Specific impulse
K	Spring constant; constant
$K_L$	Load transformation factor
$K_M$	Edge restraint factor; mass transformation factor
K.E.	Kinetic energy
L	Length; lift
lb	Pounds
M	Total mass; Mach number; moment
$M_b$	Bending moment
$M_{by}$	Yield bending moment
$M_t$	Torsional moment
m	Mass per unit length; moment per unit length; subscript "maximum"
Max	Maximum
Min	Minimum
M.S.	Margin of Safety
o	Subscript "ambient"

o/c	On center
O.D.	Outside diameter
P	Applied force; peak pressure
P.E.	Potential energy
p	Pitch; pressure; transform function of X; subscript "peak"
p.L.	Subscript "proportional limit"
psi	Pounds per square inch
Q	Static moment of a cross section
q	Dynamic pressure
R	Stress ratio; subscript "resisting"; radius
r	Radius; subscript "reflected"
S	Planform area
s	Subscript "side on"; subscript "static"; subscript "shear".
sec	Seconds
T	Tensile force; temperature
$T_N$	Natural period
t	Thickness; time; subscript "torsion"
$U_s$	Shock front velocity
u	Bar force due to a unit load; subscript ultimate
Ult	Ultimate
V	Shear force; velocity
v	Shear force per unit length
W	Total load; total work
$W_o$	Total weight of vehicle without propellant
$W_p$	Initial propellant weight
w	Load per unit length
$w_e$	Effective width
x	Coordinate direction; unknown variable
y	Coordinate direction; subscript yield
$\bar{v}$	Distance to neutral axis

$Z$	Section modulus ( $I/y$ )
$Z_p$	Plastic section modulus
$\alpha$	Angle of attack
$\delta$	Specific heat; coefficient of compressibility
$\Delta$	Deflection; change in quantity
$\eta$	Plasticity reduction factor; sled acceleration
$\lambda$	Length of Buckle
$\nu$	Poisson's Ratio
$\pi$	3.14
$\rho$	Radius of gyration; air density
$\Sigma$	Summation
$\sigma$	Stress
$\omega$	Natural frequency RAD/SEC
$\Gamma$	LaPlace transform operator
$\#$	Number

## 1.0 INTRODUCTION

This report describes the services supplied by AAI to the Aeronautical Systems Division (ASD) of the United States Air Force under contract AF33(616)-7099. These services were a part of the ASD participation in a joint Army, Navy, and Air Force (JANAF) program to determine the blast effects on swept-back type airfoils when carried on a rocket propelled sled. The purpose of the program was to obtain test data that would provide a partial determination of the pressure build-up and pressure distribution over a particular type lifting surface during the passage of shock waves. The structural response of these lifting surfaces in both the elastic and post failure regions was measured. These data will be used to correlate and modify theoretical prediction methods for determining the vulnerability of aircraft to nuclear blasts. Another goal of the program was to determine the feasibility of applying these test methods to project "BIG SEA", a proposed test program of larger scope.

This report is presented in two volumes. Volume I describes the design of the rocket sled, the design of the ASD test specimens including the laboratory test program, the composition of both the sled borne and specimen mounted instrumentation and the effort expended to accomplish the field test program at Edwards Air Force Base, California, and Wallops Island, Virginia. A summary and conclusions are included which pertain to the effort discussed in this volume. Volume II contains the processed test data obtained from the field test records by reading the raw data then analyzing, compiling, computing, and plotting it to give the parameters of interest to the program. A summary and conclusions are included which discuss the results obtained from the processed data.

The program was run with the combined efforts of the Ballistic Research Laboratories (BRL), Aberdeen, Maryland, and the Aeronautical Systems Division (ASD), Wright Patterson Air Force Base, Ohio. AAI and the Track Division of Edwards Air Force Base, contributed the effort supplied by ASD. The division of effort was broadly allocated as follows: BRL

---

Manuscript released by the authors in September 1963, for publication as an ASD Technical Documentary Report.

contributed all the effort required to generate the blast induced shock waves including the instrumentation and collection and processing of the blast field data. They supplied several fully instrumented F-84 horizontal stabilizer specimens on which they collected the test data. They also supplied several items of sled borne instrumentation. AAI designed, developed, and maintained the test sled and the ASD test specimens. They assisted BRL and EAFB in the field tests of the BRL specimens. They conducted the tests on the ASD specimens both at EAFB and Wallops Island, Virginia, including the collection and reduction of the raw data. EAFB operated the test sled, prepared the test site and supplied the many services necessary to the operation of a test program at their high speed track facility.

The program began in April 1960, with effort concentrated on the design and development of the test sled and its instrumentation. The sled was designed to use electronics and recorders supplied by BRL and ASD and specimen instrumentation was selected for both the BRL and ASD specimens that was compatible with this equipment. The sled was delivered in August 1960 and field tests at EAFB began in September 1960 and continued through April 1961. A total of twenty-three (23) tests were accomplished. Twenty (20) of the tests were run by BRL on their F-84 stabilizer specimens and three (3) tests were made on an ASD specimen. Instrumentation problems caused by the sled environment forced suspension of further tests on the ASD specimens until suitable instrumentation can be developed. Part of the ASD test program, the airloads data, was transferred to NASA's Wallops Island shock tube facility, and six (6) tests were accomplished there during July and August 1961. The remainder of the ASD test program, the testing of the structural models, was cancelled from this program and tentative plans made to include these tests in ASD's contemplated "Big Sea" program.

The data collected from the tests of the BRL specimens will be processed and the results reported by BRL. The three (3) tests on ASD specimens at EAFB did not produce useable results. However, five of the six tests at Wallops Island produced good data and this information has been

processed and the results are published in Volume II of this report.



## 2.0 SLED VEHICLE DESIGN

### 2.1 GENERAL DESCRIPTION

The blast sled consists of three major components. The first of these is the forward fuselage. This component must provide a readily accessible receptacle for all of the test specimens anticipated in the Joint ANAF Sled Test Program and Project "Big Sea." In addition, it must simulate the aerodynamic regime associated with a typical supersonic aircraft. The second component is the instrumentation compartment which is located immediately aft of the forward fuselage. It houses all of the instrumentation necessary to record the pertinent structural and aerodynamic data for each run. The third component is the motor cage. For the Mach 0.8 runs this unit acts as the first stage providing initial propulsion from (1) XM5 motor which is sustained upon burn out by two HVAR motors. For the Mach 1.5 runs first stage propulsion is provided by a seven MD-1 motor pusher vehicle. The second stage propulsion is provided by 1 genie motor which is sustained by two HVAR motors. Having summarized the function of the various components of the blast sled, the structural configuration will now be considered in greater detail. See Fig. 2.1.1.

An 1/8 inch thick 6061-T6 aluminum nose cone having a 2:1 fineness ratio is welded to the fuselage body. The internal structure of the nose cone helps to support the pressure boom which engages the apex of the nose cone.

The cylindrical fuselage body is a weldment constructed primarily of 5/8 inch thick 5086-H32 aluminum. The fuselage has a slot in its top 4.5 inches wide, 11 inches deep and 74 inches long. The purpose of the slot is to provide a receptacle for all of the test specimens anticipated in the Joint ANAF Sled Test Program and Project "Big Sea." Provision has been made along the length of the slot for a staggered bolt pattern with holes 6 inches on center. The bolts are provided to clamp the specimen to the fuselage. Access to these bolts is facilitated by removable side panels.

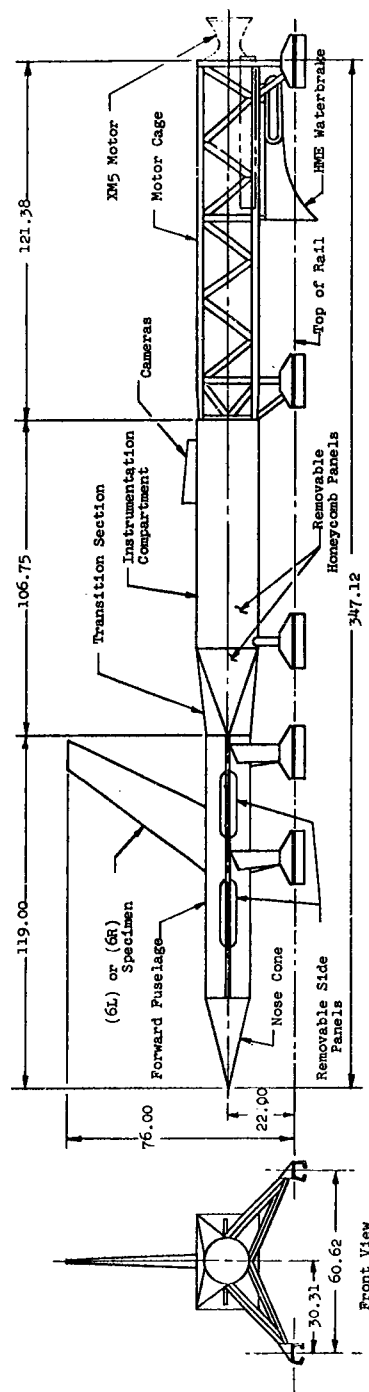
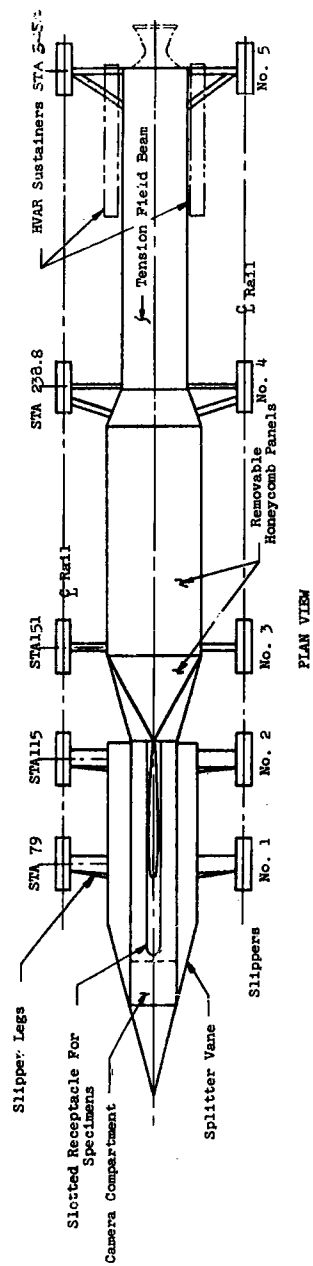


Figure 2.1.1 TEST SLED - THREE VIEW DRAWING

The fuselage body is supported by two sets of slipper legs 36 inches O/C. Each set of legs consist of four members having a wedge shape section with an approximate fineness ratio of 3:1. The legs are a weldment constructed from 3/16 inch T-1 steel plate. The members are bolted to the fuselage at such locations as to carry the large torsional moments in the most efficient manner, and at the same time limit aerodynamic interferences to a minimum.

A small compartment is provided in the fuselage between the nose cone and specimen slot to mount a camera which will record specimen deflections during sled runs.

An adapter for the F-84 test specimen serves to transfer the loads acting on the BRL mount to the forward fuselage of the sled. It consists of an aluminum plate 42 inches long, 22 inches wide and 1 inch thick made of 5086-H32 aluminum which mates with the 3/4 inch thick aluminum plate on the bottom of the mount. The two plates are held together with eight 7/16 inch bolts. Four inclined aluminum posts welded to the bottom of the 1 inch plate and bolted to the side of the forward fuselage provides the resisting couple necessary to carry the bending moment acting on the specimen. Two aluminum stems are also welded to the bottom of the 1 inch thick aluminum plate. These stems are inserted in the longitudinal slot in the forward fuselage and transfer the horizontal blast load acting on the F-84 specimen to the fuselage.

The instrumentation compartment consists of two sections. The aft portion of the compartment has a rectangular cross section 32 inches wide, 21 inches high and 77.9 inches long. The forward portion of the compartment is a transition section 29 inches long, tapering from the 32 inch by 21 inch aft section to the 15 inch diameter forward fuselage. The structure of the instrumentation section consists of a skeleton frame weldment.

The frame is made primarily from 1/4 inch 6061-T6 aluminum angles. Removable honeycomb panels are bolted to the four sides of this frame to provide ready access to the instrumentation. Several intermediate bulkheads are provided along the frame to serve as a mounting surface for the instrumentation packages. A secondary tubular truss system runs down the middle of the instrumentation compartment to help support the static loads when the side panels are removed. The instrumentation compartment has a single set of slipper legs located at the bulkhead immediately aft of the transition section. The slipper legs which are made up from 4130 steel tubing are bolted to the aluminum frame. Additional support for the instrumentation compartment is provided by bolted connections to the forward fuselage and motor cage.

The motor cage consists primarily of a rectangular truss system 22 inches wide, 21 inches high and 107.5 inches long. The two side trusses are of the Warren type, and the bottom truss is of the K type. All of the trusses are welded up from 4130 steel tubing. A tension field beam was provided in the top plane of the motor cage in order to have a member which could carry the blast loads and at the same time be readily removable in order to facilitate overhead loading of the motors. The motor cage is supported at its forward and aft ends by a set of 4130 steel tubular struts welded to T-1 steel frames. The aft panel of the bottom truss consists of a welded 1/4 inch thick T-1 torque box which provides a mounting surface for the probe brake and the H.M.E. adapter.

## 2.2 DESIGN

This section is devoted to the analysis of the rocket sled test vehicle used on the JANAF Sled Test Program and to be used on Project "Big Sea". The sled will be designed in accordance with the requirements set forth in Exhibit A of Contract AF33(616)-7099, WADD TR 60-117 and supplemental directives from the project officer. To follow the contents of this section, the appropriate AAI drawings 2113-040001-50 should be reviewed, along with material presented in Sections 2.32 and 2.33 aerodynamic and performance analysis.

### 2.2.1 DESIGN CRITERIA

The following loading conditions and performance characteristics are taken from Exhibit A of Contract AF33(616)-7099 and WADD TR 60-117. These criteria are used as the basis for the stress analysis in the following sections.

#### 2.2.1.1 PERFORMANCE CHARACTERISTICS

The sled shall be capable of attaining and sustaining the test Mach numbers of 0.4, 0.8 and 1.5. The design of the sled for the joint program shall be made utilizing model M5E1 NIKE booster units to attain 0.8 Mach no. and HVAR units to sustain the velocity. The sled shall be designed for project "Big Sea" with minimum modification utilizing MD-1 rocket motors (2K536250) and a pusher vehicle to attain (and sustain, if necessary) the test velocities.

#### 2.2.1.2 LOADING CONDITIONS

The critical load combinations which dictate the design of various components of the rocket sled shall be chosen from the Mach 0.8 and Mach

1.5 sled runs, with the associated blast overpressures. It is necessary to exercise engineering judgement in selecting the critical load conditions since it is not practical to consider all of the runs where the loads are continually changing with time.

In the analysis of conventional rocket sleds which are not subjected to large external loads, it is customary to consider loads which result from track-induced and/or aerodynamically-induced sled vibrations. This is frequently done by assuming a particular (g) level associated with the vibration. In this program, however, extremely large external loads are being applied to the sled by the blast. Since these loads are large as compared with the assumed sled vibration loads, the latter are considered insignificant and neglected in the load analysis which follows.

1) Inertia Loads - The longitudinal accelerations and decelerations along with the associated thrusts are obtained from the performance trajectories for the Mach 0.8 and Mach 1.5 sled runs. The two critical points chosen from these trajectories are points of maximum acceleration and maximum deceleration. (See Section 2.3.2)

2) Aerodynamic Loads - Those loads resulting from the aerodynamic characteristics of the vehicle shall be imposed upon the structure in combination with the associated inertia load at the design condition.

3) Blast Loads - The most severe blast condition encountered during the (BRL) series of runs occurs during the Mission #30, (Ref. 30). This test run is made with the vehicle at rest, and the sled forebody supporting the F-84 tail. The blast characteristics for this run are summarized on the following page, and the time histories of pressure loading on various portions of the sled are presented in Figures 2.3.11 and 2.3.13.

BRL MISSION NO. 30

SLED VELOCITY	v	-	0
OVERPRESSURE	i	-	17.6 psi
OVERPRESSURE	r	-	44.1 psi
IMPULSE	i	-	164.2 psi - msec
IMPULSE	r	-	410.4 psi - msec
DURATION	$\begin{matrix} p^+ \\ p \end{matrix}$	-	23.4 msec

4) Design Loads - All structural components of the sled shall be designed to the limit and ultimate loads as described below.

a) Limit Load - When the limit loads are applied to the structure and then removed, the structure shall not experience permanent set. Limit loads are the actual loads multiplied by 1.3.

b) Ultimate Load - When the ultimate loads are applied to the structure and then removed, the structure may experience permanent set but no failure will occur. Ultimate loads are the actual loads multiplied by 2.0.

2.2.2 STRUCTURAL ANALYSIS

The following structural analyses have been included to indicate the structural integrity of the forward fuselage, slipper legs, instrumentation compartment, and the motor cage sections of the sled. The detailed stress analysis of many elements has been omitted. However, the method of approach in considering the dynamic nature of the various loads imposed on the sled should be evident from the following analysis.

#### 2.2.2 1 FORWARD FUSELAGE

The forward fuselage is a 15" diameter cylinder 119" long. It is a weldment constructed entirely of 5086-H32 aluminum. This material was chosen because of its high strength - weight ratio, ease of fabrication and the elimination of local instability problems. The main body is supported by two sets of slipper legs 36" on centers. The fuselage has a slot in its top 4.5" wide, 11" deep and 74" long. The purpose of the slot is to provide a receptacle for all airfoil specimens anticipated in this, and future projects. Provision has been made along the length of the slot for a staggered bolt pattern with holes 6" on center. The bolts are provided to clamp the specimen to the fuselage. Access to these bolts is provided by removable side panels 4" wide and extending between slipper legs. See Figure 2.1.1.

It was necessary to make the fuselage cross-section a closed configuration so far as possible in order to carry the large torsional loads emanating from the test specimen, as efficiently as possible. In order to preserve the torsional capacity of the chosen section, structural shear connections are necessary between the removable side panels and the fuselage.

It is quite difficult to obtain an exact solution of the response of the fuselage to the dynamic blast loading. To simplify the solution the following assumptions were made:

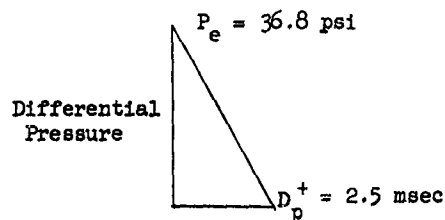
- A. The main body of the sled is hinged at slipper #2.
- B. The effect of the nose cone can be omitted when determining the response of the forward fuselage.
- C. The time function of the blast load may be approximated by a triangular shaped impulse.
- D. The response of the forward fuselage may be approximated by a single degree of freedom system such that:



1. The characteristic shape of the actual system may be approximated by the deflected shape under a uniform loading.
  2. The external work done by the equivalent system is equal to that done by the actual system.
  3. The kinetic energy of the equivalent system is equal to that of the actual system.
- E. The slipper leg supports will be considered as being rigid.
- F. The actual failure loads for the F-84 as given by BRL will be multiplied by the same D.L.F. that is found for the uniform blast loading on the side of the fuselage.
- G. The most severe blast load experienced by the sled occurs during mission #30. During this load the sled is at rest, and will not experience any inertia or aerodynamic loads.
- H. Assume the shear load in the forward fuselage is equal to the peak load applied statically. This is conservative since the magnification factor will be somewhere between 0.9 and 1.0.
- I. Assume that the 898000 in-lb torque applied to the sled fuselage by the F-84 wing is divided equally between the first and second sets of slipper legs. A D.L.F. of 2.0 will conservatively be applied to this torque in view of the difficulty of a torsional dynamic analysis.

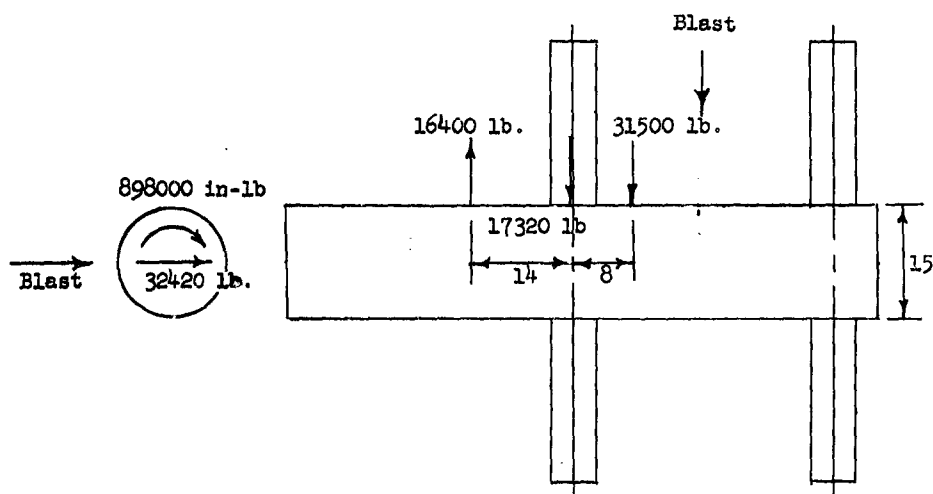
### LOADING CONDITIONS - ACTUAL

The blast load on the side of the fuselage will be approximated by an equivalent triangular impulse. See Aerodynamic Section 2.3.3, Figure 2.3.13.



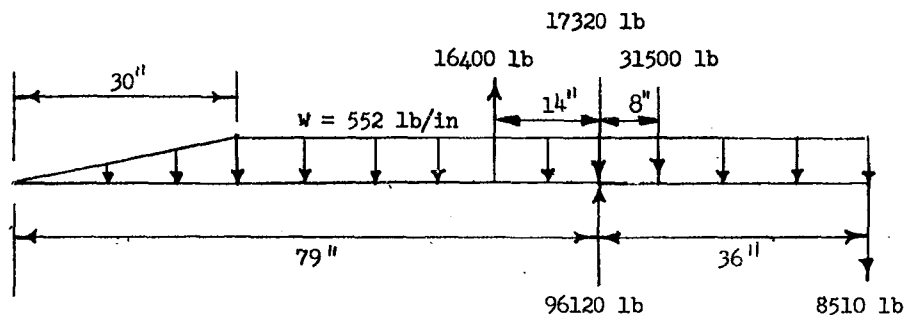
### EQUIVALENT TRIANGULAR BLAST IMPULSE

The blast pressure loading emanating from the F-84 wing will be applied at the centerline of the sled body. This loading was supplied by BRL.



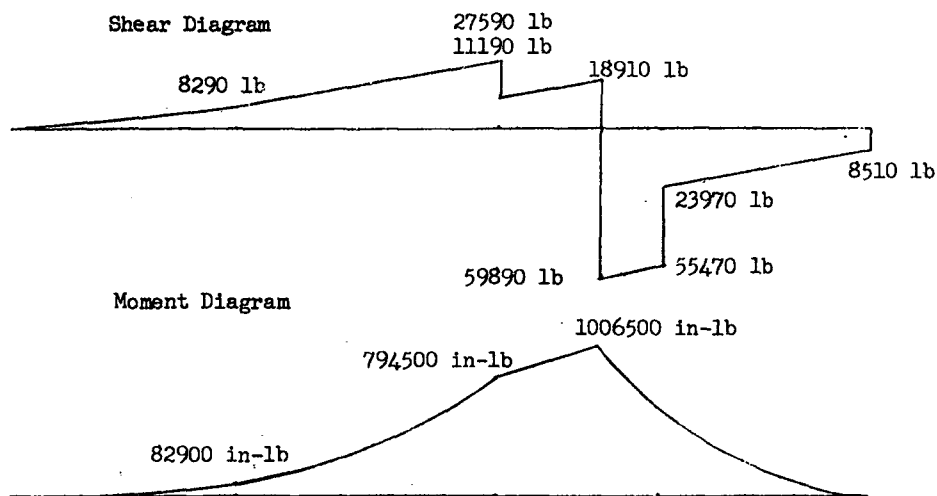
PLAN VIEW OF FORWARD FUSELAGE AND APPLIED LOADING CONDITIONS

COMBINED LOADS ON FORWARD FUSELAGE



The  $17320 \text{ lb}$  load is due to the blast loading acting on the BRL Mount and Adapter

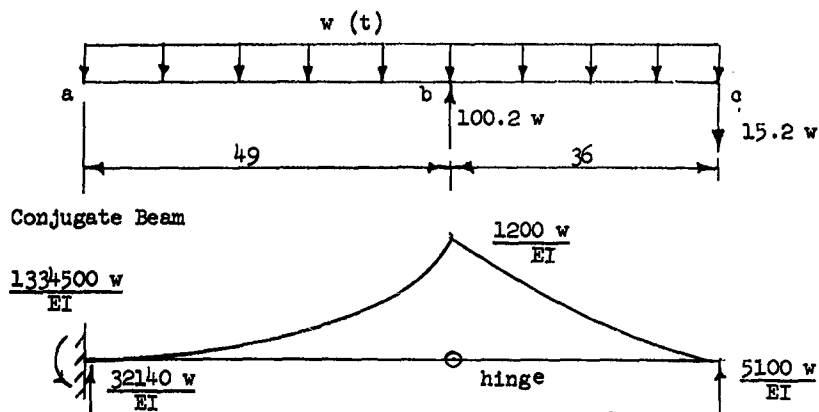
$$w = 36.8 \times 15.0 = 552 \text{ lbs/in.}$$



# RESPONSE OF FORWARD FUSELAGE

The procedures used here for obtaining the Dynamic Load Factor (D.L.F.) are outlined in Ref. (16), Sec. 7.5. The loads on, and stiffness of the nose cone will be omitted.

## Solution for the Characteristic Shape of the Forward Fuselage Load Diagram



Deflection of the Span bc, origin @ c

$$\Delta_{bc} = \frac{w}{EI} \left[ \int_0^x \left( 15.2 x' + \frac{x'^2}{2} \right) (x - x') dx - 5100 x \right]$$

$$\Delta_{bc} = \left( \frac{15.2 x^3}{6} + \frac{x^4}{24} - 5100 x \right) \frac{w}{EI}$$

Deflection of the Span ab, origin @ a

$$\Delta_{ab} = \frac{w}{EI} \left( 1334500 - 32140x + \int_0^x \frac{x'^2}{2} (x - x') dx \right)$$

$$\Delta_{ab} = \frac{w}{EI} \left( 1334500 - 32140x + \frac{x^4}{24} \right)$$

Deflection of the point a is

$$\Delta_a = \frac{w}{EI} 1334500$$

$$w = \frac{\Delta_a EI}{1334500}$$

Hence, the deflections of spans bc and ab can be written as:

$$\Delta_{bc} = \left( \frac{+15.2 x^3}{6} + \frac{x^4}{24} - 5100 x \right) \frac{\Delta_a}{1334500}$$

$$\Delta_{ab} = \left( 1334500 - 32140 x + \frac{x^4}{24} \right) \frac{\Delta_a}{1334500}$$

Solution for the Load Factor ( $K_L$ )

Total work done by actual load is

$$\begin{aligned} W_a &= \int_0^L \frac{w \Delta_{ac}}{2} dx \\ W_a &= \frac{w}{2} \int_0^{49} (1334500 - 32140x + \frac{x^4}{24}) \frac{\Delta_a}{1334500} dx \\ &\quad + \frac{w}{2} \int_0^{36} \left( \frac{15.2 x^3}{6} + \frac{x^4}{24} - 5100x \right) \frac{\Delta_a}{1334500} dx \\ W_a &= 10.62 w_a \Delta_a \end{aligned}$$

Total work done by equivalent load is

$$W_e = \frac{w_e 85 \Delta_e}{2}$$

But, from the previously listed assumptions,

$$w_a = w_e, \text{ and } \Delta_a = \Delta_e$$

Hence,

$$10.62 w_a \Delta_a = \frac{85}{2} w_e \Delta_e$$

$$w_e = 0.25 w_a$$

$$\text{or } K_L = 0.25$$

Solution for the Mass Factor ( $K_m$ )

velocity of span ab Proportional to  $\Delta$

$$V_{ab} = \frac{w}{EI} (1334500 - 32140 x + \frac{x^4}{24}) K$$

$$V_a = K \frac{w}{EI} 1334500 \quad (x = 0)$$

$$V_{ab} = \frac{V_a}{1334500} (1334500 - 32140 x + \frac{x^4}{24})$$

velocity of span bc

$$V_{bc} = \frac{w}{EI} (+ \frac{15.2 x^3}{6} + \frac{x^4}{24} - 5100 x)$$

$$V_{bc} = \frac{V_a}{1334500} (+ \frac{15.2 x^3}{6} + \frac{x^4}{24} - 5100 x)$$

Total Kinetic Energy of the actual system is:

$$KE_a = \int_0^L \frac{1}{2} m V_{ac}^2 dx$$

$$\begin{aligned}
K.E._a = & \frac{v_a^2 m_a}{2} \int_0^{49} \left[ (1334500) - 64280 x + \frac{x^4}{12} + 774 x^2 \right. \\
& \left. - \frac{32140 x^5}{16014000} + \frac{x^8}{768672000} \right] \frac{dx}{1334500} \\
& + \frac{v_a^2 m_a}{2} \int_0^{36} \left( 6.41 x^6 + \frac{15.2 x^7}{72} - 25840 x^4 + \frac{x^8}{576} \right. \\
& \left. - \frac{5100}{12} x^5 (5100)^2 x^2 \right) \frac{dx}{(1334500)^2}
\end{aligned}$$

$$\begin{aligned}
K.E._a = & \frac{v_a^2 m_a}{2} (49.0 - 57.8 + 3.53 + 22.70 - 3.47 + 0.18 \\
& + 0.04 + 0.042 - 0.175 + 0.012 - .0865 + 0.227)
\end{aligned}$$

$$K.E._a = 7.1 v_a^2 m_a$$

The Kinetic Energy of the equivalent single degree of freedom system is

$$K.E._e = \frac{1}{2} M_e v_e^2 = 42.5 m_e v_e^2$$

but, from assumptions

$$K.E._a = K.E._e \quad \& \quad v_e = v_a$$

$$7.1 v_a^2 m_a = 42.5 m_e v_e^2$$

$$m_e = .167 m_a$$

$$K_m = 0.167$$

Solution for the Spring Constant of the Equivalent System

$$K_e = \frac{w \cdot 85 EI (0.25)}{w \cdot 1334500} = \frac{EI}{63000} \text{ lb/in}$$

$$E = 10 \times 10^6 \text{ psi}$$

$$I = 870 \text{ in}^4$$

$$K_e = 1.66 \times 10^6 \text{ lb/ft}$$

$$m_a = 5.75 \text{ lb/in}$$

$$M_e = \frac{(5.75)(85)(0.167)}{32.2} = 2.54 \text{ lb-sec}^2/\text{ft}$$

Solution for the Natural Period of the Equivalent System

$$T_n = 2\pi \sqrt{\frac{M_e}{K_e}} = 2\pi \sqrt{\frac{2.54}{1.66 \times 10^6}}$$

$$T_n = .00776 \text{ Sec.}$$

From the  $D_p^+/T_n$  ratio,

$$D_p^+/T_n = \frac{.0025}{.00776} = .322$$

and Figure 7.11, Reference (16), the Dynamic Load Factor (D.L.F.)

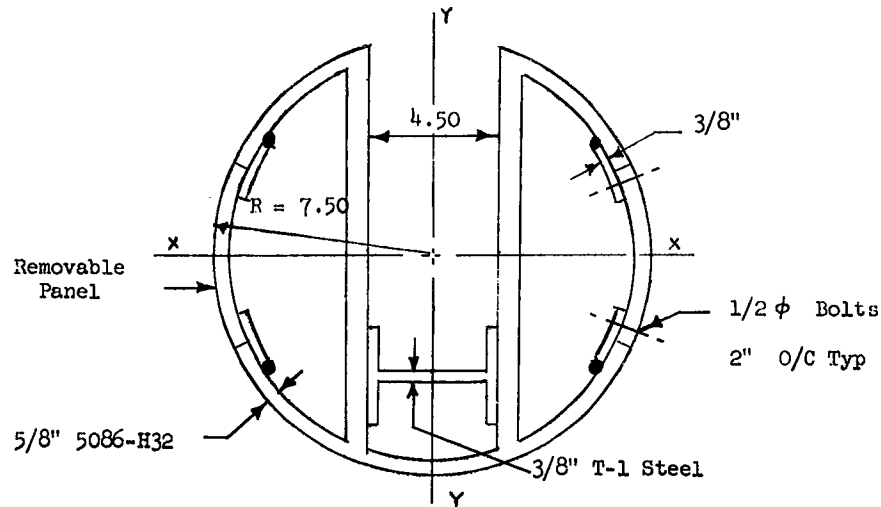
is found to be:

$$\text{D.L.F.} = 0.9$$

The forward fuselage is now analyzed as a structure under static loading using the above D.L.F. = 0.9; the critical section to be analyzed is located at the forward set of slipper legs.



# TYPICAL CROSS SECTION OF FORWARD FUSELAGE



## TORSION

Assume Forward Slippers take 1/2 of Applied Torque; D.L.F. = 2.0

$$M_t = (2.0) \left( \frac{898000}{2} \right) (1.3) = 1,168,000 \text{ in-lb YIELD}$$

$$f_s = \frac{M_t}{2At}$$

$$f_s = \frac{1168000}{(2)(110)(.625)} = 8500 \text{ psi YIELD}$$

$$F_{sy} = (17500)(0.9) = 15750 \text{ psi (After Welding)}$$

## BENDING

$$M_{by} = (0.9)(1006500)(1.3) = 1180000 \text{ in-lb YIELD}$$

$$Z_y = 116 \text{ in}^3$$

$$f_{by} = \frac{1180000}{116} = 10180 \text{ PSI}$$

$$F_{by} = (28000)(0.9) = 25200 \text{ PSI (After Welding)}$$

## SHEAR

The shear on the 5/8" aluminum web at section Y-Y will be checked by transforming the steel to aluminum. (i.e. the web thickness of the

steel I beam will be increased by ratio of  $E_{st}/E_{AL} = 3$ ).

$$V = (1.0) (59890)(1.3) = 77800 \text{ lb. YIELD}$$

$$f_s = \frac{VQ}{I_{b_{\text{transformed}}}} = \frac{77800 \times 86.7}{870.6 \times 1.750}$$

where:

$$b = .625 + 3 (.375) = 1.75 \text{ in.}$$

Q = Static moment of transformed cross section about Y-Y axis

I = Total moment of inertia of transformed cross section about Y-Y axis.

$$f_s = 4420 \text{ psi YIELD}$$

Checking the combined stress at the aluminum panel.

$$R_b = \frac{f_{by}}{F_{by}} = \frac{10180}{25200} = .404$$

$$R_s = \frac{f_s}{F_{sy}} = \frac{8500}{15750} = .540$$

The margin of safety is computed to be

$$M.S. = \frac{1}{(.404)^2 + (.540)^2} - 1.0 = +0.48$$

Checking the combined stress at the aluminum shear web

$$f_s = 8500 + 4420 = 12920 \text{ psi}$$

$$F_{sy} = 15750$$

The margin of safety is found to be

$$M.S. = \frac{15750}{12920} - 1.0 = +0.22$$

Shear Connection Between Removable Door and Fuselage

(AN-8 Bolts 2in. o/c)

$$V = 2(5/8)(8500) = 10620 \text{ lb/bolt YIELD}$$

Allowable Shear on the Bolt (single shear)

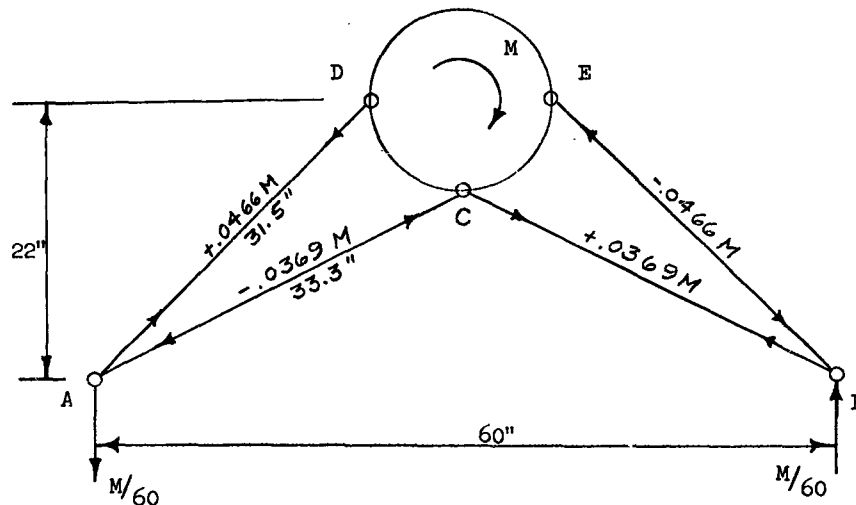
$$V_{all} = 12100 \text{ lb. Yield Ref. 20, Table 8.1.1.1.1. (a)}$$

$$M.S. = \frac{12100}{10620} - 1.0 = +.14$$

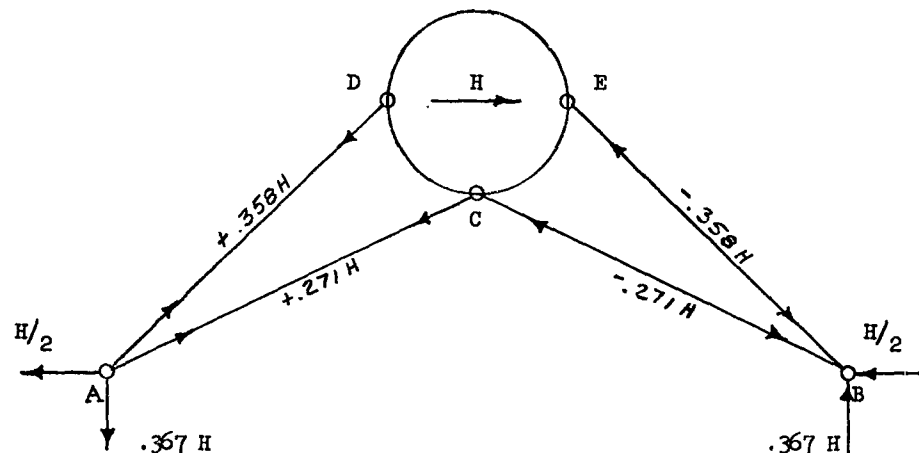
#### 2.2.2.2. SLIPPER LEGS

Two sets of slipper legs on 36 inch centers support the forward fuselage. Each set of legs consists of four members having a wedge shape built up from 3/16 in. T-1 steel plate. The T-1 steel plate was chosen primarily for its weldability, rigidity and high strength-weight ratio. The wedge shaped sections were chosen to minimize drag and interference effects on the test specimen. The members which are approximately 33 in. long are bolted to the fuselage at such locations as to carry the large torsional moments in the most efficient manner. In analyzing the slipper leg configuration, the fuselage was assumed to be a rigid body, and the ends of the legs were assumed to be pinned at the slippers and at the fuselage. When computing the equivalent  $L/\rho$  for the slipper legs, a factor of 0.8 was applied to account for the partial fixity at the fuselage.

SLIPPER LEG LOADING IN TERMS OF A UNIT MOMENT  $M$



# SLIPPER LEG LOADINGS IN TERMS OF A HORIZONTAL FORCE H



## RESPONSE OF FORWARD SLIPPER LEGS

Assume the legs act as a spring and the mass of the system is concentrated at the C.G. of the fuselage. The lateral and rotational response will be considered independently.

### LATERAL RESPONSE:

Spring Constant:

$$K = \frac{1}{\sum \frac{u^2 L}{AE}} = 5.55 \times 10^6 \text{ lb/in.}$$

where:  $A = 2.40 \text{ sq. in.}$   $L = \text{Length of Member}$

$E = 30 \times 10^6 \text{ psi}$

$u = \text{bar force due to a unit load (H)}$

Mass:

The weight of the forward fuselage and F-84 wing and mount acting on the forward slipper legs will be taken as 950 lbs.

$$m = \frac{950}{32.2 \times 12} = 2.46 \text{ lb-sec}^2/\text{in.}$$

Natural Period:

$$T_n = 2\pi \sqrt{\frac{m}{K}} = 2\pi \sqrt{\frac{2.46}{5.55 \times 10^6}}$$

$$T_n = 0.00417 \text{ sec.}$$

$$D_p^+ = 0.0025 \text{ sec.}$$

$$D_p^+ / T_n = \frac{0.0025}{0.00417} = 0.60$$

$$D.L.F. = 1.20 \quad \text{from (Ref. 16, Fig. 7.11)}$$

#### TORSIONAL RESPONSE

Spring Constant:

$$K = \frac{1}{\sum \frac{u_L^2}{AE}} = 316 \times 10^6 \text{ in-lb/rad}$$

Where:  $A = 2.40 \text{ sq. in.}$

$E = 30 \times 10^6 \text{ psi}$

$L = \text{Length of Member}$

$u = \text{bar force due to a unit moment (M)}$

Moment of Inertia (Mass)

$$I = \frac{W}{g} \frac{D^2}{8} = \frac{950}{386} \frac{(15)^2}{8} = 69.4 \text{ Lb-Sec}^2\text{-in}$$

Natural Period:

$$T_n = 2\pi \sqrt{\frac{I}{K}} = 2\pi \sqrt{\frac{69.4}{316 \times 10^6}}$$

$$T_n = 0.00294 \text{ sec.}$$

$$D_p^+ = 0.0025 \text{ sec.}$$

$$D_p^+ / T_n = \frac{0.0025}{0.00294} = 0.85$$

$$D.L.F. = 1.40 \quad \text{from (Ref. 16, Fig. 7.11)}$$

# SLIPPER LEG LOADING

Torque:

$$M_t = (898000) (1.4) (2.0) = 2515000 \text{ in-lb ULT}$$

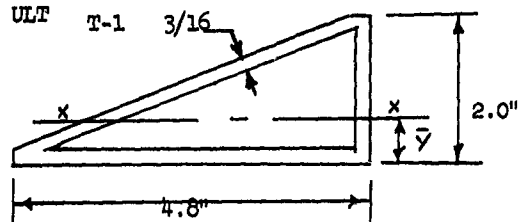
Horizontal Force:

$$H = (96120) (1.2) (2.0) = 231000 \text{ lb. ULT}$$

Member EB (Minimum Section)

$$P = (.0466) (2515000) + (.358) (231000)$$

$$P = 199,900 \text{ lb. ULT}$$



Section Through Slipper Leg  
at the Slipper

$$A = 2.11 \text{ sq. in.}$$

$$\bar{Y} = .627 \text{ in.}$$

$$I_x = .832 \text{ in.}^4$$

$$\rho_x = .628 \text{ in.}$$

$\rho$  = radius of gyration

Use average value of  $\rho$  for maximum and minimum section and an end fixity factor of 0.8.

Compression:

$$f_c = \frac{199900}{2.11} = 94740 \text{ psi ULT}$$

$$\frac{Le}{\rho_{av}} = \frac{26.0 \times 0.8}{0.712} = 29.2$$

$$F_c = 105000 \text{ psi T-1 (Reference 31, Figure 20)}$$

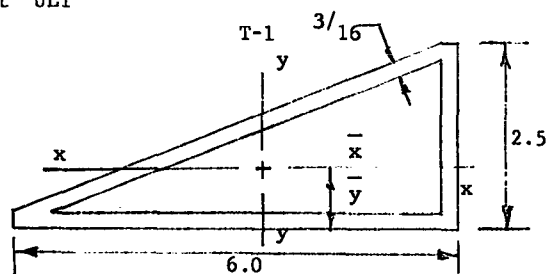
$$M.S. = \frac{105000}{94740} = +0.11$$

Member EB (Maximum Section)

Bending: Due to longitudinal inertia of slipper assembly; assume 25.0g (actual). Assume each slipper leg carries 1/2 the longitudinal inertia load.

$$M_{max} = \frac{25 \times 84.6 \times 31.5 \times 2.0}{2}$$

$$M_{max} = 66600 \text{ in-lb/strut ULT}$$



Section Through Slipper Leg at the Fuselage

$$A = 2.69 \text{ sq. in.}$$

$$\bar{Y} = .780 \text{ in.}$$

$$I_x = 1.70 \text{ in}^4$$

$$\rho_x = .796 \text{ in.}$$

$$\bar{X} = 2.53 \text{ in.}$$

$$I_y = 9.83 \text{ in}^4$$

$$Z_y = 2.83 \text{ in}^3$$

$$f_b = \frac{66600}{2.83} = 23500 \text{ psi} \quad \text{ULT}$$

$$F_b = 115000 \text{ psi} \quad \text{ULT} \quad (\text{Reference 31})$$

Compression:

$$f_c = \frac{199900}{2.69} = 74300 \text{ psi} \quad \text{ULT}$$

$$\frac{L_e}{\rho_{av}} = 29.2$$

$$F_c = 105000 \text{ psi} \quad \text{ULT} \quad (\text{Reference 31})$$

Combined Stress:

Assume maximum longitudinal inertia load and side blast load are applied simultaneously (conservative)...

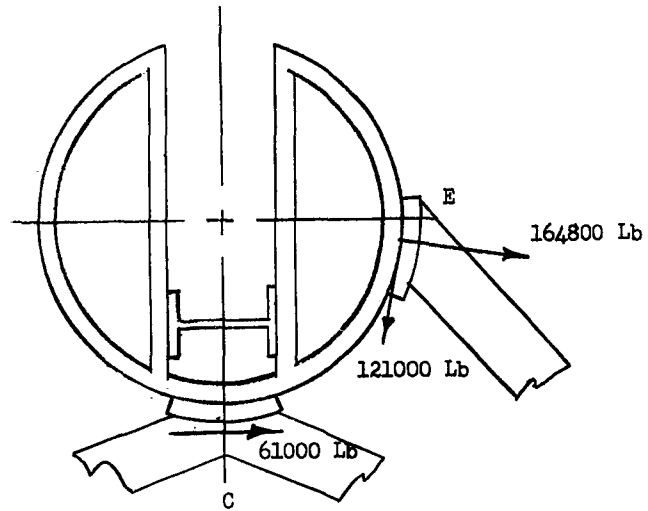
$$\frac{f_c}{F_c} = \frac{74300}{105000} = .708$$

$$\frac{f_b}{F_b} = \frac{23500}{115000} = .204$$

$$M.S. = +0.09$$

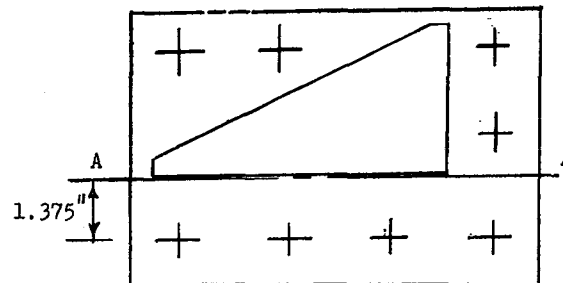


# CONNECTION OF SLIPPER LEGS TO FUSELAGE



CONNECTION E

8 - AN10 Bolts



#### TENSION ON BOLTS

$$T = \frac{164800}{8} = 20600 \text{ lb ULT}$$

#### SHEAR ON BOLTS

$$V = \frac{121000}{8} = 15130 \text{ lb ULT}$$

#### BENDING:

Assume linear stress distribution in bolt pattern

$$66600 = 16.4 P$$

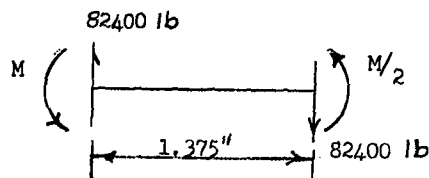
$$P = 4060 \text{ lb ULT}$$

#### COMBINED LOADS

$$\therefore \text{M.S.} = \frac{1}{\left(\frac{24660}{30100}\right)^2 + \left(\frac{15130}{23000}\right)^3} - 1.0 = +0.045$$

#### CHECK SECTION a-a FOR BENDING

Assume  $\frac{1}{2}$  the capacity of the section is developed at the bolt line due to clamping action of bolts.



$$M = \frac{82400 \times 1.375}{1.5} = 75500 \text{ in-lb ULT}$$

$$Z_p = \frac{bd^2}{4} = \frac{8.25 (.625)^2}{4} = .805 \text{ in}^3 \text{ (Plastic Section Modulus)}$$

$$f_b = \frac{75500}{.805} = 93800 \text{ psi}$$

$$F_b = 115000 \text{ psi}$$

$$\text{M.S.} = \frac{115000}{93800} - 1.0 = +0.228$$

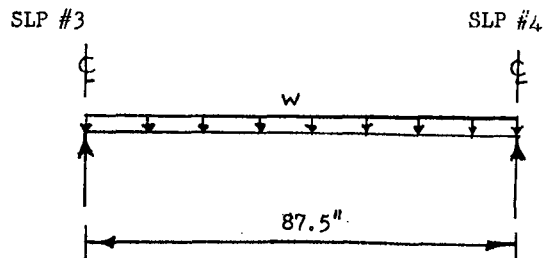
### 2.2.2.3 INSTRUMENTATION COMPARTMENT

The instrumentation section has an overall length of 106.9 inches. The aft portion of this compartment has a rectangular cross section 32 inches wide, 21 inches high and 77.9 inches long. The forward portion is a transition section 29 inches long, tapering from the 32 by 21 inch aft section to the 15 inch diameter forward fuselage. The primary structure of the instrumentation compartment consists of removable honeycomb panels and four longerons in the corners of the rectangular section. The top honeycomb panels are  $3/4$  inch thick and the side panels are 1.125 inches thick, both having .064 inch 2024-T3 aluminum facings. The longerons are  $1\frac{1}{2}$  by  $1\frac{1}{2}$  by  $\frac{1}{4}$  inch 6061-T6 built up aluminum angles. This type of construction was chosen because of its high strength-weight ratio, weldability and the accessibility it provides to service the instrumentation.

The maximum design load acting on the primary structure is the 44 psi reflected blast load which occurs while the sled is at rest. The instrumentation compartment is treated as a simple supported beam at stations 151.0 and 238.5. The response of the system to the dynamic blast load is approximated by converting the beam to an equivalent one degree system in accordance with the theory presented in Reference (16) and applying a triangular load having the same maximum amplitude and initial decay slope as the actual load.

A secondary tubular truss system runs down the middle of the instrumentation compartment to carry the 1 g loads which occur when the side panels are off.

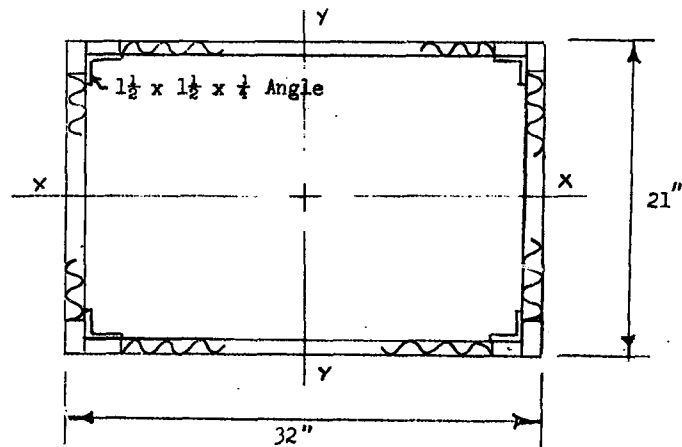
Four bulkheads are provided along the compartment to mount the instrumentation. These bulkheads must take the longitudinal, lateral and vertical inertia loads acting on the instrumentation.



ASSUME LOAD DISTRIBUTION ON  
INSTRUMENTATION COMPARTMENT

WEIGHT

Instrumentation	650 lb
Structure	<u>490</u>
	1140 lb



TYPICAL SECTION OF INSTRUMENTATION  
COMPARTMENT BETWEEN SLIPPERS #3 & #4

Assume instrumentation compartment structure has a constant moment of inertia, and assume the weight is uniformly distributed.

Moment of Inertia:  $I_y$

$$\text{Side Panels:} \quad 2.0 \times 2.69 \times (15.5)^2 = 1290$$

$$\text{Top \& Bottom Panels:} \quad \frac{0.256 (30)^3}{12} = 575$$

$$\text{Longerons:} \quad 2.0 \times 1.375 \times (14.5)^2 = 578$$

$$\text{Edge Member:} \quad 2.0 \times 3.58 \times (15.5)^2 = 1720$$

$$\text{Edge Member:} \quad 2.0 \times 1.88 \times (14.25)^2 = 764$$

$$I_y = 4927 \text{ in}^4$$

Assume aft instrumentation section is simply supported beam at slippers #3 and #4.

Equivalent System:

$$\text{Mass: } M_e = \frac{1140}{32.2} \times 0.5 = 17.70 \text{ lb-sec}^2/\text{ft}$$

$$\text{Spring Const: } K_e = \frac{384EI}{5L^3} \times K_R \quad (\text{Ref. 16, Table 7 1})$$

$$K_e = \frac{384 \times 10 \times 10^6 \times 4927 \times 0.64}{5 \times (87.5)^3}$$

$$K_e = 3.62 \times 10^6 \text{ lb/in. or } 43.5 \times 10^6 \text{ lb/ft}$$

Natural Period:

$$T_n = 2\pi \sqrt{\frac{M_e}{K_e}}$$

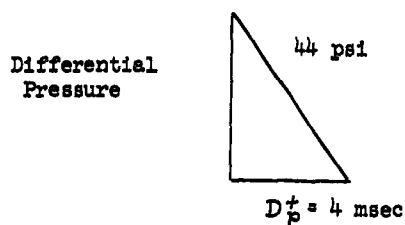
$$T_n = 2\pi \sqrt{\frac{17.70}{43.5 \times 10^6}} = 0.00401 \text{ SEC}$$

Load Duration (See Aerodynamic Section 2.3.3, Fig. 2.3.10)

$$D_p^+ = 0.004 \text{ seconds}$$

$$D_p^+ / T_n = \frac{.004}{.00401} = 1.00$$

∴ D.L.F. = 1.60 from Fig. 7.11 Ref. (16)

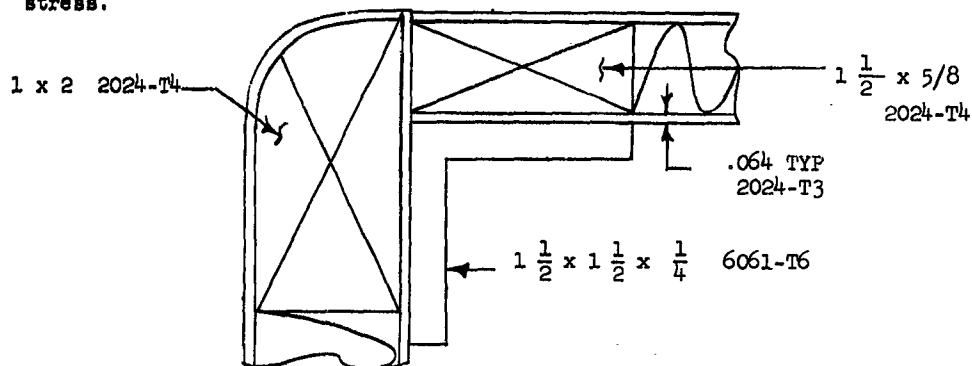


$$w = 21 \times 44 \times 1.3 = 1200 \text{ lb/in (yield)}$$

Bending:

$$M_{\max} = \frac{1.60 \times 1200 \times (87.5)^2}{8} = 1.84 \times 10^6 \text{ in-lb (yield)}$$

Assume only the longerons and edge members carry the bending stress.



CORNER STRUCTURE OF INSTRUMENTATION COMPARTMENT

Moment Carried by Longerons

$$M_L = 16000 \times 1.38 \times 29 = 640000 \text{ in-lb}$$

$$F_{ty} = 16000 \text{ psi (after welding) (yield)}$$

Moment Carried by Edge Member Side

$$M_S = 40000 \times 3.58 \times 31 = 4440000 \text{ in-lb}$$

$$F_{Ty} = 40000 \text{ psi 2024-T4 (yield)}$$

Moment Carried by Top and Bottom Edge Member

$$M_T = 40000 \times 1.88 \times 28.5 = 2140000 \text{ in-lb}$$

$$F_{Ty} = 40000 \text{ psi 2024-T4}$$

$$M.S. = \frac{7220000}{1840000} - 1.0 = +2.92 \text{ (yield)}$$

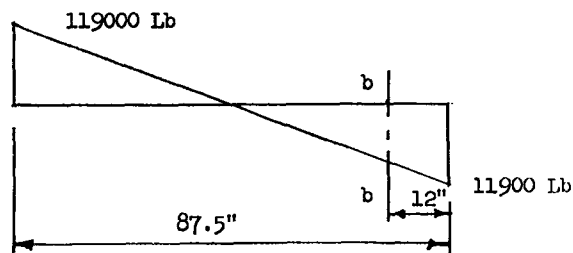
Shear:

$$V = 0.39 R + 0.11 \quad (\text{Table 7.1, Ref. 16})$$

$$V = 2.0 \left[ (0.39 \times 44 \times 21 \times 87.5 \times 1.6) + (0.11 \times 44 \times 21 \times 87.5) \right]$$

$$V = 119000 \text{ lb ULT}$$

Assume shear diagram varies linearly between slippers #3 and #4.



SHEAR DIAGRAM FOR INSTRUMENTATION COMPARTMENT

Assume faces of top and bottom panels carry shear.

$$V = 119000 \text{ lb. ULT}$$

$$A = 7.66 \text{ sq. in.}$$

$$f_s = \frac{119000}{7.66} = 15500 \text{ psi}$$

$$F_s = 40000 \text{ psi ULT 2024-T3 facing}$$

$$\text{M.S.} = \frac{40000}{15500} - 1.0 = +1.56$$

Connection of Side Panel to Longerons

$$v = \frac{VQ}{I} = \frac{119000 \times 3.58 \times 15.5}{3062 \times 2}$$

$$v = 1078 \text{ lb/in/side ULT}$$

Use 3/8 inch bolt, 6 inch o/c. (Bearing not critical)

$$v_{all} = \frac{8280}{6} = 1380 \text{ lb/in ULT}$$

$$\text{M.S.} = \frac{1380}{1078} - 1.0 = +.28$$

Connection of Top and Bottom Panel to Longerons

$$v = \frac{VQ}{I} = \frac{119000 \times 75.5}{3062 \times 2}$$

$$v = 1470 \text{ lb/in/side ULT}$$

Use 3/8 inch bolts 4.75 inch o/c

$$v_{all} = \frac{8280}{4.75} = 1740 \text{ lb/in ULT}$$

$$\text{M.S.} = \frac{1740}{1470} - 1.0 = +.118 \text{ ULT}$$



Connection of top and bottom panel to flanges of fore and aft bulkheads.

$V = 119000 \text{ Lb ULT}$

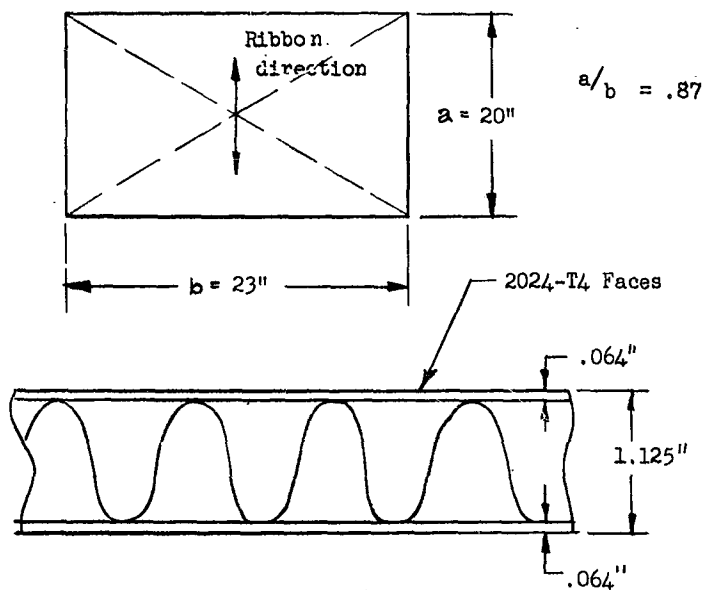
Use  $3/8"$  Bolts  $3.5"$  O/C

$V_{All} = 8280 \times 18 = 149000 \text{ Lb ULT}$

M.S. =  $\frac{149000}{119000} - 1.0 = +0.25$

#### SIDE PANELS

Assume Panels are simply supported



SECTION THROUGH SIDE PANEL

$$I = 2 \times .064 (.532)^2 = .0362 \text{ in}^4/\text{in}$$

Wt. of Panel

Faces	5.9
Core	4.2
TOTAL	10.1 lb.

Equivalent System (Ref. 16, Table 7.4)

$$\text{Mass: } M_e = M_t \cdot K_m$$

$$M_e = \frac{10.1 \times .37}{32.2} = 0.116 \text{ lb. sec}^2/\text{ft}$$

$$\text{Spring Constant: } K_e = \frac{242 EI_a \times K_R}{a^2}$$

$$K_e = \frac{242 \times 10 \times 10^6 \times .0362}{(20)^2} \times .47$$

$$K_e = 10.30 \times 10^4 \text{ lb/in}$$

$$K_e = 12.35 \times 10^5 \text{ lb/ft}$$

Natural Period.

$$T_n = 2\pi \sqrt{\frac{M_e}{K_e}}$$

$$T_n = 2\pi \sqrt{\frac{0.116}{1235000}} = .00192 \text{ Sec.}$$

$$R = 1/a (12 M_{pa} + 11.0 M_{pb})$$

$$m_p = \frac{W}{24.7}$$

$$D_p^+ = .004 \text{ Sec.}$$

$$D_p^+/T_n = \frac{.004}{.00192} = 2.10$$

$$D.L.F. = 1.80 \text{ (Ref. 16 Fig. 7.11)}$$

$$m_p = \frac{1.80 \times 460 \times 44 \times 1.30}{24.7} = 1920 \text{ in-lb/in (Yield)}$$

$$Z = \frac{.0362}{.564} = .0643 \text{ in}^3$$

$$f_b = \frac{1920}{.0643} = 29900 \text{ psi (Yield)}$$

$$F_{ty} = 40000 \text{ psi} \quad 2024 - T4 \quad (\text{Reference 21})$$

$$M.S. = \frac{40000}{29900} = + 0.34$$

Use 15.8 Lb/cu.ft. core

1/8" Cell Size

.004" Foil Gauge

Shear Strength

$$F_s^* = 1575 \text{ psi Longitudinal}$$

\*See Honeycomb Corp.  
of America Design  
Data.

$$F_s^* = 882 \text{ psi Transverse}$$

Shear:

$$V_A = 0.06 P + 0.16 R \quad (\text{Ref. 16 Table 7.4})$$

$$V_A = \left[ 0.06 (460 \times 44) + .16 (460 \times 44 \times 1.8) \right] 2.0$$

$$V_A = 14100 \text{ Lb ULT}$$

$$f_s = \frac{14100}{20 \times 100} = 705 \text{ psi ULT}$$

$$V_B = 0.08 P + 0.20 R$$

$$V_B = \left[ 0.06 (460 \times 44) + 0.20 (460 \times 44 \times 1.8) \right] 2.0$$

$$V_B = 17000 \text{ Lb ULT}$$

$$f_s = \frac{17000}{23 \times 1.00} = 740 \text{ psi ULT}$$

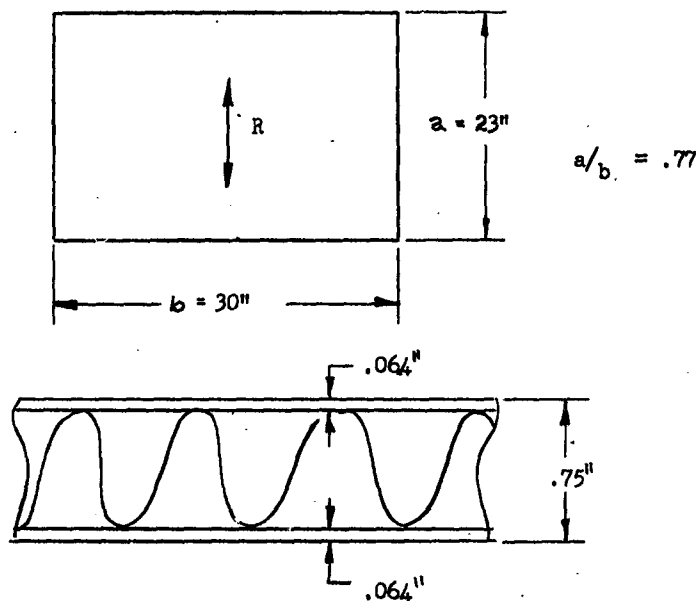
$$M.S. = \frac{882}{740} - 1.0 = + 0.19$$

Deflection:

$$\Delta_{\max} = \frac{1.8 \times 460 \times 44}{224,000} = 0.163" \text{ (Actual)}$$

Actual deflection will probably be larger due to shear deflection, which was neglected.

TOP AND BOTTOM PANELS



SECTION THROUGH TOP AND BOTTOM PANELS

$$I = 2 \times .064 (.343)^2 = .0151 \text{ in}^4/\text{in}$$

Equivalent System (Ref. 16, Table 7.4)

$$\text{Mass: } M_e = \frac{11.8 \times .35}{32.2} = .128 \text{ Lb-sec}^2/\text{ft}$$

Spring Constant:

$$K_e = \frac{228 EI_a}{a^2} K_R$$

$$K_e = \frac{228 \times 10^6 \times 10^6 \times .0151 \times .49}{(23)^2}$$

$$K_e = 3.19 \times 10^4 \text{ Lb/in}$$

$$K_e = 38.3 \times 10^4 \text{ Lb/ft}$$

Natural Period

$$T_n = 2\pi \sqrt{\frac{.128}{383000}} = .00363 \text{ sec.}$$

The top and bottom panels will feel the side-on positive overpressure for 23.4 msec decaying exponentially. The dynamic overstress factor will conservatively be taken as 2.0.

$$D.L.F. = 2.0$$

$$R = 1/a (12 M_{pa} + 10.3 M_{pb})$$

$$m_p = R/25.5$$

$$m_p = \frac{2.00 \times 690 \times 17.6 \times 1.30}{25.5}$$

$$m_p = 1237 \text{ in-Lb/in (Yield)}$$

$$Z = \frac{.0151}{.375} = .0402 \text{ in}^3/\text{in}$$

$$f_b = \frac{1237}{.0402} = 30700 \text{ psi (Yield)}$$

$$F_{by} = 40000 \text{ psi (Yield)}$$

$$M.S. = \frac{40000}{30700} - 1.0 = + 0.302$$

Shear:

$$V_A = 0.06 P + .14 R \quad (\text{Ref. 16 Table 7.4})$$

$$V_A = \left[ 0.06 (690 \times 17.6) + .14 (690 \times 17.6 \times 2.0) \right] 2.0$$

$$V_A = 8260 \text{ Lb ULT}$$

$$f_s = \frac{8260}{23 \times .625} = 574 \text{ psi}$$

$$V_B = 0.08 P + .22 R$$

$$V_B = \left[ 0.08 (690 \times 17.6) + .22 (690 \times 17.6 \times 2.0) \right] 2.0$$

$$V_B = 12620 \text{ Lb ULT}$$

$$f_s = \frac{12620}{30 \times .625} = 674 \text{ psi}$$

Use 11.9 Lb/cu.ft core

1/8" Cell Size

.003" Foil Gauge

Shear Strength

$$F_s = 1108 \text{ psi Longitudinal}$$

$$F_s = 633 \text{ psi Transverse}$$

$$M.S. = \frac{633}{574} - 1.0 = + 0.102$$

Deflection

$$\Delta_{max} = \frac{2.0 \times 690 \times 17.6}{65100} = 0.373" \text{ (Actual)}$$

#### 2.2.2.4 MOTOR CAGE

The motor cage has an overall length of 107.5". Its rectangular section is 22" wide, 21" high and is located behind the silhouette of the instrumentation compartment in order to minimize drag. The section is supported at its forward and aft ends by 4130 steel tubular struts. The main longerons are built up 1/4" thick T-1 boxes. The primary design loads come from braking at Mach 1.5, and compressive loads from the 7 genie pusher. The side truss web members are 2" O.D. 4130 steel tubing and they carry the shear loads associated with braking and vertical vibrations. A tension field beam in the top plane, and a welded steel tubular truss in the bottom plane provide the necessary shear capacity to carry the side blast pressures. The aft panel of the bottom truss consists of a welded 1/4" thick T-1 torque box which provides a mounting surface for the probe brake and transfers the braking loads into the side frame. During the Mach 0.8 runs the probe brake will be used without any tie rods. During the Mach 1.5 run the HME-6 water brake will be used, or the probe brake can be run if tie rods are added to transfer braking loads more efficiently.

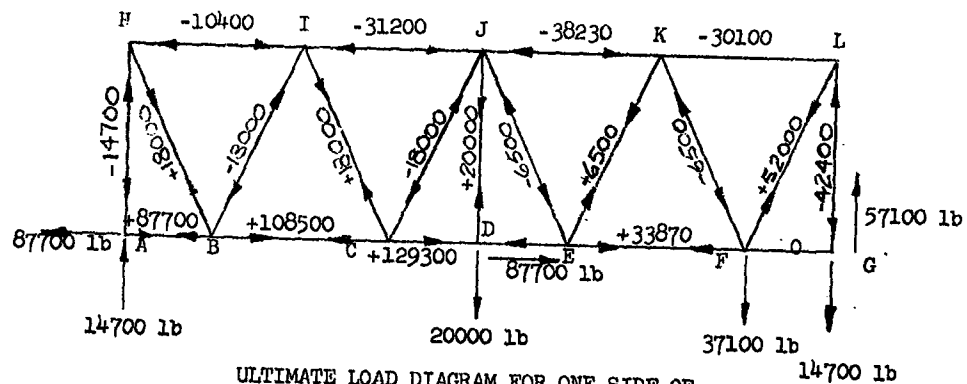
The aft frame of the motor cage is a combination rigid frame and truss. The top portion of the rigid frame is removable, in order to permit overhead loading of the motors. Seat clips are attached to the frame to provide motor support. The principal design load for the aft frame is the side blast loading.

The forward frame of the motor cage consists of a truss system to carry side blast loadings. Motor thrust is taken out in beam action by the top and bottom truss members.

Braking Load @ Mach 1.5

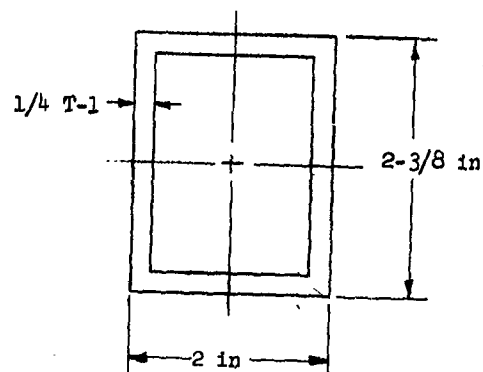
Probe Brake and Tie Rod

Braking Force = 87700 Lb. Applied



ULTIMATE LOAD DIAGRAM FOR ONE SIDE OF  
MOTOR CAGE TRUSS  
Member AG

Load = + 129300 Lb. ULT (Tension)



$$A = 1.93 \text{ in}^2$$

$$f_t = \frac{129300}{1.93} = 67000 \text{ psi}$$

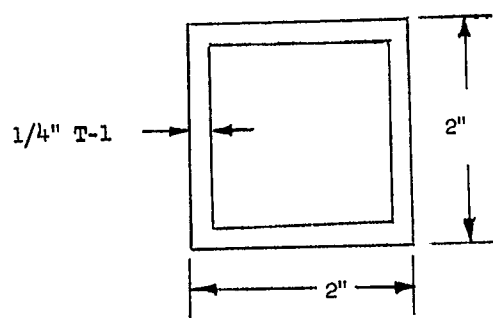
$$F_T = 115000 \text{ psi}$$

$$\text{M.S.} = \frac{115000}{67000} - 1.0 = + 0.72$$



Member HL - Pusher Load Controls (7 Genies; 25g Acceleration)

$$\text{Load} = \frac{7 \times 33600 - 25 \times 3280}{4} = 38300 \text{ lb. (Applied)}$$



$$P = 2.0 \times 38300 = 76600 \text{ lb. Ult.}$$

$$A = 1.75 \text{ in}^2$$

$$f_c = \frac{76600}{1.75} = 43800 \text{ psi}$$

$$F_c = 105000 \text{ psi}$$

$$\text{M.S.} = \frac{105000}{43800} - 1.0 = +1.40$$

#### Typical Webs

$$\text{Load}_{\text{max.}} = -18000 \text{ lb. Ult (Comp.)}$$

Use 2" O.D. .065 W. Thk. 4130 Steel

$$A = 0.395 \text{ in}^2$$

$$f_c = \frac{18000}{.395} = 45500 \text{ psi}$$

$$\frac{L}{\rho} = \frac{.75 \times 23.4}{.685} = 25.6$$

$$F_c = 67000 \text{ psi}$$

$$\text{M.S.} = \frac{67000}{45500} - 1.0 = +0.47$$

Member FL

Load = + 52000 Lb. ULT (Tension)

Use 2" O.D. 0.12 W.Thk. 4130

$$A = 0.709 \text{ in}^2$$

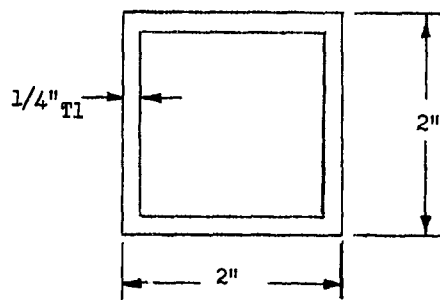
$$f_t = \frac{52000}{0.709} = 73500 \text{ psi}$$

$$F_t = 84000 \text{ psi}$$

$$\text{M.S.} = \frac{84000}{73500} - 1.0 = +.143$$

Member GL

Load = -42400 Lb. ULT (Comp)



$$A = 1.75 \text{ in}^2$$

$$f_c = \frac{42400}{1.75} = 24200 \text{ psi}$$

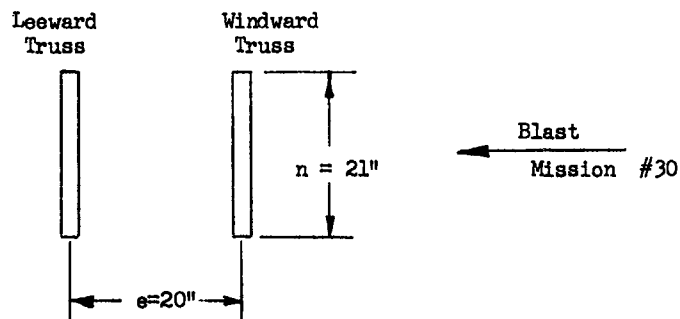
$$F_c = 105000 \text{ psi}$$

$$\text{M.S.} = \frac{105000}{24200} - 1.0 = +3.34$$

Blast Loading on Side Truss Member

Due to the small size of the members only the dynamic effects of the shock front will be evaluated.

See Ref. 16 Sec. 11.2



Solidity Ratio:

$$G = \frac{7.4}{21.0} = 0.35$$

Drag Overpressure Windward Truss

$$P_D = C_D q \quad (\text{See Ref. (16)}) \quad (\text{Fig. 11.33})$$

$$P_D = 1.6 \times 7.0 = 11.2 \text{ psi}$$

Drag Overpressure Leeward Truss

$$P_D = C_D q \quad (\text{See Ref. (16)}) \quad (\text{Fig. 11.34})$$

$$P_D = 0.58 \times 1.6 \times 7.0 = 6.5 \text{ psi}$$

Total Load on Truss

$$w = (11.2 + 6.5) 7.4 = 131.2 \text{ Lb/in (Actual)}$$

Dynamic Response of Truss to Side Blast

Moment of Inertia of Truss Members

$$I = 2 \times 3.69 \times (10.0)^2 = 738 \text{ in}^4 \text{ (Conservative)}$$

Equivalent System:

$$\text{Mass: } M_e = \frac{360 \times 0.5}{32.2} = 5.59 \text{ Lb.} \cdot \text{sec}^2/\text{ft}$$

$$\text{Spring Const. } K_e = \frac{384 EI \times K_R}{5 \times L^3}$$

$$K_e = \frac{384 \times 30 \times 10^6 \times 738 \times 0.64}{5 \times (108)^3}$$

$$K_e = 0.862 \times 10^6 \text{ Lb./in or } 10.35 \times 10^6 \text{ Lb./ft}$$

Natural Period

$$T_n = 2\pi \sqrt{\frac{M_e}{K_e}}$$

$$T_n = 2\pi \sqrt{\frac{5.59}{10.35 \times 10^6}} = .0046 \text{ sec.}$$

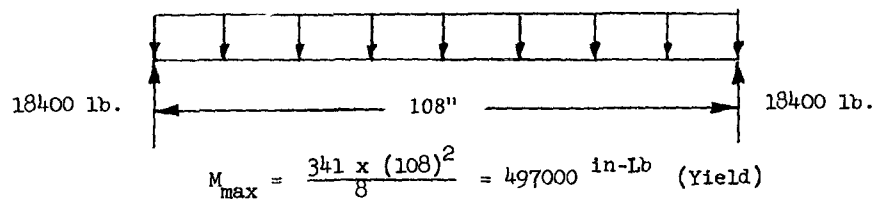
The load will be applied for 23.4 msec decaying exponentially.  
The dynamic overstress factor will conservatively be taken as 2.00.

$$\text{D.L.F.} = 2.00$$

Bending Stress in Chords Due to Blast Load

$$W_B = 131 \times 2.00 \times 1.3 = 341 \text{ Lb./in (Yield)}$$

$$W_B = 341 \text{ Lb./in}$$



#### Chord Stress

$$f_b = \frac{M_{max}}{e A}$$

$$f_b = \frac{497000}{20 \times 3.69}$$

$$f_b = 6740 \text{ psi YIELD}$$

Where:

$e$  is arm between trusses

$A$  is combined area of members HL and AG

#### Allowable Bending Stress

$$F_b = 90000 \text{ psi YIELD T-1 Steel Ref. 31}$$

$$M.S. = \frac{90000}{6740} - 1.0 = +12.3$$

#### TOP TENSION FIELD BEAM

Assume it takes 1/2 side load shear:

$$V_{max} = 0.39 R + 0.11 P \text{ (Ref. 16 Table 7.1)}$$

$$V_{max} = \frac{2.0}{2.0} (0.39 \times 2.00 \times 108 \times 131 + 0.11 \times 108 \times 131)$$

$$V_{max} = 12570 \text{ Lb. (Ultimate)}$$

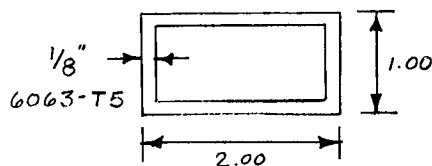
Use .064 2024 - T3 Al. Plate

$$f_s = \frac{12570}{.064 \times 22} = 8930 \text{ psi (Ultimate)}$$

$$F_s = 40000 \text{ psi (Ultimate)}$$

$$M.S. = \frac{40000}{8930} - 1.0 = +3.48$$

#### Stiffener Spacing



$$A = 0.688 \text{ in}^2$$

$$\rho = 0.39$$

$$\frac{L}{\rho} = \frac{18.0}{0.39} = 46.2$$

#### Section Through Tension Field Beam Stiffener

Assume pinned end fixity factor  $K = 1.0$

$$F_c = 17000 - 60 \frac{KL}{\rho} \quad \text{Ref. 21, Table 4f}$$

$$F_c = 17000 - 60 \times 1.0 \times 46.2 = 14230 \text{ psi}$$

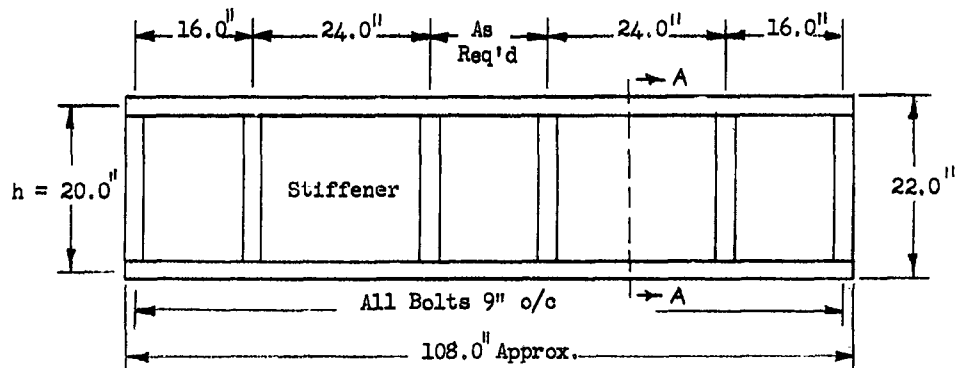
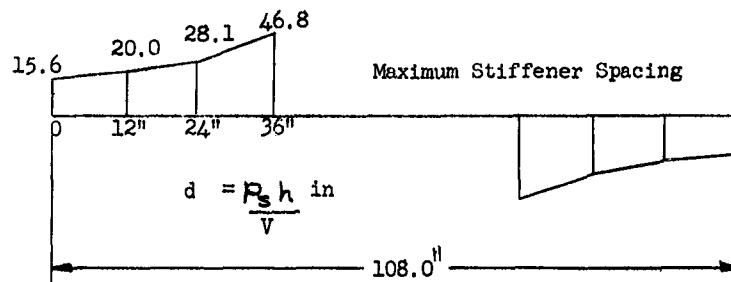
Stiffener Spacing (d)

$$d = \frac{P_s \times h}{V} \quad (\text{Ref. 23 Sec. C.7})$$

$$P_s = F_c \times A$$

$$P_s = 14230 \times 0.688 = 9790 \text{ Lb.}$$

$$h = 20''$$



Plan View of Tension Field Beam

Bolted Connection of Tension Field Beam to Longerons of Motor Cage

$$\text{Bolt Load/Inch} = 1.41 V/h = \frac{1.41 \times 12570}{20} = 886 \text{ lb/in}$$

Use 3/8" AN-6 Bolt 9" O/C and 2" x 1-1/4" x 1/4" L

6061-T6 For Edge Member

Shear Capacity of Bolt = 8280 lb. (ULT)

Bearing Capacity of Angle =  $0.331 \times 88000 \times 3/8" = 10920 \text{ lb. (ULT)}$

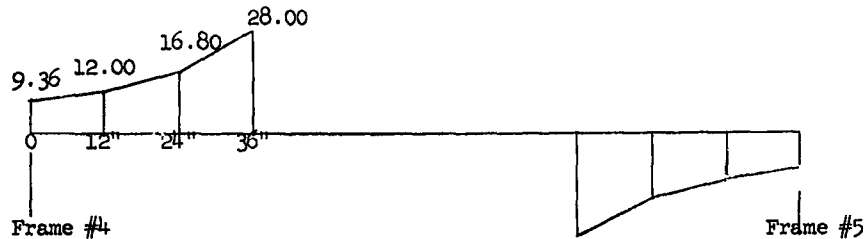


Diagram of Maximum Allowable Bolt Spacing

Bolt Spacing: (Fore and Aft Edge Member to Frame #4 and #5)

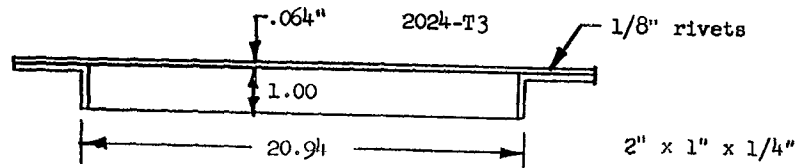
$$V = 12570 \text{ lb. (ULT)}$$

Use 2 - 3/8" Bolt

$$V_{All} = 2.0 \times 8280 = 16600 \text{ Lb. (ULT)}$$

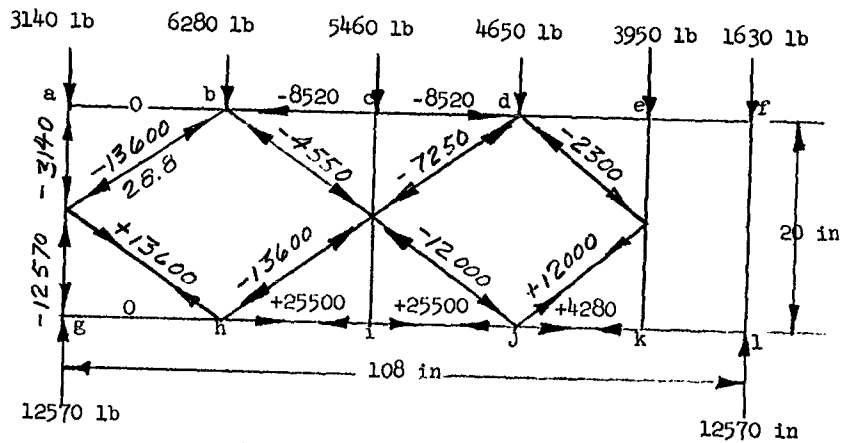
$$\text{M.S.} = \frac{16600}{12570} - 1.0 = +.32$$

Section A-A Through Tension Field Beam



Bottom Truss

Assume it carries 1/2 of side load as follows:



Ultimate Loading of Bottom Truss

Typical Web Member

Load - (-13600 Lb.) ULF (Comp)

Use 2" O.D. .120 W. thk. 4130 Steel

$$A = 0.709 \text{ in}^2$$

$$F_c = \frac{13600}{.709} = 19200 \text{ psi}$$

$$\frac{L}{\rho} < 40$$

$$F_c = 67500 \text{ psi} \quad 4130 \text{ Steel}$$

$$\text{M.S.} = \frac{67500}{19200} - 1.0 = +2.52$$



#### 2.2.2.5 SLIPPER LOADS

The slipper loads for the most critical BRL blast condition (mission # 30) are indicated in Figure 2.2.1. These slipper loads were computed by assuming the 44.1 psi reflected overpressure was applied as a static load. No attempt has been made to determine the magnification of these loads due to their dynamic nature.

#### 2.2.2.6 SUMMARY OF MARGINS OF SAFETY

The most critical margin of safety for each section of the sled is listed in Table 2.2.1.

TABLE 2.2.1

#### SUMMARY OF MARGINS OF SAFETY

<u>Structural Component</u>	<u>Critical Element</u>	<u>M.S.</u>
Forward Fuselage	Slipper Leg	+9.0%
Instrumentation Compartment	(Shear Connection of Top and Bottom Panels to Longerons)	+6.0%
Motor Cage	(Side Truss Web Member)	+14.0%

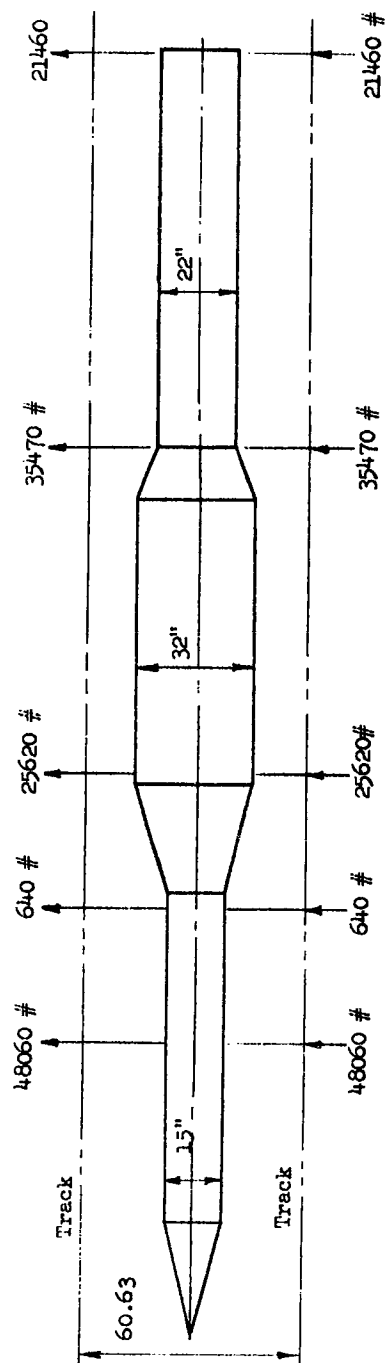
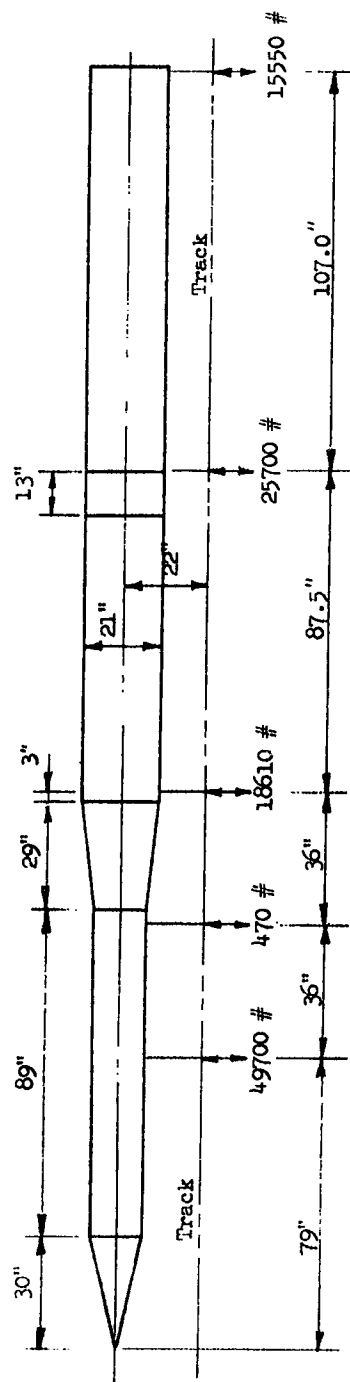


FIG. 2.2.1 SLIPPER LOADS FOR MISSION #30

### 2.2.3 WEIGHT SUMMARY

A summary of the computed weights for the sled and associated equipment is described in Table 2.2.2.

TABLE 2.2.2  
WEIGHT SUMMARY

<u>Structural Component</u>	<u>Weight</u>
Forward Fuselage	857
Instrumentation Compartment	588
Motor Cage	711
Slippers	<u>450</u>
TOTAL	2606
<u>Removable Accessories:</u>	
Cameras	33
* Probe	38
HME-6 and Adapter	227
Instrumentation	800
BRL Adapter	85
BRL Mount	225
BRL F-84 Specimen	150
ASD Structural Specimen	100
ASD Aero Specimen	660
<u>Motors:</u>	
XM5 Loaded	1165
Expendable	427
HVAR Loaded	85
Expendable	61
* Probe omitted when HME brake is used	

## 2.3 AERODYNAMICS

### 2.3.1 AERODYNAMIC DRAG

In order to obtain an estimate of the performance characteristics of the chosen sled configuration, the retarding effects of the aerodynamic drag force must be computed. The overall retarding drag force experienced by the sled during its motion down the test track can be expressed in the form:

$$D = C_D A q,$$

where:

$D$  represents the aerodynamic drag force (#);

$C_D$  represents an empirical coefficient,  
the "drag coefficient"

$A$  represents a particular area ( $\text{ft}^2$ ) associated  
with the configuration on which the experi-  
mentally determined drag coefficient is based;

and  $q$  is the dynamic pressure defined as

$$q = \frac{1}{2} \rho v^2 = \frac{1}{2} \gamma \rho M^2$$

where:

$\rho$  is the air density (slugs/ $\text{ft}^3$ );

$V$  is the forward velocity of the sled (ft/sec);

$\gamma$  is the ratio of atmospheric specific heats;

and  $M$  is the Mach number defined as:

$$M = V/a$$

where:  $a$  is the local acoustical velocity (ft/sec).

The magnitude of the empirical drag coefficient  $C_D$  is a function of the particular body shape under consideration and the forward velocity  $V$  of the sled. Various source references can be used to obtain the experimentally determined values of the drag coefficient. In general, the major drag components of interest in the consideration of the overall drag experienced

by a sled configuration can be taken to be due to the following component drags:

a. Forebody drag component of the configuration, which may or may not include the effect of the base drag as discussed below. The pressure drag component is due primarily to the necessity of removing the air from the space occupied by the vehicle.

b. Base Pressure Drag component of the forebody, due essentially to the separation of the flow boundary layers in the after regions of the configuration, resulting in a negative pressure field in the wake pattern of the vehicle. The resulting energy defect of the flow field, evidenced by the disturbed wake flow pattern, must be overcome by the sled. The net effect is the production of a retarding drag force component tending to oppose the motion of the sled.

c. Skin Friction Drag component generated by the viscous action of the boundary layer fluid in the regions adjacent to the sides of the vehicle. The shear force in the fluid generated by the motion of the vehicle can be shown to produce an effective force tending to oppose the motion of the sled. Generally, this drag component is small compared to the other components of the overall drag.

d. Drag due to the various appendages attached to the sled, such as water brakes, rail slippers and supporting legs, etc. Each of these mechanical components have a drag composed of the first three types (a, b, and c) just described.

e. Overall ground interference drag component of the configuration, which may tend to lessen somewhat the undesirable base drag component, but increase the tendency of choking the flow between the bottom of the sled and the ground. This may result in an excessive air load (normal pressure distribution) on the bottom panels of the sled.

Table 2.3.1 illustrates the overall drag coefficient of the basic sled as a function of Mach Number. It is to be noted that the

"acceleration" and deceleration" magnitudes of  $C_D$  are different by virtue of the fact that during the acceleration phase the positive pressure region downstream of the rocket motor nozzles tends to overcome the ordinary wake defect pressure field on base drag component and thus decrease the overall configuration drag. The drag coefficients presented in this section are all referenced to the basic projected frontal area of the sled,  $4.67 \text{ ft}^2$

Several of the component drag coefficients included in the total figures noted in Table 2.3.1 are illustrated in the following set of curves.

The overall configuration drag coefficients including the effects of the airfoil specimens (and mounts) are shown in Figure 2.3.5. These overall coefficients are used to evaluate the performance capabilities of the sled in the following section.

TABLE 2.3.1 OVERALL DRAG COEFFICIENT OF BASIC SLED  
(Basic Data obtained from Reference 32)

<u>Mach Number</u>	<u><math>C_D</math> Sled (Referenced to <math>4.67 \text{ ft}^2</math>)</u>	
	<u>Acceleration</u>	<u>Deceleration</u>
.0	2.24	2.46
.2	2.23	2.45
.4	2.22	2.44
.6	2.29	2.52
.7	2.35	2.58
.8	2.39	2.63
.9	2.65	2.92
1.0	2.89	3.23
1.1	2.91	3.20
1.2	2.77	3.04
1.4	2.65	2.95

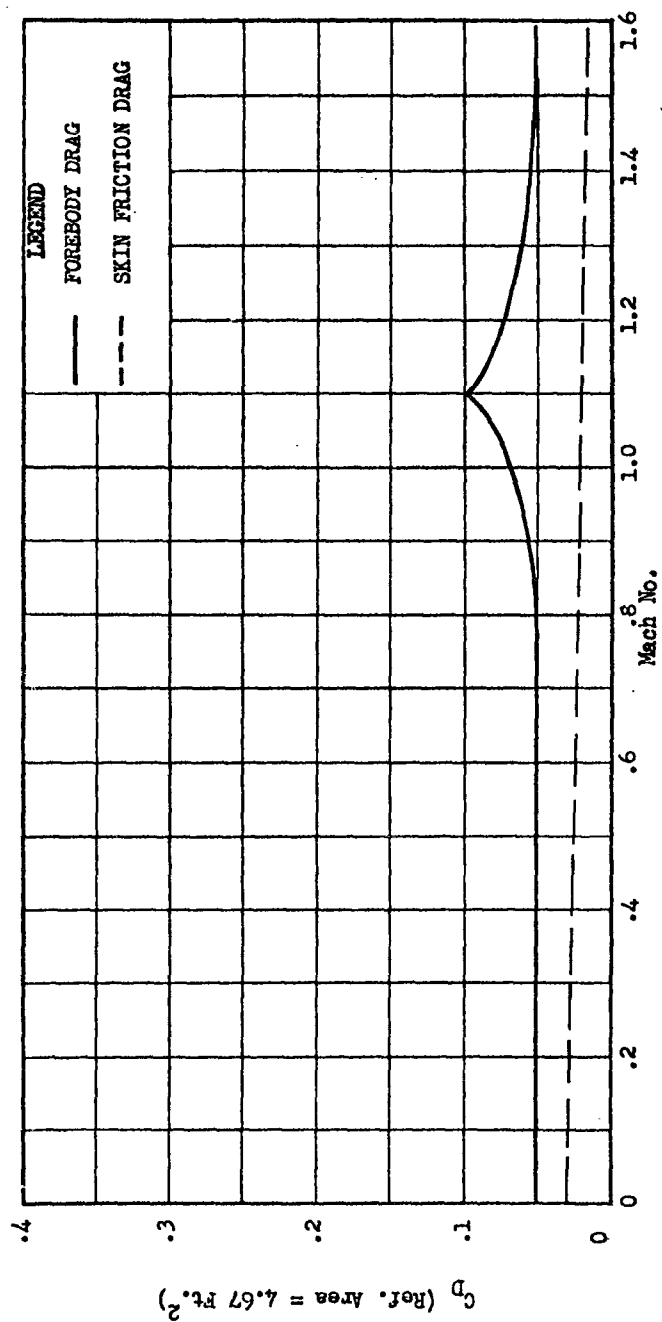


FIG. 2.3.1.1 DRAG COEFFICIENT FOR NOSE CONE

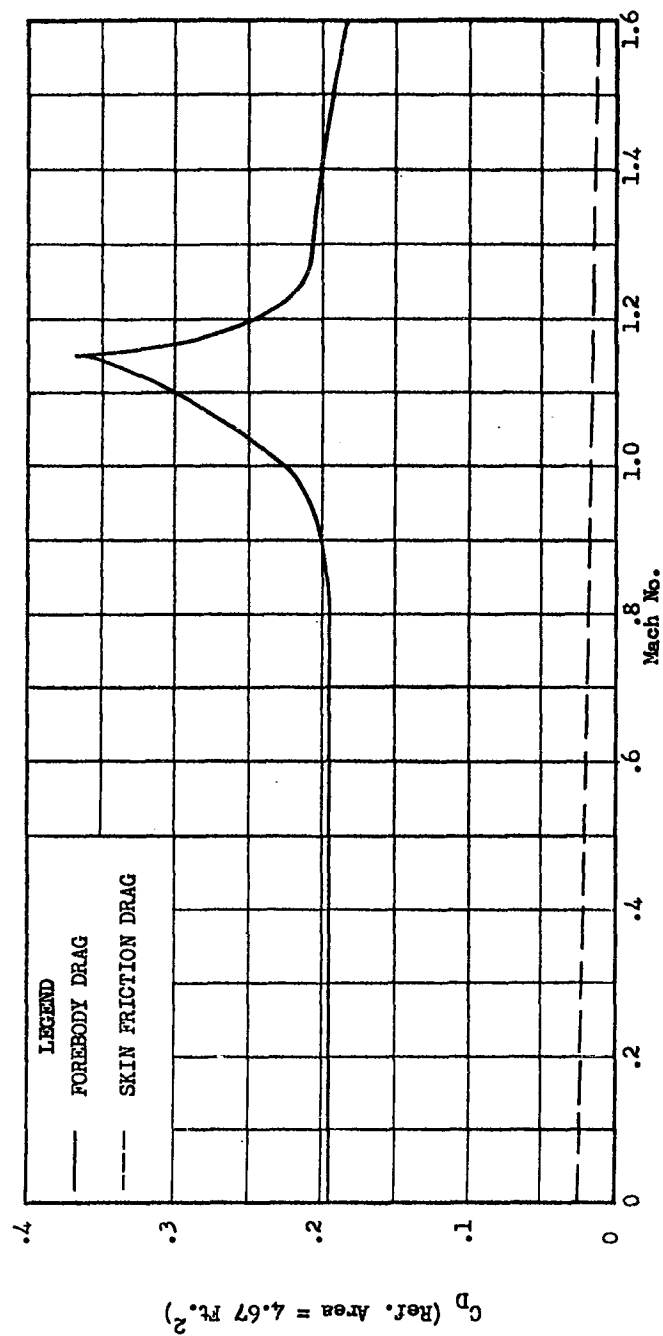


FIG. 2.3.2 DRAG COEFFICIENT FOR TRANSITION SECTION



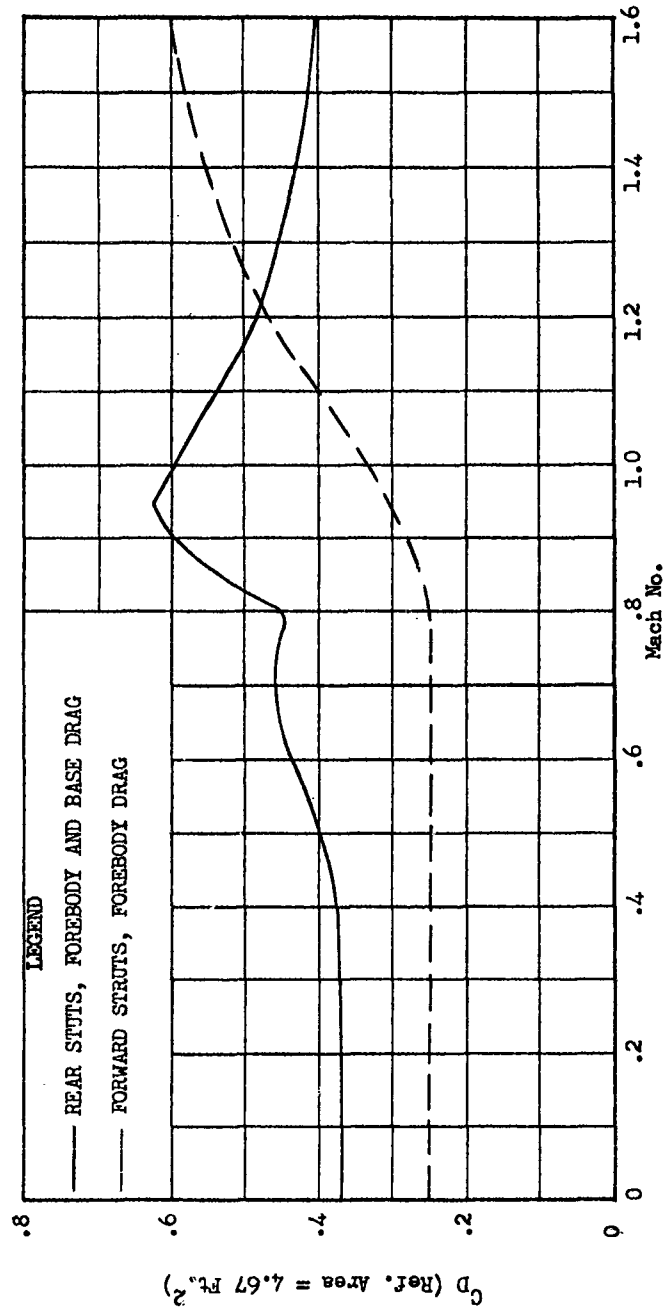


FIG. 2.3.3 DRAG COEFFICIENTS FOR SLIPPER LEGS

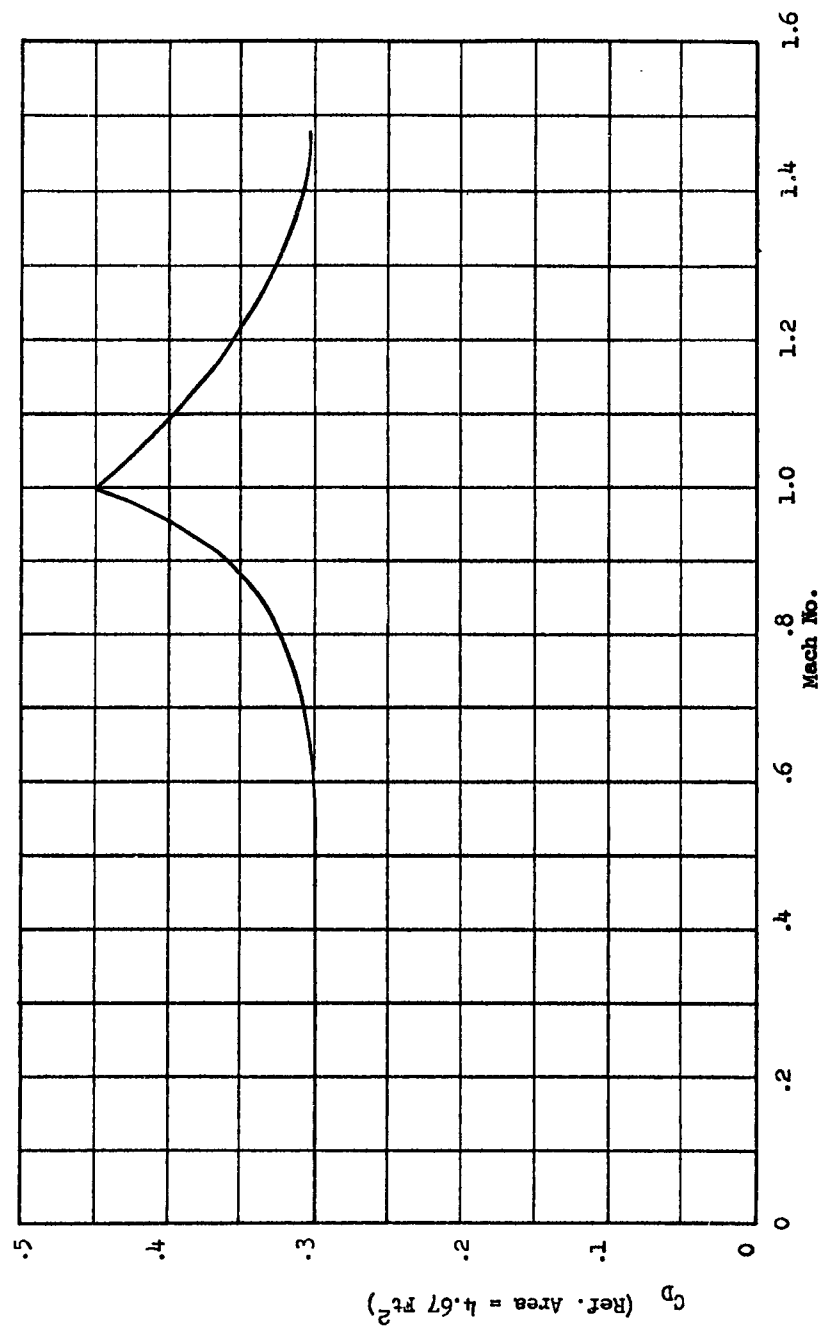


FIG. 2.3.4 MAIN BODY BASE DRAG

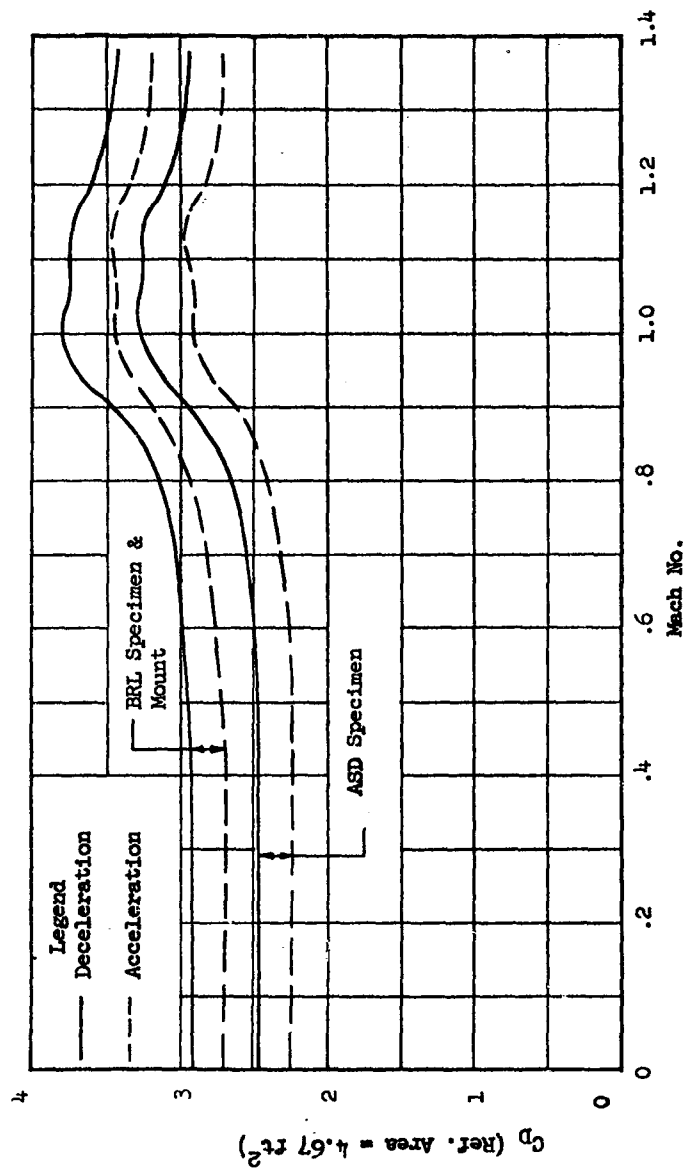


FIG. 2-3.5 OVERALL DRAG COEFFICIENTS FOR DIFFERENT SLED CONFIGURATIONS

### 2.3.2. BLAST SLED PERFORMANCE CHARACTERISTICS

The analyses presented in this section illustrate the techniques and mathematical expressions used to evaluate the performance capabilities of the blast sled. The basic assumptions involved for these analyses are:

1. The vehicle is a point mass constrained to move in a straight horizontal line.
2. The external forces acting on the vehicle are due to the rocket motor thrust, aerodynamic drag, and where applicable, water brake drag and slipper-rail frictional forces.
3. The aerodynamic retarding forces can be expressed as  $K V^2$ , where

$$K = \frac{1}{2} \rho C_D A \quad (2.3.1)$$

The motion of the sled can be conveniently divided into two major phases: a powered or finite thrust phase, and a zero-thrust coasting or braking phase. During the phase of the sled run with finite thrust, the equation of motion can be expressed as:

$$\frac{1}{g} \left[ W_0 + W_p - \int_0^t \frac{T(t)}{I_{sp}(t)} dt \right] \frac{dv}{dt} + K(V)V^2 = T(t), \quad (2.3.2)$$

where:

- $g$  = acceleration of gravity,  
 $W_0$  = total weight of vehicle without propellant,  
 $W_p$  = initial propellant weight,  
 $T(t)$  = rocket motor thrust, a function of time.  
 $I_{sp}(t)$  = rocket motor specific impulse, a function of time  
 $t$  = time,  
 $V$  = sled velocity, a function of time,

$$K(V) = \text{drag factor, } K(V) = \frac{1}{2} \rho C_D A$$

$$\rho = \text{air density,}$$

$$C_D = \text{vehicle drag coefficient, a function of velocity,}$$

$$A = \text{reference area.}$$

Equation 2.3.2 is most conveniently solved on a digital computer because of the variable coefficients appearing in this relationship, for the velocity of the sled as either a function of time or distance traveled down the track. In addition, the computer can be programmed to provide the acceleration magnitudes experienced by the sled. These acceleration levels can be written as:

$$\eta = \frac{1}{g} \frac{dv}{dt} = \frac{T(t) - K(V) V^2}{W_o + W_p - \int_0^t \frac{T(\tau)}{I_{sp}(\tau)} dt} \quad (2.3.3)$$

During the unpowered portion of the sled trajectory, the sled is either allowed to coast, or is decelerated by the waterbrake attached to the vehicle. During the coasting phase, aerodynamic drag forces are the only external forces acting on the sled. For this portion of the sled run, the equation of motion is:

$$\frac{W_o}{g} \frac{dv}{dt} + K(V) V^2 = 0 \quad (2.3.4)$$

During the waterbraking phase, the equation of motion of the sled can be written as:

$$\frac{W_o}{g} \frac{dv}{dt} + K(V) V^2 + f W_o + D_B = 0, \quad (2.3.5)$$

where:

$f W_o$  = the frictional force generated by the relative motion of the sled slippers with respect to the track rail.  $f$  is the coefficient of sliding friction between the slippers and rails. Generally, for  $V > 300$  fps,  $f W_o \approx 0$ ,

and

$D_B$  represents the braking force generated by the brake attached to the sled. For a horizontal momentum exchange type of waterbrake,  $D_B$  can be expressed as:

$$D_B = \frac{1}{2} \rho_w C_{D_W} A_L V^2 + \rho_w A_o V^2 \left[ 1 - \frac{V_{e_x}}{V} \cos \theta \right], \quad (2.3.6)$$

where,

$\rho_w$  = density of water,

$C_{D_W}$  is the drag coefficient associated with the lip of the brake,

$A_L$  is the area of the submerged portion of the lip,

$A_o$  is the area of the submerged portion of the inlet passage of the brake,

$\theta$  is the angle through which the water is turned in the brake,

and  $V_{e_x}/V$  expresses the magnitude of the water velocity at the brake exit ( $V_{e_x}$ ) to the inlet velocity of the water ( $V$ ).

The LGP-30 digital computer at AAI has been programmed to effect solutions of these equations for a variety of input parameter magnitudes. The following figures illustrate the sled trajectories achieved for the following conditions:

Run #1 - BRL Wing Specimen and Mount

$$W_o = 4675 \text{ lb.}^*$$

$$W_{PMS} = 738 \text{ lb.}$$

$$W_{PHVAR} = 48 \text{ lb.} \quad (2 \text{ Units})$$

Run #2 - ASD Aero Wing Specimen

$$W_o = 4875 \text{ lb.}^*$$

$$W_{PMS} = 738 \text{ lb.}$$

$$W_{PHVAR} = 48 \text{ lb.} \quad (2 \text{ Units})$$

Run #3 - ASD Struc. Wing Specimen

$$W_o = 4315 \text{ lb.}^*$$

$$W_{PMS} = 738 \text{ lb.}$$

$$W_{PHVAR} = 48 \text{ lb.} \quad (2 \text{ Units})$$

\* HME brake used - no probe

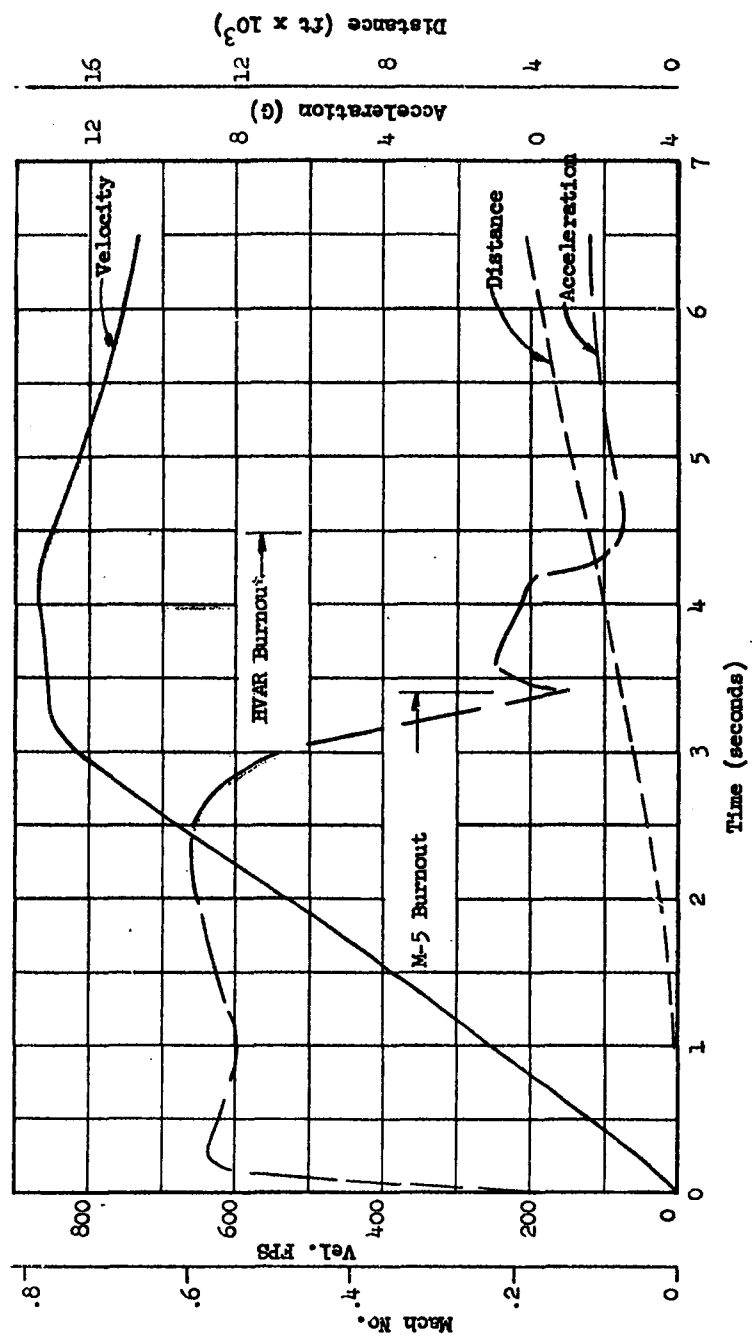


FIG. 2.3.6 PERFORMANCE CHARACTERISTICS FOR ASD SLED WITH F-84 TAIL AND MOUNT



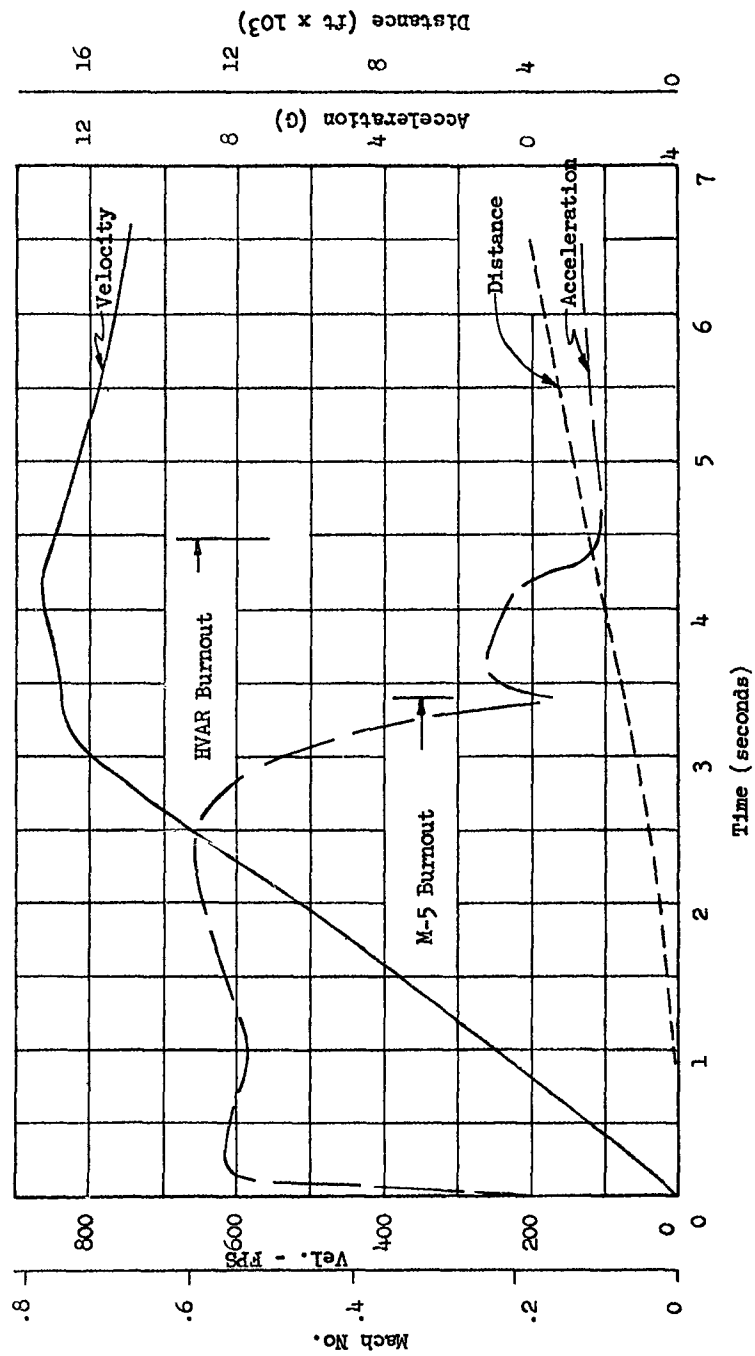


FIG. 2.3.7 PERFORMANCE CHARACTERISTICS FOR ASD SLED WITH AIRLOAD SPECIMEN (6L)

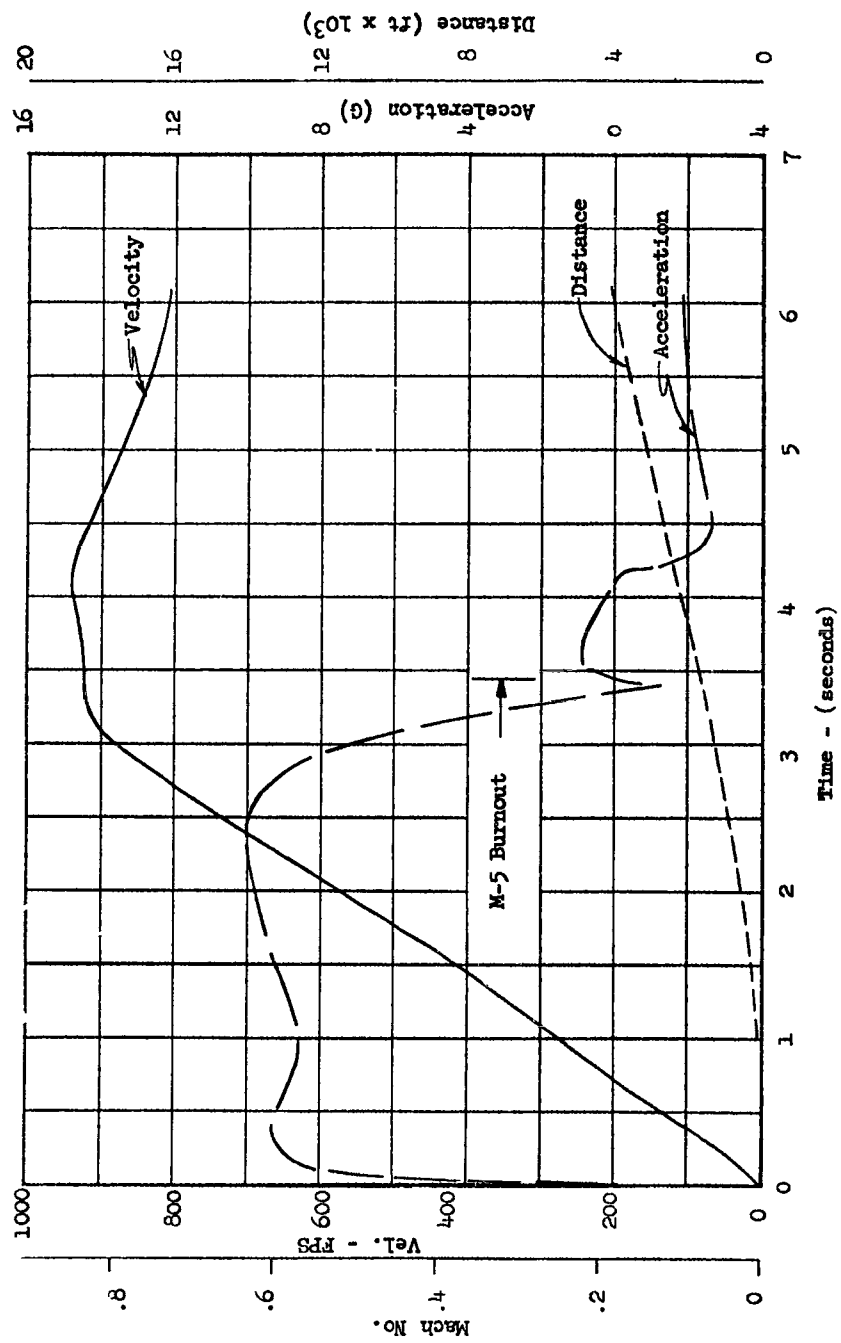


FIG. 2.3.8 PERFORMANCE CHARACTERISTICS FOR ASD SILED WITH STRUCTURAL SPECIMEN (6R)

### 2.3.3 BLAST WAVE LOADING ON SLED BODY STRUCTURE

The passage of the externally generated blast wave over the main body of the sled can be expected to produce severe pressure loadings on the structure of the sled. The blast loading on the sled structure is a function of both the incident blast wave characteristics and the size, shape, orientation, and response parameters associated with the sled. The following analyses are presented in order to illustrate the techniques necessary to achieve some knowledge of the loadings exerted on the sled by the blast wave. The major elements of these analyses are extracted from the data and techniques presented in Reference 16, 26, 27, and 28.

The two major periods of interest, with respect to the air burst of an explosive and resulting shock or blast wave phenomena, are:

1. The Diffraction Loading Period during which the forces on the structure are a result of the direct and reflected pressure associated with the blast in the initial phases of the envelopment of the structure, and,

2. The Drag Loading Period which is associated with the forces on the structure resulting from the high velocity air particles in the blast wave envelope behind the shock front.

It will be assumed that the blast or shock wave approaching the structure is plane and can be characterized by an incident peak overpressure,  $\Delta P_0$ , and a time,  $D_p^+$ , the duration of the positive phase of the blast. Two basic structures are examined in this discussion: a closed rectangular structure, and a closed cylindrical structure, positioned such that the longitudinal axis of the cylinder is perpendicular to the direction of motion of the blast front. These two basic structures characterize the major elements of the ASD sled. The angle of incidence of the approaching blast front with respect to each structure will be assumed to be zero in order to arrive at the maximum pressure loadings exerted on the structure.

Consideration is first given to the initial or peak values of parameters affecting a structure immersed in a blast field. The Rankin-Hugoniot Relations are valid only across the shock front discontinuity. The relations can be written in terms of the peak incident overpressure,  $P_o$ , where:

$$\Delta P_o \equiv P_s - P_o \quad (2.3.7)$$

$P_s$  = Peak pressure immediately behind the shock front

$P_o$  = Ambient pressure

The magnitude of the incident overpressure, at any point,  $r$ , from the center of the blast producing explosion, for any given charge weight,  $W$ , can be determined from the data presented in Reference 27 and 28. It is to be noted that the data of Figure 1 of Reference 27 can be put in terms of the corresponding data of Reference 28 through relating (Brode's dimensionless distance in Reference 27) to (Brode's dimensionless distance in Reference 28) by:

$$\chi = 78.8 \lambda \quad (2.3.8)$$

This relationship is based on the assumption that  $E_{TOT} = 1760$  cal/gm this value being one that was suggested by personnel at BRL, APG. As the blast front strikes a surface, at normal incidence, a reflected shock wave is formed and the overpressure on this structural face is increased to a value in excess of the peak overpressure in the incident shock wave. The magnitude of the reflected overpressure,  $\Delta P_r$ , can be expressed as:

$$\Delta P_r = 2 \Delta P_o \left[ \frac{7P_o + 4\Delta P_o}{7P_o + \Delta P_o} \right] \quad (2.3.9)$$

or can be read directly from the data of Figures 1 a. and 1 b. of Reference 27.

The shock front velocity  $U_s$ , and the particle velocity,  $u_s$ , immediately behind the shock front can be found from,

$$U_s = C_o \left( 1 + \frac{6 \Delta P_o}{7 P_o} \right)^{1/2} \quad (2.3.10)$$

and,

$$u_s = \frac{5}{7} \frac{\Delta P_o}{P_o} \left[ \frac{C_o}{\left( 1 + \frac{6 \Delta P_o}{7 P_o} \right)^{1/2}} \right] \quad (2.3.11)$$

In Equations 2.3.10 and 2.3.11,  $C_o$  is the acoustical speed defined by,

$$C_o = \sqrt{\gamma g R T_o} = \sqrt{\gamma g \frac{P_o}{\rho_o}} \quad (2.3.12)$$

where:

$$\gamma = \frac{C_p}{C_v} = \text{the ratio of specific heats of the ambient atmosphere.}$$

$T_o$  is the absolute ambient temperature

and,  $\rho_o$  is the ambient density.

The density of the fluid behind the shock front,  $\rho_s$ , can be computed from:

$$\frac{\Delta \rho}{\rho_o} = \frac{\frac{2}{\gamma-1} \left( \frac{\Delta P_s}{P_o} \right)}{\frac{\gamma+1}{\gamma-1} + \frac{\Delta P_s}{P_o} + 1} \quad (2.3.13)$$

$$\text{where } \Delta \rho = \rho_s - \rho_o \quad (2.3.14)$$

The dynamic pressure,  $q_s$ , immediately behind the shock front, defined as

$$q_s = \frac{1}{2} \rho_s u_s^2 \quad (2.3.15)$$

can be computed from:

$$q_s = \frac{5}{2} \left( \frac{\Delta P_o^2}{7 P_o + \Delta P_o} \right) \quad (2.3.16)$$

The Rankin-Hugoniot relationships given in the previous equations merely define the fluid dynamical parameters in the region immediately behind the shock front, as this front passes a fixed point in space.

The major problem of interest, however, is the determination of the fluid dynamic characteristics at this fixed point in space, as a function of time after the initial passage of the blast wave. Following this determination, the characteristics of the flow field behind the shock front for a point that moves with respect to the blast origin must be evaluated.

Following the method presented in References 27 and 28, the time dependence of the overpressure,  $\Delta P$ , at a fixed point in space can be approximated by the relationship:

$$\Delta P = \Delta P_0 (1 - z_p) e^{-\alpha z_p} \quad (2.3.17)$$

where  $z$  is a dimensionless time, expressed in terms of the duration of the positive phase of the incident blast wave. Generally,  $z$  can be taken to be

$$z_p = t/D_p^+ \quad (2.3.18)$$

Where  $t$  is the time of interest, measured from incidence of the shock front, and  $D_p^+$  is the duration of the positive phase of the blast wave. The magnitude of  $D_p^+$  can be found from Figure 3 of Reference 27, or from Figure 8 of Reference 28. The magnitude of the coefficient  $\alpha$  appearing in Equation 2.3.17 can be evaluated from the analyses of Reference 28; however, Figure 9 of this reference can be used to reduce the computational complexity of the analysis.

The dynamic pressure time decay relationship can be expressed as

$$q = q_s (1 - z_u)^2 e^{-\beta z_u} \quad (2.3.19)$$

where

$$z_u \equiv t/D_u^+ \quad (2.3.20)$$

such that  $D_u^+$  is the time duration of the positive phase of the particle velocity after arrival of the shock-pressure pulse. Magnitudes of  $D_u^+$  can be obtained from Figure 8 of Reference 28. The magnitude of

the coefficient  $\beta$  appearing in Equation 2.3.19 can be computed from the analyses presented in Reference 28. However, Figure 11 of this reference presents the typical time decay curves for the dynamic pressure, which can be used to evaluate the time history of the dynamic flow effects during the drag loading phase. The data of Reference 29 can also be used to evaluate the various pressure field parameters for comparison purposes with the data of References 27 and 28.

The data of Reference 30 indicates that "Mission No. 30" produces the largest pressure loadings on the sled structure. Consequently, the particular blast parameters associated with this mission were used to effect the basic structural design of the ASD sled. The parameters associated with Mission 30 are given in the following Table.

TABLE 2.3.2 BLAST CHARACTERISTICS OF MISSION #30					
Mission No.	Charge Wt. (Lb)	Charge Dist. (ft)	$\Delta P_o$ (psi)	$\Delta P_r$ (psi)	$D_p^+$ (m sec)
30	2500	110.0	17.6	44.1	23.4

Applying the techniques presented in Reference 16 and 26, for evaluating the structural loading conditions resulting from the incident blast, the following figures present the blast wave characteristics and the loads experienced by the rectangular and cylindrical structures described in the introduction of this section. Figure 2.3.9 illustrates the incident overpressure and dynamic pressure decay characteristics for this particular blast front. In Figure 2.3.10 are shown the pressure loads acting on a closed rectangular structure subjected to the chosen blast. The rectangular structure is 21 inches high and 32 inches long in the direction parallel to the motion of the shock front. It is to be noted that the dynamic pressure, or drag loading characteristics, are included in the overpressures indicated in Figure 2.3.10. The maximum impulsive

pressure is that due to the reflected overpressure exerted on the front face of the rectangular structure. The top and bottom surface shock wave loadings have not been included in this summary since, in the absence of ground interference effects, the net vertical force on the structures is identically zero.

Figure 2.3.11 indicates the same type of overpressure loadings associated with a circular cylinder 21 inches in diameter, and in Figure 2.3.12, these pressure loadings are directly compared to those associated with the rectangular body. From this last figure, it can be immediately noted that, for a given body length in the cross flow direction the height of the rectangular body must be approximately 80% of the diameter of a cylindrical body in order to secure the same maximum horizontal loading on each structure.

For purposes of determining impulsive loading on the actual sled cylindrical structure, Figure 2.3.13 presents the blast loading on a 15" diameter cylinder.

It is to be noted that the duration times  $D_p^+$  and  $D_u^+$ , defined in Equations 2.3.18 and 2.3.20 respectively, are such that:

$$D_u^+ > D_p^+, \text{ generally.}$$

However, the character of the dynamic pressure-time decay relationship (Equation 2.3.19) is such that it is difficult to define  $D_u^+$  to an accuracy comparable to the accuracy of  $D_p^+$ . (See Reference 28 for amplification of this statement.) In order to circumvent this difficulty, and provide a practical approach to the problem, Reference 26 indicates that assuming  $D_u^+ = D_p^+$  is sufficient for the majority of cases. This assumption will be used where necessary in the following sections of this report.



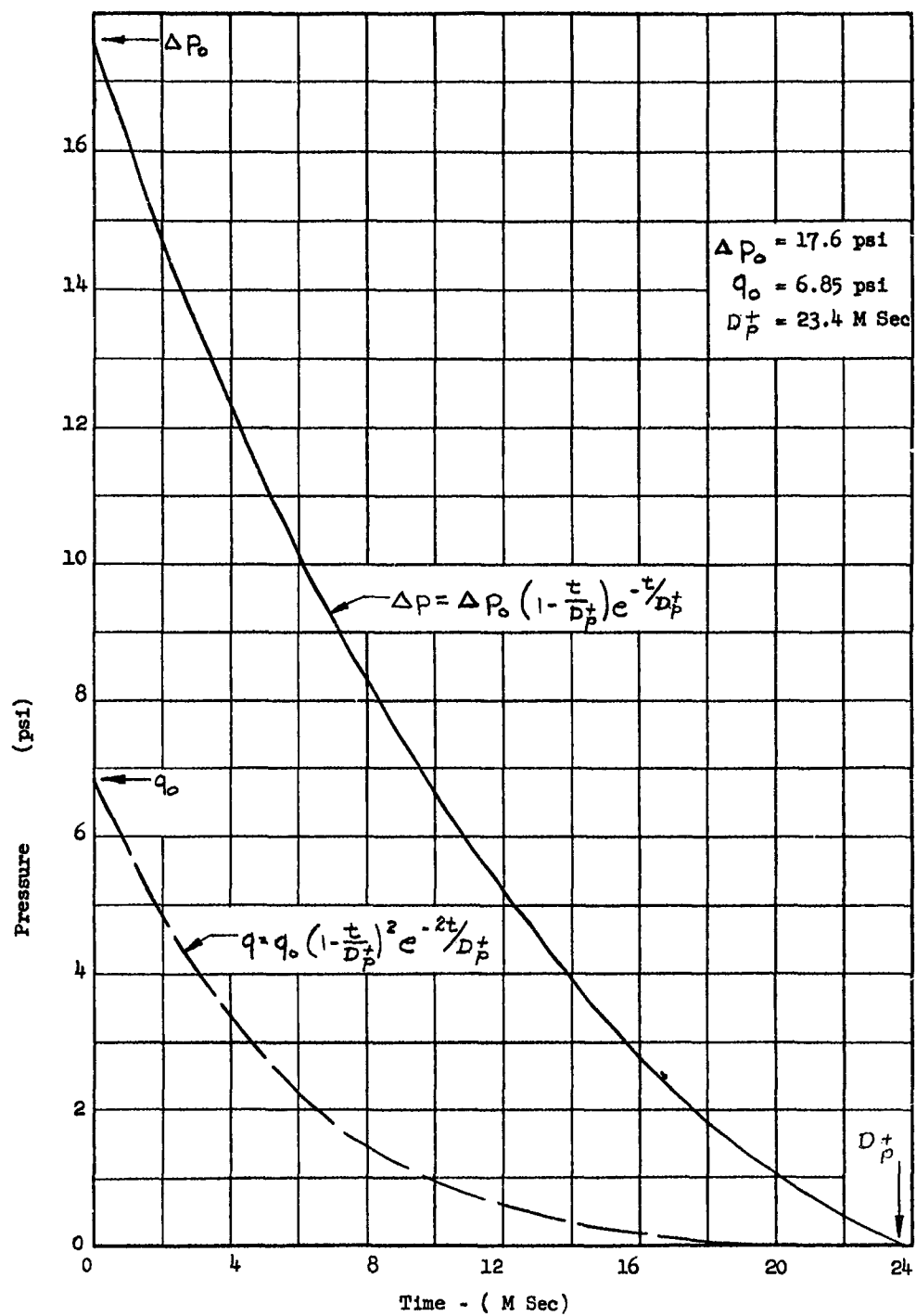


FIG. 2.3.9 BLAST WAVE PARAMETERS FOR MISSION NO. 30

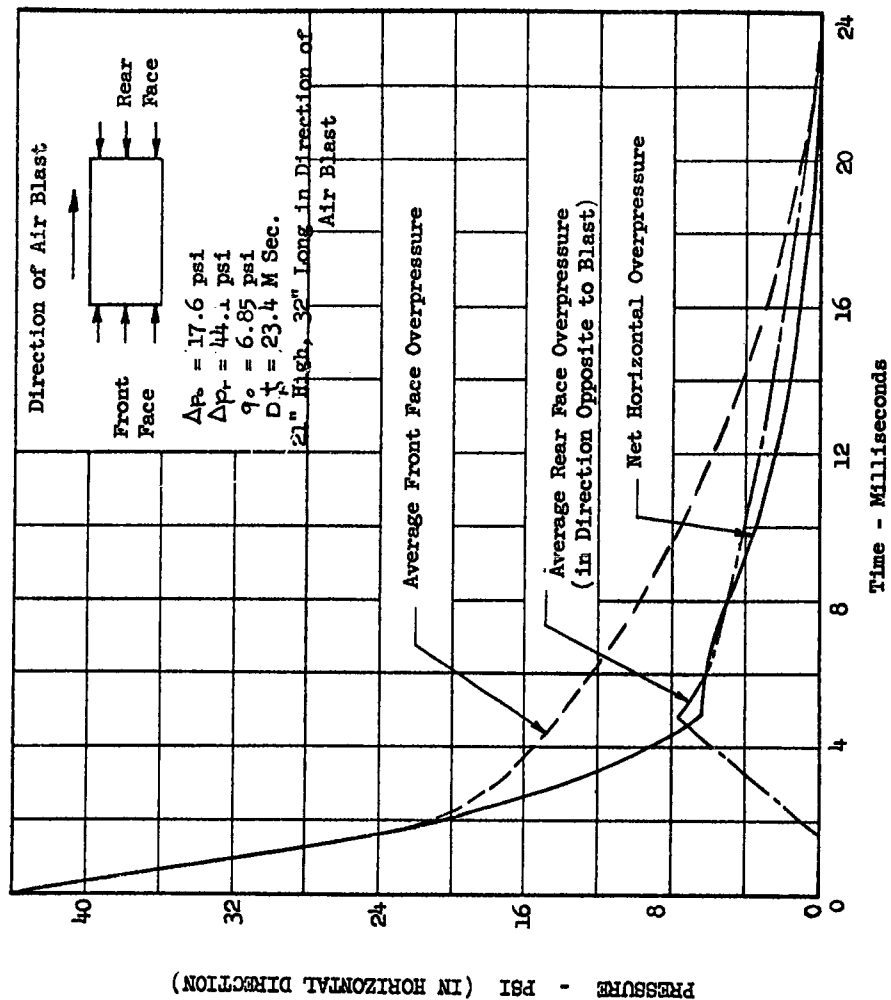


FIG. 2.3.10 AIR BLAST LOADING ON CLOSED RECTANGULAR STRUCTURE

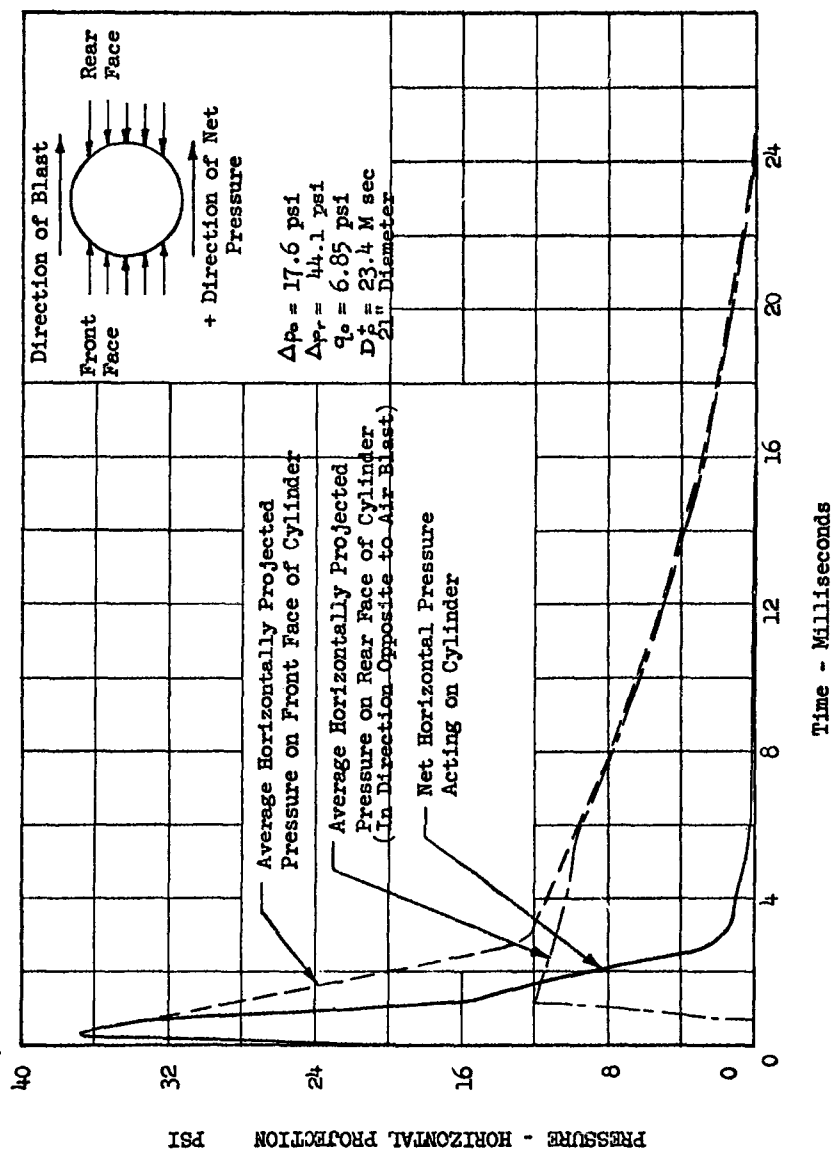


FIG. 2.3.11 AIR BLAST LOADING ON CLOSED CYLINDRICAL STRUCTURE

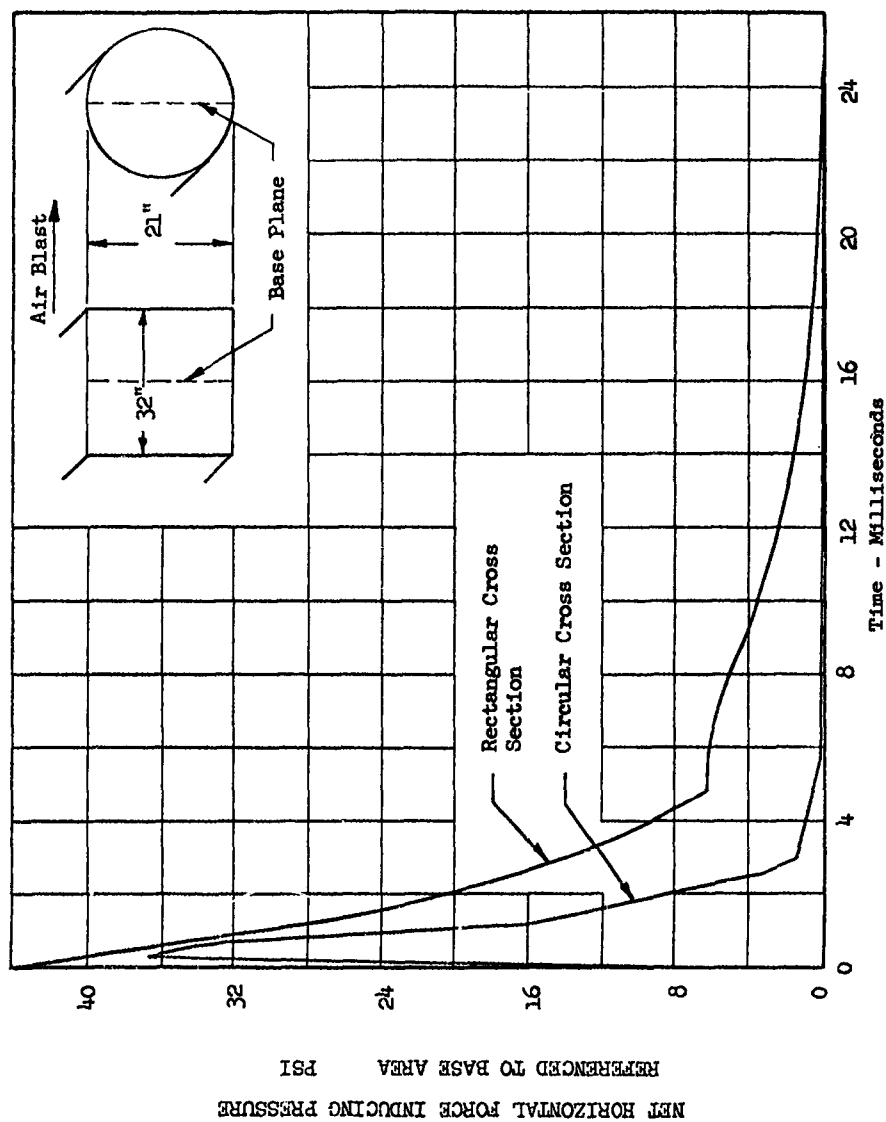


FIG. 2.3.12 COMPARISON OF PRESSURE FORCES ACTING ON RECTANGULAR AND CYLINDRICAL STRUCTURES.

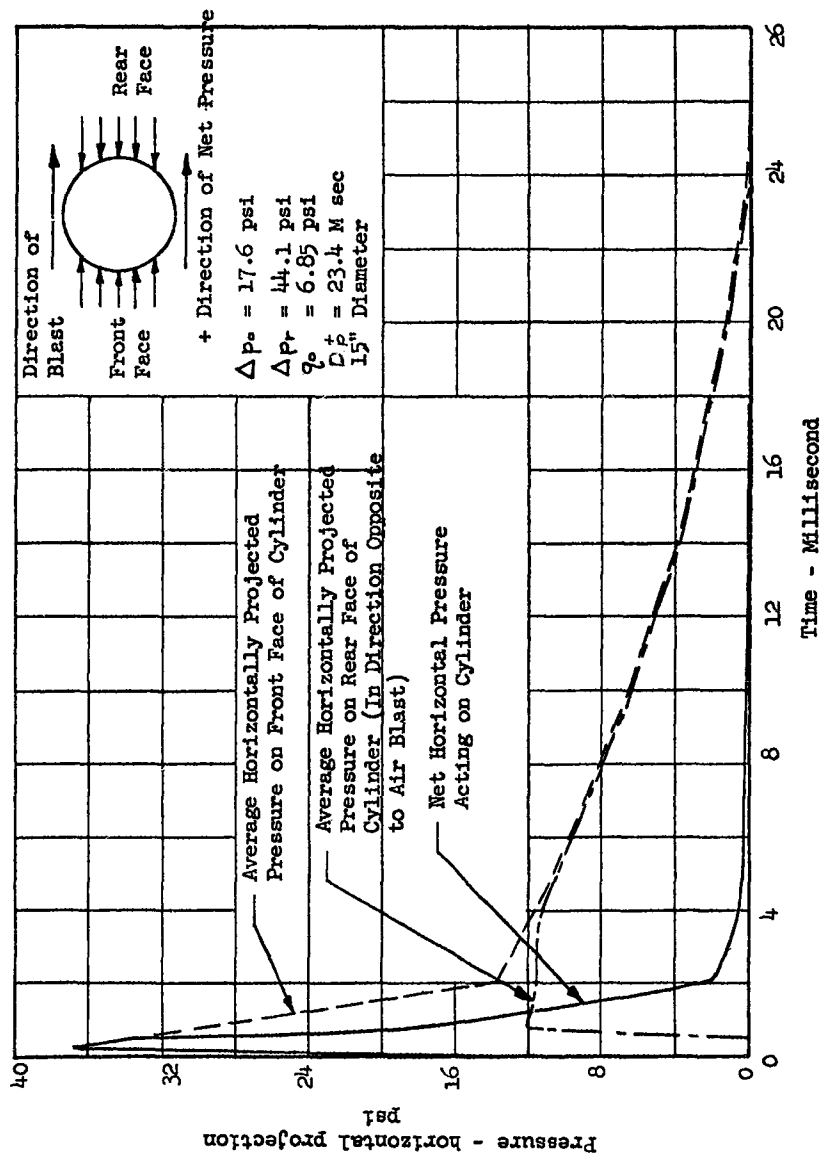


FIG. 2.3.13 AIR BLAST LOADING ON CLOSED CYLINDRICAL STRUCTURE

#### 2.3.4 EFFECT OF SLED MOTION ON BLAST WAVE PARAMETER

The blast wave characteristics used to effect the basic structural design of the sled, as discussed in the previous section, correspond to a case in which the sled is stationary. For cases in which the sled is moving, the blast wave characteristics (overpressure, dynamic pressure, etc.) imposed on the sled structure will be different from those associated with a stationary vehicle subjected to the same charge-distance relationships. For example, the moving sled will encounter overpressures and dynamic pressures that vary with time as functions of the relative velocity of the sled and blast front in addition to the normal (stationary) time decay characteristics of these parameters. Hence, in order to accurately predict the pressure functions encountered by the moving vehicle, it is necessary to modify the stationary time decay characteristics of the blast, with respect to the relative motion of the sled and blast front.

Table 2.3.3, taken from Reference 30, presents the overpressure functions and positive phase duration times for Missions 1, 2, and 3 as obtained from the methods outlined in the previous section.

The positive phase duration times given in Table 2.3.3 correspond to a stationary sled subjected to the given blasts. However, for each of these experimental runs, the sled is actually moving at a Mach Number of 0.8. Hence the data of this table must be modified to reflect the motion of the sled.

TABLE 2.3.3 BLAST CHARACTERISTICS FOR ASD MISSIONS							
Mission No.	Charge Wt. (Lb)	$r_0$ Charge Distance (ft)	$\Delta P_0$ (psi)	$\Delta P_r$	$D_p^+$ (msec)	$\alpha_i$ (°)	Angle of OBL (°)
1	20	60	3.0	6.17	8.32	8	90
2	20	25.8	13.5	32.4	5.35	30	90
3	12000	217	13.5	32.4	44.0	30	90

To evaluate the effect of the sled motion on the positive phase duration times given in Table 2.3.3, the overpressure - distance data given in Figure 1 of Reference 29 can be used to compute the magnitude of the shock front velocity  $U_s$  as a function of distance from the detonation point with the aid of

$$U_s = C_0 \left[ 1 + \frac{6}{7} \left( \frac{\Delta P_0}{P_0} \right) \right]^{\frac{1}{2}} \quad (2.3.21)$$

Knowing  $U_s$  as a function of radial distance,  $r$ , from the point of detonation, the time,  $\tau$ , corresponding to the sequence of events along  $r$  can be obtained by

$$\tau = \int_{r_1}^{r_2} \frac{dr}{U_s(r)} \quad (2.3.22)$$

The time,  $\tau$ , in Equation 2.3.22 defines the time it takes the shock front to move from  $r_1$  to  $r_2$ . The duration of the positive phase corresponding to each  $r$  of interest can be obtained from the data of

Figure 3 of Reference 29.

However, the location of the shock front and magnitude of the positive phase duration time must be related to track site locations rather than radial distance from the point of detonation. This can be accomplished with reference to the following sketch and the relationship:

$$d = r_0 \cos \vartheta \pm \sqrt{r_0^2 \cos^2 \vartheta + r^2 - r_0^2}, \quad (2.3.23)$$

where

$\vartheta$  is the angle of obliquity (OBL) appearing in the previous table,

$r_0$  corresponds to the charge distance magnitudes listed in Table 2.3.3.

and  $d$  represents distance along the track

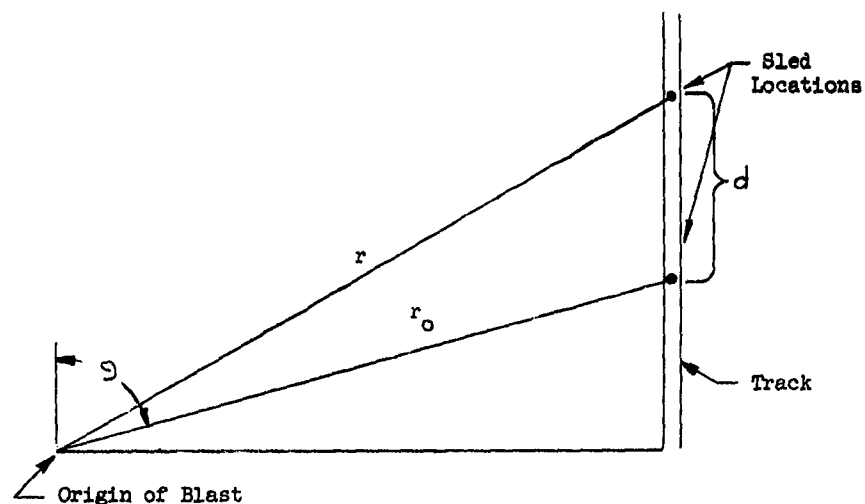


Figure 2.3.14 GEOMETRICAL RELATIONSHIP BETWEEN BLAST ORIGIN AND TRACK



For the specific missions of interest,  $\theta = 90^\circ$ ; hence Equation 2.3.23 reduces to:

$$d = \sqrt{r^2 - r_0^2} \quad (2.3.24)$$

Since  $t = f(r)$  is available from Equation 2.3.22,  $d = f(t)$  can be obtained from either Equation 2.3.23 or Equation 2.3.24. In addition, the times of duration of the positive phase are known as a function of  $r$  from the data of Reference 29; hence, these times can be related to distance along the track,  $d$ , from the same equations.

These results can be represented on a  $d$  vs  $t$  diagram, as shown in Figure 2.3.15.

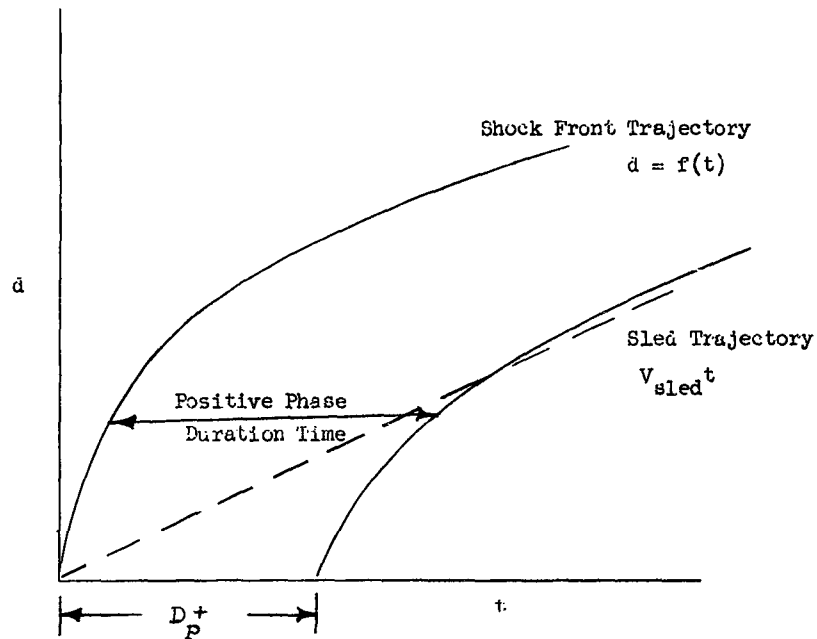


Figure 2.3.15 SLED TRAJECTORY VERSUS TIME DIAGRAM

Superposition of the sled trajectory on this diagram defines

$$d_{\text{sled}} = v_{\text{sled}} t \quad (2.3.25)$$

the positive phase duration time experienced by the moving sled in contrast to the stationary sled duration time (  $D_p^+$  ) noted in Table 2.3.3.

Figures 2.3.16 and 2.3.17 illustrate the moving sled duration times for each of the three missions previously illustrated. It is evident that, for these particular missions, the increase in positive phase duration time is negligible as noted by the tabulated results included in this figure.

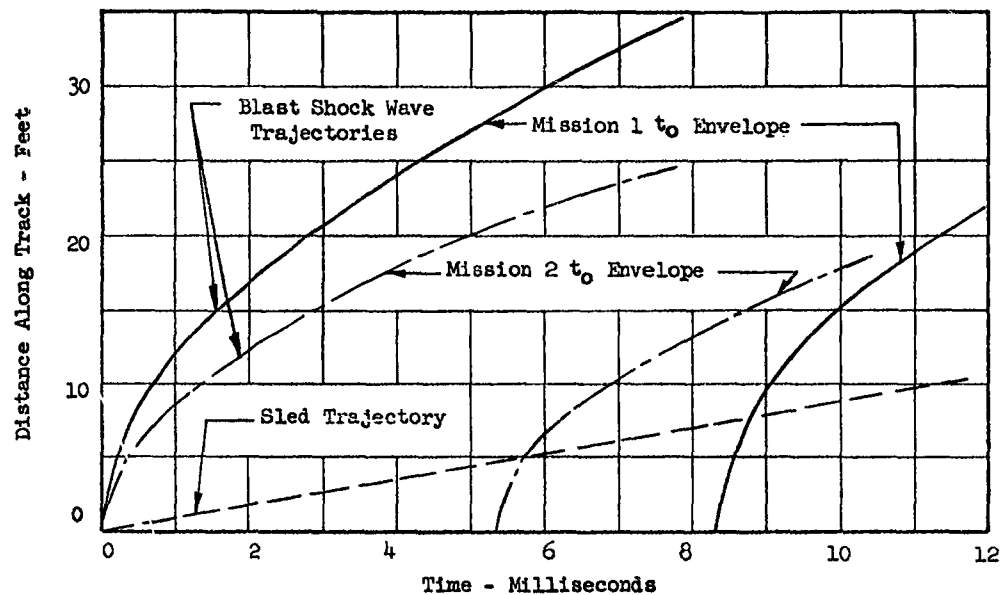
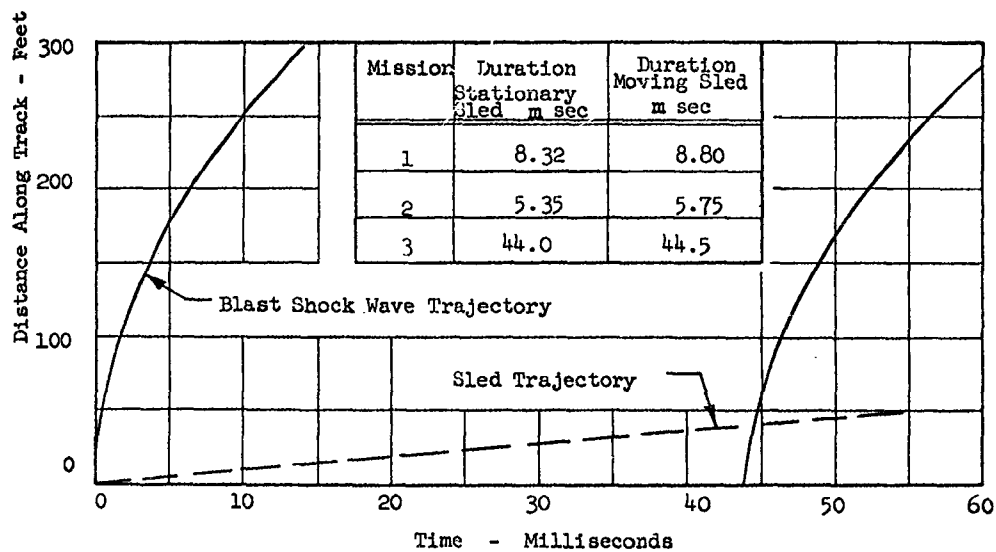


FIG. 2.3.16 EFFECT OF MOVING SLED ON POSITIVE PHASE  
DURATION MISSION #1 AND 2



Blast Shock Wave is Tangent to Track and Meets Sled at Time Zero and Distance Zero

FIG. 2.3.17 EFFECT OF MOVING SLED ON POSITIVE PHASE DURATION MISSION #3

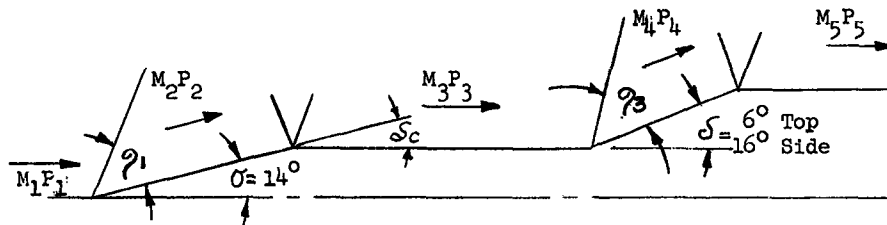
### 2.3.5 PRESSURE DISTRIBUTION AND CHOKING EFFECTS

The task of predicting the pressure distributions over a body moving at high speed and in close proximity to the ground is quite complex; indeed, an exact theoretical analysis is impossible. For simple shapes, the procedure is rather straightforward, but as the configuration becomes more involved, shock wave interactions become more numerous and an exact analysis becomes out of the question. The fact that a body is in close proximity to the ground further complicates the analysis since a reinforcing phenomena takes place as the shock wave is reflected back and forth between the ground and the body. The method developed by this contractor to analyze the pressure distribution over a vehicle of this type is felt to be a reasonable, conservative approach. The first step is to investigate the rather simple flow fields over the top and sides of the vehicle. Next, the region between the bottom of the sled and the ground is considered. Included in this area of the investigation is an analysis of the effect of shock wave reflection and the possibility of and effects of a choking action. Finally, an overall pressure distribution is developed, taking into account the pressure relieving effects which exist when a high pressure area is bounded by a low pressure area.

Pressure distributions for the subject vehicle are investigated at Mach 1.2 with the water trough between the track empty, and at Mach 1.5 with one foot of water in the trough. These velocity - water level conditions are chosen for analysis since these are the actual conditions experienced by the sled during the track-site test program. At speeds lower than Mach 1.2 the initial shock wave is detached. Although there are high pressures on the foremost section of the nose associated with a detached shock front, the reflective phenomena of ground interference does not occur and the overall pressures on the sled are less severe than with an attached shock front. The most severe case occurs at the sled velocity of Mach 1.5 because of the greater dynamic pressure and the smaller height of the sled above the ground which allows more shock wave reflections between the ground and the sled. Hence, the pressure distribution corresponding to

a sled speed of Mach 1.5 is calculated here.

Consider the flow along the top and sides of the vehicle.



From Reference 25, for  $M = 1.5$ ,

$$\theta_1 = 44.5^\circ \text{ for a conical forebody.}$$

Now,

$$q_1 = \frac{1}{2} \gamma M_1^2 P_1 \quad (2.3.26)$$

where,

$$q_1 = \text{dynamic pressure, PSIA}$$

$$\gamma = \text{ratio of specific heats of air} = 1.4$$

$$M_1 = \text{Mach Number} = 1.5$$

$$P_1 = \text{local pressure} = 14.7 \text{ PSIA (conservatively high for EAFB)}$$

Using Equation 2.3.26 and Reference 25,  $P_2$  is found to be 19.65 PSIA.

Knowing  $P_2$ , from Reference 25,  $M_2 = 1.3$

As the flow turns the corner at the rear of the cone, a Prandtl-Meyer expansion occurs. Substitution into the expression

$$\sigma = \delta_c = \sqrt{\frac{\gamma+1}{\gamma-1}} \left\{ \tan^{-1} \left[ \frac{\gamma-1}{\gamma+1} (M_3^2 - 1) \right]^{1/2} - \tan^{-1} \left[ \frac{\gamma-1}{\gamma+1} (M_2^2 - 1) \right]^{1/2} \right. \\ \left. \tan^{-1} \left[ M_2^2 - 1 \right]^{1/2} - \tan^{-1} \left[ M_3^2 - 1 \right]^{1/2} \right\} = .245 \text{ radians } (14^\circ) \quad (2.3.27)$$

gives  $M_3 = 1.78$

The downstream pressure  $P_3$  is computed from

$$P_3 = P_2 \left[ \frac{1 + \frac{\gamma-1}{2} M_2^2}{1 + \frac{\gamma-1}{2} M_3^2} \right] \left( \frac{\gamma}{\gamma-1} \right) \quad (2.3.28)$$

$$P_3 = 10.5 \text{ PSIA}$$

The flow remains undisturbed along most of the cylindrical surface until the transition to the rectangular instrumentation section begins. At this transition the flow along the top of the vehicle will be deflected through  $6^\circ$  and that along the sides through  $16^\circ$ . These deflections are effectively three dimensional and the same method of computing the variables is employed as far as the initial deflection at the front of the sled. These computations yield the results shown in Table 2.3.4.

These pressures exist at the transition area, with a gradual decay towards atmospheric pressure further back on the sled. It should be noted that the pressures calculated so far are actually centerline pressures. Edge effects and crossflow phenomena will be investigated after the flow along the bottom of the sled has been considered.

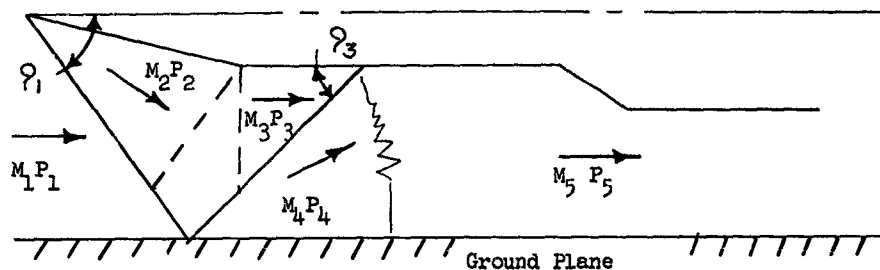
Table 2.3.4 SLED SURFACE PRESSURE & MACH NO. FUNCTIONS @ $\phi$		
	SIDE	TOP
$\theta_3$	$38.3^\circ$	34.3
$M_4$	1.50	1.69
$M_5$	2.05	1.90
$P_4$	14.77 PSIA	10.93 PSIA
$P_5$	6.40 PSIA	7.95 PSIA

The investigation of flow phenomena in the region between the bottom of the sled and the ground involves a more complex calculational procedure. Most of the complexity arises from the possibility of the reflection of the initial shock wave between the sled and the ground. Two undesirable effects of this interaction are immediately obvious; the reinforcing action of the shock waves, causing an increase in pressure on the bottom of the vehicle, and the possibility of a "choking" phenomena should the flow decelerate to a Mach Number of unity.

This choking may affect the performance of the vehicle due to drag increase, as well as result in undesirably large pressures on the sled bottom. In the following analysis, the position of the reflected shock waves and the corresponding pressures are determined, and the presence of any choking condition will be revealed.

The initial shock front is conical; however, the reflected por-

tion that contacts the bottom of the sled is more closely approximated by a two dimensional plane.



The effect of the reflected wave is to deflect the flow upward through an angle of  $14^\circ$ . From Reference 25,  $\theta_3 = 50.5^\circ$ ,  $M_4 = 1.27$ , and  $P_4 = 19.6$  psia. For a two-dimensional deflection, the shock front is detached at  $M = 1.27$ . The longitudinal position at which this detachment occurs is computed from sled-trough geometry as approximately 60 inches from the apex of the cone. The stagnation pressure immediately behind the detached shock wave,  $P_{s5}$  is given by

$$\frac{P_{s5}}{P_4} = \left( \frac{\gamma+1}{2} M_4^2 \right) \left( \frac{\gamma}{\gamma-1} \right) \left[ \frac{\gamma+1}{2\gamma M_4^2 - (\gamma-1)} \right] \left( \frac{1}{\gamma-1} \right) \quad (2.3.29)$$

Since  $P_4$ ,  $M_4$  and  $\gamma$  are known, substitution of these quantities into Equation 2.3.29 gives

$$P_{s5} = 51.4 \text{ PSIA}$$

This pressure decays longitudinally to  $P_5$  where the flow velocity,  $M_5$ , becomes Mach 1 relative to the sled.

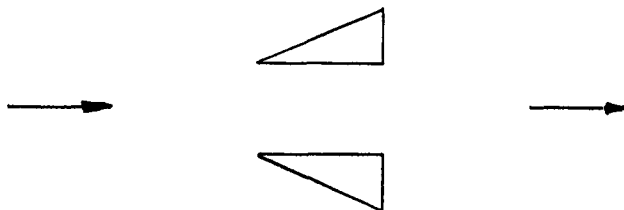
$$P_5 = P_{s5} \left( \frac{2}{\gamma+1} \right) \left( \frac{\gamma}{\gamma+1} \right) \quad (2.3.30)$$



$$P_5 = 27.1 \text{ PSIA}$$

Since the flow slows to sonic velocity, it becomes "choked" (a maximum flow rate is attained) and a relatively constant pressure in the vicinity of  $P_5$  is maintained along the sled bottom. Once the shock front becomes detached, there are no further reflections between the sled and the ground. The protruding transition section has little effect on the pressures on the bottom of the sled since the relative flow velocity is already at Mach 1.0 and will not be further decreased.

Consideration was also given to the possibility of a choking effect in the design of the front slipper strut supports. The approximate "flow channel" geometry between the struts of each slipper is illustrated:



Neglecting the boundary layer on the inner surfaces of the struts, which is quite thin at the design Mach Number, the "between-strut" flow channel is of constant width in the flow direction. Hence, there will be little, if any, tendency to decelerate the flow in this region, and, a choked flow condition is quite unlikely.

Having analyzed the flow conditions on all sides of the sled, it is now necessary to consider them in combination, taking into account edge effects and cross flows. The edge pressures and consequent average pressures are approximated by use of the following equations:

$$P_{\text{Side (Edge)}} = .1/2 P_{\text{Side}} \left( \frac{Q}{L} \right) \quad (2.3.31)$$

$$\overline{P}_{\text{Side}} = 1/2 \left[ P_{\text{Side}} (\text{Edge}) + P_{\text{Side}} (\phi) \right] \quad (2.3.32)$$

$$\overline{P}_{\text{Top}} = 1/2 \left[ P_{\text{Side}} (\text{Edge}) + P_{\text{Top}} (\phi) \right] \quad (2.3.33)$$

$$\overline{P}_{\text{Bottom}} = 1/2 \left[ P_{\text{Side}} (\text{Edge}) + P_{\text{Bottom}} (\phi) \right] \quad (2.3.34)$$

All of the pressures are considered gage. Application of these equations yields the following average gage pressure, which are illustrated in Figures 2.3.18 and 2.3.19 for  $M_1 = 1.5$  and 1.2 respectively.

for  $M_1 = 1.5$

$\overline{P} = 4.95$  psig, all surfaces  
sta 0-30

$\overline{P} = -5.05$  psig, sides and top,  
sta 30-119

$\overline{P} = \frac{36.7 + (-5.05)}{2} = 15.8$  psig, bottom  
sta 60

$\overline{P}_{\text{Side}} (\text{Edge}) = 1/2 (14.77 - 14.7) = +0.035$  psig  
sta 119-150

$\overline{P}_{\text{Side}} (\text{Edge}) = 1/2 (6.40 - 14.7) = -4.15$  psig  
sta 150

$\overline{P}_{\text{Side}} = 1/2 (.035 + .07) \approx 0$  psig  
sta 119-150

$\overline{P}_{\text{Top}} = 1/2 [.035 + (10.93 - 14.7)] = -1.87$  psig  
sta 119-150

$\overline{P}_{\text{Side}} = 1/2 [-4.15 + (-8.3)] = -6.23$  psig  
sta 150

$\overline{P}_{\text{Top}} = 1/2 [-4.15 + (.675)] = -5.45$  psig  
sta 150

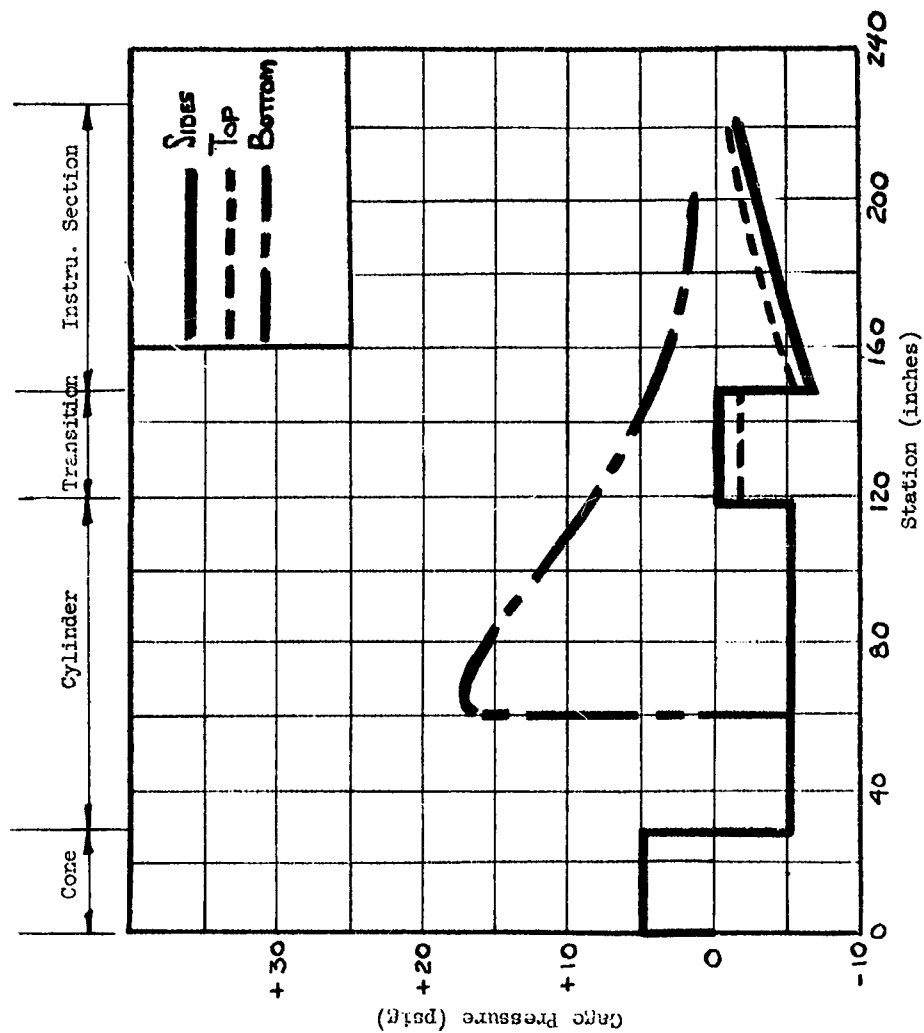


Fig. 2.3.18 AVERAGE PRESSURES ON SLID SURFACES  
 $M = 1.5$ , 12"  $H_2O$  IN TROUGH

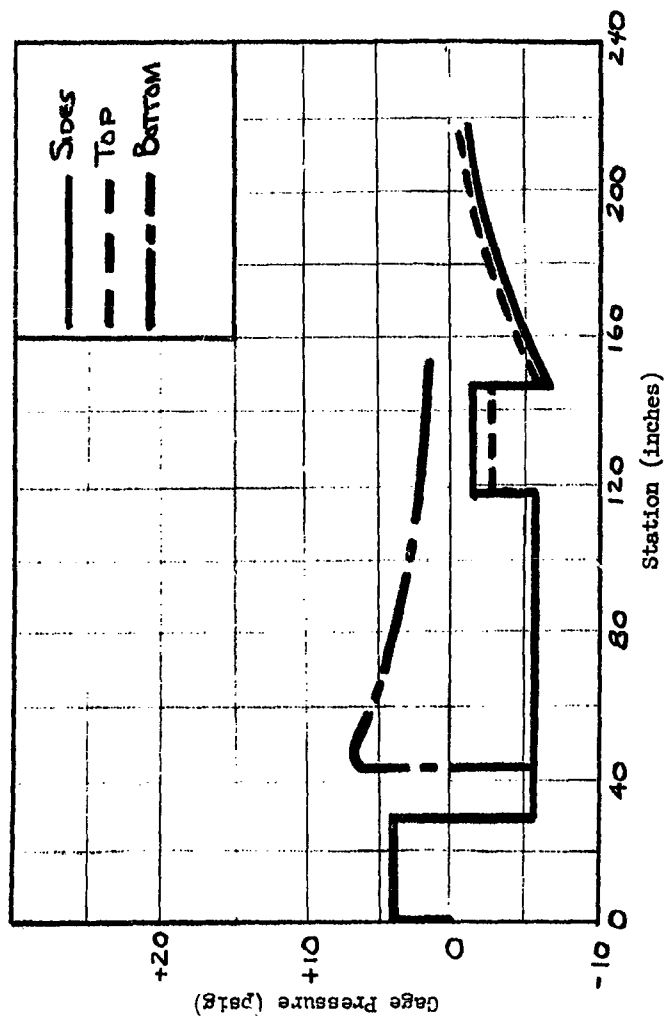


FIG. 2.3.19 AVERAGE PRESSURES ON SLED SURFACES  
M = 1.2, no H<sub>2</sub>O IN TROUGH

### 3.0 AIRFOIL SPECIMEN DESIGN

#### 3.1 DESCRIPTION

Both the structural and airload specimens used in the "ASD Program", duplicate Model 6 described in Ref. 1. This is a swept-back and tapered wing model having the following configurational properties.

Profile	NACA 64
Root Thickness (%)	15.17
Tip Thickness (%)	10
Exposed Root Chord (in.)	22.33
Tip Chord (in.)	12.00
Exposed Semispan (in.)	46.50
Sweep-back Angle	35° - 1/4 CHORDLINE

##### 3.1.1 AIRLOAD SPECIMEN

The airload model was contour machined from a solid block of 410 stainless steel heat treated to a minimum ultimate tensile strength of 160,000 psi. It would be impractical to contour machine the stainless steel at a higher hardness, and heat treating after machining would result in too much residual twist and waviness. The transducer, accelerometer, and strain gage instrumentation and wiring depicted in Figure 3.1.1 necessitates access to the wing interior. This was accomplished by splitting the wing on the horizontal (in flight) plane of symmetry and milling out the wing interior instrumentation installation following machining of the external contour.

The structural connection which joins the two halves and ensures that the wing bends as an integral unit was made with (52) - 3/4 in. diameter shear pin connectors distributed throughout the wing planform as dictated by strength requirements. This method of fastening, as shown in Figure 3.1.2, was chosen because a pilot hole can be line

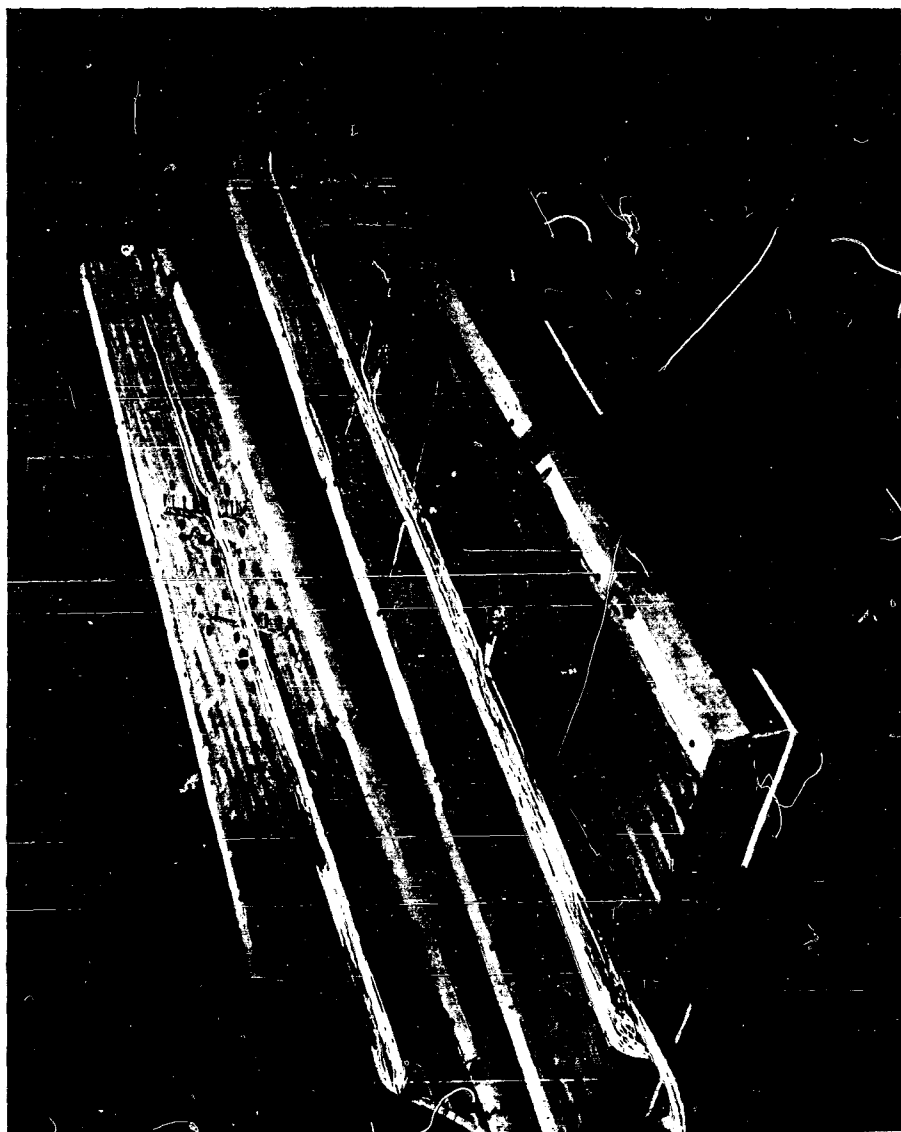


Fig. 3.1.1.1 (6L) AIRLOAD MODEL

drilled through both halves of the specimen making it relatively easy to provide the close tolerance fit between the pin and hole necessary to prevent slippage of the fasteners under dynamic loading. The fastener arrangement suggested in Ref. 1 was first attempted on the ASD airload model since it did not involve machining out much of the tension side. However, it became impractical to locate the mating holes without opening up the tolerances on concentricity beyond acceptable limits.

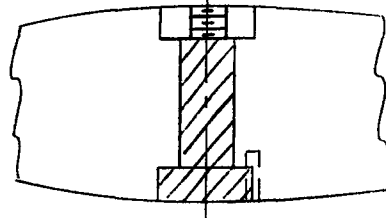


Fig. 3.1.2 SHEAR CONNECTOR (6L) MODEL

The base of the airload model consists of a rectangular stub. The stub is shimmed in the slotted portion of the sled fuselage and clamped in place with (6) - 3/4 in. diameter high strength bolts as shown in Fig. 3.1.3.

#### 3.1.2 STRUCTURAL SPECIMEN

The structural specimen is basically of thick-skin multi web type construction typical of high speed low aspect ratio wings. The specimen has a constant (1/8) inch skin thickness formed from 7075-T6 aluminum sheet. The internal structure which is evident in Fig. 3.1.4 consists of three spars, a solid leading and trailing edge member and six ribs outboard of the wing root. The three spars depicted in Fig. 3.1.5 are fabricated from 2024 - T4 aluminum angle extrusions bolted to 2024 - T3 aluminum web members. The outer two bays of the leading edge spar and the outer three bays of the trailing edge spar consists of a formed channel fabricated from .094" 5052 - H34 aluminum sheet. This member was

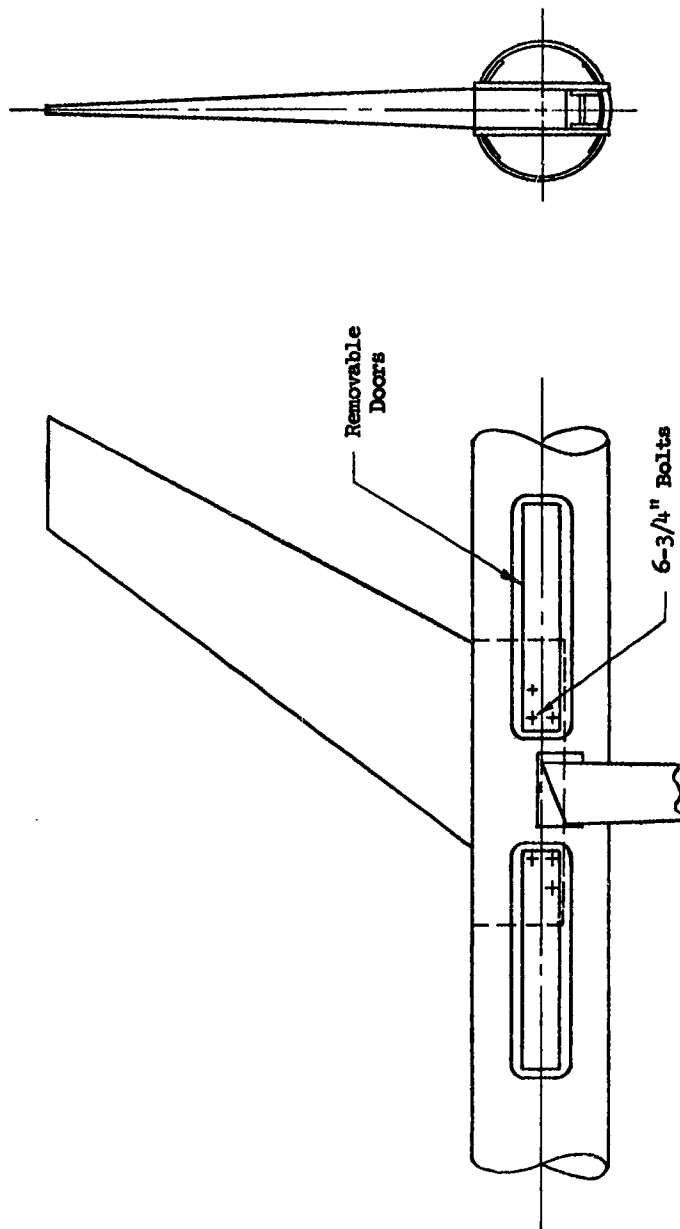


Fig. 3.1.3 AIRLOAD SPECIMEN INSTALLED





Fig. 3-1.1.4 (6R) STRUCTURAL MODEL

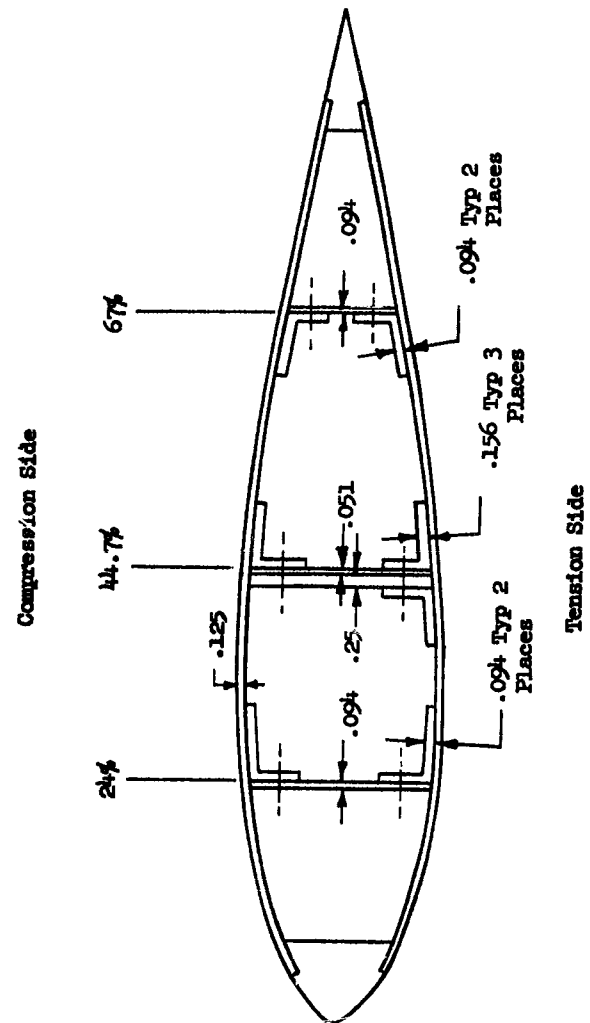


FIGURE 3.1.5 TYPICAL SECTION OUTSIDE OF FAILURE RAY

spliced to the built up spars. The formed-channel was necessary near the tip because the limited depth between skins did not permit space for a shear connector between the web and spar cap. The center spar was discontinued entirely in the last outboard bay of the specimen. The three spar arrangement was selected in order to develop a relatively high critical buckling stress in the compression skin. In the original design, the internal structure located on the 44.7% chordline consisted only of stringers. The web was added in order to make the structure more amenable to a theoretical post-failure analysis.

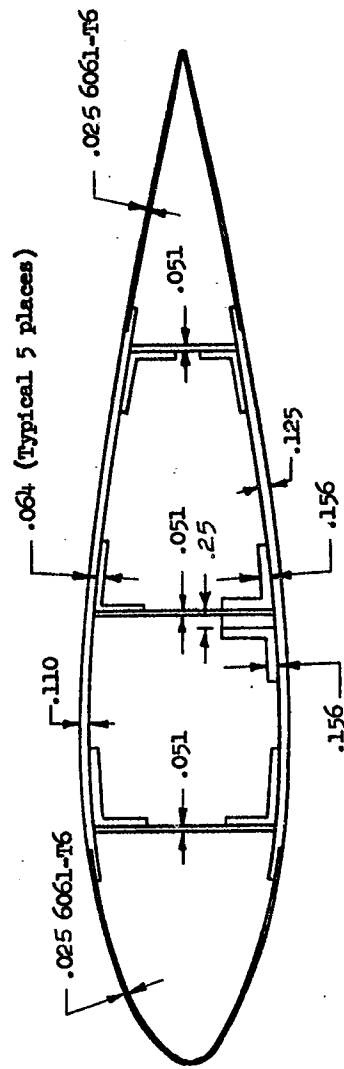
A solid leading and trailing edge member was cast from 356-T51 aluminum alloy. These members were provided in order to facilitate fabrication of the specimen and make it relatively easy to remove the skin on one side of the structural model to provide access to the internal instrumentation. The tension skin was chosen to be removable since the mode of failure is critically sensitive to the type and location of compression skin fastener. As a consequence, the compression skin was riveted to the three spars and screwed to the leading and trailing edge members. The tension skin was fastened to the three spars by means of screws and floating basket nuts.

A predetermined breakline was built into the structural specimen in order to eliminate the problems associated with a random type failure. The selected breakline intersects the 25% chordline at 25% of the exposed half span length and is directed perpendicular to the 50% chordline which is taken as the structural axis. Two ribs 4.5 inches apart are located symmetrically about the breakline; and parallel to it. These ribs are made of (1/4) inch thick 5083-H113 aluminum plate which is heavier than the (1/8) inch thick plate used for the other outboard ribs. This was done in order to provide essentially a fixed edge support for the compression skin and also to confine the local effects of the failure within the failure bay as much as possible.

In order to ensure that the failure would occur at the preselected break line, this section was considerably weakened as evidenced by the moment capacity curve shown in Fig. 3.3.5. The leading and trailing edge members were discontinued in the failure bay area. Both the tension and compression skins outside of the fore and aft spars were removed. In its place, a removable (.025) inch 6061-T6 aluminum skin was provided. While this thin skin was designed to support the blast-induced dynamic pressures, it does not have sufficient strength to contribute significantly to the bending capacity at the break line nor will it greatly influence the mode of failure. The resultant structure in the failure bay is essentially a multi web box which is quite amenable to a theoretical post-failure analysis. A (4.5) inch wide strip of the compression skin in the failure bay is milled down from .125 inch to .110 inch  $\pm$  .002 inch. A close tolerance is required on the compression skin thickness since the ultimate bending strength is quite sensitive to this parameter. The spar caps on the fore and aft spars are milled down from (.094) inch to (.064) inch thickness. In addition the legs of these spar caps are trimmed down from (1.12) inch to (0.75) inch. The webs of the fore and aft spars are milled down from (.094) inch to (.051) inch thickness. The center spar caps are milled down from (.156) inch to (.064) inch thickness on the compression side only. In addition the legs of this spar cap are trimmed from (1.00) inch to (.75) inch. The 1/4 inch thick center spar web is omitted in the failure bay except for a short piece on the tension side as shown in Fig. 3.1.6. The purpose of the large center spar cap in the failure bay is to raise the asymptotic value of the post failure bending moment and as a consequence, limit the magnitude of the post-failure hinge angle.

The configuration of the root support was dictated by several functional requirements. It must be sufficiently rigid to provide essentially a fixed support. It must be adaptable to the slotted fuselage receptacle. It must facilitate the removal of the tension skin in order

Compression Side



Tension Side

Fig. 3.1.6 SECTION THROUGH BREAKLINE

to provide access to the internally mounted instrumentation. The solution to these problems is shown in Fig. 3.1.7. The basic specimen structure was carried (10) inches below the root line. Three stream-wise ribs fabricated from 1/4 inch 5083-H113 aluminum plate were provided in the root area. The internal portion of the specimen below the root line was then filled with epoxy resin. The inside surface of the tension skin was lubricated to prevent a bond with the resin. A rectangular aluminum box fabricated from (3/8) inch 5083-H113 aluminum plate and internally reinforced was built around the specimen in two halves. The outside skin of the specimen was lubricated, and the box was filled with the epoxy resin. The outside surfaces of the aluminum box were machined to a (.005) inch tolerance in order to provide a snug fit between the specimen root and the slotted receptacle in the sled fuselage. The six (3/4) inch mounting holes were lined drilled through the box and specimen, and two (1.12) inch wiring holes were line drilled through the epoxy root parallel to the structural axis.

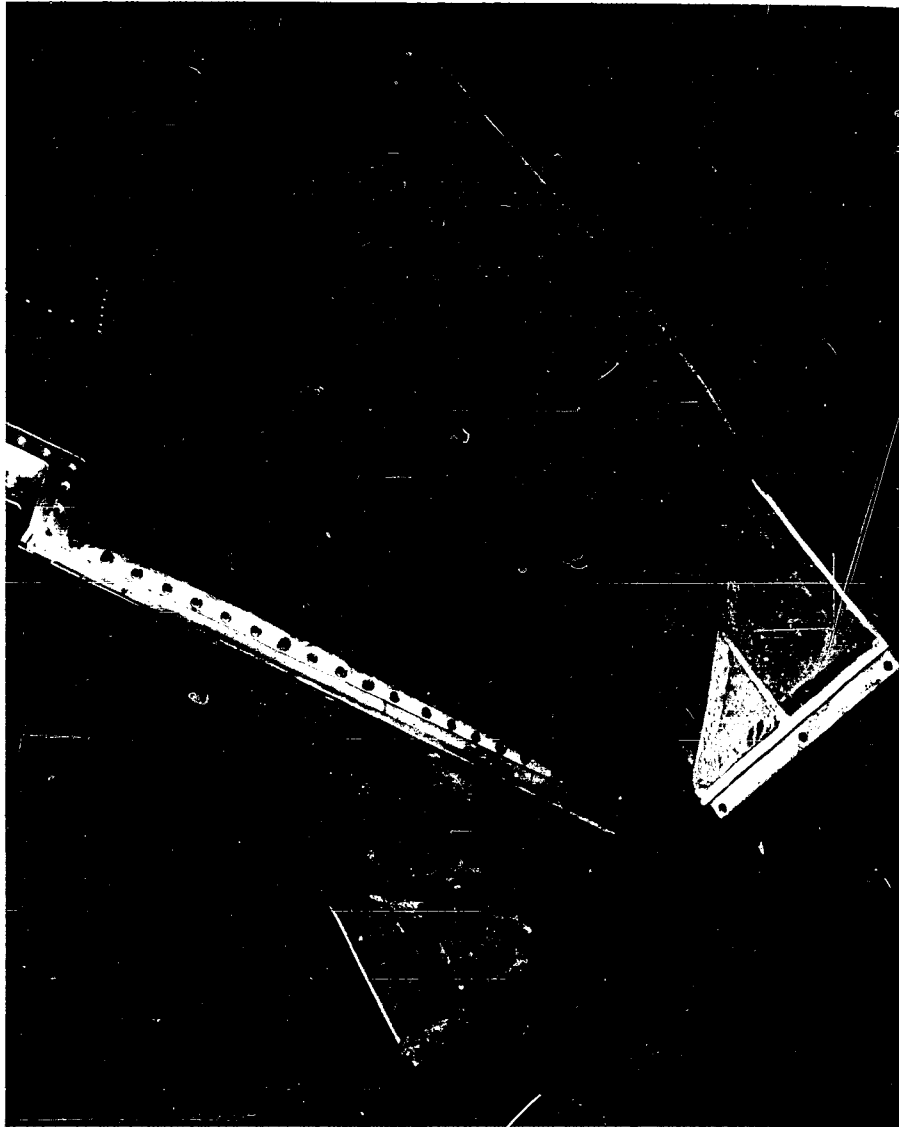


Fig. 3.1.7 ROOT SUPPORT FOR (6R) STRUCTURAL MODEL

### 3.2 PRELIMINARY DESIGN

#### 3.2.1 AIRLOADS

The preliminary airloads acting on both the structural and airload specimens for the three different sled missions will be evaluated using quasi-steady aerodynamics to determine the lift-time curves. Further refinements in the airloads which would include wing motion and stall effects are unwarranted at this time due to the approximate nature of computing the dynamic response in this phase of the design. The ASD sled missions are described in Table 3.2.1.

#### Quasi - Steady Lift vs. Time

##### Notation

U	shock velocity - fps
u	particle velocity - fps
C	sound velocity - fps
q	peak dynamic pressure - psi
P	peak overpressure - psi
$\rho$	air density - $\frac{\text{lb} - \text{sec}^2}{\text{ft}^4}$
V	sled velocity
t	time - sec
$D_p^+$	duration of positive pressure - sec
$C_L$	slope of lift coefficient vs. angle of attack curve - 1/RAD.
S	plan form area - $\text{ft}^2$
$\gamma$	coefficient of compressibility
$L_t$	lift at time (t) - lb
subscript o - Ambient Conditions	
time zero is measured from the instant the shock front hits the specimen.	



FIELD TESTS ON ASD WING MODELS									
Table 3-2.1									
Mission No.	Wing Model	Actual Charge Weight lb.	Charge Distance ft.	Angles of OBL	$\alpha_1$ Degrees	Over-Pressure Psi Side-on	Duration Millisec Sta. Ft.	Sled Velocity (Mach No.)	
1	Aero	Pent. 20	60.0	90°	8	3.0	8.32	0.8	
2	Aero	Pent. 20	25.8	90°	30	13.5	5.35	0.8	
3	Aero	TNT 12000	217.0	90°	30	13.5	44.0	0.8	
4	Struc.	Pent. 20	60.0	90°	8	3.0	8.32	0.8	
#5	Struc.	Pent. 20	25.8	90°	30	13.5	5.35	0.8	
#6	Struc.	TNT 12000	217.0	90°	30	13.5	44.0	0.8	
* Destruction Missions									

In developing the lift-time curve for the various blast conditions, it will be assumed that the motion of the sled during the blast duration is negligible, and the lift builds up instantaneously.

The expression for the quasi-steady lift is:

$$L(t) = 1/2 \rho(t) \left[ V(t)^1 \right]^2 S C_{L\alpha} \text{TAN}^{-1} \left[ \frac{u(t)}{V} \right] \quad (3.2.1)$$

Where:

$$V(t)^1 = \left[ V^2 + u(t)^2 \right]^{\frac{1}{2}}$$

$$S = 5.54 \text{ ft}^2 \quad (\text{PLANFORM AREA})$$

$$C_{L\alpha} = 5.2 \quad (\text{Table 22 REFERENCE 1})$$

$$V = 0.8 \times 1120 = 896 \text{ fps}$$

The following blast equations which are necessary to obtain an analytical expression for eq. 3.2.1 are taken from Ref. 26

Shock Velocity

$$U = C_o \left( 1 + \frac{6P}{7P_o} \right)^{\frac{1}{2}} \quad (3.2.2)$$

Particle Velocity

$$u = \frac{5P}{7P_o} \frac{C_o}{\left( 1 + \frac{6P}{7P_o} \right)^{\frac{1}{2}}} \quad (3.2.3)$$

Air Density

$$\rho = \rho_o \left( \frac{7 + 6 P/P_o}{7 + P/P_o} \right) \quad (3.2.4)$$

Peak Dynamic Pressure

$$q = \frac{1}{2} \rho u^2 = 5/2 \cdot \frac{P^2}{7P_o + P} \quad (3.2.5)$$

Overpressure

$$P(t) = P \left( 1 - \frac{t}{D_p^+} \right) e^{-\frac{t}{D_p^+}} \quad (3.2.6)$$

Dynamic Pressure

$$q(t) = q \left( 1 - \frac{t}{D_p^+} \right)^2 e^{-2 \frac{t}{D_p^+}} \quad (3.2.7)$$

In addition

$$\frac{P_o + P(t)}{[\rho(t)]^{1/4}} = \text{constant} = A \quad (3.2.8)$$

Mission No. 1

$$P = 3.0 \text{ psi}$$

$$P_o = 14.7 \text{ psi}$$

$$\rho_o = .00238 \frac{\text{lb} - \text{sec}^2}{\text{ft}^4}$$

$$C_o = 1120 \text{ fps}$$

From eq. 3.2.3 the particle velocity at time zero is given by

$$u = \frac{5 \times 3.0}{7 \times 14.7} \frac{1120}{\left( 1 + \frac{6 \times 3.0}{7 \times 14.7} \right)^{1/2}} = 150 \text{ fps}$$

The air density at time zero may be computed from eq. (3.2.4)

$$\rho = .00238 \left( \frac{7 + \frac{6 \times 3.0}{14.7}}{7 + \frac{3.0}{14.7}} \right) = .00272 \frac{\text{lb} - \text{sec}^2}{\text{ft}^4}$$

Evaluating A at time zero we obtain

$$A = \frac{14.7 + 3.0}{(.00272)^{1/4}} = 6.92 \times 10^4$$

Substituting into eq. 3.2.8

$$\rho(t) = \left[ \frac{P_o + P(t)}{A} \right]^{1/4} = \left\{ \left[ \frac{P_o}{A} \right] + \left[ \frac{P(t)}{A} \right] \left( 1 - \frac{t}{D_p^+} \right)^2 e^{-2 \frac{t}{D_p^+}} \right\}^{1/4}$$

$$\rho(t) = \left[ .000213 + .0000433 \left( 1 - \frac{t}{D_p^+} \right)^2 e^{-2 \frac{t}{D_p^+}} \right]^{1/4} \quad (3.2.9)$$

The dynamic pressure at time zero may be computed from eq. 3.2.5

$$q_0 = 5/2 \frac{(3.0)^2 \times 144}{7 \times 14.7 + 3.0} = 30.6 \text{ psf}$$

$$q(t) = 27.8 \left(1 - \frac{t}{D_p}\right)^2 e^{-2 \frac{t}{D_p}} \quad (3.2.10)$$

From eq. 3.2.5

$$u(t) = \left( \frac{2 q(t)}{\rho(t)} \right)^{\frac{1}{2}} \quad (3.2.11)$$

The duration of the positive portion of the lift curve is divided into (10) increments of time, and the necessary parameters to compute the total lift are summarized in Table 3.2.2.

Mission No. 2 and No. 3

$$p = 13.5 \text{ psi}$$

$$p_0 = 14.7 \text{ psi}$$

$$\rho_0 = .00238 \frac{\text{lb} - \text{sec}^2}{\text{ft}^4}$$

$$C_0 = 1120 \text{ fps}$$

From eq. 3.2.3, the particle velocity at time zero is given by

$$u = \frac{5 \times 13.5}{7 \times 14.7} \left( \frac{1120}{1 + \frac{6 \times 13.5}{7 \times 14.7}} \right)^{\frac{1}{2}} = 547 \text{ fps}$$

The air density at time zero may be computed from eq. 3.2.4

$$\rho = .00238 \left( \frac{7 + \frac{6 \times 13.5}{14.7}}{7 + \frac{13.5}{14.7}} \right) = .00376 \frac{\text{lb} - \text{sec}^2}{\text{ft}^4}$$

Evaluating A at time zero, we obtain

$$A = \frac{14.7 + 13.5}{(.00376)^{1.4}} = 7.05 \times 10^4$$

LIFT DATA MISSION NO. 1									
Table 3.2.2	$t/D_p^+$	$(1 - \frac{t}{D_p^+})e^{\frac{t}{D_p^+}}$	$q(t)$	$\rho(t)$	$u(t)$	$\frac{u(t)}{V}$	$TAN^{-1} \frac{u(t)}{RAD. V}$	$V'^2 \times 10^4$	$L(t) / lb.$
	0	1.000	27.8	.00272	142	.159	.158	82.12	5080
	.10	.813	18.4	.00267	117	.131	.131	81.47	4100
	.20	.655	11.9	.00261	95.5	.107	.107	81.01	3260
	.30	.518	7.45	.00257	76.0	.0850	.0850	80.68	2540
	.40	.402	4.49	.00253	59.5	.0665	.0665	80.46	1950
	.50	.303	2.55	.00249	45.2	.0505	.0505	80.31	1450
	.60	.220	1.35	.00247	33.0	.0369	.0369	80.21	1050
	.70	.149	0.62	.00244	22.5	.0252	.0252	80.15	710
	.80	.090	0.22	.00242	13.5	.0151	.0151	80.12	420
	.90	.041	0.05	.00240	6.5	.0073	.0073	80.11	200
	1.00	0	0	.00238	0	0	0	80.10	0

$$\rho(t) = \left[ \frac{P_o + P(t)}{A} \right] \frac{1}{\delta} = \left[ \frac{P_o}{A} + \frac{P(o)}{A} \left( 1 - \frac{t}{D_p^+} \right) e^{-\frac{t}{D_p^+}} \right] \frac{1}{\delta}$$

$$\rho(t) = \left[ .000208 + .000192 \left( 1 - \frac{t}{D_p^+} \right) e^{-\frac{t}{D_p^+}} \right] \frac{1}{\delta} \quad (3.2.12)$$

The dynamic pressure at time zero may be computed from eq. 3.2.5

$$q = 5/2 \cdot \frac{(13.5)^2 \times 144}{7 \times 14.7 + 13.5} = 564 \text{ psf}$$

$$q(t) = 564 \left( 1 - \frac{t}{D_p^+} \right)^2 e^{-2 \frac{t}{D_p^+}} \quad (3.2.13)$$

From eq. 3.2.5

$$u(t) = \left( \frac{2 q(t)}{\rho(t)} \right)^{1/2} \quad (3.2.14)$$

The duration of the positive portion of the lift curve is divided into (10) increments of time, and the necessary parameters to compute the total lift are summarized in Table 3.2.3.

In order to facilitate a more general solution to the response of a single degree of freedom system subjected to blast induced type loading, the normalized lift curves of Fig. 3.2.1 will be approximated by exponential functions.

#### Mission No. 1

Let the lift curves in Figure 3.2.1 be approximated by the following expression

$$\frac{L(t)}{L(o)} = \left( 1 - \frac{t}{D_p^+} \right) e^{-d \frac{t}{D_p^+}}$$

The exponential decay coefficient (d) can be determined from the shape of the curves in Figure 3.2.1. This coefficient (d) will be taken as the average value as determined from the above expression at three increments of normalized time

$$t/D_p^+ = 0.3, 0.4, 0.5$$

LIFT DATA MISSION NO. 2 AND NO. 3									
Table 3.2.3	$t/D_p^+$	$(1 - \frac{t}{D_p^+})e^{\frac{t}{D_p^+}}$	$q(t)$	$\rho(t)$	$u(t)$	$\frac{u(t)}{V}$	$TAN^{-1} \frac{u}{V}$ RAD	$V'^2 \times 10^4$	$L(t)$ lb.
	0	1.000	564	.00376	548	.612	.550	110.1	32,700
	.10	.813	372	.00350	460	.514	.476	101.3	24,400
	.20	.655	242	.00329	382	.427	.403	94.7	18,100
	.30	.518	151	.00311	311	.348	.335	89.8	13,500
	.40	.402	91	.00294	248	.277	.271	86.2	9,900
	.50	.303	52	.00280	193	.216	.213	83.8	7,200
	.60	.220	27	.00268	142	.159	.158	82.1	5,000
	.70	.149	13	.00258	100	.112	.112	81.0	3,370
	.80	.090	5	.00249	63	.070	.070	80.5	2,020
	.90	.041	1	.00241	29	.0325	.0325	80.1	905
	1.00	0	0	.00238	0	0	0	80.1	0

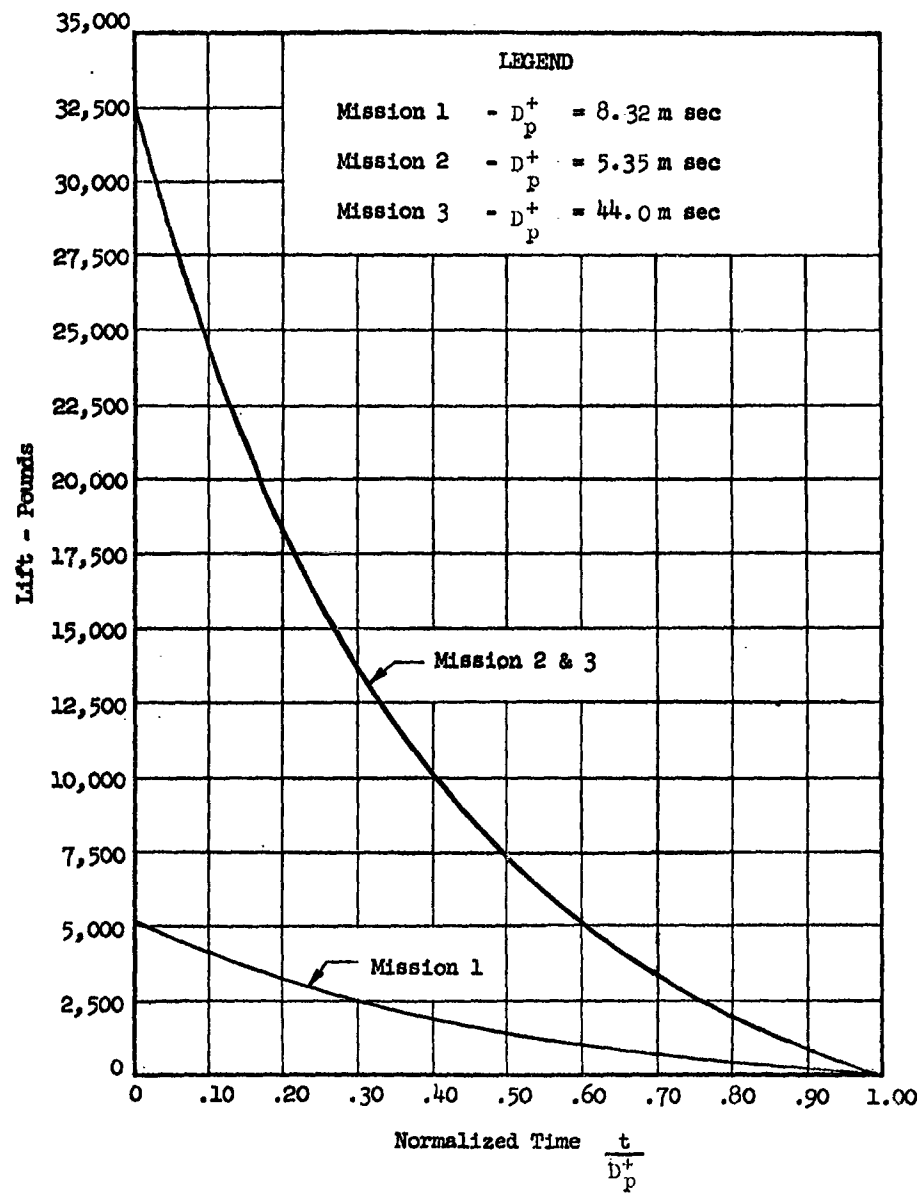


Fig. 3.2.1 LIFT TIME CURVE FOR ASD MODELS



$$d_{AV} = \frac{1.11 + 1.12 + 1.13}{3}$$

$$d_{AV} = 1.12$$

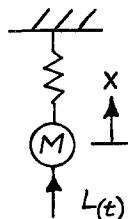
Mission No. 2 and No. 3

$$d_{AV} = \frac{1.76 + 1.71 + 1.64}{3}$$

$$d_{AV} = 1.70$$

### 3.2.2 DYNAMIC RESPONSE

As demonstrated in Section 3.2.3.1 the response of the wing models can be reduced to the consideration of a single degree of freedom system subjected to an exponential type loading. In order to expedite the solution of this problem, the Laplace Transform will be applied to equation 3.2.15.



$$M \ddot{X}(t) + K X(t) = L(t) \quad (3.2.15)$$

Where:

$$L(t) = L_0 \left( 1 - \frac{t}{D} \right) e^{-d \frac{t}{D}} \quad (3.2.16)$$

Initial Conditions

$$X_0 = \dot{X}_0 = 0$$

A dot above (X) indicates differentiation with respect to time.

$\Gamma$  is the laplace transform operator.

Operating on eq. 3.2.15

$$M\Gamma(\ddot{X}) + K\Gamma(X) = \Gamma(L(t)) \quad (3.2.17)$$

Noting that

$$\Gamma(\ddot{X}) = p^2 \Gamma(X) - p X_{(0)} - \dot{X}_{(0)} = p^2 \Gamma(X) \quad (3.2.18)$$

eq. 3.2.17 becomes

$$\Gamma(X) = \frac{\Gamma(L(t))}{m p^2 + K} = \frac{\Gamma(L(t))}{m(p^2 + \omega^2)} \quad (3.2.19)$$

$$\Gamma(L(t)) = \int_0^\infty L(t) e^{-pt} dt = \int_0^\infty L_{(0)} \left(1 - \frac{t}{D+p}\right) e^{-\frac{d}{D+p}t} e^{-pt} dt$$

$$\Gamma(L(t)) = L_{(0)} \left[ \int_0^\infty e^{\left(\frac{-d}{D+p} - p\right)t} dt - \int_0^\infty \frac{t}{D+p} e^{\left(\frac{-d}{D+p} - p\right)t} dt \right]$$

$$\Gamma(L(t)) = L_{(0)} \left[ \frac{1}{p + \frac{d}{D+p}} - \frac{1}{\frac{D+p}{p} \left(p + \frac{d}{D+p}\right)^2} \right] \quad (3.2.20)$$

Substituting eq. 3.2.20 into 3.2.19

$$\Gamma(X) = \frac{L_{(0)}}{m} \left[ \frac{1}{\left(p + \frac{d}{D+p}\right) (p^2 + \omega^2)} - \frac{1}{\frac{D+p}{p} \left(p + \frac{d}{D+p}\right)^2 (p^2 + \omega^2)} \right] \quad (3.2.21)$$

Obtaining the transform of this expression

$$X = \frac{L_{(0)}}{m} \left\{ \frac{e^{-\frac{d}{D+p}t}}{\omega^2 + \left(\frac{d}{D+p}\right)^2} \left[ 1 - \frac{t}{D+p} - \frac{2d}{D+p^2 \left(\omega^2 + \left(\frac{d}{D+p}\right)^2\right)} \right] \right\} \quad (3.2.22)$$

$$+ \sin \frac{(\omega t - \tan^{-1} \frac{\omega D+p}{d})}{\omega \left(\omega^2 + \left(\frac{d}{D+p}\right)^2\right)^{1/2}} - \frac{\sin \left(\omega t - 2 \tan^{-1} \frac{\omega D+p}{d}\right)}{\omega \frac{D+p}{p} \left(\omega^2 + \left(\frac{d}{D+p}\right)^2\right)}$$

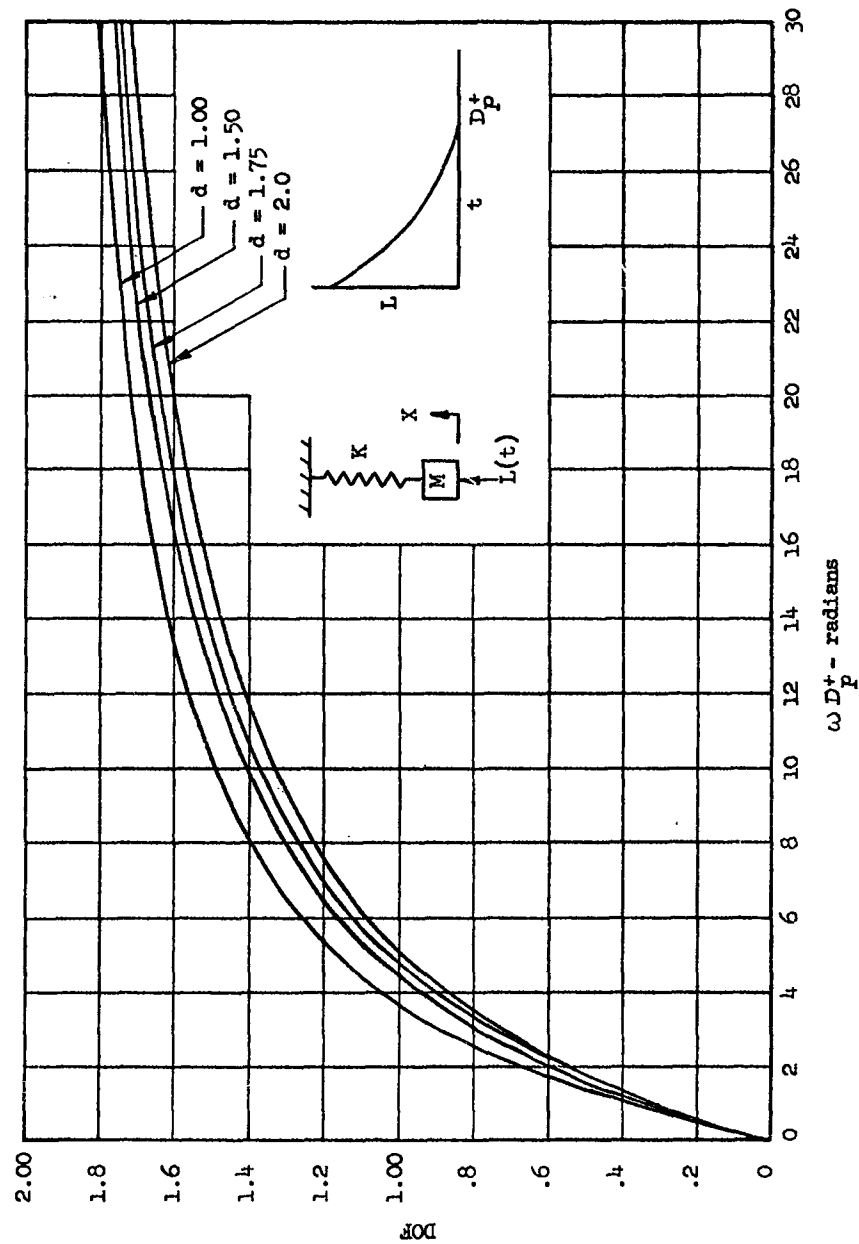


Fig. 3.2.2 DYNAMIC OVERSTRESS FACTOR FOR SINGLE DEGREE OF FREEDOM SYSTEM AND EXPONENTIAL LOADING

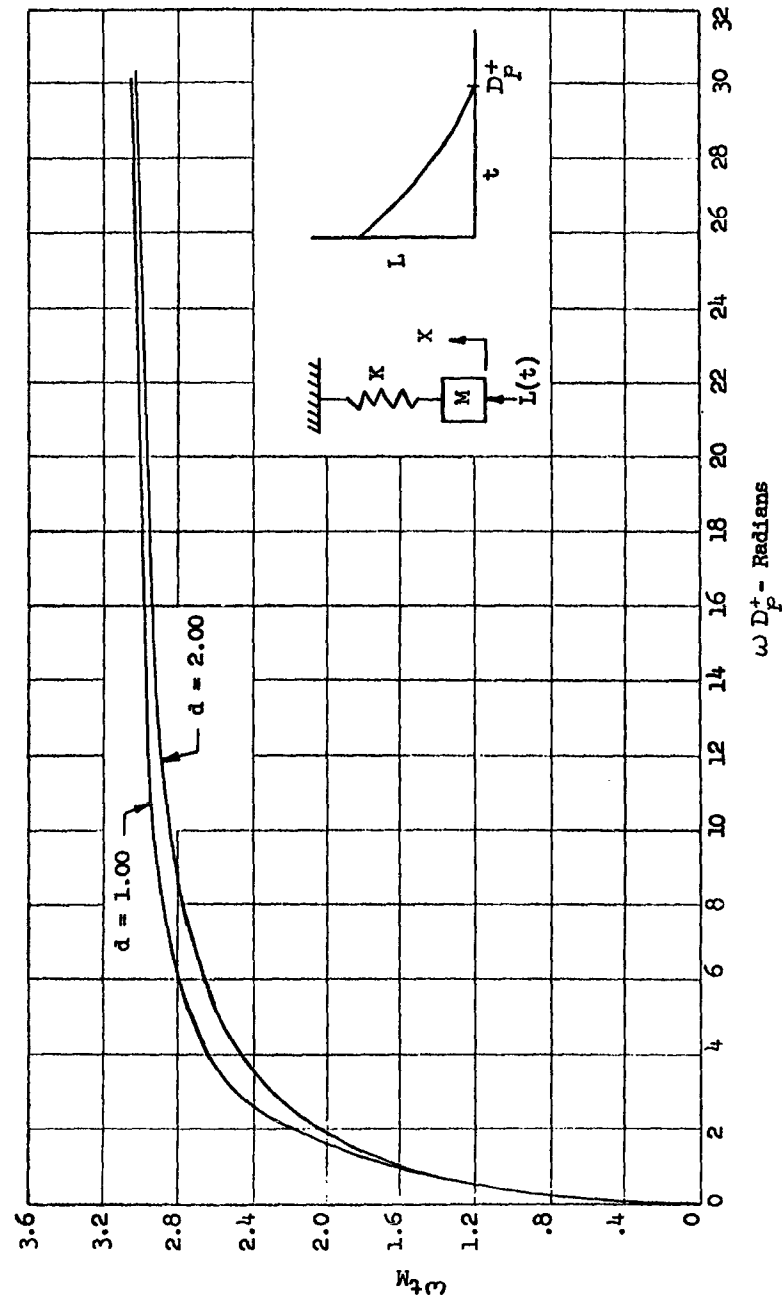


Fig. 3.2.3 TIME OF MAXIMUM RESPONSE FOR BLAST INDUCED LOADINGS WITH EXPONENTIAL DECAY RATE

Differentiating the displacement with time and setting the result equal to zero, we obtain

$$\omega t_M = \tan^{-1} \left\{ \frac{\left[ 1 - \left( \frac{d}{\omega D_p^+} \right)^2 \right] + d \left[ 1 - \left( \frac{d}{\omega D_p^+} \right)^2 \right]}{2 \frac{d}{\omega D_p^+} - \omega D_p^+ \left[ 1 + \left( \frac{d}{\omega D_p^+} \right)^2 \right]} \right\} \quad (3.2.23)$$

The dynamic overstress factor (DOF) is defined as

$$\text{DOF} = \frac{X_m}{X_s} \quad (3.2.24)$$

where the static deflection for a steady load application of  $L_{(0)}$  is given as

$$X_s = \frac{L_{(0)}}{K} = \frac{L_{(0)}}{m(\omega)^2} \quad (3.2.25)$$

Substituting eqs. 3.2.22 and 3.2.25 into 3.2.24

$$\begin{aligned} \text{DOF} = & \frac{e^{-\frac{d}{\omega D_p^+} \omega t_m}}{1 + \left( \frac{d}{\omega D_p^+} \right)^2} \left[ \frac{1 - \frac{\omega t_m}{\omega D_p^+} - \frac{\left( \frac{2d}{\omega D_p^+} \right)^2}{1 + \left( \frac{d}{\omega D_p^+} \right)^2}}{1 + \left( \frac{d}{\omega D_p^+} \right)^2} \right] \\ & + \frac{\sin \left( \omega t_m - \tan^{-1} \frac{\omega D_p^+}{d} \right)}{\left[ 1 + \left( \frac{d}{\omega D_p^+} \right)^2 \right]^{1/2}} - \frac{\sin \left( \omega t_m - 2 \tan^{-1} \frac{\omega D_p^+}{d} \right)}{\omega D_p^+ \left[ 1 + \left( \frac{d}{\omega D_p^+} \right)^2 \right]} \end{aligned} \quad (3.2.26)$$

Equations 3.2.23 and 3.2.26 were programmed and the values of DOF and  $\omega t_m$  were determined for various values of  $(d)$  and  $\omega D_p^+$ . The results are presented in Fig. 3.2.2 and 3.2.3.

### 3.2.3 AIRLOAD SPECIMEN

In order to determine the structural adequacy of the airload specimen when subjected to the blast-induced loads shown in Fig. 3.2.1. certain simplifying assumptions were made. The specimen was assumed to be cantilevered from a fixed support located at the intersection of the 50% chordline and the root, and directed normal to the 50% chordline.

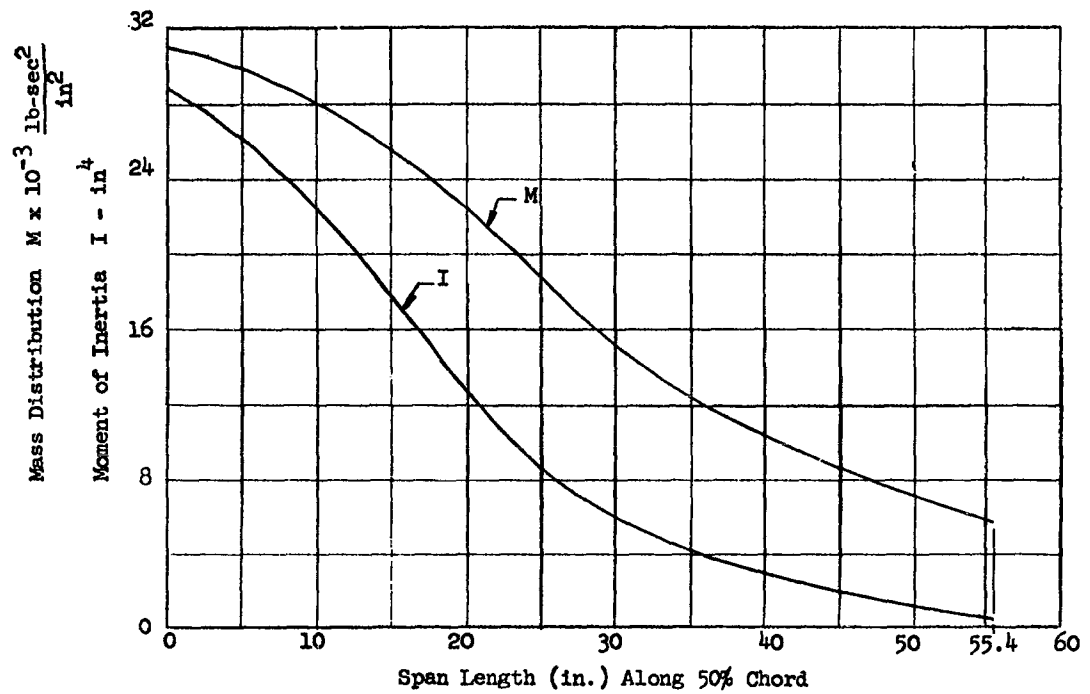


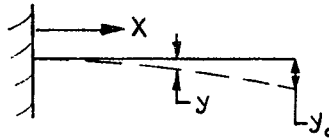
Fig. 3.2.4 AIRLOAD SPECIMEN PRELIMINARY MASS AND MOMENT OF INERTIA DISTRIBUTION

The 50% chordline was taken as the elastic axis, and torsional effects have been neglected. The mass and stiffness distribution of the idealized specimen is given in Fig. 3.2.4.

### 3.2.3.1 NATURAL FREQUENCY OF IDEALIZED MODEL

In order to simplify the dynamic response analysis, the idealized cantilevered beam was reduced to a system having a single degree of freedom. The natural frequency of this reduced system was estimated by two independent methods.

The first method utilizes the fundamental frequency of the idealized cantilevered beam as the natural frequency of the single degree of freedom system. This is accomplished using Rayleigh's Method as outlined on pg. 142 of Ref. 24.



$$\text{Kinetic Energy}_{\max} = \text{Potential Energy}_{\max}$$

$$\text{K.E.} = 1/2 \omega^2 \int_0^L m(x) y^2 dx \quad (3.2.27)$$

Where  $m(x)$  - mass distribution

$$\text{P.E.} = \frac{E}{2} \int_0^L I(x) \left( \frac{d^2 y}{dx^2} \right)^2 dx \quad (3.2.28)$$

Where  $I(x)$  - moment of inertia distribution

The assumed mode shape is taken as

$$y = y_0 \left( 1 - \cos \frac{\pi x}{2L} \right) \quad (3.2.29)$$

$$y^2 = y_0^2 \left( 1 - \cos \frac{\pi x}{2L} + \cos^2 \frac{\pi x}{2L} \right) \quad (3.2.30)$$

$$\frac{dy}{dx} = y_0 \frac{\pi}{2L} \sin \frac{\pi x}{2L} \quad (3.2.31)$$

$$\frac{d^2 y}{dx^2} = y_0 \frac{\pi^2}{4L^2} \cos \frac{\pi x}{2L} \quad (3.2.32)$$

$$\left( \frac{d^2 y}{dx^2} \right)^2 = y_0^2 \frac{\pi^4}{16L^4} \cos^2 \frac{\pi x}{2L} \quad (3.2.33)$$

Substituting into equations 3.2.27 and 3.2.28

$$\omega_n = \sqrt{\frac{\int_0^L EI(x) \frac{\pi^4}{16L^4} \cos^2 \frac{\pi x}{2L} dx}{\int_0^L m(x) \left( 1 - 2 \cos \frac{\pi x}{2L} + \cos^2 \frac{\pi x}{2L} \right) dx}} \quad (3.2.34)$$

The solution of eq. 3.2.34 was programed using the variable mass and moment of inertia distribution shown in Fig. 3.2.4, with the result:

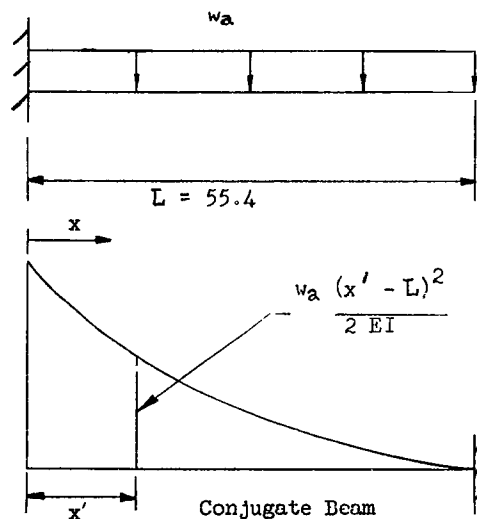
$$\begin{aligned} \omega_n &= 275 \text{ rad/sec.} \\ f_n &= \frac{\omega}{2\pi} = 43.8 \text{ cps.} \end{aligned}$$

The second method of computing the natural frequency of the single degree of freedom system involves transforming the mass and stiffness properties of the idealized cantilevered beam into those of an equivalent single degree of freedom system. The transformation is made by equating the kinetic energy and external work of the idealized



cantilevered beam to that of the equivalent system. The deflected shape of the airload model is assumed to be that resulting from a uniformly distributed dynamic load. It is assumed that the deflected shape is the same as that which would be caused by the load applied statically. This shape is assumed to be constant with time so that the ratio of any two ordinates of deflection along the beam is always constant. This procedure is not quite the same as considering only the first mode of vibration since the slope of the first mode is not the same as the static-deflection curve. It is believed that the transformation method which is outlined on pg. 149 of Ref. 16 makes an approximation of the contribution of the higher modes and as a consequence is somewhat more accurate.

Idealized Representation of (6L) Model



Load Transformation Factor

$$K_L = \frac{\text{Load applied to equivalent system}}{\text{Load applied to actual system}}$$

Work done by actual system

$$W_a = \frac{wa}{2} \int_0^L \Delta_x dx \quad (3.2.35)$$

Where

$$\Delta_x = \frac{wa}{2E} \int_0^x \frac{(x' - L)^2}{I_{x'}} (x - x') dx' \quad (3.2.36)$$

$$\Delta_{(x=L)} = \frac{wa}{2E} \times 1244.6 \times 10^2 \quad (3.2.37)$$

Equation 3.2.37 was evaluated on the computer using the moment of inertia distribution shown in Fig. 3.2.4

$$w_a = \frac{\Delta_{x=L} 2E}{1244.6 \times 10^2} \quad (3.2.38)$$

Substituting equation 3.2.38 into 3.2.36

$$\Delta_x = \frac{\Delta_{x=L}}{1244.6 \times 10^2} \int_0^x \frac{(x' - L)^2 (x - x')}{I_{x'}} dx' \quad (3.2.39)$$

Substituting equation 3.2.39 into 3.2.35 and evaluating the integral on the computer

$$W_a = 9.7 w_a \Delta_{x=L}$$

Work done by equivalent system

$$W_e = \frac{55.4 \times w_e \times \Delta_e}{2} = 27.7 \times w_e \times \Delta_e \quad (3.2.40)$$

But

$$W_e = W_a$$

And

$$\Delta_e = \Delta_{x=L}$$

$$\therefore K_L = \frac{w_e}{w_a} = \frac{9.7}{27.7} = 0.350 \quad (3.2.41)$$

Mass Transformation Factor

$$K_m = \frac{\text{Mass of equivalent system}}{\text{Mass of actual system}}$$

Kinetic Energy of Actual System

$$KE_a = 1/2 \int_0^L m(x) v^2(x) dx \quad (3.2.42)$$

$$v(x) = K \Delta(x) \quad (3.2.43)$$

$$v_{x=L} = K \Delta_{x=L} \quad (3.2.44)$$

$$K = \frac{v_{x=L}}{\Delta_{x=L}} \quad (3.2.45)$$

Substituting equation 3.2.43 into 3.2.42

$$KE_a = \frac{v_{x=L}^2}{2 \Delta_{x=L}^2} \int_0^L m(x) \Delta^2(x) dx \quad (3.2.46)$$

Evaluating the integral on the computer

$$KE_a = .0507 v_{x=L}^2 m_a \quad (3.2.47)$$

Kinetic Energy of Equivalent System

$$KE_e = 1/2 v_e^2 \int_0^L m(x) dx \quad (3.2.48)$$

$$KE_e = .493 v_e^2 m_e$$

$$K_m = \frac{m_e}{m_a} = \frac{.0507}{.493} = 0.103 \quad (3.2.49)$$

Natural Period

$$T_n = 2\pi \sqrt{\frac{m_e}{K_e}} \quad (3.2.50)$$

Mass of Equivalent System

$$M_e = M_a \times K_m = .987 \times .103$$

$$M_e = .1016 \text{ Slugs}$$

Stiffness of Equivalent System

$$K_e = K_a K_L = \frac{110.8 \times 29 \times 10^6 \times .350}{1244.6 \times 10^2}$$

$$K_e = 9040 \text{ lb/in}$$

$$T_n = 2\pi \sqrt{\frac{.1016}{9040}} = 0.02105 \text{ sec.}$$

$$f_n = 47.5 \text{ cps}$$

$$\omega_n = 298 \text{ rad/sec}$$

#### 3.2.3.2 DYNAMIC OVERSTRESS FACTOR

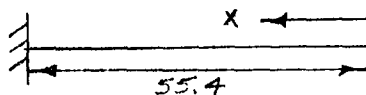
The most critical dynamic overstress factor will be determined from Fig. 3.2.2 using the blast duration from mission No. 3 and the higher of the two natural frequencies computed for the airload specimen.

$$\omega_{D_p} = 298 \times .0440 = 13.15 \text{ rad}$$

$$D.O.F. = 1.49$$

### 3.2.3.3. BENDING STRENGTH OF AIRLOAD SPECIMEN

The total lift as presented in Figure 3.2.1 is assumed to be uniformly distributed over the surface of the wing.



APPLIED BENDING MOMENT

$$M_x = \frac{L(o)}{A} \text{ D.O.F. } \int_0^x b_{x'} (x - x') dx' \quad (3.2.51)$$

where

$$L(o) = 32700 \text{ lb.} \quad \text{Fig. 3.2.1}$$

$$A = 798 \text{ in}^2 \quad (\text{area of wing})$$

$$\text{D.O.F.} = 1.49$$

$$b_{x'} = 10.086 + \frac{8.685}{55.4} x' \quad (\text{width perpendicular to 50\% chordline})$$

$$M_x = 61.1 (5.05x^2 + .0262x^3)$$

The critical loading condition occurs at the root as indicated in Figure 3.2.5.

$$M_{\max} = 1,200,000 \text{ in-lb applied}$$

$$f_b = \frac{Mc}{I}$$

$$\text{where } c = \frac{15.17 \times 22.33}{2} = 1.694 \text{ in.}$$

$$I = 28.8 \text{ in}^4 \quad \text{Fig. 3.2.4}$$

$$f_b = \frac{1,200,000(1.694)}{28.8} = 70,600 \text{ psi}$$

Allowable bending stress

$$F_{tu} = 160,000 \text{ psi Ult}$$

$$F_{ty} = 140,000 \text{ psi Yield}$$

$$\text{M.S.} = \frac{140000}{70600} - 1.0 = +.98$$

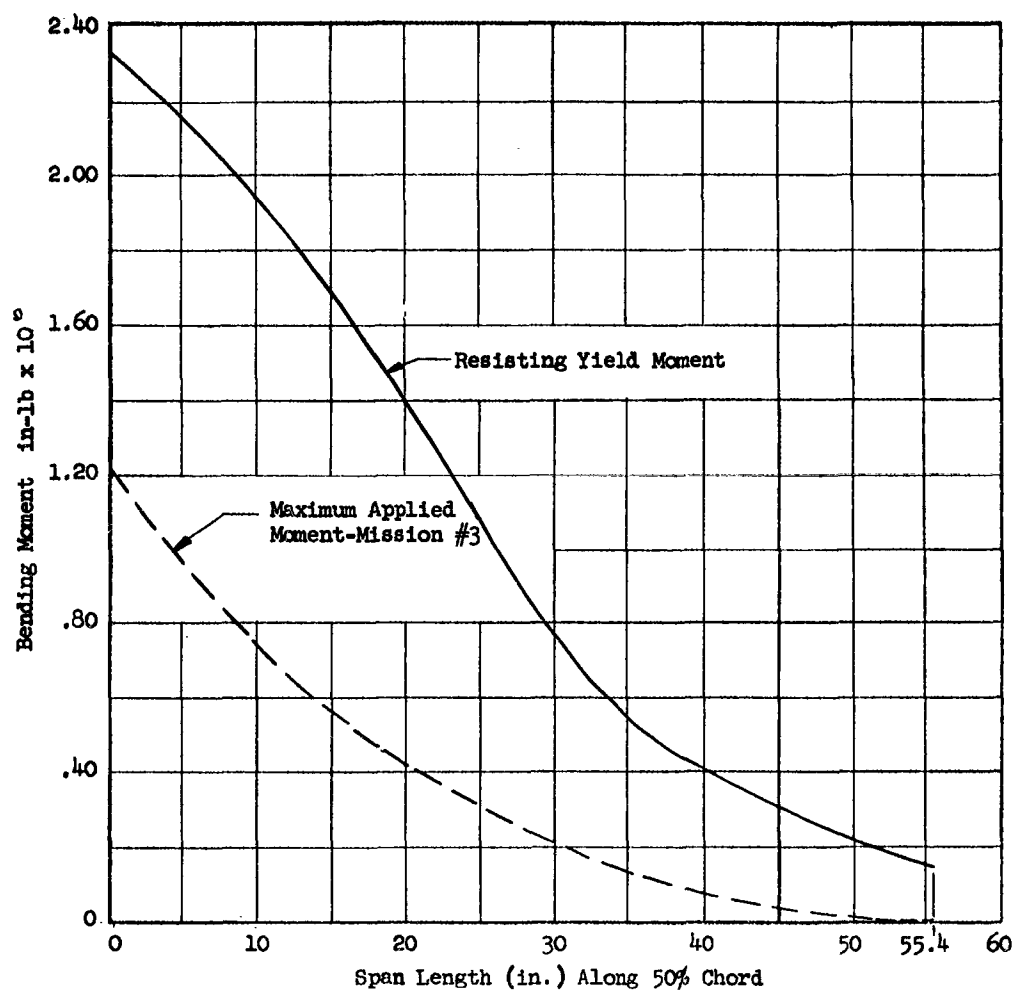
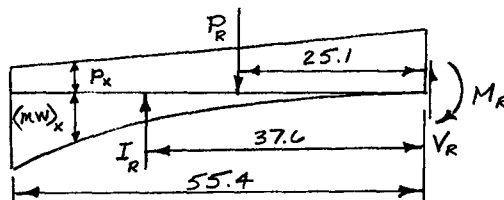


Fig. 3.2.5 THE MAXIMUM APPLIED BENDING MOMENT AND THE RESISTING YIELD MOMENT FOR THE AIRLOAD SPECIMEN

### 3.2.3.4 SHEAR CONNECTORS

The dynamic reaction of the equivalent system at any time is simply equal to the spring force. However, this is not representative of the dynamic reaction on the actual beam. In order to determine the latter, the distribution of the actual inertia forces along the beam must be considered. It is assumed that the inertia forces are at all points proportional to the ordinates of the deflected shape and the running mass. This is justified, because, if each point is in simple harmonic motion, the maximum acceleration is proportional to the maximum deflection. As a consequence, the resultant inertia force outboard of the section in question will be located at the centroid of the weighted deflection curve.



Dynamic Freebody Diagram of (6L) Model

Taking moments about the inertia force

$$V_R \times 37.6 - M_R - P_R \times 12.5 = 0$$

$$V_R = \frac{M_R + 12.5 P_R}{37.6} \quad (3.2.52)$$

Assume that the maximum shear occurs when the dynamic bending moment is a maximum. From Fig. 3.2.3, the time at which the peak bending moment is reached may be obtained.

$$\omega t_M = 2.94$$

$$t_M = \frac{2.94}{298} = .00987 \text{ sec}$$

$$\frac{t_m}{t_p} = \frac{.00987}{.0440} = 0.224$$

From Fig. 3.2.1

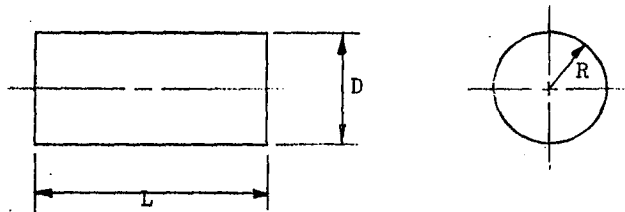
$$p = 17200 \text{ lb}$$

Substituting into equation 3.2.52

$$V = \frac{1220000 + 12.5 \times 17200}{37.6}$$

$$V = 38200 \text{ lb}$$

Capacity of Shear Connector .



The shear pin will be assumed to be placed in equilibrium by the linear stress distribution shown in Fig. 3.2.6. Neglecting friction between the pin and hole and assuming a linear stress distribution will lead to conservative results.

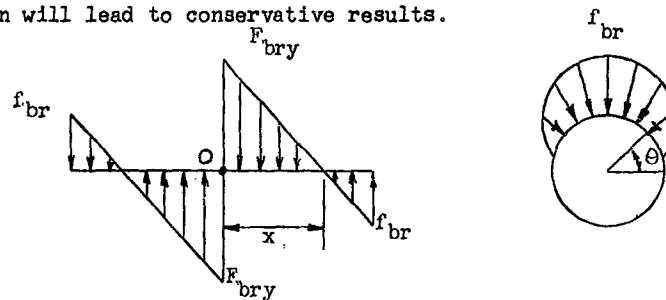


Figure 3.2.6  
Assumed Stress Distribution on Shear Connector



Integrating the stress in Fig. 3.2.6

$$V = 2 \int_0^{\pi/2} f_{br} R \sin^2 \theta d\theta = \frac{\pi}{2} R f_{br} \quad (3.2.53)$$

Summing the moments about point (0)

$$\frac{\pi}{6} R F_{bry} x^2 = \frac{\pi}{4} R f_{br} \left(\frac{L}{2} - x\right) \left(L - L/3 + 2/3 x\right)$$

Solving for  $f_{br}$

$$f_{br} = 2/3 \frac{F_{bry} x^2}{\left(\frac{L^2}{3} - \frac{Lx}{3} - \frac{2}{3} x^2\right)} \quad (3.2.54)$$

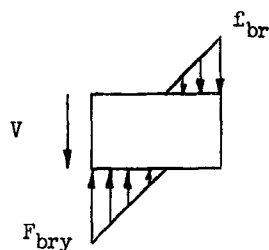


Figure 3.2.7  
Bearing Load Diagram

Summing the vertical forces for the free body shown in

Fig. 3.2.7

$$\frac{\pi}{4} R F_{bry} x - \frac{\pi}{4} R f_{br} \left(\frac{L}{2} - x\right) = f_{s_{AV}} \pi R^2$$

Solving for  $x$

$$x = \frac{R f_{s_{AV}} + \frac{f_{br} L}{8}}{\frac{F_{bry}}{4} + \frac{f_{br}}{4}} \quad (3.2.55)$$

From the Geometry of the stress diagram

$$f_{br} = \frac{(\frac{L}{2} - x)}{x} F_{bry} \quad (3.2.56)$$

Substituting equation 3.2.56 into 3.2.54

$$x = \frac{L}{3} \quad (3.2.57)$$

Substituting  $x$  into equation 3.2.56

$$f_{br} = \frac{F_{bry}}{2} \quad (3.2.58)$$

Substituting equation 3.2.57 and 3.2.58 into 3.2.55

$$L = \frac{16 R f_{sav}}{F_{bry}} = \frac{12 R f_{smax}}{F_{bry}} \quad (3.2.59)$$

For a round pin

$$f_{smax} = 1.33 \times f_{sav} \quad (3.2.60)$$

And

$$V = f_{sav} \pi R^2 = 2.36 R^2 f_{smax} \quad (3.2.61)$$

The load capacity for several shear pin diameters as a function of shear pin length is summarized in Fig. 3.2.8. The bending stresses on the shear pins have been neglected. The critical shear load condition occurs at the root where the minimum margin of safety on yield is

$$M.S. = \frac{20250}{18900} - 1.0 = +.072 \quad (\text{See Fig. 3.2.9})$$

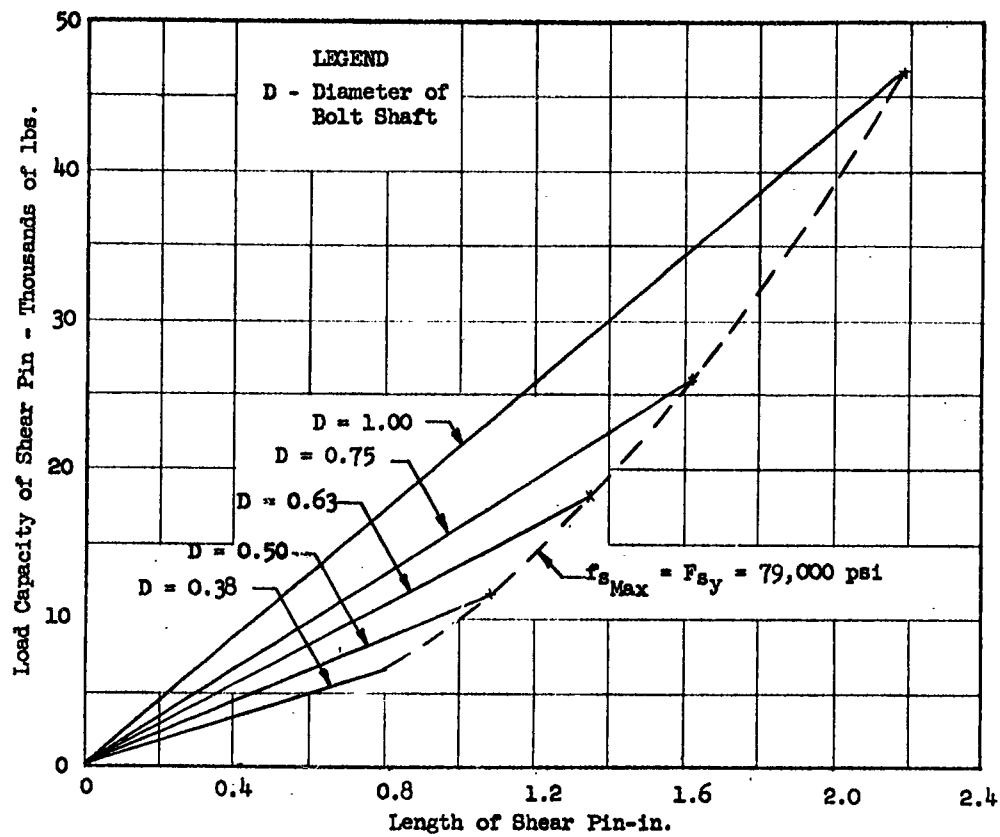


Fig. 3.2.8 LOAD CAPACITY OF SHEAR CONNECTORS FOR AIRLOAD SPECIMEN

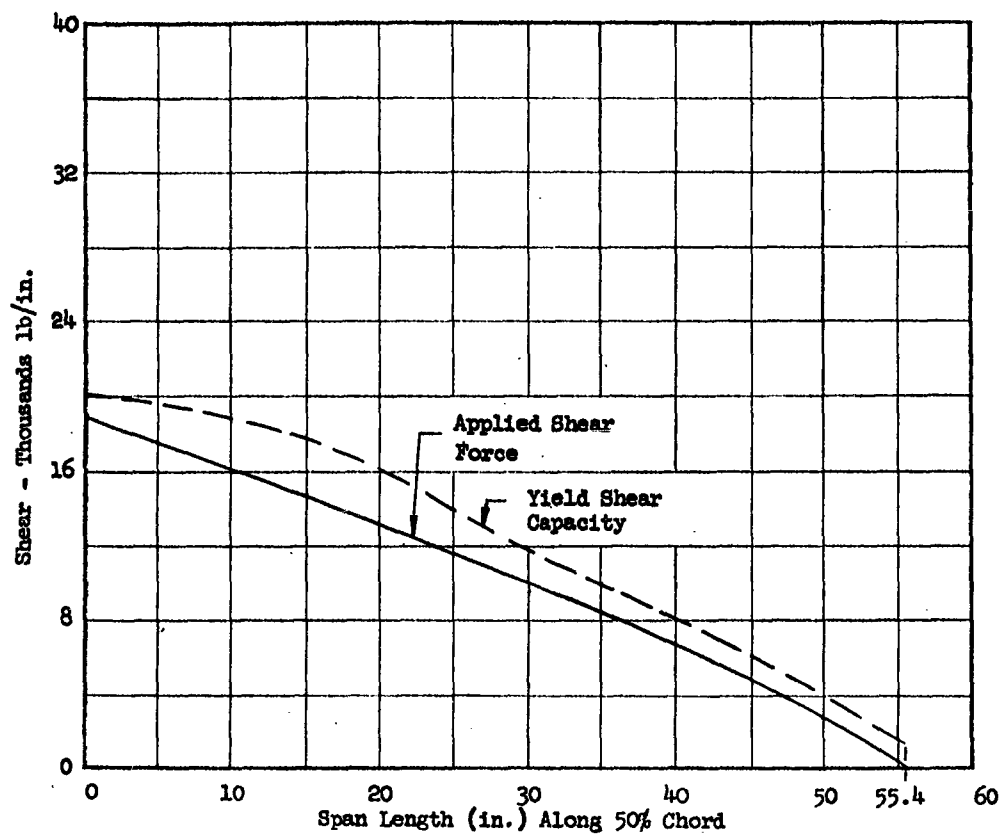


Fig. 3.2.9 THE MAXIMUM APPLIED SHEAR FORCE AND THE YIELD SHEAR CAPACITY ALONG THE SPLIT PLANE OF THE AIRLOAD SPECIMEN

### 3.2.4 STRUCTURAL SPECIMEN

#### 3.2.4.1 FIRST PRELIMINARY TRIAL

The original preliminary design of the structural specimen was based on the detailed requirements set forth in the addendum to Purchase Request NR. 65507. The principal applicable paragraphs are reproduced as follows:

4.9.3 The specimens shall be designed with sufficient strength to withstand the aerodynamic forces resulting from an induced angle of attack ranging between 15 and 20 degrees before failure of the specimen. At a later date, the ASD Project Engineer will specify the exact angle between 15 and 20 degrees.

4.9.4 The specimens shall be designed to fail at a particular station. This is required in order that the problems involved in random (or unknown) failure locations may be eliminated. Before selecting the designed break station, the basic un-modified structure shall be analyzed in a manner sufficient to predict where a break would logically occur in the un-modified specimen. After the logical break station has been selected by analysis, the structure will then be designed with the modifications necessary that the structural test specimen will always fail during the tests at this station.

During a conference held at AAI on 5 April 1960, it was agreed that the controlled failure be positioned at 25% of the half span length. During a subsequent conference held at AAI on 10 May 1960, an induced angle of attack of 15 degrees was specified for the figure to be used in paragraph 4.9.3 of the specifications. It was also agreed that the break

angle should be slightly swept back. On 14 June 1960, another conference was held during which AAI outlined a design approach which was to use a peak induced angle of attack of 15 degrees along with the blast load time history of Mission No. 4 in Table 3.2.1 to determine the ultimate moment at the break station. The failure line was to be located at the intersection of 25% of the exposed half span length and the 25% chordline and the break line was to be swept back 15 degrees. This design approach was accepted as the method to be used for the design of the specimen.

Accordingly, AAI proceeded to design the structural specimen to reach a condition of incipient failure at an induced angle of attack of 15 degrees. The amount of postfailure rotation which would occur during the two destruction runs described as Missions Nos. 5 and 6 in Table 3.2.1 was not regarded as a design requirement. During the course of this preliminary analysis, the design approach was drastically changed. As a consequence, only a cursory summary of the results of this phase of the design will be presented.

The basic structure selected to meet the original design criteria is shown in Figure 3.2.10. The compression skin in the break area was reduced in thickness to .080 inch, and the spar caps and stringers were milled down to .064 inch. The failure bay was made 9 inches between ribs in order to ensure that buckling of the stringers would occur here rather than in an adjacent bay.

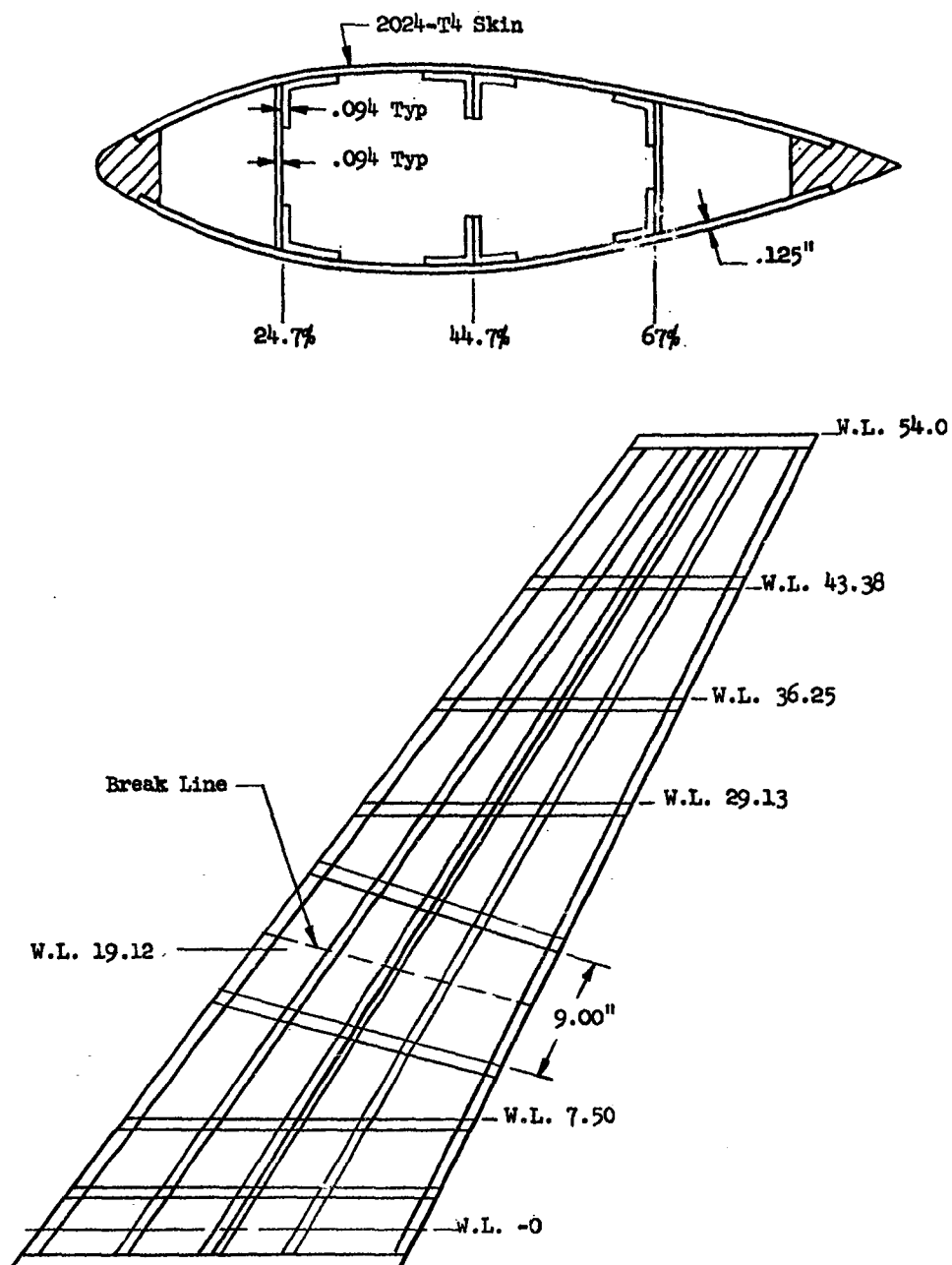


Fig. 3.2.10 STRUCTURAL SPECIMEN- FIRST PRELIMINARY TRIAL

Lift Load for an Induced Angle of Attack of 15 Degrees

Peak Lift

$$L = 1/2 \rho [V]^2 S C_{L\alpha} \text{TAN}^{-1} \left[ \frac{u}{V} \right] \quad (3.2.62)$$

Particle Velocity

$$\text{TAN}^{-1} \frac{u}{V} = 15^\circ$$

$$u = .268 \times 895 = 240 \text{ fps}$$

Peak Overpressure

$$u = \frac{5p}{7p_o} \times \frac{C_o}{(1 + \frac{6p}{7p_o})^{\frac{1}{2}}} \quad (3.2.63)$$

$$240 = \frac{5p}{7 \times 14.7} \times \frac{1120}{(1 + \frac{6}{7 \times 14.7} p)^{\frac{1}{2}}}$$

$$p^2 - 1.133 p - 19.47 = 0$$

$$p = 5.02 \text{ psi}$$

Air Density

$$\rho = \rho_o \left( \frac{7 + 6 \frac{p}{p_o}}{7 + \frac{p}{p_o}} \right) \quad (3.2.64)$$

$$\rho = \frac{.00238 (7 + \frac{6 \times 5.02}{14.7})}{7 + \frac{5.02}{14.7}}$$

$$\rho = .00294 \frac{\text{lb sec}^2}{\text{ft}^4}$$



Peak Dynamic Pressure

$$q = 1/2 \rho u^2 = \frac{.00294 (240)^2}{2} \quad (3.2.65)$$

$$q = 84.5 \text{ psf}$$

$$V^2 = 895^2 + 240^2 = 85.8 \times 10^4 \text{ ft}^2/\text{sec}^2$$

Substituting into equation 3.2.62

$$L = 1/2 .00294 \times 85.8 \times 10^4 \times 5.54 \times 5.2 \times .268$$

$$L = 9720 \text{ lb}$$

In order to determine the dynamic response of the structural specimen to this load the swept wing will be idealized as a cantilevered beam whose elastic axis is located along the 50 % chordline as in the case of the airload model. The moment of inertia and mass distribution of the idealized specimen is given in Figs. 3.2.11 and 3.2.12. The response of the structural specimen will be approximated by a single degree of freedom system. The natural frequency of this system will be determined using the transformation factor method outlined for the airload model in Sec. 3.2.3. The results of this analysis, which was performed on the computer, are summarized below:

Load Factor

$$K_L = 0.381$$

Mass Factor

$$K_m = 0.198$$

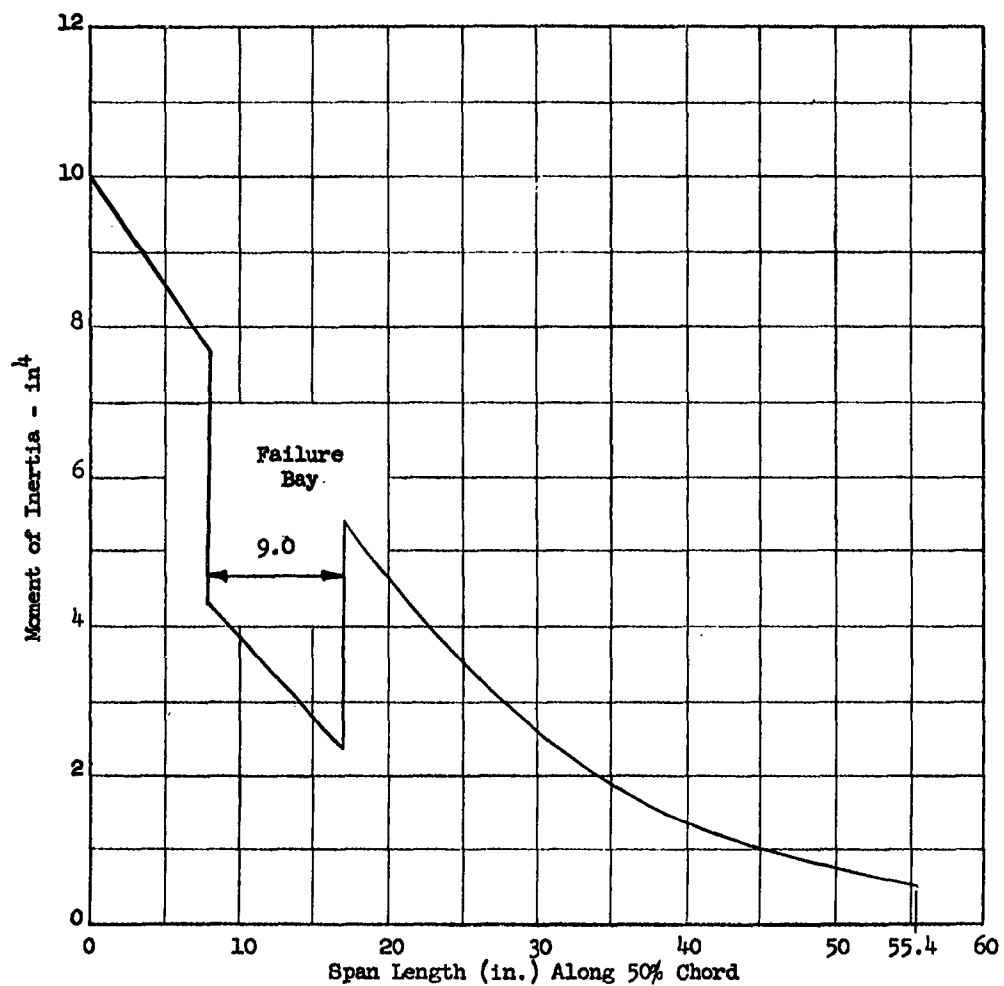


Fig. 3.2.11 MOMENT OF INERTIA OF STRUCTURAL SPECIMEN  
NORMAL TO THE 50% CHORD-FIRST PRELIMINARY TRIAL

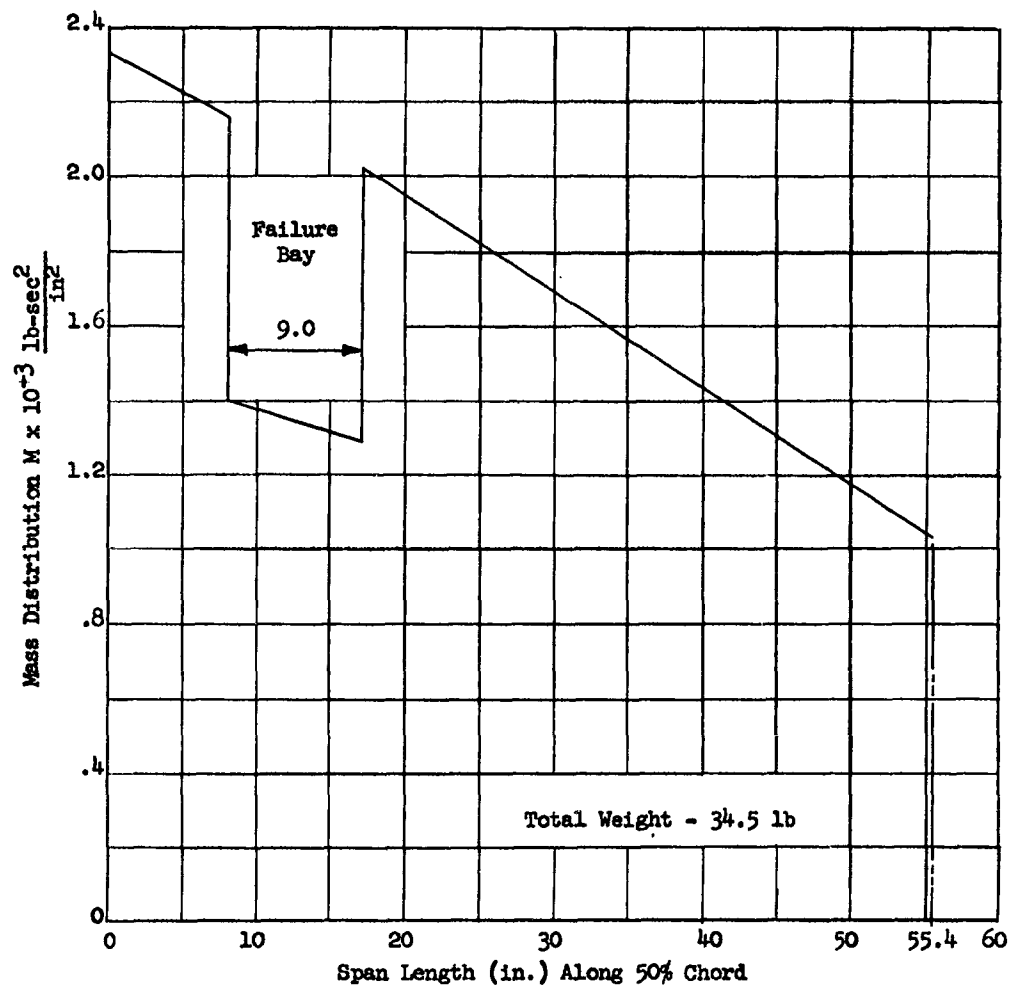


Fig. 3.2.12 SPANWISE MASS DISTRIBUTION OF STRUCTURAL SPECIMEN-FIRST PRELIMINARY TRIAL

Mass of Equivalent System

$$m_e = .0886 \times .198 = .0176 \frac{\text{lb sec}^2}{\text{in}}$$

Spring Constant of Equivalent System

$$K_e = \frac{2 \times 55.4 \times 10^7 \times .381}{393 \times 10^3} = 1075 \text{ lb/in}$$

Natural Period

$$T_n = 2\pi \sqrt{\frac{.0176}{1075}} = .0254$$

Natural Frequency

$$f_n = 39.4 \text{ cps}$$

$$\omega_n = 247 \text{ rad/sec}$$

The dynamic overstress factor can now be determined from Figure 3.2.2 using the effective blast load duration from Mission No. 4.

$$\omega_{D+P} = 247 \times .00832 = 2.06$$

$$\text{D.O.F.} = 0.55$$

Bending Moment Distribution at Failure Load



(See equation 3.2.51)

$$M_x = \frac{L(o)}{A} \text{ D.O.F. } (5.05 x^2 + .0261 x^3)$$

Where:  $L(o) = 9720 \text{ lb.}$  Figure 3.2.1

$A = 798 \text{ in}^2$  (Area of Wing)

$$M_x = \frac{9720}{798} 0.55 (5.05 x^2 + .0261 x^3)$$

The critical bending moment at the break line is given as

$$M_{(42.9)} = 76200 \text{ in-lb}$$

The critical bending capacity at the break line is given as

$$M_u = \frac{F_{cy} I}{c}$$

Where

$$F_{cy} = 40000 \text{ psi} \quad 2024 - T4$$

$$I = 3.30 \times 10^4 \text{ (See Fig. 3.2.11)}$$

$$c = 1.73 \text{ IN}$$

$$M_u = \frac{40000 \times 3.30}{1.73} = 76200 \text{ in-lb}$$

The minimum margin of safety outside of the failure bay occurs at the root, as seen from Figure 3.2.13.

$$M.S. = \frac{230000}{143000} - 1.0 = +.61$$

The postfailure factor which is defined as the ratio of the peak value of the applied load to the maximum value of the applied static load required to initiate failure at the break line may be computed for the two destruction Missions Nos. 5 and 6.

$$P.F.F. = \frac{32700}{.55 \times 9720} = 6.12$$

The effect of the blast load during Mission No. 6 on the postfailure hinge rotation is, of course, more severe than during Mission No. 5 due to its longer duration.

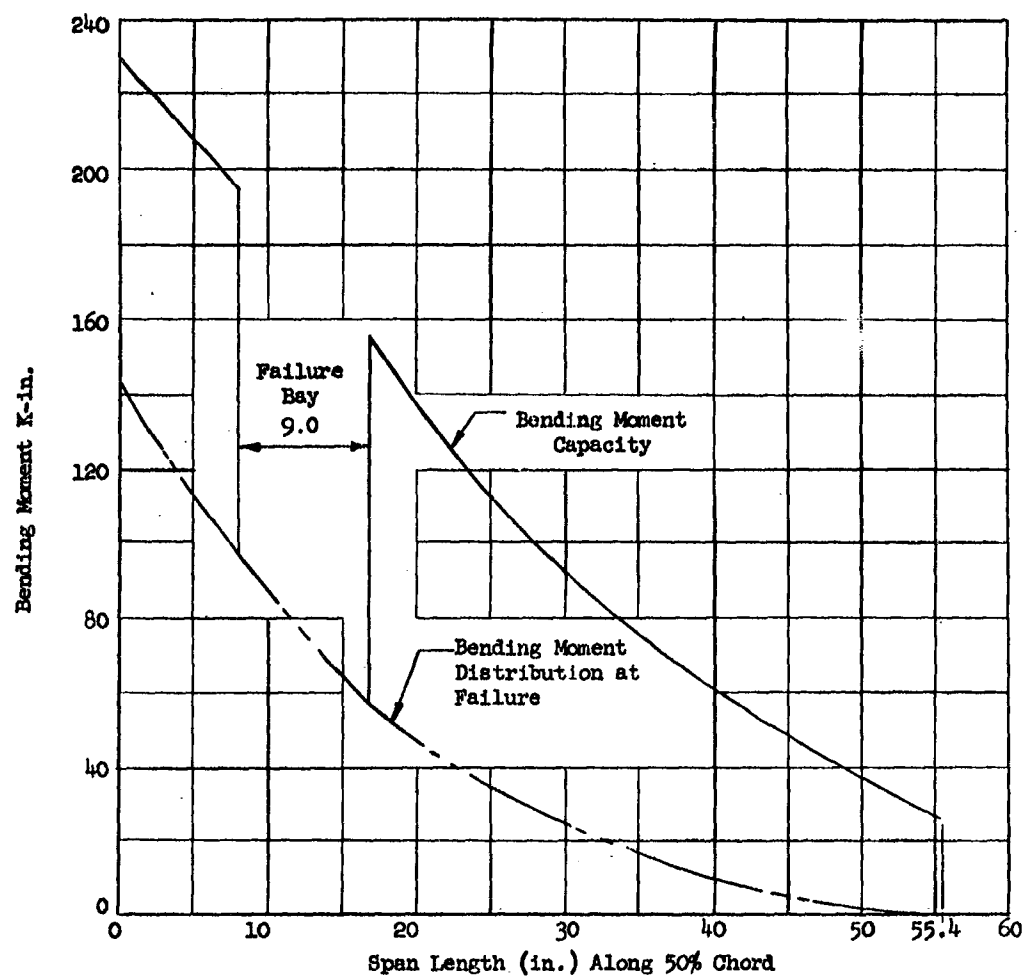


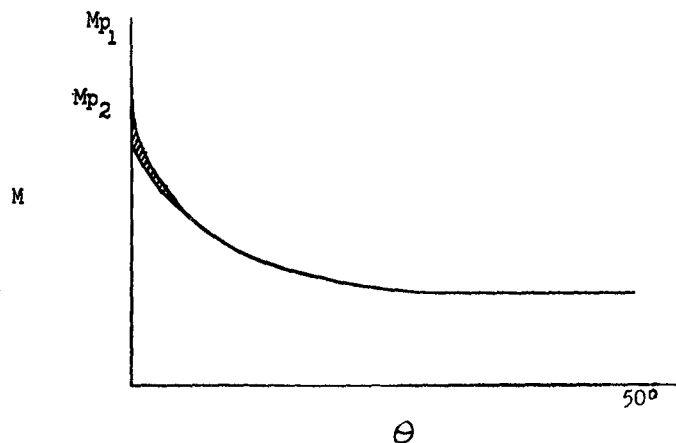
Fig. 3.2.13 BENDING MOMENT CAPACITY AND DISTRIBUTION AT FAILURE LOAD FOR STRUCTURAL SPECIMEN-FIRST PRELIMINARY TRIAL

#### 3.2.4.2 SECOND PRELIMINARY TRIAL

In August 1960, upon the recommendation of MIT and Avidyne, it was decided to revise the approach to the design of the structural specimens. The failure line was to be located at the intersection of 25% of the exposed half span length and the 25% chordline as previously indicated. However, it was recommended that it be swept back approximately 30 degrees or normal to the structural axis which was taken as the 50% chordline. In addition, the peak postfailure hinge angle which would occur during Mission No. 6 of Table 3.2.1 was to be approximately 50 degrees. The peak postfailure rotation angle which would occur during Mission No. 5 was to be approximately 5 - 10 degrees. MIT advised that the leading and trailing edge members be omitted in the failure bay and the two stringers previously used in the original preliminary design be joined by a web. These latter changes were deemed necessary in order to make the failure bay more amenable to a theoretical postfailure moment rotation analysis.

Using this revised approach, the procedure was to first estimate the ultimate failure moment at the break line required to give a peak postfailure rotation angle of 50 degrees for Mission No. 6. The postfailure moment rotation curve could then be computed theoretically using the methods outlined in Ref. 4. The postfailure dynamic response computation would then be programmed by Avidyne and the necessary structural and aerodynamic parameters supplied by AAI and MIT respectively. The peak postfailure hinge angles for Missions Nos. 5 and 6 would be checked, and if they were not satisfactorily close to the desired values, the structure would be adjusted accordingly and the process repeated.

In order to proceed with the revised design approach, it was necessary to first make a preliminary estimate of the required ultimate bending capacity at the break line. Based on the advice of Dr. Hobbs of Avidyne and Mr. D'Amato of MIT, who have had a great deal of experience in the areas of postfailure characteristics and response of built-up sections, a preliminary estimate of 3.5 for the postfailure factor for Mission No. 6 was selected. In addition, the asymptotic value of the postfailure bending moment was to be approximately 20 % of the ultimate bending moment capacity. Actually, the peak postfailure hinge angle is far more sensitive to the asymptotic value of the postfailure bending moment than to the ultimate bending moment. This fact is quite evident if a typical postfailure moment rotation curve is considered.



TYPICAL POSTFAILURE MOMENT ROTATION CURVE

For a given amount of energy associated with a finite blast-induced airloading, the amount of postfailure rotation required to absorb this energy is primarily a function of the area under the M-Θ



curve. For very large failure angles on the order of 40 to 50 degrees, it is obvious that only a very small percentage of this area is changed for a sizable reduction in the peak bending strength. This conclusion is based on the assumption that the asymptotic value of the bending moment is not significantly altered by the reduction in peak strength. It is obvious that a much greater effect on the peak postfailure hinge angle can be realized by altering the asymptotic value of the bending moment. As a consequence, it is logical to employ this factor as the design variable in the process of converging on an acceptable solution.

Based on these preliminary design requirements, the structural configuration gradually converged on the final configuration described in Sec. 3.1 with only minor exceptions. While the heavy strongback shown in Fig. 3.1.6, located on the tension side of the break line section, does not seem to reflect good design for a built-up wing specimen, it should be pointed out that it is far more economical to achieve sufficient strength by raising the asymptotic value of the postfailure bending strength than by increasing the peak bending moment capacity. When the peak value of bending strength is increased at the break line, the strength of the entire specimen must be increased proportionately in order to maintain an adequate margin of safety on a controlled failure.

#### 3.2.4.2.1 PRELIMINARY FAILURE BAY ANALYSIS

The ultimate bending strength of the break line will be considered first since the rest of the structure will simply be proportioned to provide an adequate margin of safety on a controlled failure. While the peak bending moment capacity and postfailure moment rotation characteristics were to be predicted analytically, it was deemed necessary by MIT and Avidyne that the results be substantiated experimentally. This was to involve a laboratory test of the failure bay and

a representative portion of the structure on either side. If good agreement were obtained between the theoretical and experimental results, then further revisions in the failure bay structure could be predicted theoretically. If the agreement were not good, then additional models would have to be made and tested as the failure bay characteristics converged on acceptable values.

Required Peak Bending Strength for P.F.F. = 3.5  
(see equation 3.2.51)

$$M_x = \frac{32700}{798} \times \frac{1}{3.5} (5.05x^2 + .0262x^3)$$

@ Breakline Z = 44.4

$$M_p = 143500 \text{ in-lb}$$

Required Asymptotic Value of Postfailure Bending Strength

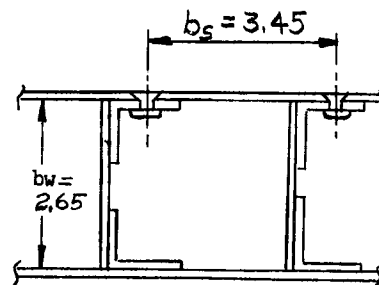
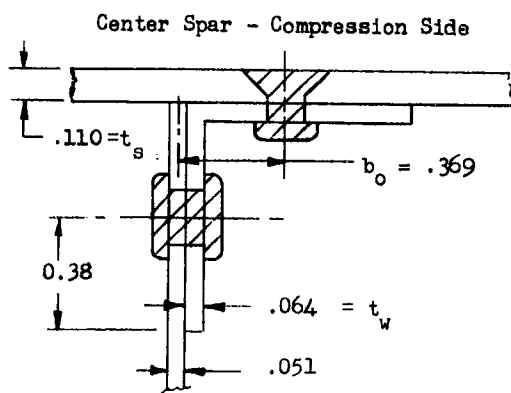
$$M_a = .20 \times 143500 = 28800 \text{ in-lb}$$

A section through the break line is shown in Fig. 3.1.6.

$$I = 4.49 \text{ in}^4 \text{ (without leading and trailing edge covers)}$$

$$\bar{y} = \frac{.8237}{3.584} = +.23$$

The maximum resisting moment for this section will be computed utilizing the stability analysis presented in Ref. 13. From Fig. 3 of Ref. 15, it appears that the structure will fail in the local mode. However, the section is on the borderline between a local and wrinkling type failure. As a consequence, both modes of failure will be investigated to determine an upper and lower limit on the maximum strength.



$$\beta = \frac{b_w/t_w}{b_s/t_s} = \frac{2.65/.064}{3.45/.110} = 1.32$$

$$P/d = \frac{0.875}{0.188} = 4.65$$

$$b_o/t_w = \frac{0.369}{.064} = 5.77$$

From Fig. 8 Reference 13

$$f/t_w = 5.50$$

$$f = 0.352$$

$$f/b_w = \frac{0.352}{2.65} = 0.133$$

$$\frac{f t_s}{t_w b_s} = \frac{.352 \times .110}{.064 \times 3.45} = 0.176 < 0.180$$

Where:

$f$  = is distance from centerline.  
of web to point at which  
skin and spar cap are  
effectively clamped.

# Peak Strength for Wrinkling Mode of Failure

From equation 7 of Ref. 13

$$K_m = \left[ \frac{\frac{48}{\pi^4} \left( 3 \frac{f}{b_w} + 1 \right)}{\left( \frac{f}{b_w} \beta \right)^3 \left( 3 \frac{f}{b_w} + 4 \right)} \right]^{\frac{1}{2}} \quad (3.2.66)$$

$$K_m = \left[ \frac{\frac{48}{\pi^4} \left( 3 \times .133 + 1 \right)}{\left( .133 \times 1.32 \right)^3 \left( 3 \times .133 + 4 \right)} \right]^{\frac{1}{2}}$$

$$K_m = 5.37$$

From equation 3 of Ref. 13

$$\frac{\sigma_m}{\eta} = \frac{K_m \pi^2 E}{12 (1-\nu^2)} \left( \frac{t_s}{b_s} \right)^2 \quad (3.2.67)$$

$$\frac{\sigma_m}{\eta} = \frac{5.37 \times 9.86 \times 10.6 \times 10^6}{12 \times .91} \left( \frac{.110}{3.45} \right)^2$$

$$\frac{\sigma_m}{\eta} = 52,400 \text{ psi}$$

From Fig. 9 Ref. 10

$$\frac{\sigma_m}{\eta \sigma_{0.7}} = \frac{52400}{77200} = 0.678$$

$$\sigma_m = .662 \times 77200 = 51100 \text{ psi}$$

$$M = \frac{I \sigma_m}{c} = \frac{51100 \times 4.50}{1.712}$$

$$M = 134,200 \text{ in-lb}$$

This value represents a lower limit on the maximum resisting moment, since the wrinkling mode of failure always occurs at a lower stress than the local mode.

#### Peak Strength for Local Mode of Failure

The maximum resisting moment in the local mode of failure will be computed in the following manner. A value for the ultimate compressive strain will be assumed and a guess will be made as to the location of the neutral axis. This establishes a first approximation for the strain throughout the section. Knowing the strain the stress can be determined for every element in the section based on the stress strain properties of the material. The effective width of compression elements can be determined from Figs. 3.2.14 and 3.2.15. The sum of the axial forces acting on a section should equal zero. If they do not, the neutral axis will be relocated accordingly and the process repeated. Having determined the neutral axis by a trial process, the moment capacity for that particular ultimate strain can be determined by summing the moments of all axial forces about the neutral axis. The process would be repeated for several values of maximum compressive strain in order to define the moment rotation curve in the region between elastic yield and incipient failure. The point of incipient failure would be assumed to occur when the spars have reached their critical buckling stress, and are no longer able to support the compression skin.

#### Effective Width of Compression Elements

$$\sigma = \eta \frac{K \pi^2}{12 (1 - \nu^2)} E \left( \frac{t}{w_e} \right)^2 \quad (3.2.68)$$

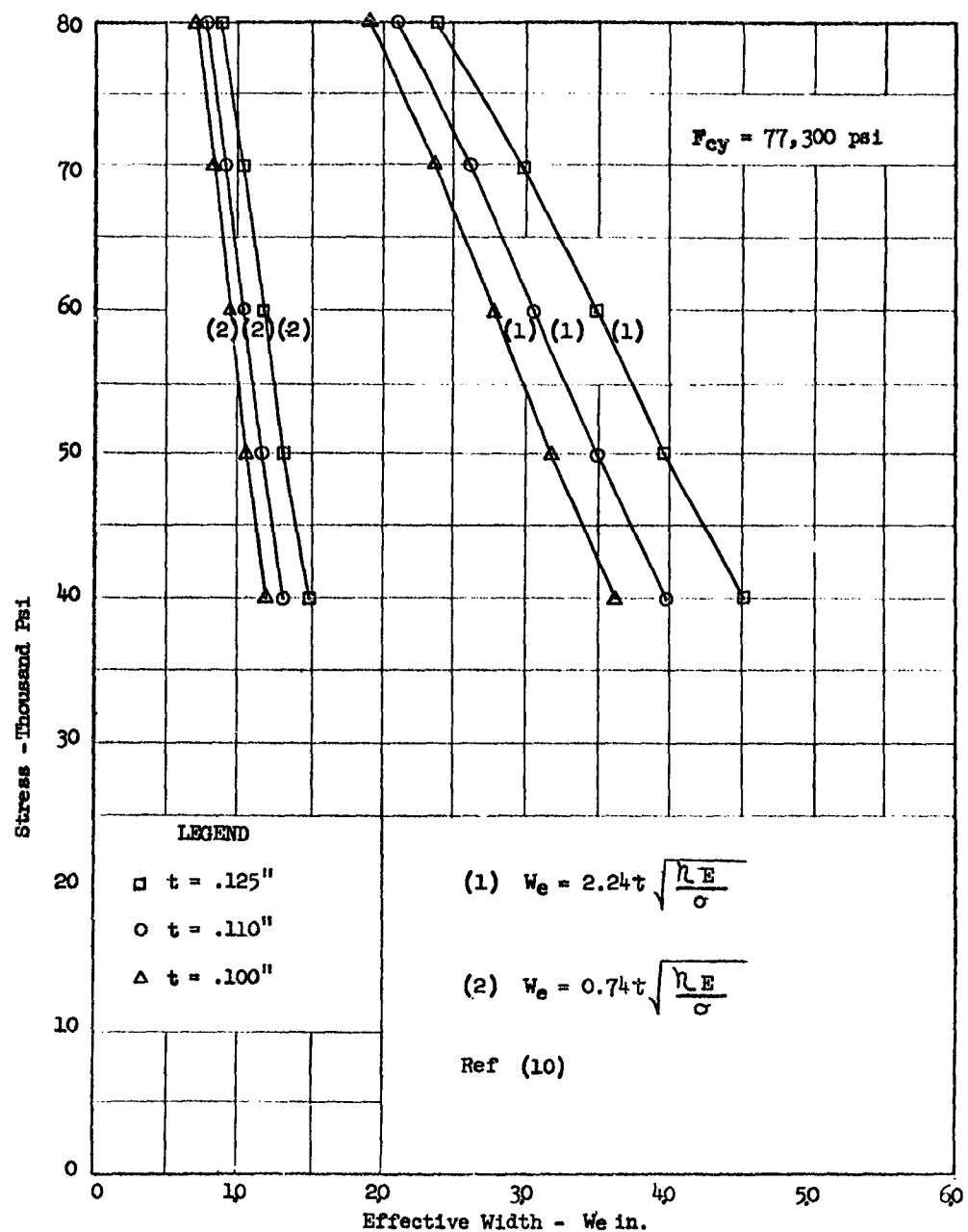


Fig. 3.2.14 EFFECTIVE WIDTH OF COMPRESSION SKIN 7075-T6

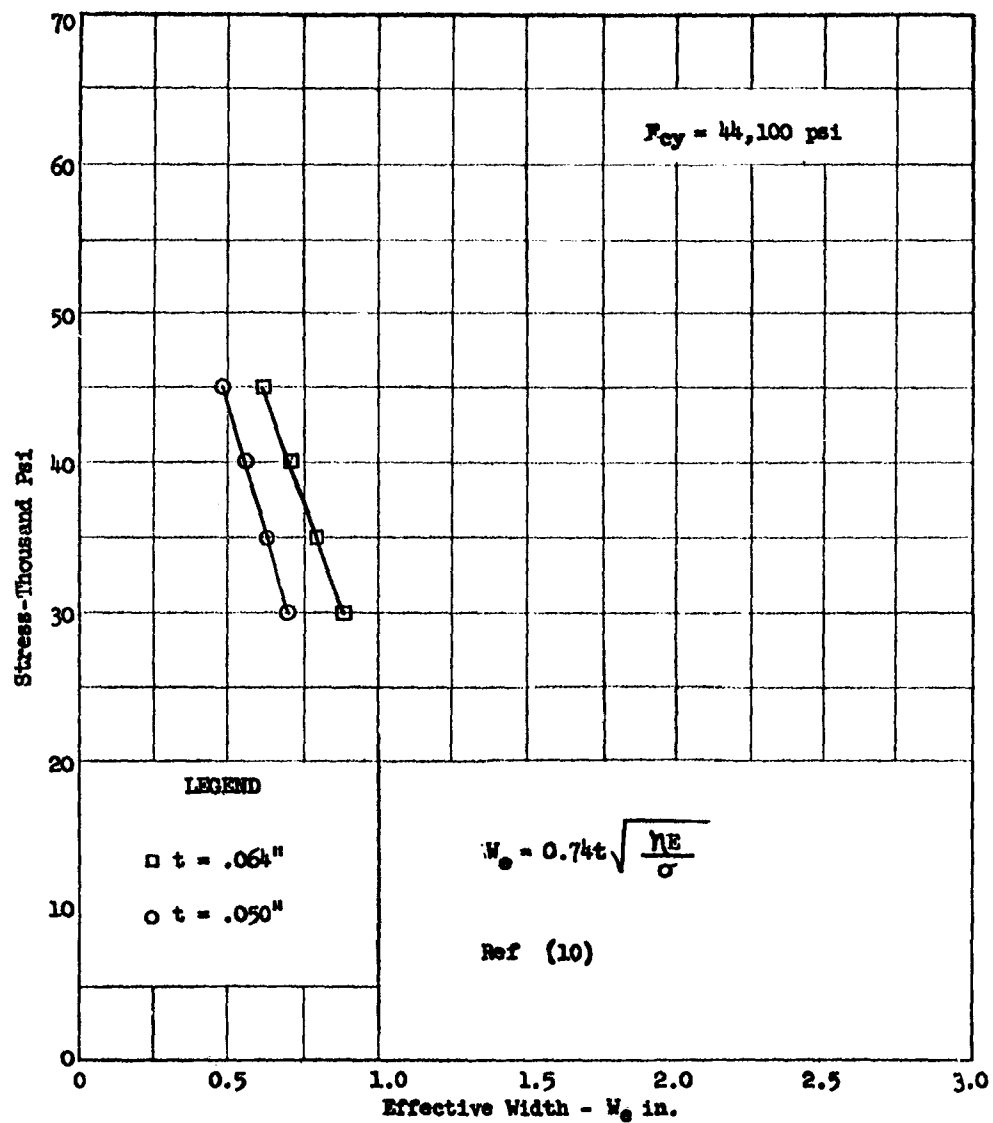


Fig. 3.2.15 EFFECTIVE WIDTH OF COMPRESSION FLANGE 2024-T3

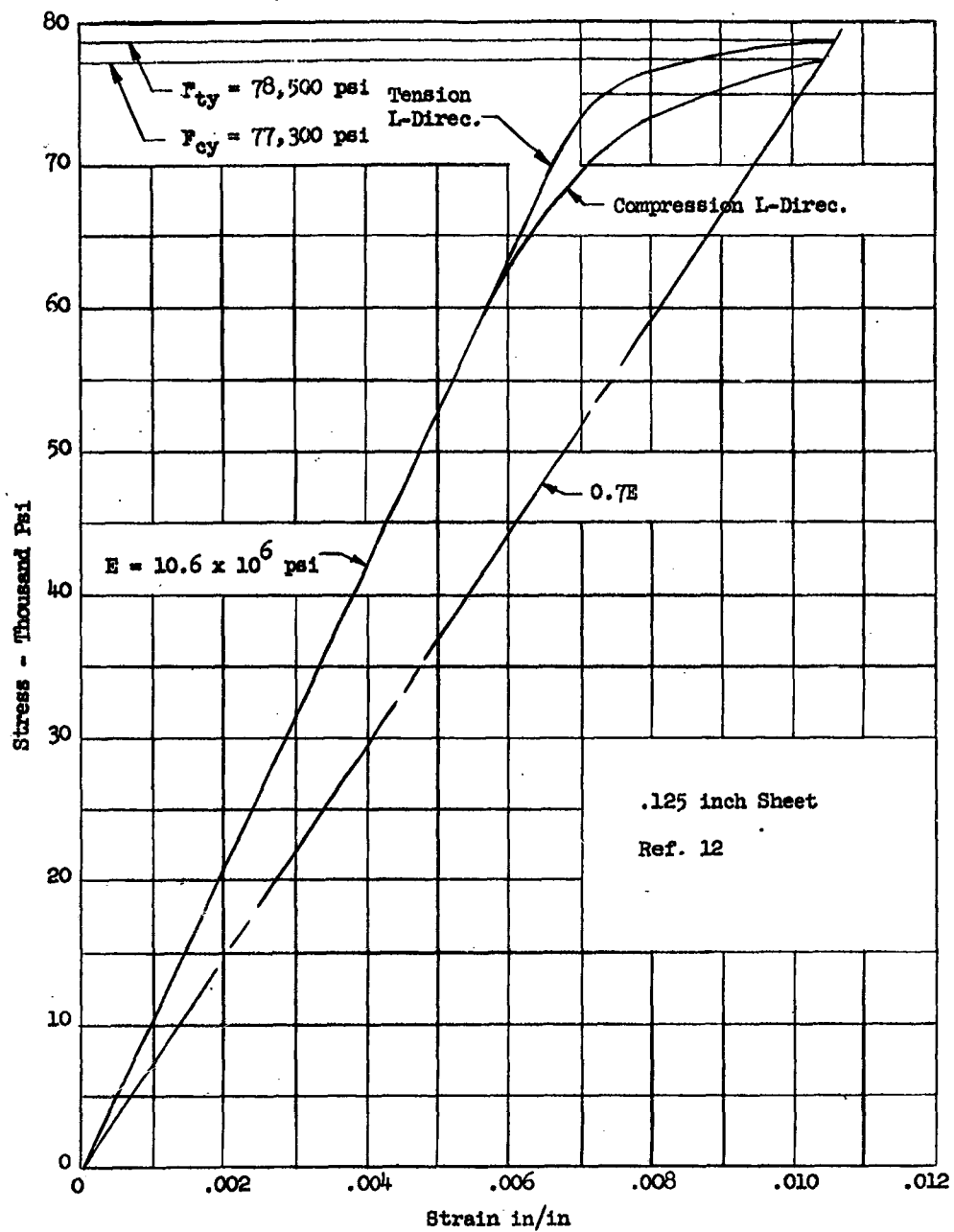


Fig. 3.2.16

STRESS STRAIN CURVE 7075-T6



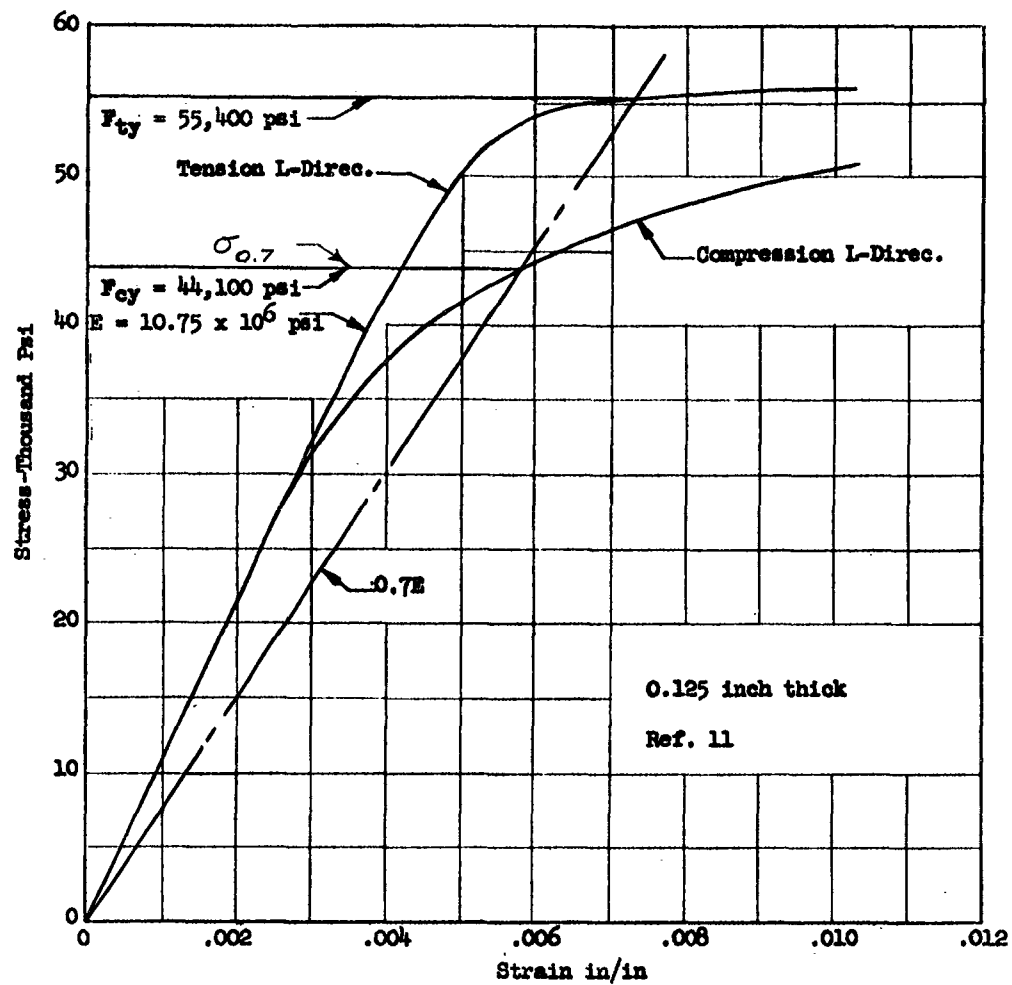


Fig. 3.2.17

STRESS STRAIN CURVE 2024-T3.

Where  $\sigma$  - compressive stress in element

$\eta$  - plasticity reduction factor

K - edge restraint factor

E - modulus of elasticity

t - thickness of element

$w_e$  - effective width of element

$\nu$  - poisson's ratio

Solving equation 3.2.68 in terms of the effective width

$$w_e = .95 t \sqrt{\frac{K E \eta}{\sigma}} \quad (3.2.69)$$

Effective width of compression skin

Assume compression skin is clamped at the rib lines,  
simply supported at the webs, and free along leading and trailing edge  
connection.

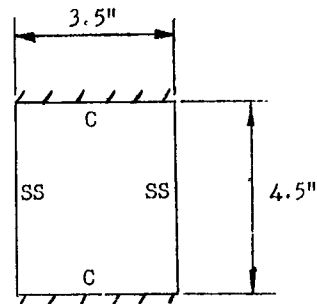
Panel (1)

$$a/b = \frac{4.5}{3.5} = 1.3$$

See Figure 14, Ref. 10

$$K_c = 5.5$$

$$w_e = 2.24 t \sqrt{\frac{\eta E}{\sigma}}$$



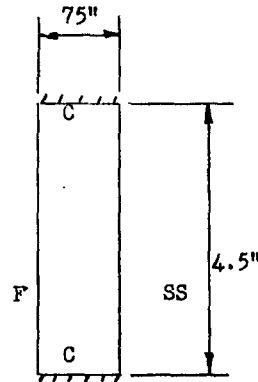
Where  $\eta$  is plasticity reduction factor, see Fig. 9, Reference 10.

Panel (2)

$$a/b = \frac{4.5}{.75} = 6.0$$

$$K_c = 0.6$$

$$w_e = 0.74 t \sqrt{\frac{\eta E}{\sigma}}$$

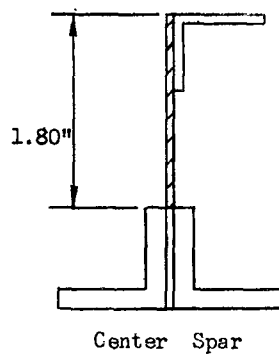


The maximum resisting bending moment at incipient failure in the local mode has been calculated in Table 3.2.4. utilizing Figs. 3.2.14 through 3.2.18.

$$M = 152800 \text{ in-lb}$$

This value represents an upper limit on the maximum resisting moment.

It will now be shown that for a maximum compressive strain of .0063 in/in a portion of the web taken from the center spar has reached its critical buckling stress. Assume shaded portion of web is simply supported at both ends.



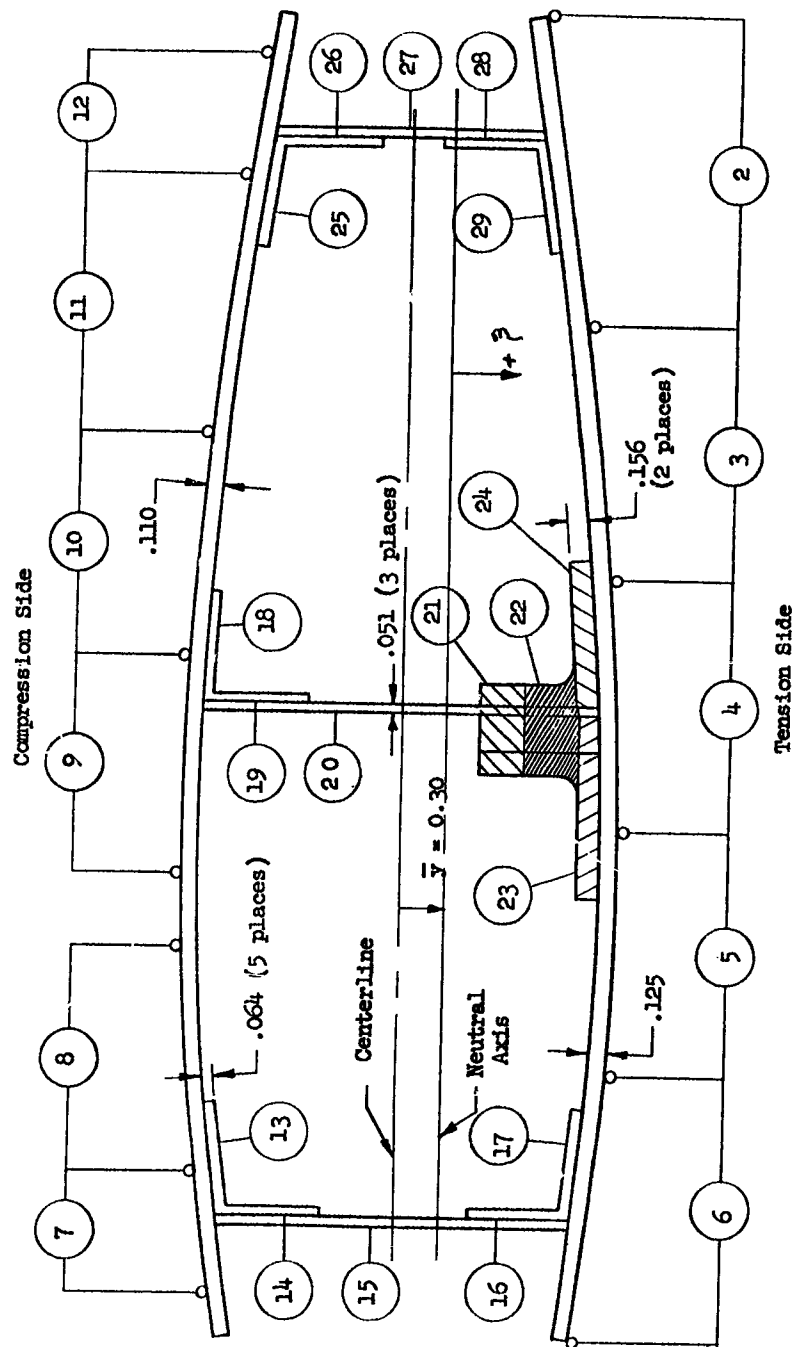


Fig. 3.2.18

EFFECTIVE BREAKLINE SECTION AT PEAK LOAD

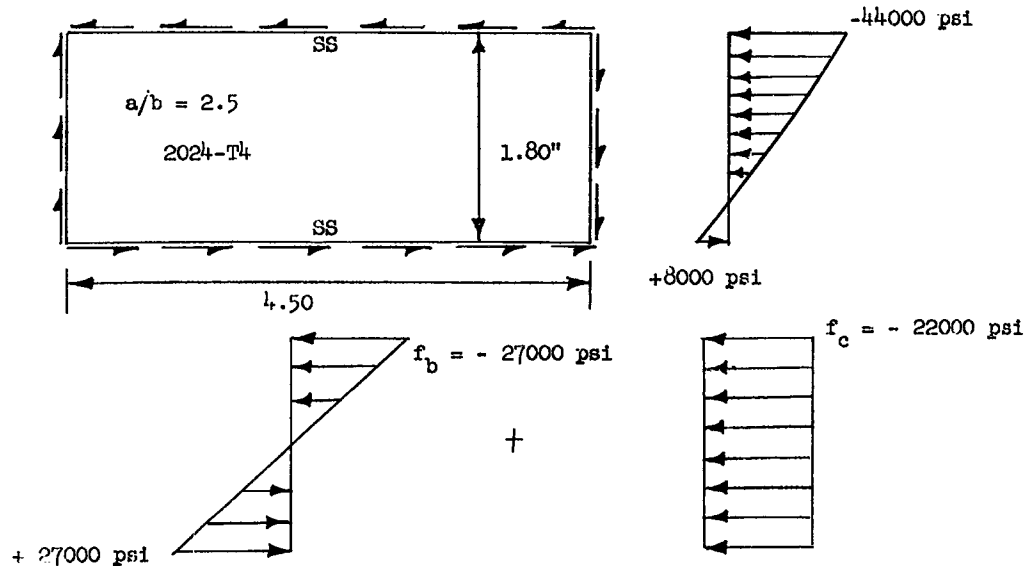
Table 3.2.4 ULTIMATE BENDING MOMENT AT BREAKLINE FOR LOCAL FAILURE MODE						
Strip No.	Strip Area in <sup>2</sup>	$\phi$ in. *	e in/in	Unit Stress $\sigma$ psi	F = $\sigma A$ lbs	Mx in-lbs
2	.261	+0.69	+.00244	+25850	+6750	4650
3	.214	+0.95	+.00336	+35600	+7620	7240
4	.211	+1.085	+.00384	+40650	+8580	9300
5	.205	+1.09	+.00385	+40800	+8360	9110
6	.225	+0.95	+.00336	+35600	+8000	7600
7	.089	-1.50	-.00530	-56200	-5000	7500
8	.166	-1.65	-.00584	-61600	-10220	16880
9	.162	-1.72	-.00608	-63300	-10250	17620
10	.165	-1.67	-.00590	-62000	-10230	17100
11	.189	-1.40	-.00495	-52200	-9870	13800
12	.0902	-1.21	-.00428	-45400	-4090	4950
13	.0429	-1.50	-.00530	-42600	-1830	2740
14	.0712	-1.16	-.00410	-38100	-2710	3140
15	.055	-0.30	-.00106	-11200	-615	185

Break Station -  $\bar{Y} = .30$   $E_{cu} = .0063$   $\tau_{cs} = .110$

\* See Fig 3.2.18

Table 3.2.4(Cont.)ULTIMATE BENDING MOMENT AT BREAKLINE FOR LOCAL FAILURE MODE						
Strip No.	Strip Area in <sup>2</sup>	$\phi$ in.	$e$ in/in	Unit Stress $\sigma$ psi	$F = \sigma A$ lbs	$M_x$ in-lbs
16	.0712	+0.58	+0.00208	+22000	+1570	910
17	.044	+0.89	+0.00315	+32500	+1430	1270
18	.0416	-1.58	-.00559	-43400	-1805	2850
19	.0712	-1.31	-.00463	-40300	-2870	3760
20	.060	-0.38	-.00134	-14200	-850	320
21	.1835	+0.38	+0.00134	+14200	+2505	950
22	.226	+0.71	+0.00251	+26600	+6000	4260
23	.203	+0.97	+0.00343	+34500	+7000	6790
24	.156	+0.92	+0.00325	+33200	+5180	4760
25	.044	-1.24	-.00439	-39400	-1730	2150
26	.0712	-0.90	-.00318	-32800	-2340	2100
27	.027	-0.30	-.00106	-11200	-300	90
28	.0712	+0.28	+0.00099	+10500	+750	210
29	.044	+0.62	+0.00218	+23100	+1020	630
					+55	152865

The actual stress distribution acting on the shaded portion of the web is taken from table 3.2.4.



EQUIVALENT STRESS DIAGRAM

Shear:

Assume web carries 1/3 total shear

$$V = \frac{7200}{3} = 2400 \text{ \#}$$

$$b_w = 2.65 \text{ in}$$

See Page 150

$$f_s = \frac{V}{A} = \frac{2400}{.051 \times 2.65} = 17800 \text{ psi}$$

$$t_w = .051 \text{ in}$$

From Figure 22, Reference 10.

$$\frac{F_{s_{cr}}}{\gamma \sigma_{0.7}} = \frac{K_s \pi^2 E}{12 (1 - \nu^2) \sigma_{0.7}} \left( \frac{t}{b} \right)^2 = \frac{6.0 \times .905 \times 10.6 \times 10^6}{44100} \left( \frac{.051}{1.8} \right)^2$$

$$\frac{F_{s_{cr}}}{\eta \sigma_{0.7}} = 1.05$$

From Figure 10, Reference 10

$$\frac{F_{s_{cr}}}{\sigma_{0.7}} = 0.55$$

$$F_{s_{cr}} = 0.55 \times 44100 = 24300 \text{ psi}$$

$$R_s = \frac{f_s}{F_{s_{cr}}} = \frac{17800}{24300} = .733$$

Bending:

$$f_b = 27000 \text{ psi}$$

From Figure 26, Reference 10

$$K_c = 24.0$$

$$\frac{F_{b_{cr}}}{\eta \sigma_{0.7}} = \frac{K_c \pi^2 E}{12 (1 - \nu^2) \sigma_{0.7}} \left( \frac{t}{b} \right)^2 = \frac{24.0 \times .905 \times 10.6 \times 10^6}{44100} \left( \frac{.051}{1.8} \right)^2$$

$$\frac{F_{b_{cr}}}{\eta \sigma_{0.7}} = 4.20$$

From Figure 9, Reference 10

$$\frac{F_{b_{cr}}}{\sigma_{0.7}} = 1.20$$



$$F_{b_{cr}} = 1.20 \times 44100 = 53000 \text{ psi}$$

$$R_b = \frac{f_b}{F_{b_{cr}}} = \frac{27000}{53000} = .510$$

Compression

$$f_c = 22000 \text{ psi}$$

From Figure 14, Reference 10

$$K_c = 4.4$$

$$\frac{F_{cr}}{\eta \sigma_{0.7}} = \frac{K_c \pi^2 E t^2}{12 (1 - \nu^2) \sigma_{0.7} b^2} = \frac{4.4 \times .905 \times 10.6 \times 10^6}{44100} \frac{(.051)^2}{(1.8)^2}$$

$$\frac{F_{cr}}{\eta \sigma_{0.7}} = 0.77$$

From Figure 9, Reference 10

$$\frac{F_{cr}}{\sigma_{0.7}} = 0.73$$

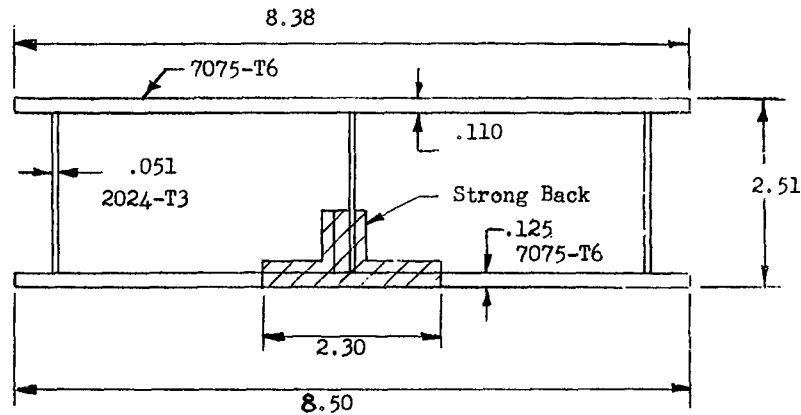
$$F_{cr} = .73 \times 44100 = 32200 \text{ psi}$$

$$R_c = \frac{f_c}{F_{cr}} = \frac{22000}{32200} = .69$$

From Figure 27(a) Reference 10, it is apparent that under this combination of shear, compression, and bending, the web is approximately at its critical buckling load.

### Postfailure Moment Rotation Curve for Local Failure Mode

The failure bay section shown in Fig. 3.1.6 will be idealized as shown below in order to make it amenable to the analysis outlined in Ref. 4.



IDEALIZED REPRESENTATION OF FAILURE BAY

The total postfailure moment will be assumed to be composed of the following contributions:

$$M_T = m_{\text{Web}} + m_{\text{Tension Skin}} + m_{\text{Compression Skin}} + m_{\text{Strong Back}} \quad (3.2.70)$$

#### Web Contribution

From equations 2.4 and 2.9 of Ref. 4

$$m_{\text{Web}} = M_{ow} h n (2\psi_1 + \psi_2) + m_{ow} \frac{h^2}{r} n \psi_4 \quad (3.2.71)$$

Where  $h$  - is height of web  
 $r$  - see Fig. 2.7 Ref. 4  
 $n$  - number of webs  
 $m_{ow}$  - plastic section modulus per unit length of web  
 $\psi_1, \psi_2, \psi_4$  - defined in Tabs. 2.1 through 2.5 Ref. 4

Assume an average plastic tensile strength of 67000 psi for 2024-T3 from Fig. 5 Ref. 11

$$m_{Web} = \frac{67000 (.051)^2}{4} 2.40 \times 3 (2\psi_1 + \psi_2) + 43.5 \left(\frac{2.40}{r}\right)^2 \times 3 \psi_4$$

$$m_{Web} = 313 (2\psi_1 + \psi_2) + \frac{754}{r} \psi_4$$

Tension Skin Contribution

$$m_{Tension Skin} = m_{ost} c_T \quad (3.2.72)$$

Where  $m_{ost}$  - plastic section modulus per unit length of skin  
 $c_T$  - width of tension skin

Assume an average plastic tensile strength of 80000 psi for 7075-T6 from Fig. 5 Ref. 12

$$m_{Tension Skin} = \frac{80000 (.125)^2}{4} \times (8.50 - 2.30)$$

$$m_{Tension Skin} = 1940 \text{ in-lb}$$

### Compression Skin Contribution

From Figs. 2.4 (b) and 2.19 of Ref. 4 and employing the principle of virtual work, the following expression is obtained:

$$\begin{aligned} m_{\text{Comp. Skin}} = m_{\text{osc}} C_c \frac{d\beta_4}{d\theta} - m_{\text{osc}} C_c \frac{d\beta_3}{d\theta} \\ + m_{\text{osc}} C_c \frac{d\beta_5}{d\theta} \end{aligned} \quad (3.2.73)$$

From a consideration of geometry

$$2\beta_4 + 2\beta_5 + 2\beta_3 = 360^\circ$$

$$\beta_5 = 180^\circ - \beta_3 - \beta_4 \quad (3.2.74)$$

Differentiating equation 3.2.74 with respect to  $\theta$

$$\frac{d\beta_5}{d\theta} = -\frac{d\beta_3}{d\theta} - \frac{d\beta_4}{d\theta}$$

Substituting equation 3.2.74 into 3.2.73

$$m_{\text{Comp. Skin}} = -2 m_{\text{osc}} C_c \frac{d\beta_3}{d\theta}$$

$$\psi_3 = -2 \frac{d\beta_3}{d\theta} \quad (3.2.75)$$

$$m_{\text{Comp. Skin}} = m_{\text{osc}} C_c \psi_3$$

Where  $m_{\text{osc}}$  - plastic section modulus per unit length of compression skin.

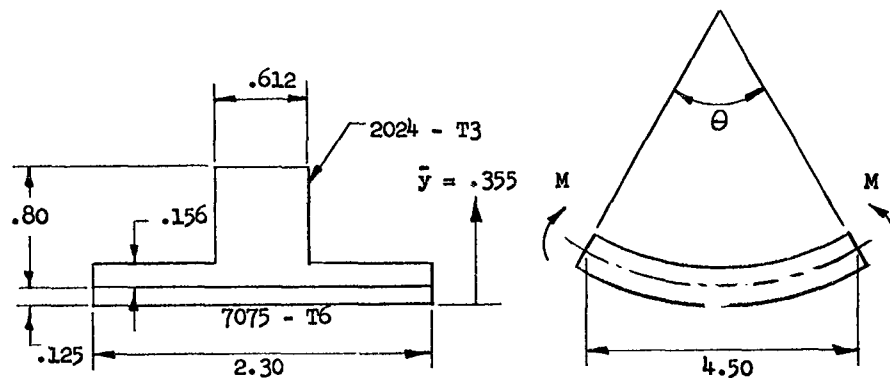
$C_c$  - width of compression skin

$$m_{\text{Comp. Skin}} = \frac{80000(.110)^2}{4} \quad 8.34 \quad \psi_3$$

$$m_{\text{Comp. Skin}} = 2025 \quad \psi_3$$

#### Strongback Contribution

The moment rotation curve for the strongback in the plastic region will be computed by assuming maximum values for the compressive strain and guessing the location of the neutral axis. This establishes a first approximation for the strain throughout the strongback. Knowing the strain, the stress can be determined for every element in the section based on the stress-strain properties of the material. The sum of the axial forces acting on a section should equal zero. If they do not, the neutral axis will be relocated and the process repeated.



#### Moment Capacity at Proportional Limit

$$M = \frac{f_{p.l.} I}{C}$$

$$I = .0590 \text{ in}^4$$

$$C = .570 \text{ in}$$

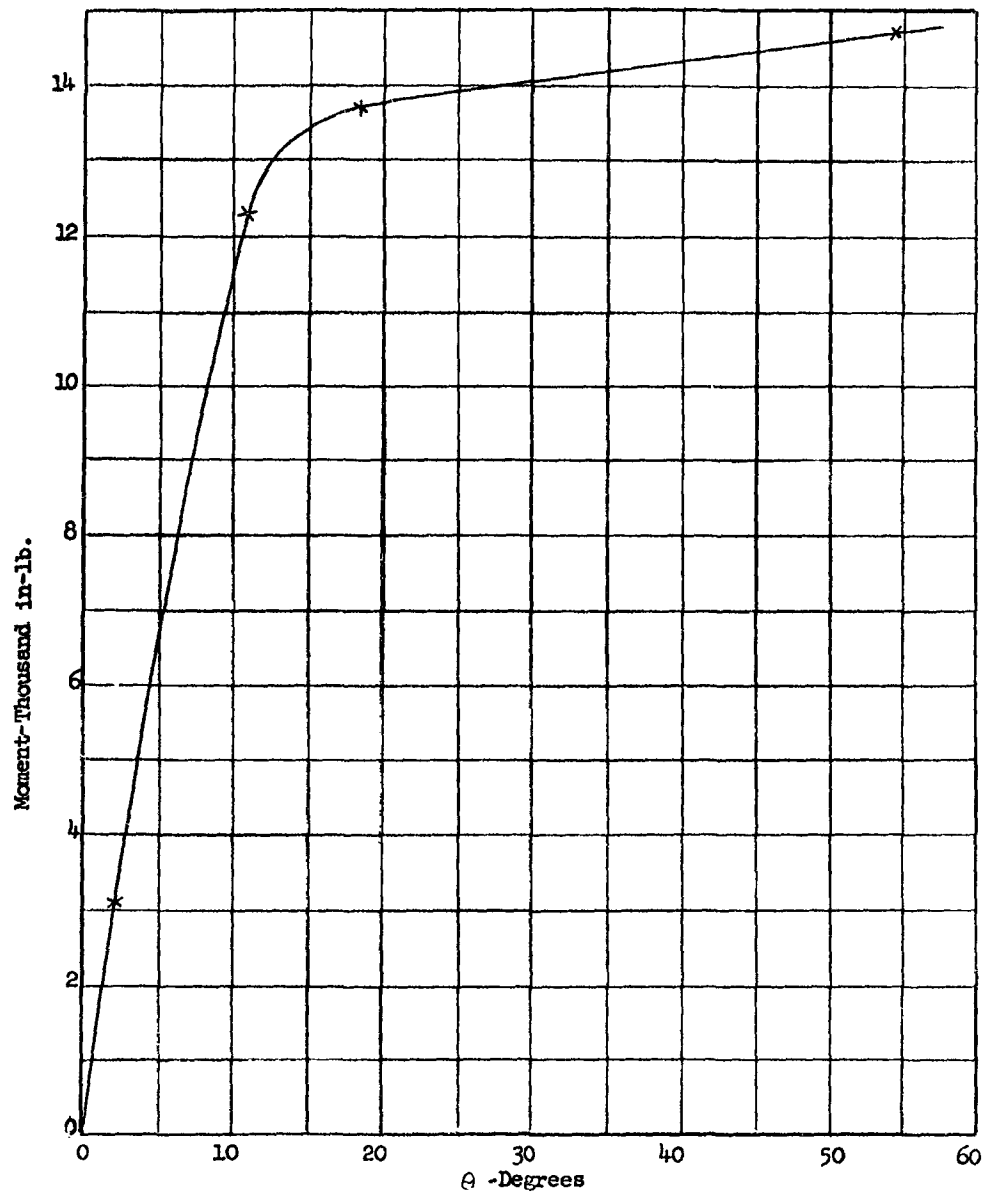


Fig. 3.2.19 MOMENT ROTATION CURVE FOR STRONGBACK

From Fig. 3.2.17, the proportional limit stress is given as

$$f_{p.l.} = 30000 \text{ psi}$$

$$M_{p.l.} = \frac{30000 \times .0590}{.570} = 3100 \text{ in-lb}$$

Rotation of ribs adjacent to break station

$$\Theta = \frac{M \times L}{E I} = \frac{3100 \times 4.5}{10 \times 10^6 \times .0590}$$

$$\Theta = .0227 \text{ rad or } 1.3 \text{ degrees}$$

The moment rotation calculations in the plastic region are summarized in Figure 3.2.19.

The total postfailure moment can be written as

$$M_T = 313 (2 \psi_1 + \psi_2) + \frac{754}{r} \psi_4 + 1940 + 2025 \psi_3 + m_{\text{Strongback}} \quad (3.2.76)$$

Assume the buckled length ( $\lambda$ ) has a lower limit equal to the average distance between webs and an upper limit equal to twice this value.

$$\phi_{\text{lower}} = \frac{\lambda}{2h} = \frac{3.65}{2 \times 2.4} = 0.76$$

From equation 2.11 Ref. 4 binding occurs at

$$\Theta_{\text{max}} = 56.6 \text{ degrees}$$

$$\phi_{\text{upper}} = \frac{2\lambda}{h} = 1.52$$

$$\Theta_{\text{max}} = 71.8 \text{ degrees}$$

For the moment rotation computation employing Tables 2.1 through 2.5 of Ref. 4, a value for  $\phi = .75$  will be assumed. In addition,  $r$  will be taken as  $\infty$  which implies that the corner of the spar cap cracks upon entering the postfailure region. The results of these computations are summarized in Figs. 3.2.20 and 3.2.21.

#### Postfailure Moment Rotation Curve for Wrinkling Failure Mode

The total postfailure moment for the wrinkling mode is the same as that for the local mode except for the contribution of the compression skin.

#### Compression Skin Contribution

From Fig. 2.4 (b), the following expression is obtained: (Ref. 4)

$$m_{\text{Comp. Skin}} = C_c \left( -m_{\text{osc}} \frac{d\beta_3}{d\theta} + 2 m_{\text{osc}} \frac{d\beta_4}{d\theta} \right) \quad (3.2.77)$$

From which

$$m_{\text{Comp. Skin}} = C_c m_{\text{osc}} (\psi_3 - 1)$$

$$m_{\text{Comp. Skin}} = 2025 (\psi_3 - 1)$$

The total postfailure moment can be written as

$$M_T = 313 (2\psi_1 + \psi_2) + \frac{754}{r} \psi_4 + 1940 + 2025 (\psi_3 - 1) + m_{\text{Strongback}} \quad (3.2.78)$$

For the equivalent buckle length,  $\lambda$  will be taken as twice the value of the buckle halfwave length computed from equation 8 of Ref. 13.

$$\lambda = b_s \sqrt{\frac{2}{K_m}}$$

Where:

$b_s$  is ave. distance between webs in failure bay. (3.2.79)

$K_m$  is edge restraint factor computed from Eq. 3.2.66.



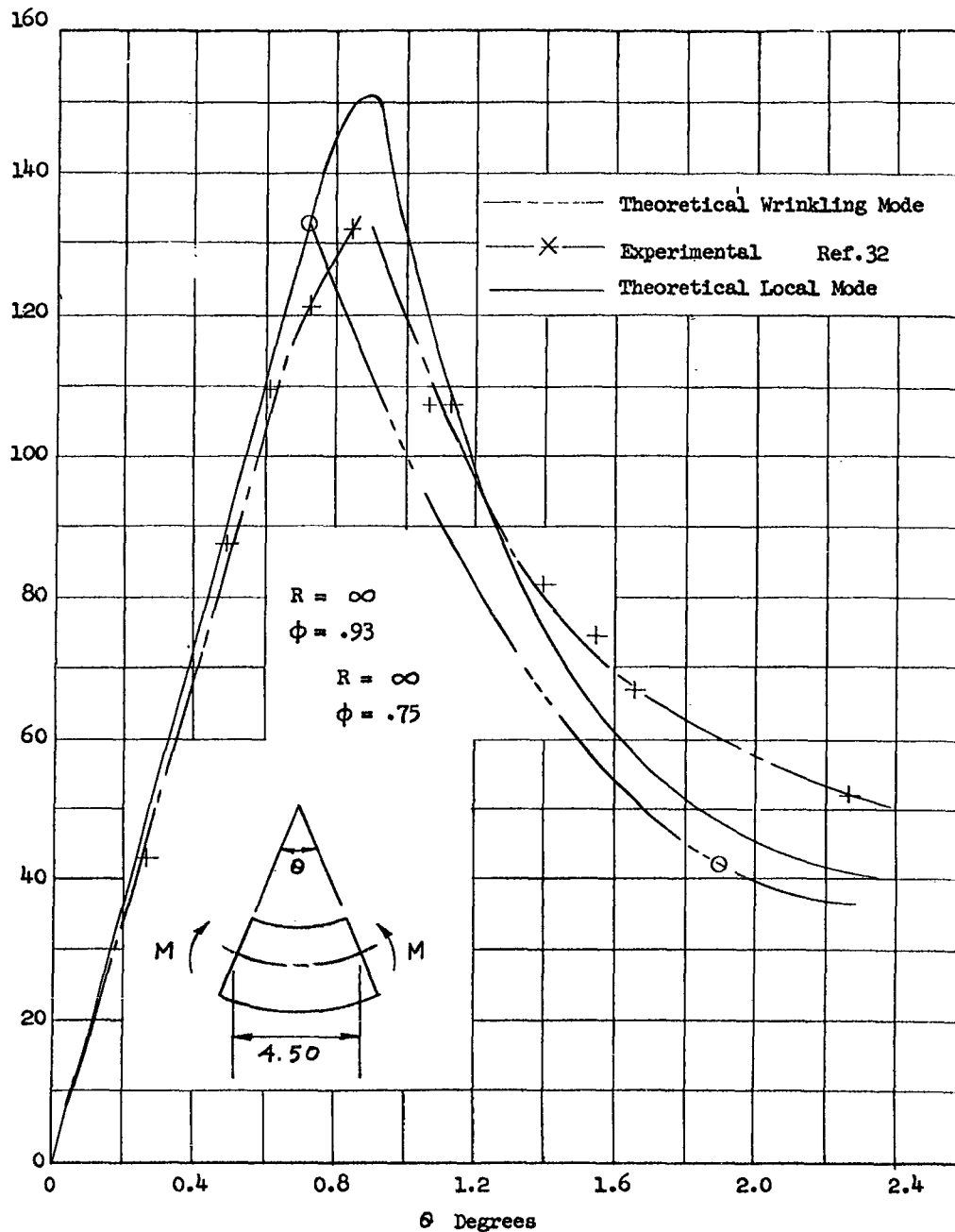


Fig. 3.2.20 RELATIVE ROTATION OF RIBS ADJACENT TO BREAK STATION AS A FUNCTION OF A MOMENT AT BREAK LINE

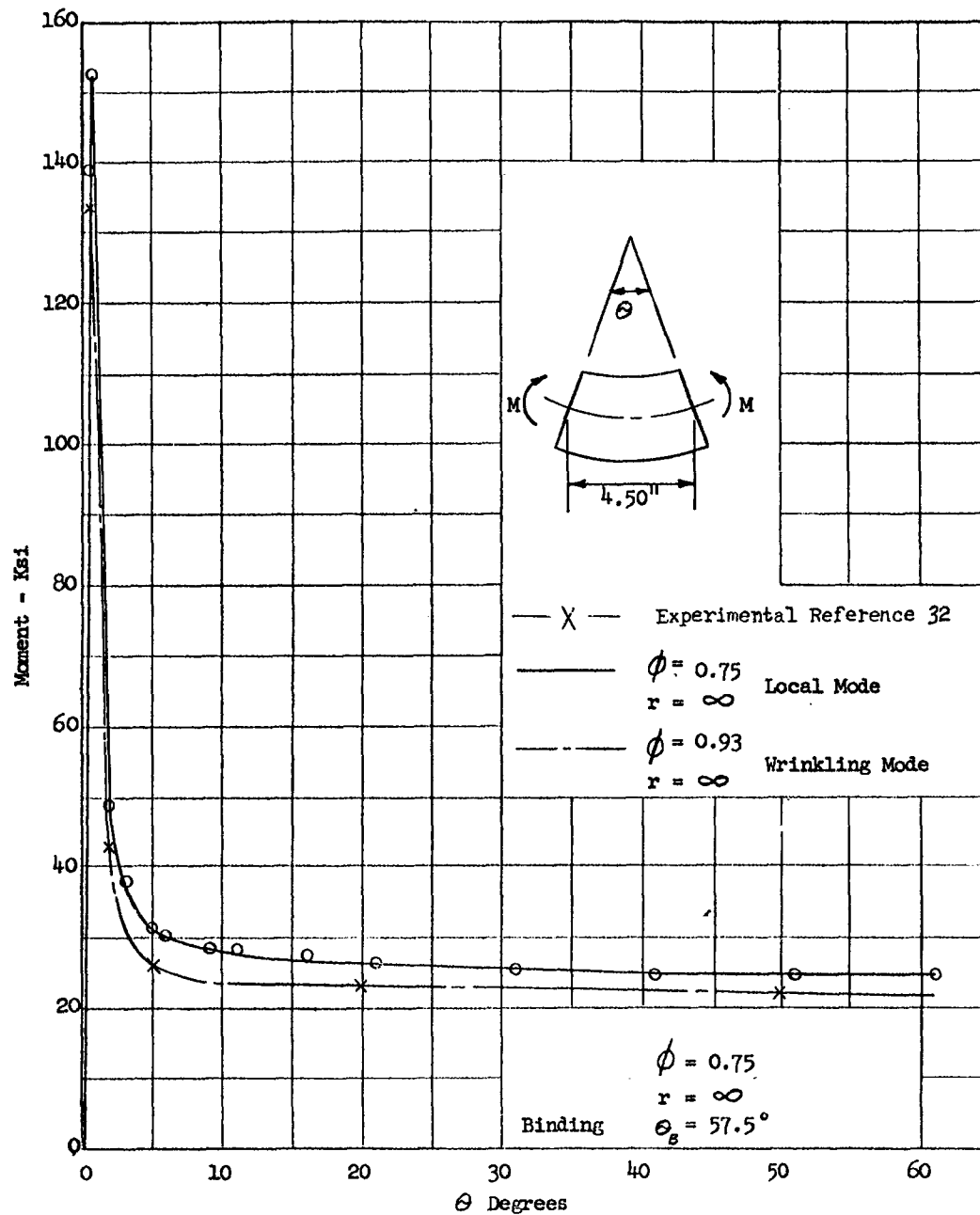


Fig. 3.2.21 RELATIVE ROTATION OF RIBS ADJACENT TO BREAK  
 STATION AS A FUNCTION OF MOMENT AT BREAK LINE

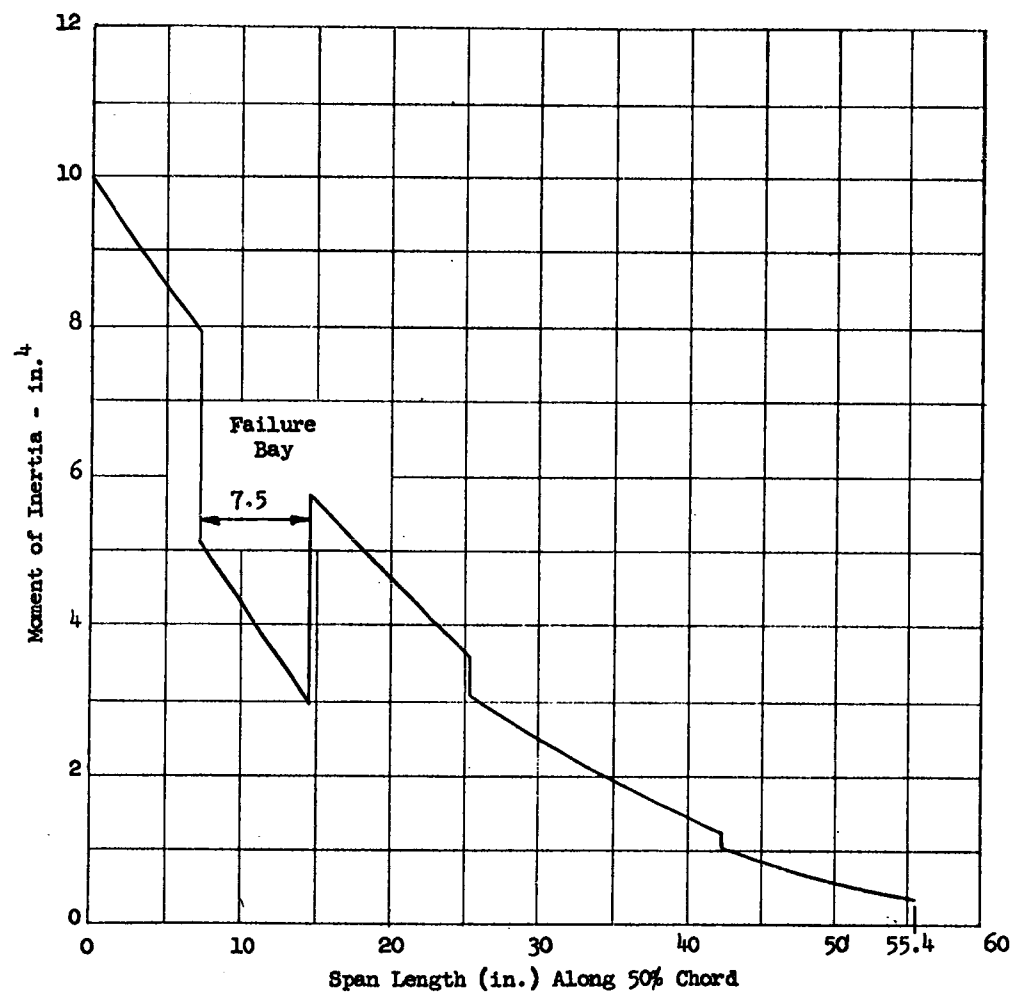


Fig. 3.2.22 MOMENT OF INERTIA OF STRUCTURAL SPECIMEN  
NORMAL TO THE 50% CHORD-SECOND PRELIMINARY TRIAL

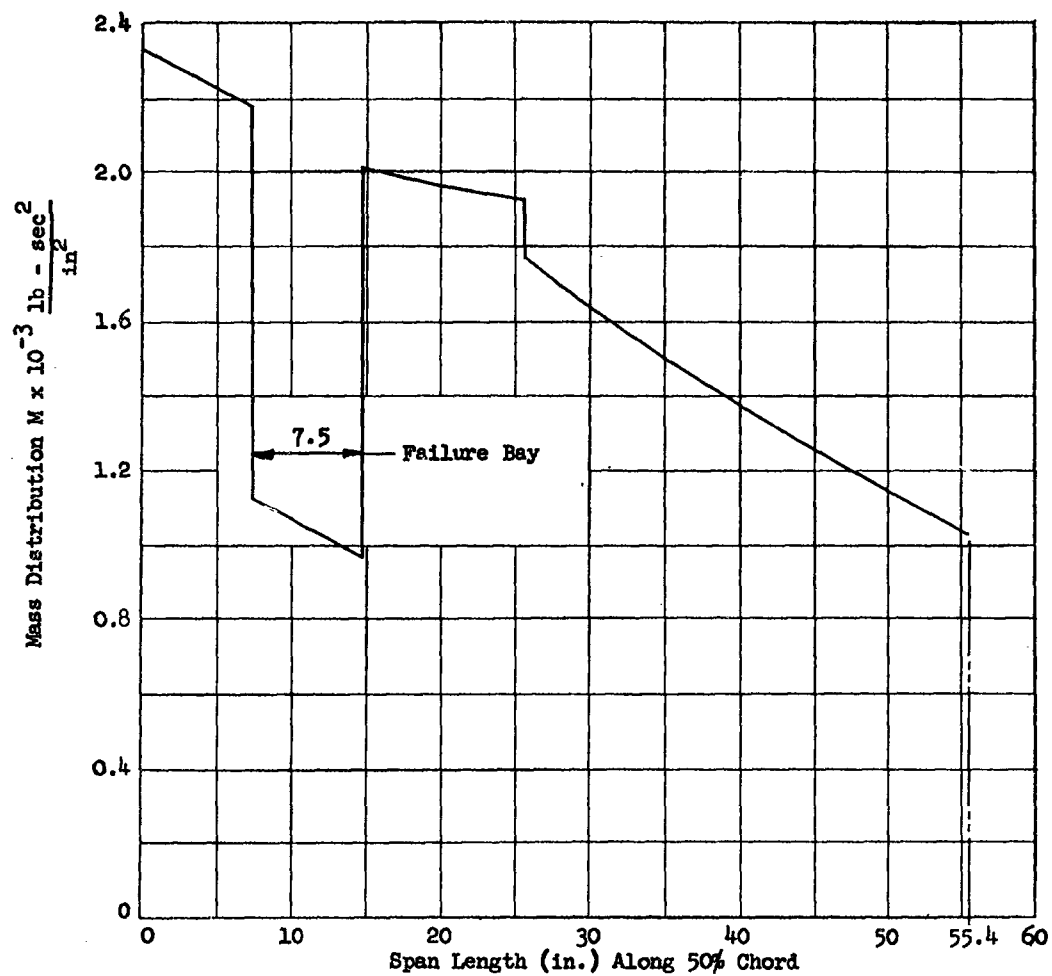


Fig. 3.2.23 SPANWISE MASS DISTRIBUTION OF STRUCTURAL SPECIMEN-SECOND PRELIMINARY TRIAL

$$\lambda = 3.65 \sqrt{\frac{2}{5.37}} = 2.22$$

$$\phi = \frac{2\lambda}{2h} = \frac{2 \times 2.22}{2 \times 2.4} = .93$$

As for the local mode of failure, the spar cap will be assumed to crack upon entering the postfailure region. As a consequence,  $r$  will be taken as  $\infty$ . The results of the moment rotation computations for the wrinkling failure mode are summarized in Figures 3.2.20 and 3.2.21.

Having determined the strength properties of the failure bay, it is now possible to proportion the remainder of the structural specimen to insure an adequate margin of safety on a controlled failure. The moment of inertia and mass distribution of the specimen is given in Figures 3.2.22 and 3.2.23. It should be noted that the width of the failure bay in Figure 3.2.22 and 3.2.23 is 7.5 inches rather than the 4.5 inch width which was finally established. These curves are presented because the bending mode shapes and natural frequencies computed in Figure 3.2.31 which were used by Avidyne in the postfailure response analysis, were based on the moment of inertia and mass distribution given in these curves. The change of the failure bay width from 7.5 to 4.5 inches came at a time when it was not expedient to recalculate the mode shapes and natural frequencies. In addition, the effect of the change on mode shapes and natural frequencies was found to be small. This is evident when comparing natural frequencies in Figures 3.2.31 and 3.3.7.

#### 3.2.4.2.2 PRELIMINARY FLUTTER ANALYSIS OF STRUCTURAL SPECIMEN

A first approximation of the critical flutter speed will be made by idealizing the structural specimen as a simple system with two degrees of freedom. The representative system shown in Figure 3.2.24

The basic equations of motion are given as

$$s_{\alpha} \ddot{h} + I_{\alpha} \ddot{\alpha} + I_{\alpha} \omega_{\alpha}^2 \alpha = Q_{\alpha} \quad (3.2.81)$$

$$\mathcal{M} = \text{mass per unit span}$$

177

$S_d = mb \chi_d$  = static mass moment per unit span about  
 $x = ba$ , positive when the center of  
gravity is aft

$\omega_h$  = uncoupled natural bending frequency

$\omega_d$  = uncoupled natural torsional frequency

$Q_h, Q_d$  = generalized external forces

The solution of these equations of motion leads to the following characteristic determinant (3.2.82)

$$\begin{vmatrix} \left\{ \frac{m}{\pi \rho b^2} \left[ 1 - \frac{\omega_h^2}{\omega_d^2} \frac{\omega_d^2}{\omega^2} \right] + L_h \right\} \left\{ \frac{\chi_d m}{\pi \rho b^2} + L_d - L_h (1/2 + a) \right\} \\ \left\{ \frac{\chi_d m}{\pi \rho b^2} + 1/2 - L_h (1/2 + a) \right\} \left\{ \frac{r_d^2 m}{\pi \rho b^2} \left[ 1 - \frac{\omega_d^2}{\omega^2} \right] + m_d \right. \\ \left. - (L_d + 1/2) (1/2 + a) + L_h (1/2 + a)^2 \right\} \end{vmatrix} = 0$$

where

$a$  = the axis location

$\chi_d = \frac{S_d}{mb}$  = the dimensionless static unbalance

$r_d = \sqrt{\frac{I_d}{mb^2}}$  = the dimensionless radius of gyration

$\frac{m}{\pi \rho b^2}$  = the density ratio

$\rho$  = density of air

The shear and mass center locations for a section located at 75% of the span length is given in Figure 3.2.25.

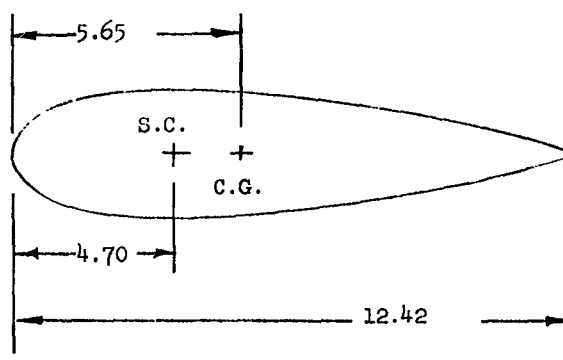


Figure 3.2.25  
Three Quarter Semi-Span Section

The fundamental bending frequency used in the flutter analysis was computed in Section 3.2.4.2.3 based on the preliminary properties of the specimen given in Figures 3.2.22 and 3.2.23.

$$\omega_h = 239 \text{ RAD/SEC.}$$

The first torsional frequency used in the flutter analysis will be computed by the Holzer Method outlined in Reference 18 using the preliminary properties of the structural specimen given in Figures 3.2.26, 3.2.27 and 3.2.28. The torsional mass moment of inertia will be assumed to be concentrated at the eight span wise stations indicated in Figure 3.2.28. The torsional stiffness between mass points will be taken as the average value. The calculations for the fundamental torsional frequency have been summarized in Table 3.2.5



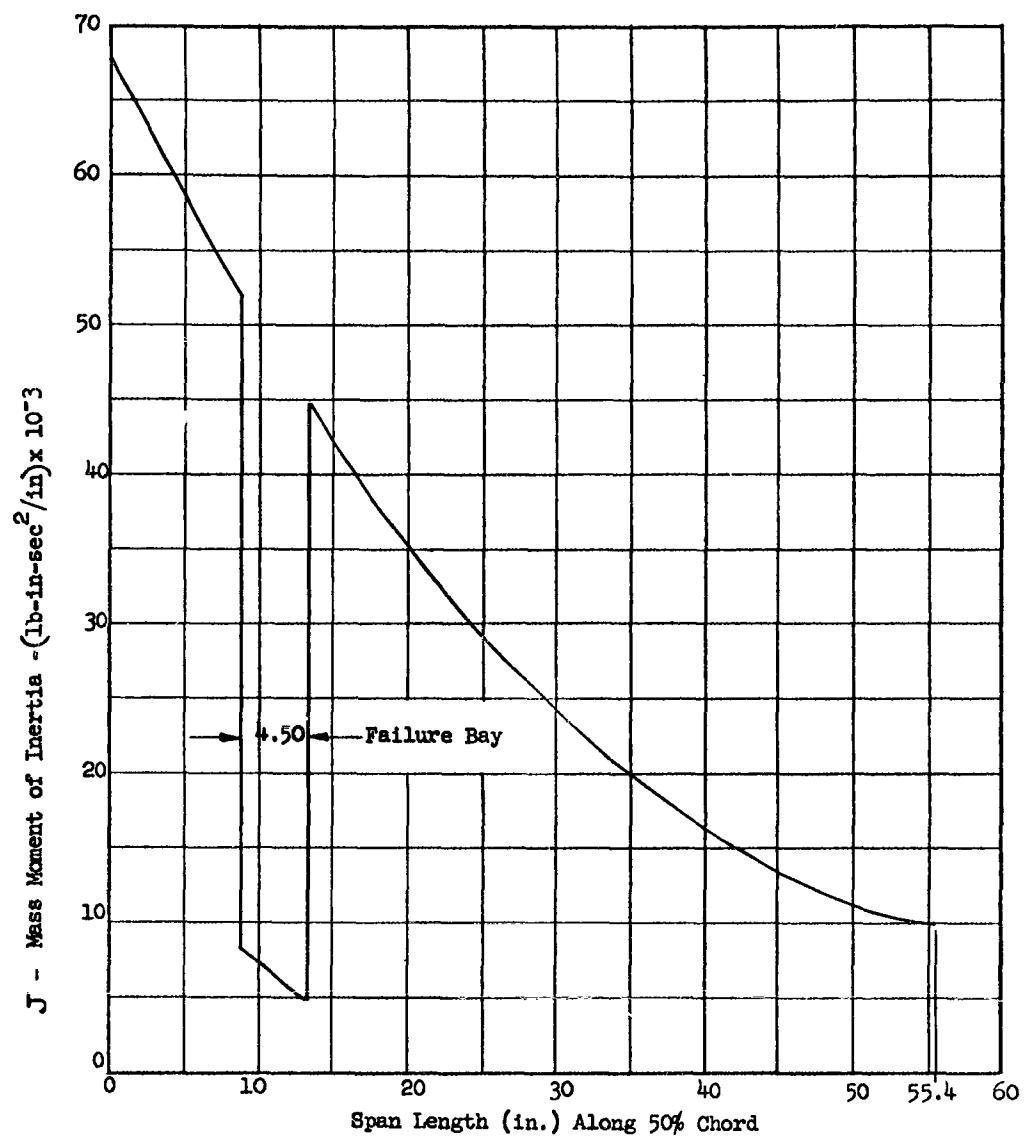


Fig. 3.2.26 TORSIONAL MASS MOMENT OF INERTIA FOR STRUCTURAL SPECIMEN-SECOND PRELIMINARY TRIAL

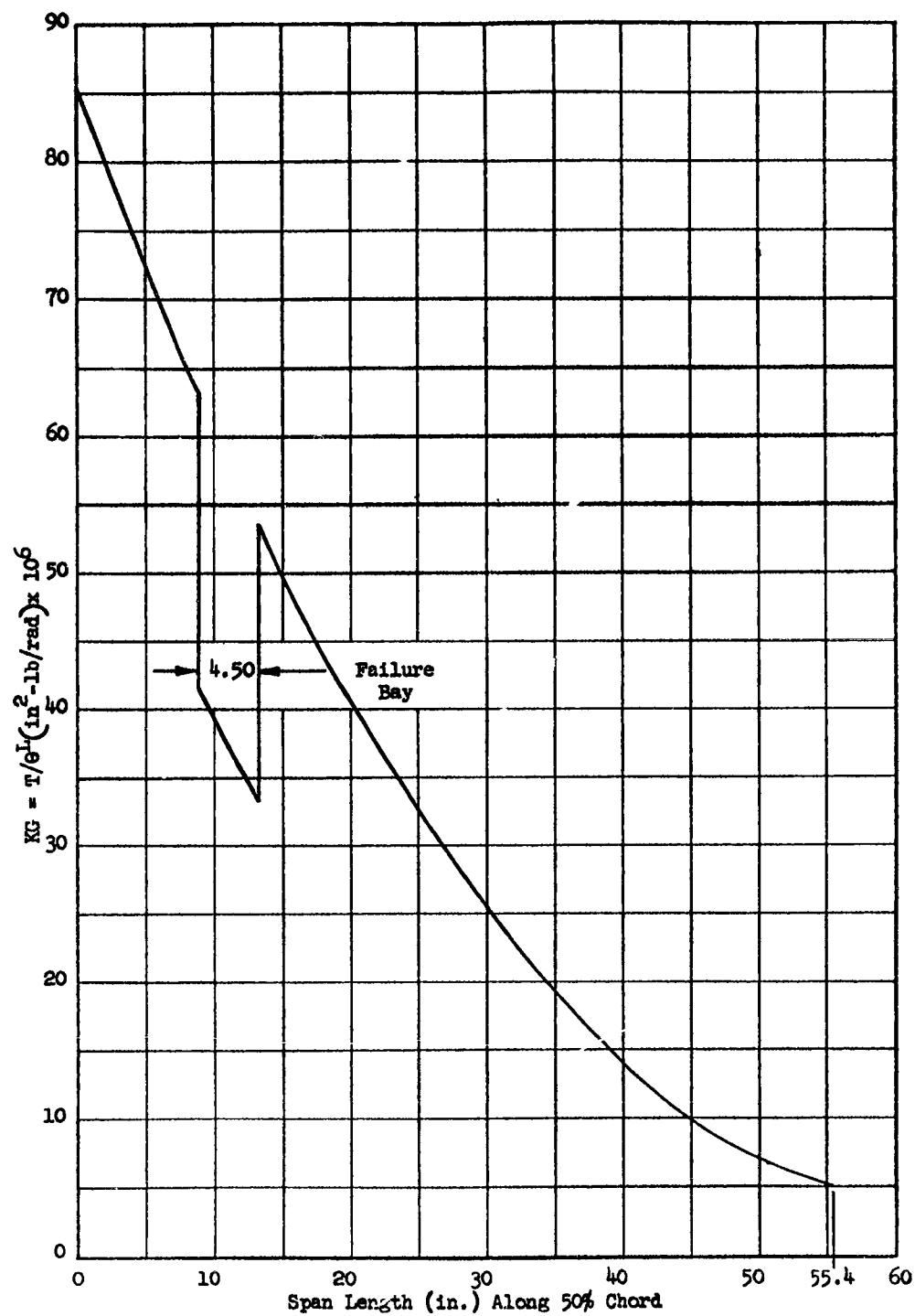


Fig. 3.2.27 TORSIONAL STIFFNESS OF STRUCTURAL WING-  
SECOND PRELIMINARY TRIAL

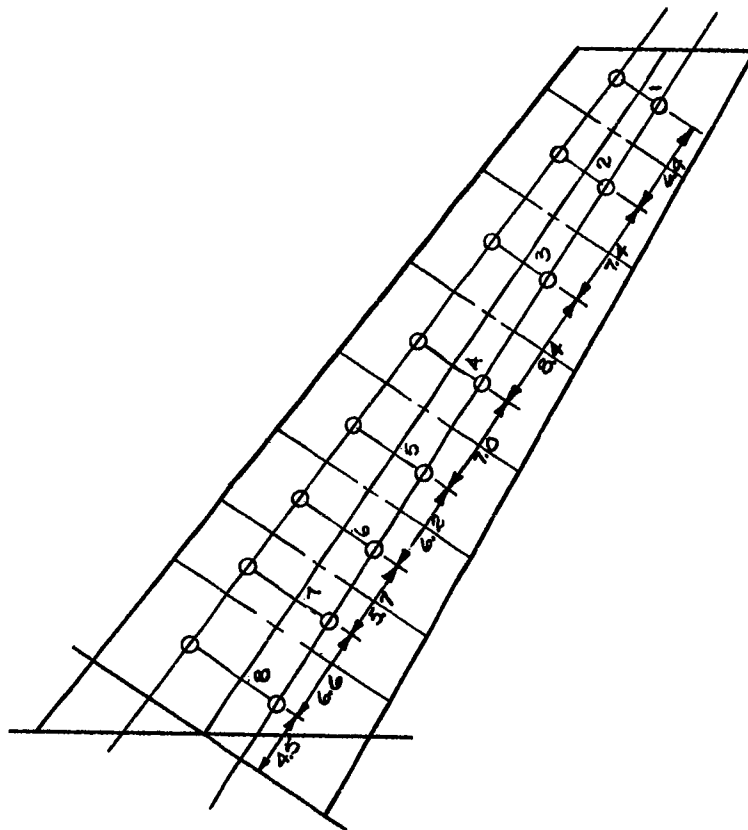


FIGURE 3.2.28 TORSIONAL MASS MODEL

# First Torsion Mode

$$\theta_{M+1} = \theta_M - \frac{\omega^2}{C_M} \sum J_i \theta_i$$

Reference 18

Where:  $\theta_M$  is the amplitude of angular displacement of mth dumbbell Figure 3.2.28

$J_i$  is the torsional mass moment of inertia assigned to the ith dumbbell in Figure 3.2.28. from the distribution in Figure 3.2.26

$C_M = \frac{KG}{L_i}$  is the torsional stiffness between M and M + 1 as determined from Figure 3.2.27

$L_i$  is length between M and M + 1

Estimate

$$f_n = 215 \text{ cps}$$

$$\omega = 1350 \text{ rad/sec}$$

$$\theta_i = 1.0$$

$$\omega^2 = 1822000 \text{ (rad/sec)}^2$$

Table 3.2.5 FUNDAMENTAL TORSIONAL FREQUENCY SECOND PRELIMINARY TRIAL

MASS PT.	$\theta_M$ Rad	$J \times 10^{-3}$ lb-in-sec <sup>2</sup>	$\theta \times 10^{-3}$	$C_m \times 10^{-6}$	$\frac{\omega^2}{C_M}$	$\frac{\omega^2}{C_M} \sum J \theta$
1	1.000	68.5	68.5	1.19	1.53	0.1048
2	0.8952	84.4	75.5	1.62	1.123	0.1620
3	0.7332	149.0	109.2	2.44	0.746	0.1889
4	0.5443	207.0	112.8	4.52	0.403	0.1477
5	0.3966	175.0	69.4	6.45	0.283	0.1232
6	0.2734	272.0	74.4	7.90	0.231	0.1178
7	0.1556	30.8	4.8	8.35	0.219	0.1128
8	0.0428	522.0	22.4	18.40	0.099	0.0531
root	-0.0103					

The necessary parameters required to solve the characteristic determinant are

$$b = 6.21"$$

$$a = - \frac{(6.21 - 4.70)}{6.21} = - .243$$

$$x_d = \frac{(5.65 - 4.70)}{6.21} = + .153$$

The torsional mass moment of inertia at the 75% span length is obtained from Figure 3.2.26.

$$J = I_d = 15.4 \times 10^{-3} \text{ LB} \cdot \text{SEC}^2$$

The mass per unit length at the 75% span length is obtained from Figure 3.2.23

$$m = 1.33 \times 10^{-3} \frac{\text{LB} \cdot \text{SEC}^2}{\text{IN}^2}$$

$$r_d = \sqrt{\frac{I_d}{mb^2}} = \sqrt{\frac{15.4 \times 10^{-3}}{1.33 \times 10^{-3} (6.21)^2}}$$

$$r_d = 0.550$$

The density of air is given as

$$\rho = 1.145 \times 10^{-7} \frac{\text{LB} \cdot \text{SEC}^2}{\text{in}^4}$$

$$\frac{m}{\pi \rho b^2} = \frac{1.33 \times 10^{-3}}{3.14 \times 1.145 \times 10^{-7} \times 38.6} = 95.8$$

In order to solve the characteristic determinant two values of  $\frac{v}{b\omega}$  were assumed. From Table A.6 of Reference 19, corresponding

values of  $L_\alpha$ ,  $L_h$ , and  $M_\alpha$  for each  $\frac{U}{b\omega}$  were obtained. The real and imaginary roots were then determined from the characteristic determinant for each value of  $\frac{U}{b\omega}$ . The critical velocity was then determined from Figure 3.2.29 at the intersection of the curves drawn through the real and imaginary roots.

Point (1)

Assume  $\frac{U}{b\omega} = 6.25$

From Table A. 6, Reference 19 Note:  $L_\alpha$ ,  $L_h$ , and  $M_\alpha$  are independent of  $e$

Substituting into equation 3.2.82

$$\begin{vmatrix} \left[ 94.5 - \frac{5.46 \times 10^6}{\omega^2} - 9.535i \right] & \left[ -46.44 + 1.32i \right] \\ \left[ 15.55 + 2.45i \right] & \left[ +98.98 - \frac{52.6 \times 10^6}{\omega^2} - 18.06i \right] \end{vmatrix} = 0$$

$$+ 4190 - \frac{5215 \times 10^6}{\omega^2} + \frac{286 \times 10^{12}}{\omega^4} - 1019i + \frac{535 \times 10^6}{\omega^2} = 0$$

Real Part

$$\omega_R^4 - 1.25 \times 10^6 \omega_R^2 + 6.84 \times 10^{10} = 0$$

$$\omega_R = 1100 \text{ RAD/SEC}$$

Imaginary Part

$$535 \times 10^6 - 1019 \omega_I^2 = 0$$

$$\omega_I = 725 \text{ RAD/SEC}$$

Point (2)

Assume  $\frac{U}{b\omega} = 12.50$

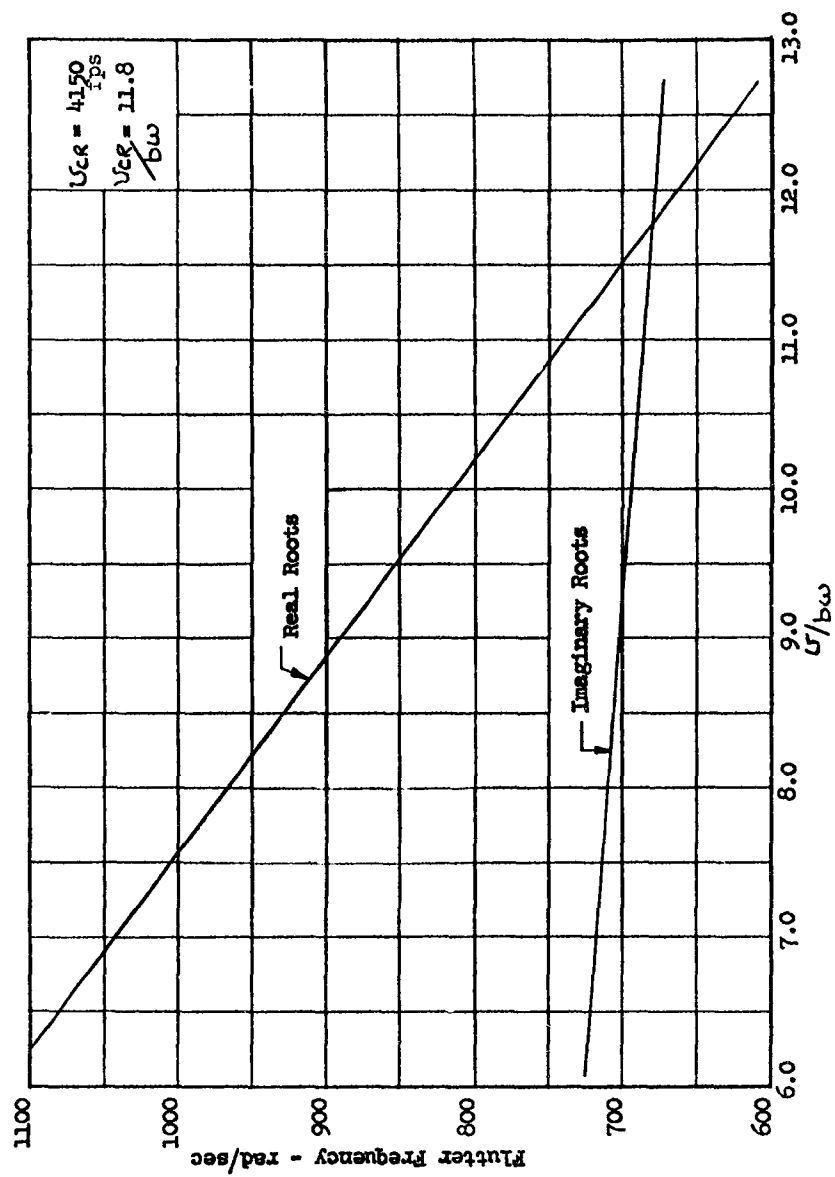


Fig. 3.2.29 CRITICAL FLUTTER SPEED FOR THE STRUCTURAL WING

$$\begin{aligned} & \left[ \begin{array}{c} 92.8 - \frac{5.46 \times 10^6}{\omega^2} - 12.51 i \\ 15.92 + 5.53 i \end{array} \right] \left[ \begin{array}{c} -257.02 + 21.64 i \\ +98.98 - \frac{52.6 \times 10^6}{\omega^2} - 18.06 i \end{array} \right] = 0 \\ & + 13012 - \frac{5420 \times 10^6}{\omega^2} + \frac{288 \times 10^{12}}{\omega^4} - 3801 i + \frac{1231 \times 10^6}{\omega^2} = 0 \end{aligned}$$

Real Part

$$\omega_R^4 - 0.417 \times 10^6 \omega_R^2 + 2.21 \times 10^{10} = 0$$

$$\omega_R = 625 \text{ RAD/SEC}$$

Imaginary Part

$$1231 \times 10^6 - 2725 \omega^2 i = 0$$

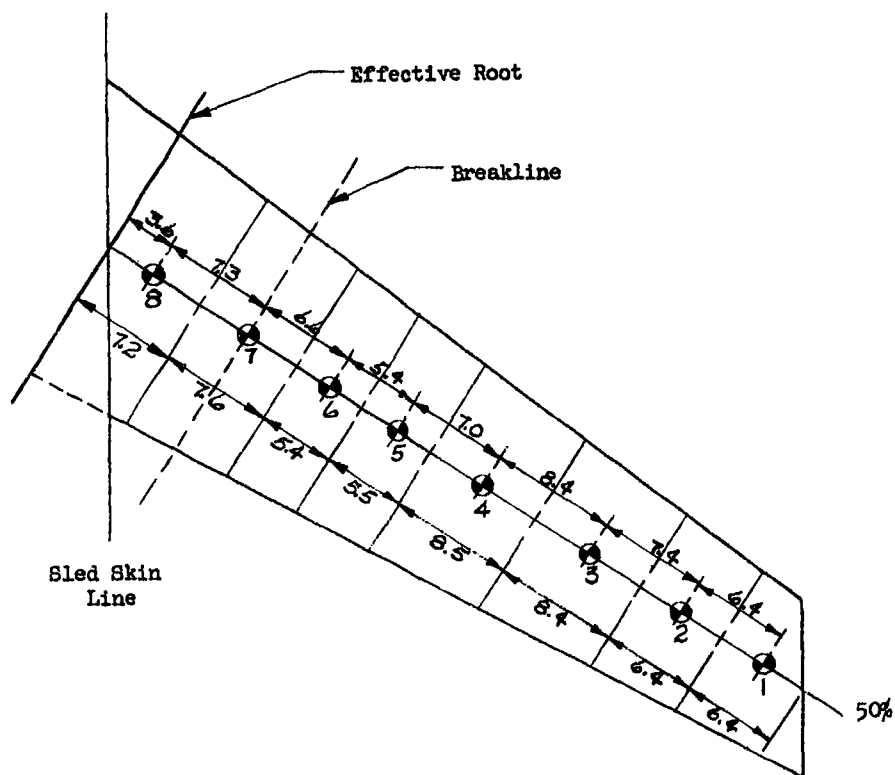
$$\omega_i = 674 \text{ RAD/SEC}$$

Since the critical flutter frequency of 4150 fps as determined from Figure 3.2.29 is much greater than the sled velocity of Mach 0.8, there is no danger of flutter prior to blast interception.

### 3.2.4.2.3 BENDING MODES AND NATURAL FREQUENCIES

The natural frequencies and mode shapes for the first three bending modes of vibration were computed using the preliminary moment of inertia and mass properties indicated in Figures 3.2.22 and 3.2.23. The vibration modes were determined utilizing the "Myklestad Method" outlined in Reference 18. The lumped mass distribution for the idealized structural specimen is shown in Figure 3.2.30. The center of gravity of the lumped mass was determined for each individual bay utilizing the mass distribution given in Figure 3.2.23. The elastic coefficients were computed by using the "Area-Moment Method", assuming a trapezoidal stiffness distribution between lumped masses. These coefficients have been summarized in Table 3.2.6. The orthogonality of the bending vibration modes plotted in Figure 3.2.31 have been checked in Table 3.2.7.





Bay No.	Mass $\frac{\text{lb-sec}^2}{\text{in.}}$	Area $\text{in.}^2$
1	.00712	131.0
2	.00801	129.3
3	.01205	86.4
4	.01412	84.4
5	.01075	119.0
6	.01083	106.7
7	.00808	73.8
8	.01624	67.7

Fig. 3.2.30 LUMPED MASS DISTRIBUTION FOR IDEALIZED  
STRUCTURAL SPECIMEN-SECOND PRELIMINARY TRIAL

Table 3.2.6 SUMMARY OF LUMPED MASSES AND ELASTIC COEFFICIENTS STRUCTURAL SPECIMEN - SECOND PRELIMINARY TRIAL					
N	$M_N$	$L_N$	$V_M \times 10^{-6}$	$V_F \times 10^{-6}$ $d_M \times 10^{-6}$	$d_F \times 10^{-6}$
1	.00712	6.4	.8792	2.607	10.72
2	.00801	7.4	.5984	1.992	9.346
3	.01205	8.4	.4022	1.561	8.417
4	.01412	7.0	.2103	.6782	3.042
5	.01075	5.4	.1146	.2976	1.047
6	.01083	6.6	.1413	.4861	2.184
7	.00808	7.3	.1170	.3719	1.696
8	.01624	3.6	.0379	.0673	.1518

Definition of the elastic coefficients for the  $n^{\text{th}}$  section of a beam

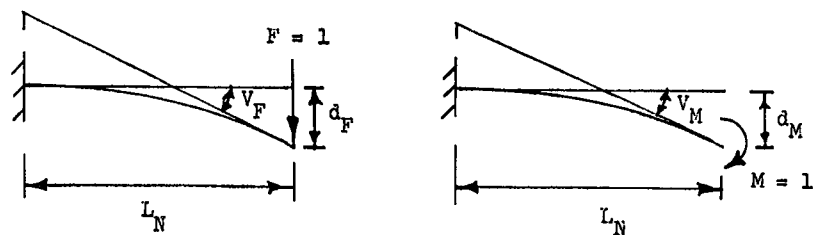


Table 3.2.7 ORTHOGONALITY OF MODES FOR STRUCTURAL SPECIMEN									
Bay No. i	Mass $\frac{\text{lb-sec}^2}{\text{in}}$ M <sub>i</sub>	Root to Mass C.G. in.	Mode Deflection			Orthogonality of Modes			
			$\phi_i^{(1)}$	$\phi_i^{(2)}$	$\phi_i^{(3)}$	$m_i \phi_i^{(1)} \phi_i^{(2)}$ $\times 10^{-3}$	$m_i \phi_i^{(1)} \phi_i^{(3)}$ $\times 10^{-3}$	$m_i \phi_i^{(2)} \phi_i^{(3)}$ $\times 10^{-3}$	
1	.00712	52.1	1.00000	1.00000	1.00000	7.1200	7.1200	7.1200	
2	.00801	45.7	.79449	.19877	-.68611	1.2649	-4.3663	-1.0924	
3	.01205	38.3	.57245	-.44055	-.96625	-3.0389	-6.6652	5.1294	
4	.01412	29.9	.35512	-.68665	.14256	-3.4430	.7149	-1.3822	
5	.01075	22.9	.20992	-.58112	.82509	-1.3114	1.8619	-5.1544	
6	.01083	17.5	.12081	-.40509	.88002	-.5300	1.1514	-3.8608	
7	.00808	10.9	.04239	-.17477	.52080	-.0599	.1784	.7354	
8	.01624	3.6	.00430	-.02036	.07190	-.0015	.0050	.0237	
					$\Sigma$	.0002	.0001	.0005	

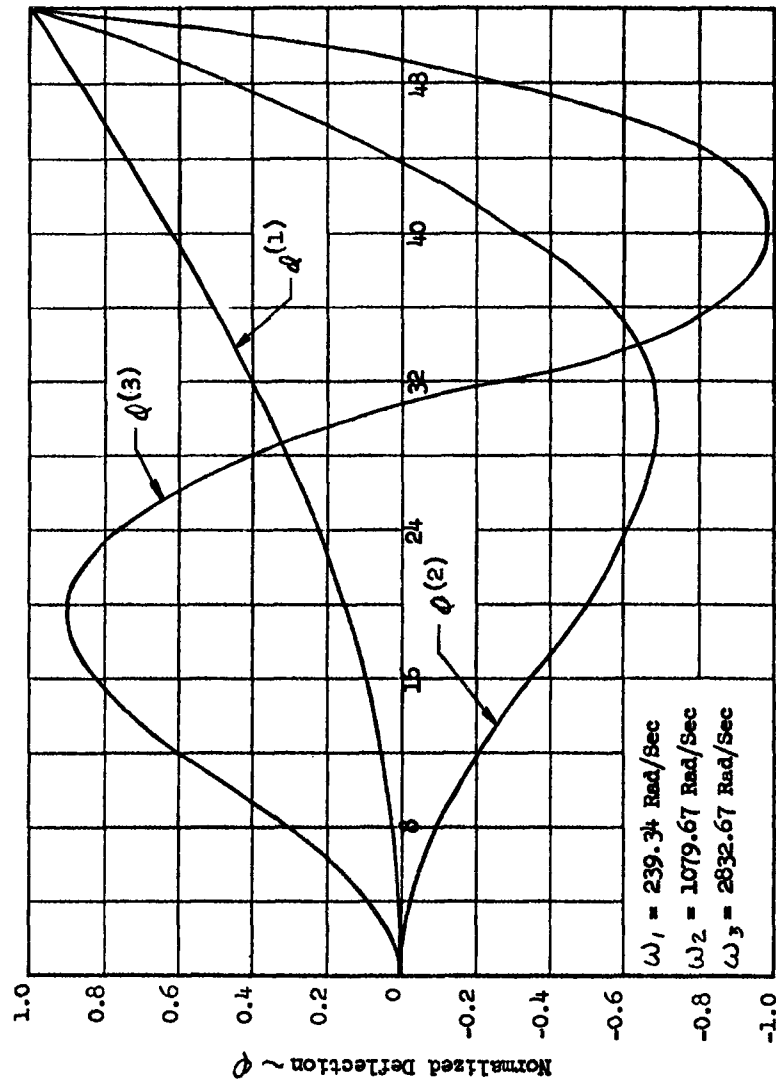


Fig. 3.2.31 BENDING VIBRATION MODES - STRUCTURAL SPECIMEN  
SECOND PRELIMINARY TRIAL

#### 3.2.4.2.4. POSTFAILURE RESPONSE ANALYSES OF STRUCTURAL SPECIMEN

It was originally AAI's intent that the final postfailure response analysis of the structural specimen be based on elastic properties which accounted for the plate like behavior of the swept back wing. As a consequence, the structural specimen was idealized as shown in Figures 3.2.32 and 3.2.33. The total mass of the structure was lumped into twelve (12) mass points located on the 25% and 65% chordlines. The elastic properties of the structure were determined by an energy method which accounted for the coupling of bending and torsional effects characteristic of a swept wing. Before the final elastic analysis was consummated Avidyne recommended that the post-failure response analysis, which was to determine the adequacy of the structural specimen to meet the test objectives imposed by the missions described in Table 3.2.1, be based on the elastic properties of the idealized structure shown in Figure 3.2.30 of the preliminary analysis. Furthermore, only the first two bending modes of this idealized structure was to be utilized in the postfailure response analysis. One of the primary reasons Avidyne had for taking this approach was based on the fact that there are, at present, no adequate means for measuring torsion in the postfailure region of response. As a consequence, this would limit the value of accounting for coupling of bending and torsional effects in the correlation phase of the program. If it is determined in the correlation phase that such effects need be accounted for, they would be based on the experimentally determined elastic properties of the structural specimen. In any case, it was believed that these refinements would not be required to determine the adequacy of the specimen to meet the test objectives. As a result of these recommendations, the indeterminate analysis was abandoned.

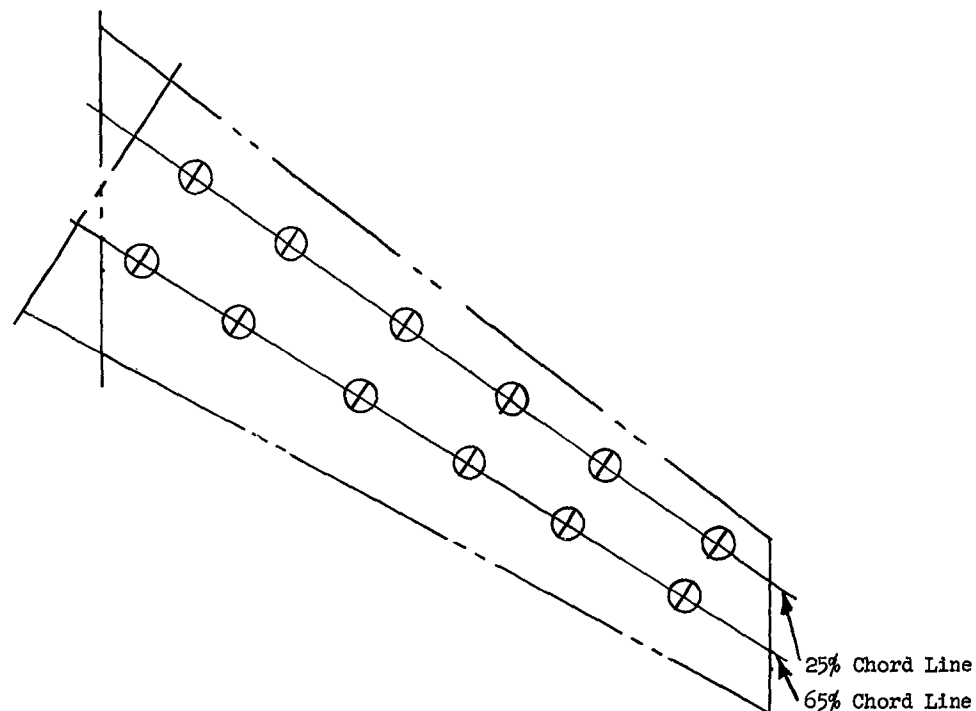


FIGURE 3.2.32 IDEALIZED LUMPED MASS DISTRIBUTION FOR STRUCTURAL SPECIMEN

In order for Avidyne to proceed with the postfailure response analysis AAI was required to supply the first two bending natural frequencies and mode shapes, the mass distribution and the geometric properties of the structural specimen. These structural characteristics were computed from the properties presented in Figures 3.2.22 and 3.2.23. The postfailure moment rotation curve supplied to Avidyne was based upon a laboratory test of the failure bay described in Section 3.1.2.

This test specimen was built by AAI and tested at the MIT, Aeroelastic and Structures Research Laboratory by Mr. D'Amato. The results of this test are described in Reference 32. The final airloads used in the postfailure response analysis were generated by Dr. Witmer. The results of the postfailure response analysis performed by Avidyne along with a description of airloads used is presented in Appendix A.

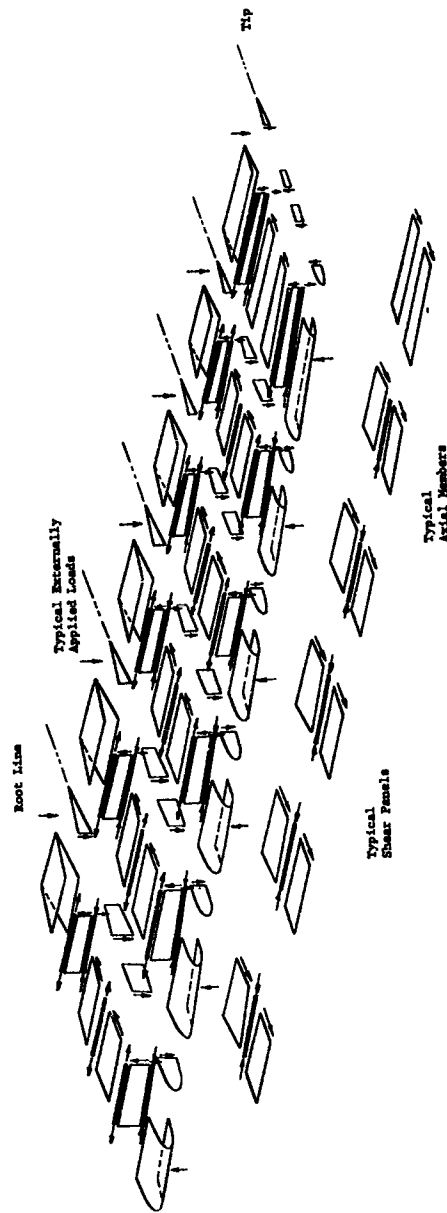


Figure 3.2.33 IDEALIZED STRUCTURAL ELEMENTS OF (6A) MODEL

### 3.3 FINAL DESIGN

#### 3.3.1 AIRLOAD SPECIMEN

Since the primary design requirement for the airload specimen was to insure its structural adequacy during runs No. 1 - 3, Table 3.2.1, there is no need for a more elaborate theoretical analysis than that presented in Section 3.2.3. A more accurate method of computing response is unwarranted in view of the difficulty of estimating the airloads more accurately. During the laboratory tests of the airload specimen, it was determined that the actual fundamental frequency of the model in the sled body was considerably lower than that which was estimated in Section 3.2.3.1. Consequently, the dynamic over-stress factor is actually lower than that determined in Section 3.2.3.2 and the subsequent preliminary stress analysis was conservative. The preliminary properties of the airload specimen which were presented in Figure 3.2.4 may be taken as the final values.

#### 3.3.2 STRUCTURAL SPECIMEN

##### 3.3.2.1 SPECIMEN PROPERTIES

The properties given in this section are the theoretical values computed for the finalized structural specimen described in Section 3.1, and taken from AAI Drawings 2113-040069 and 2113-040090. The mass distribution given is for the fully instrumented structural specimen. The final theoretically computed moment rotation curve was presented in Figure 3.2.21 and will not be duplicated in this section. Specimen properties are given in Figures 3.3.1 through 3.3.4.

##### 3.3.2.2 BENDING STRENGTH

Computation of the ultimate strength of the structural specimen will be based on the correlation of theory and the experimental results obtained from the failure test of the model break station. The correlation indicated that the theory for computing the ultimate strength of built-up sections which fail in the wrinkling mode as presented in References 15 and 13 is applicable to the structural specimen.



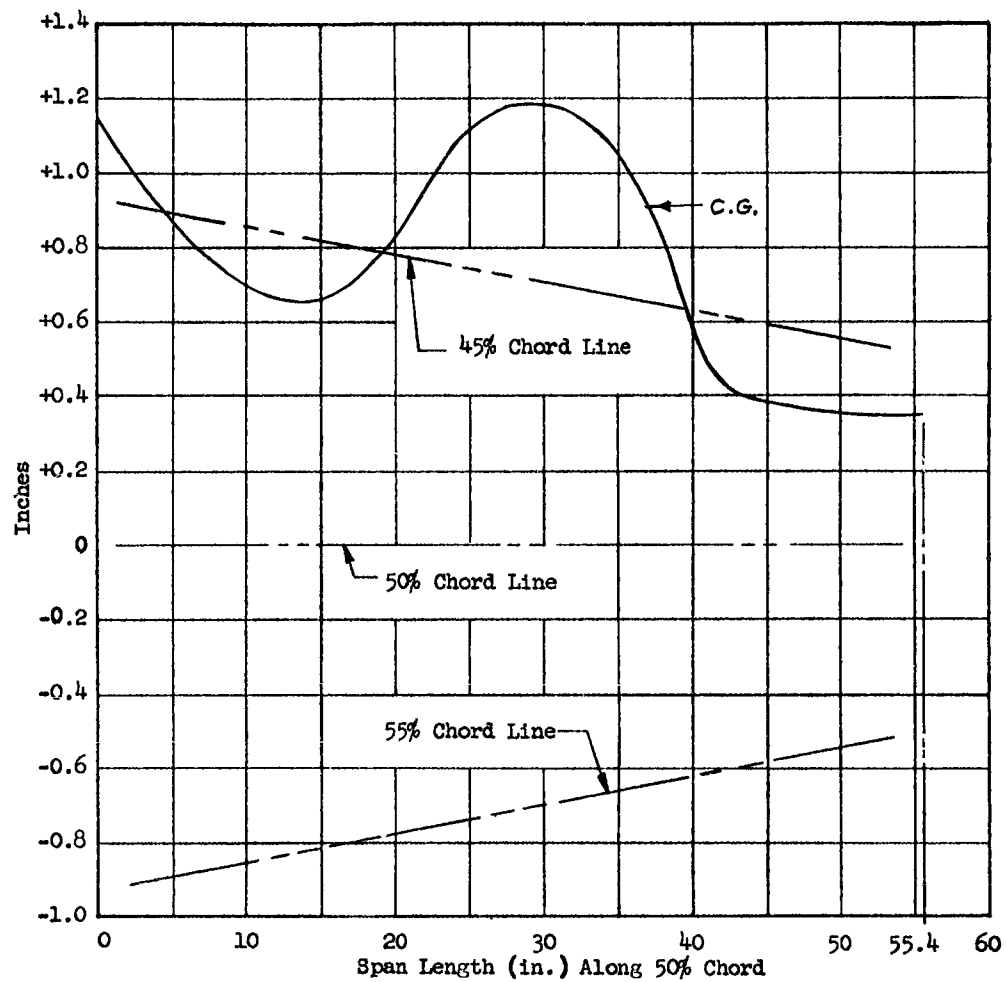


Fig. 3.3.1 CHORDWISE CENTER OF GRAVITY LOCATION  
OF STRUCTURAL SPECIMEN MEASURED NORMAL TO 50% CHORD LINE-FINAL

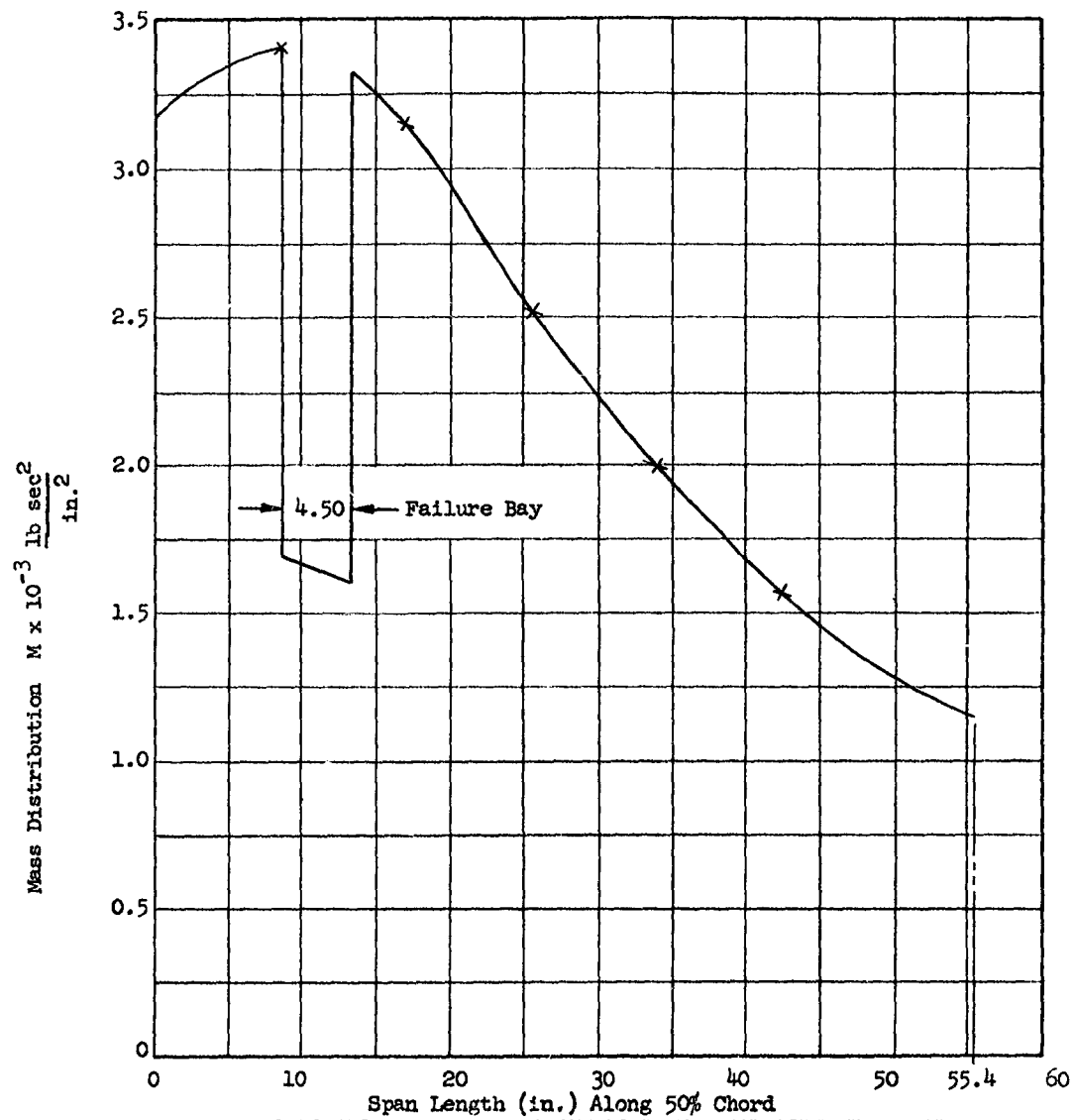


Fig. 3.3.2 SPANWISE MASS DISTRIBUTION OF STRUCTURAL SPECIMEN-FINAL

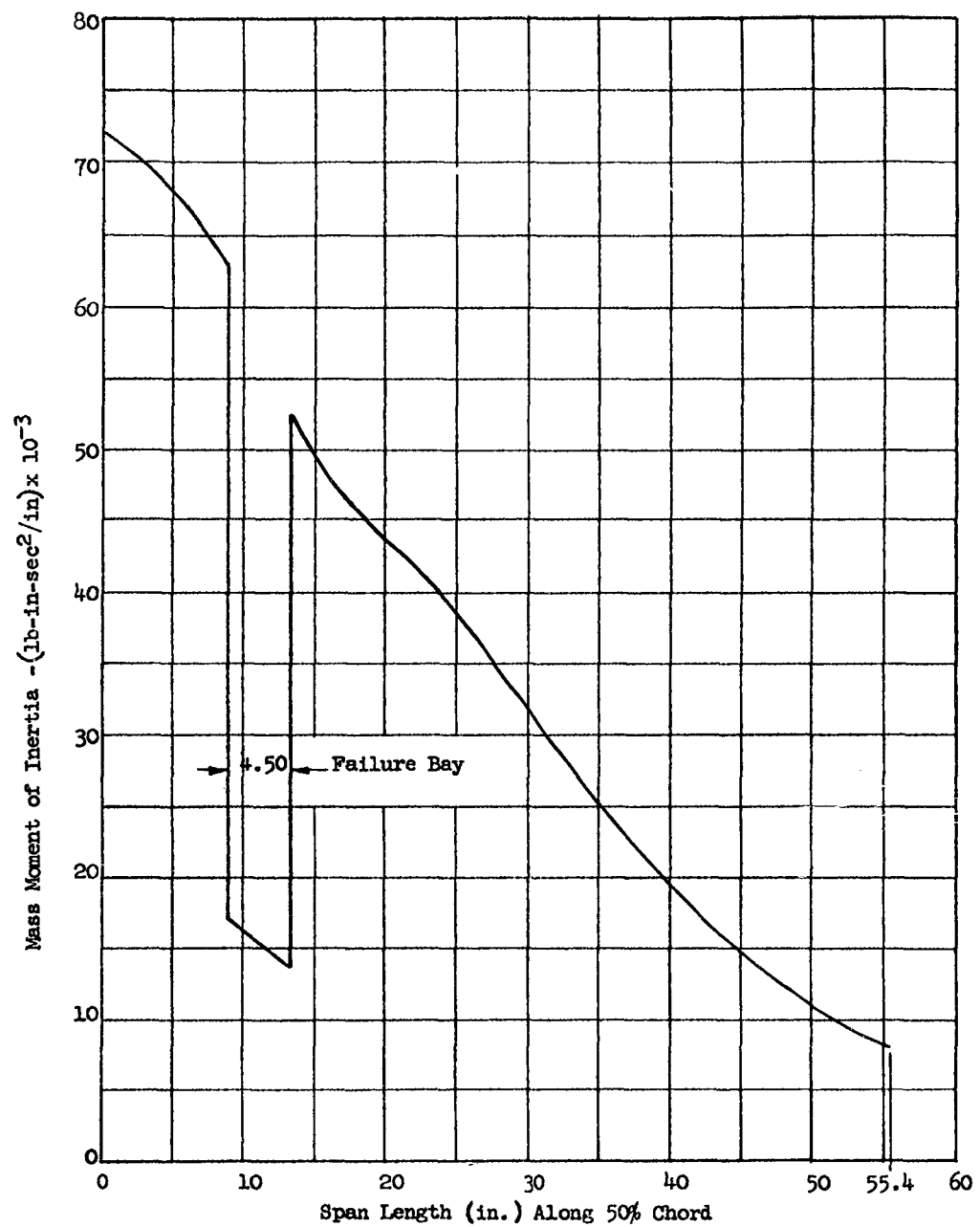


Fig. 3.3.3 TORSIONAL MASS MOMENT OF INERTIA OF STRUCTURAL SPECIMEN ABOUT 50% CHORDLINE-FINAL

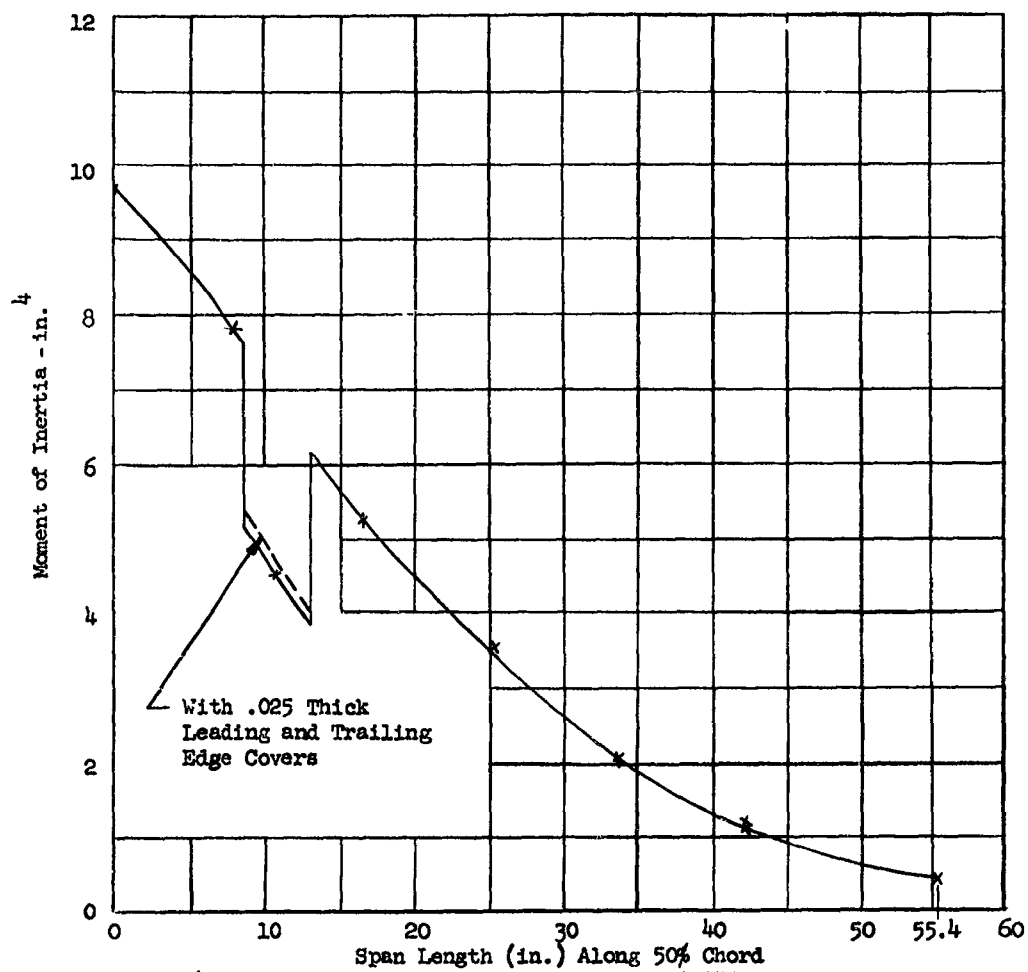
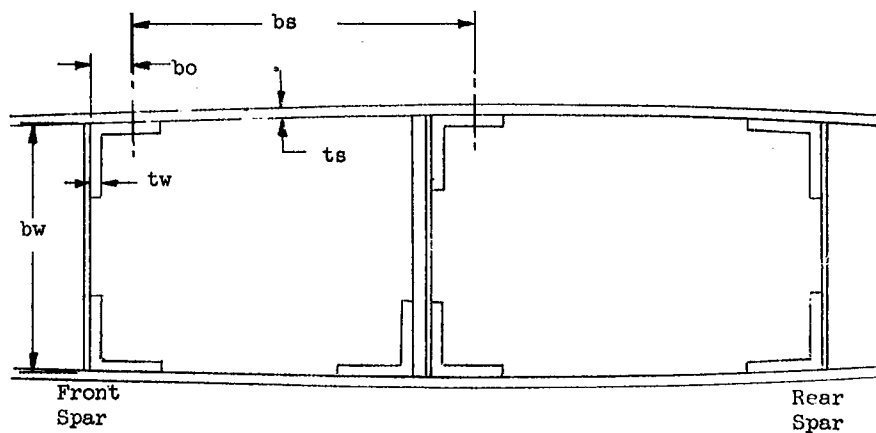


Fig. 3.3.4

MOMENT OF INERTIA OF STRUCTURAL SPECIMEN  
NORMAL TO THE 50% CHORDLINE-FINAL

Because of relative spar cap thicknesses, the wrinkling mode of failure will be initiated at the front spar. As a consequence, the geometric parameters used in the strength computations will be those for the forward spar. Even if the parameter  $\frac{fts}{t_{ws}}$  is  $< .180$ , indicating

a local buckling mode of failure, the ultimate strength will still be computed on the basis of a wrinkling mode of failure which will always give conservative results. This is done to avoid the tedious calculations involved in determining a local mode of failure.



at W.L. 7.5

$$\beta = \frac{b_w/t_w}{b_s/t_s} = \frac{2.90/.094}{4.50/.125} = 0.860$$

$$P/d = \frac{.875}{.188} = 4.65$$

$$b_o/t_w = \frac{.485}{.094} = 5.16$$

From Figure 8 of Reference 13

$$f/t_w = 5.20$$

$$f = .489$$

$$f/b_w = \frac{.489}{2.90} = 0.1685$$

$$\frac{f t_s}{t_w b_s} = \frac{.489 \times .125}{4.50 \times .094} = 0.144 < .180$$

From Reference 15, a local mode of failure is indicated. However, as noted in the previous paragraph, it will be conservative to compute the bending moment capacity based on a wrinkling mode of failure. The skin panel, edge restraint factor can be computed using equation 7 of Reference 13.

$$K_M = \sqrt{\frac{\frac{48}{\pi^4} (3 f/b_w + 1)}{(f/b_w \beta)^3 (3 f/b_w + 4)}}$$

$$K_M = \sqrt{\frac{\frac{48}{\pi^4} (3 \times .1685 + 1)}{(.1685 \times .86)^3 (3 \times .1685 + 4)}}$$

$$K_M = 7.37$$

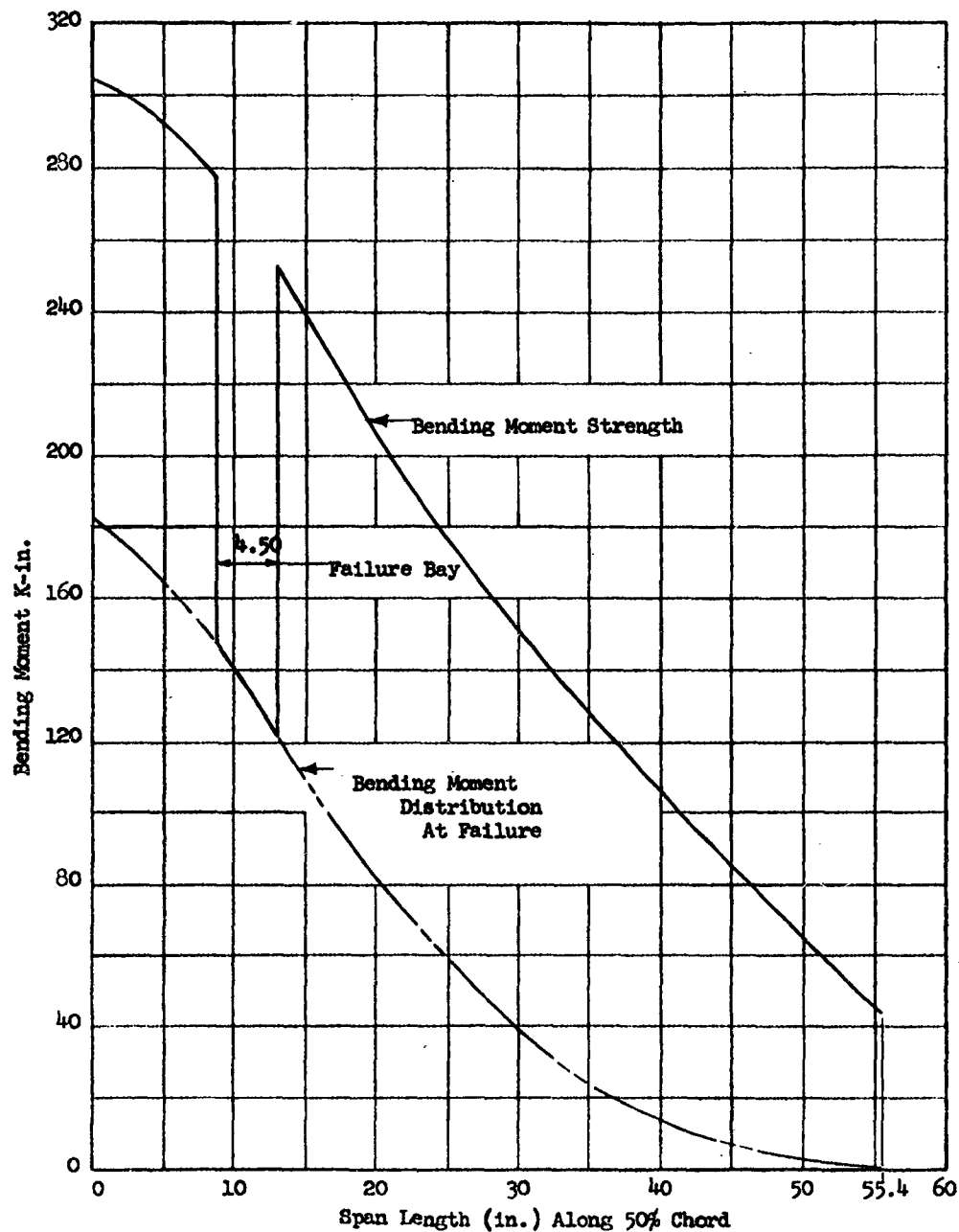


Fig. 3.3.5

BENDING MOMENT STRENGTH AND DISTRIBUTION  
AT FAILURE LOAD FOR STRUCTURAL SPECIMEN-FINAL

Substituting into equation 3, Reference 13

$$\frac{\sigma_m}{\eta} = \frac{K_M \pi^2 E}{12 (1 - \nu)^2} \left( \frac{t_s}{b_s} \right)^2$$

$$\frac{\sigma_m}{\eta} = \frac{7.37 \times 9.86 \times 10.6 \times 10^6}{12 \times .91} \left( \frac{.125}{4.50} \right)^2$$

$$\frac{\sigma_m}{\eta} = 54600 \text{ psi}$$

From Figure 9, Reference 10

$$\sigma_m = 51000 \text{ psi}$$

$$M = \frac{I \sigma_m}{c} = \frac{9.70 \times 51000}{1.63}$$

$$M = 304,000 \text{ in-lb}$$

The bending moment capacity for the structural specimen normal to the 50% chordline is summarized in Figure 3.3.5.

The minimum margin of safety on obtaining a controlled breakline occurs at the root

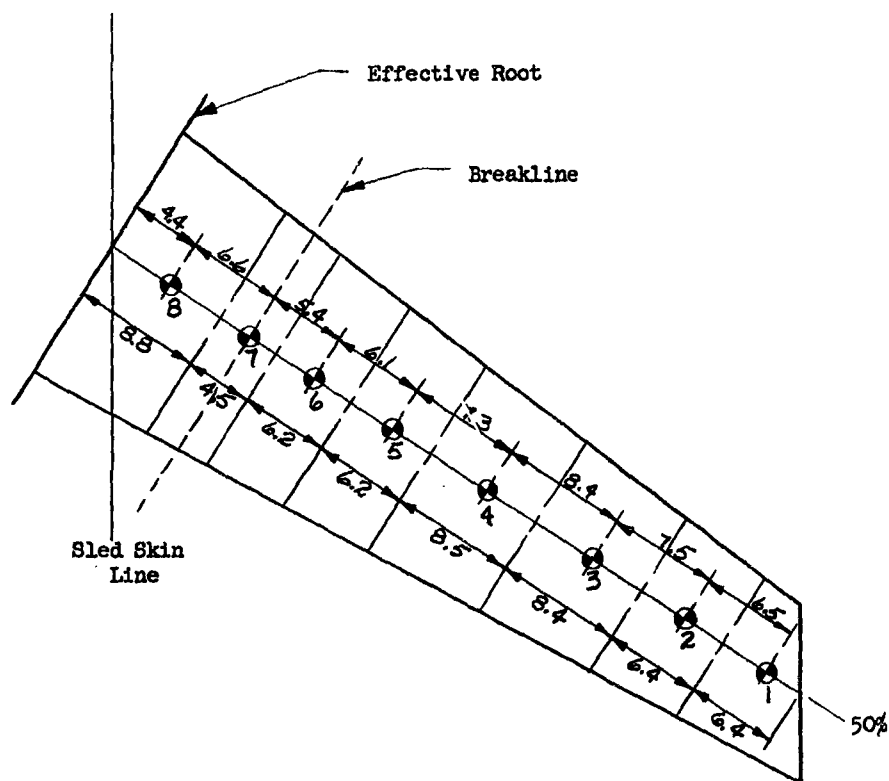
$$M.S. = \frac{304000}{183000} - 1.0 = +.66$$

### 3.3.2.3 BENDING MODES AND NATURAL FREQUENCIES

The natural frequencies, and mode shapes for the first three bending modes of vibration were computed, using the final moment of inertia and mass properties indicated in Figures 3.3.2 and 3.3.4. The vibration modes were determined utilizing the "Myklestad Method" outlined



in Reference 18. The lumped mass distribution for the idealized structural specimen is shown in Figure 3.3.6. The center of gravity of the lumped mass was determined for each individual bay, utilizing the mass distribution given in Figure 3.3.2. The elastic coefficients were computed by assuming a trapezoidal stiffness distribution between lumped masses. These coefficients have been summarized in Table 3.3.1. The orthogonality of the bending vibration modes shown in Figure 3.3.7 have been checked in Table 3.3.2.



Bay No.	Mass $\frac{\text{lb-sec}^2}{\text{in.}}$	Area $\text{in}^2$
1	.00790	159.6
2	.00912	76.6
3	.01489	100.3
4	.01925	94.3
5	.01715	119.0
6	.01963	106.7
7	.00738	73.8
8	.02920	67.7

Fig. 3.3.6 LUMPED MASS DISTRIBUTION FOR IDEALIZED STRUCTURAL SPECIMEN-FINAL

Table 3.3.1 SUMMARY OF LUMPED MASSES AND ELASTIC COEFFICIENTS FOR STRUCTURAL SPECIMEN-FINAL					
N	$M_N$	$L_N$	$V_M \times 10^6$	$V_F \times 10^6$ $d_M \times 10^6$	$d_F \times 10^6$
1	.00790	6.5	.9440	2.794	11.58
2	.00912	7.5	.6349	2.167	10.31
3	.01489	8.4	.4005	1.514	8.068
4	.01925	7.3	.2099	0.7120	3.344
5	.01715	6.1	.1269	0.3724	1.483
6	.01963	5.4	.1077	0.2973	1.062
7	.00738	6.6	.1017	0.3011	1.251
8	.02920	4.4	.04761	0.1028	0.2998

Table 3.3.2 ORTHOGONALITY OF MODES FOR STRUCTURAL SPECIMEN-FINAL										
Bay No. 1	Mass $\frac{\text{lb-sec}^2}{\text{in}}$ MI	Root to Mass C.G. in.	MODE DEFLECTION							
			$\phi_i(1)$	$\phi_i(2)$	$\phi_i(3)$		$m_i \phi_i^{(1)} \phi_i^{(2)}$ $\times 10^{-3}$	$m_i \phi_i^{(1)} \phi_i^{(3)}$ $\times 10^{-3}$	$m_i \phi_i^{(2)} \phi_i^{(3)}$ $\times 10^{-3}$	
1	.00790	52.2	1.00000	1.00000	1.00000		7.9000	7.9000	7.9000	7.9000
2	.00912	45.7	.79131	.24262	-.58083		1.7509	-4.1917	-1.2852	
3	.01489	38.2	.56713	-.36390	-.93562		-3.0730	-7.9009	5.0696	
4	.01925	29.8	.35217	-.59729	.01339		-4.0492	.0908	-.1539	
5	.01715	22.5	.20258	-.50990	.68458		-1.7715	2.3784	-5.9865	
6	.01963	16.4	.10603	-.33409	.74201		-.6954	1.5444	-4.8662	
7	.00783	11.0	.04492	-.16734	.4793		-.0588	.1686	-.6280	
8	.02920	4.4	.00692	-.02963	.1000		-.0060	.0202	-.0865	
					$\Sigma$		-.0070	+.0098	-.0633	

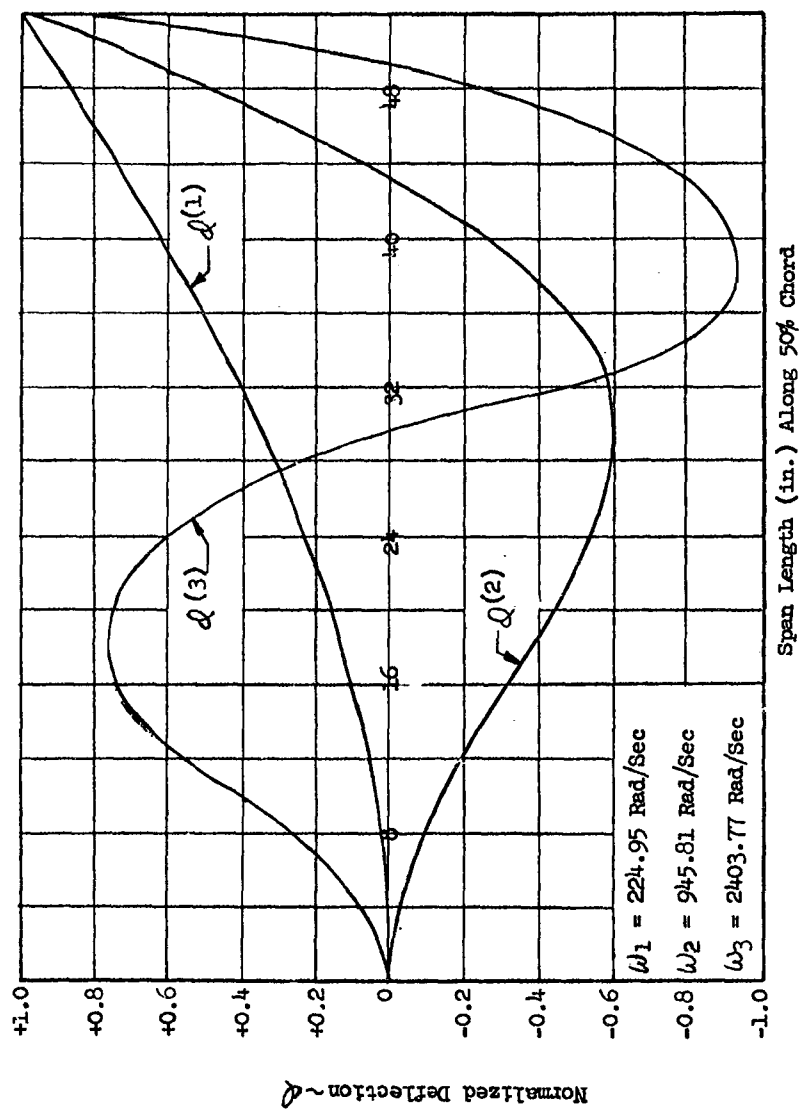


Fig. 3.3.7 BENDING VIBRATION MODES FOR STRUCTURAL SPECIMEN-FINAL

#### 4.0 SPECIMEN LABORATORY TESTS

##### 4.1 AIRLOAD SPECIMEN

##### 4.1.1 DYNAMIC TESTS

###### 1. Description of Test

The purpose of the vibration test was to determine the first five or six natural frequencies, mode shapes and node line locations of the wing mounted in the sled forebody. In order to measure the vibration characteristics of this specimen, an electromagnetic shaker was attached to the tip of the specimen on the 25% chordline as shown in Figure 4.1.1. The shaker was powered by a 100 watt amplifier and frequency oscillator. The shaker has its own signal generator which was monitored by an MB vibration meter to read displacement. A second hand probe was also monitored by the vibration meter to read displacement. A second hand probe was also monitored by the vibration meter to read displacement at any of the 16 locations shown on Figure 4.1.2. The signals of both probes were fed to a phase scope which determined the relative signs of the displacement signals.

A frequency survey was made from 0-500 cps with a constant shaker force. From this survey the resonant frequencies were obtained. The model structural damping coefficients were also approximated from this survey. The mode shapes of each resonant frequency were then measured at the 16 locations shown in Figure 4.1.2. Node line locations could not be obtained visually, as it was impossible to shake the model with sufficient amplitude to obtain a distinguishable pattern of filings. However, node lines may be extrapolated from the mode shape data.

###### 2. Results of Test

The frequency survey data recorded during the test is presented in Table 4.1.1 and plotted on log-log paper in Figure 4.1.3. At each natural frequency, the wing displacement was measured at the locations shown in Figure 4.1.2, and tabulated in Table 4.1.2. Model structural damping coefficients were approximated from the response data plotted in



Fig. 4.1.1 SHAKER ARRANGEMENT FOR MODEL (6L)

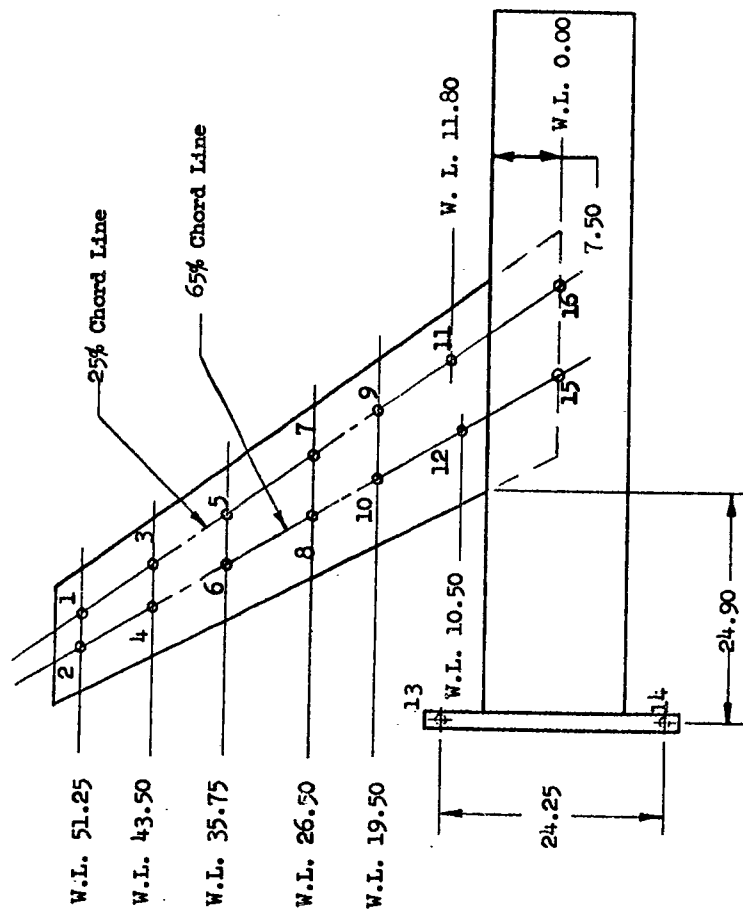


Fig. 4.1.2 TENSION PAD LOCATIONS FOR INFLUENCE COEFFICIENT TEST  
AND PROBE POINT LOCATIONS FOR DYNAMIC TEST  
(AIRLOAD SPECIMEN)



TABLE 4.1.1 FREQUENCY SURVEY DATA FOR AIRLOAD SPECIMEN					
Freq. (CPS)	Ampl. (in.)	Freq. (CPS)	Ampl. (in.)	Freq. (CPS)	Ampl. (in.)
5.0	.010	100	.0038	300	.0001
9.2	.028	105	.014	320	.00021
10.0	.0024	110	.0069	340	.00067
15.0	.010	120	.0019	360	.00059
20.0	.010	130	.0010	365	.00060
25.0	.033	140	.00065	372	.00160
25.8	.081	150	.00040	380	.00018
28.0	.051	160	.00013	400	.00044
30.0	.027	170	.00019	410	.00072
35.0	.010	180	.00013	418	.0012
40.0	.0030	190	.00055	430	.00027
43.0	.013	200	.0012	450	.00064
45.0	.010	206	.0090	470	.0012
50.0	.0041	210	.0011	480	.00013
55.0	.0026	215	.00024	500	.00034
60.0	.0014	220	.00080		
65.0	.0015	227	.00340		
70.0	.0010	230	.0015		
75.0	.00060	240	.00043		
80	.0018	249	.0021		
85	.0010	260	.00052		
90	.0010	270	.00059		
95	.0034	280	.00016		
97	.010	290	.0001		

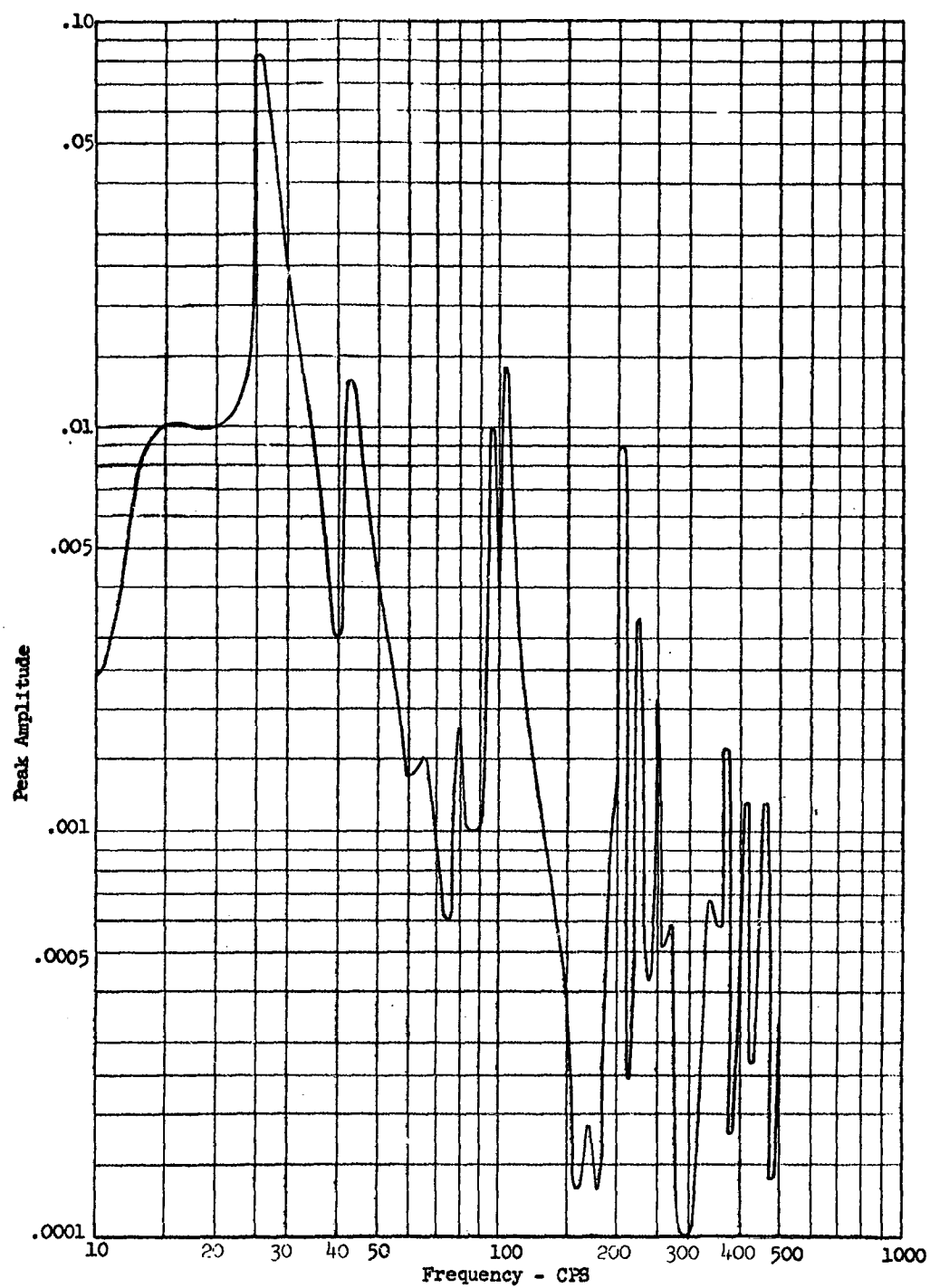
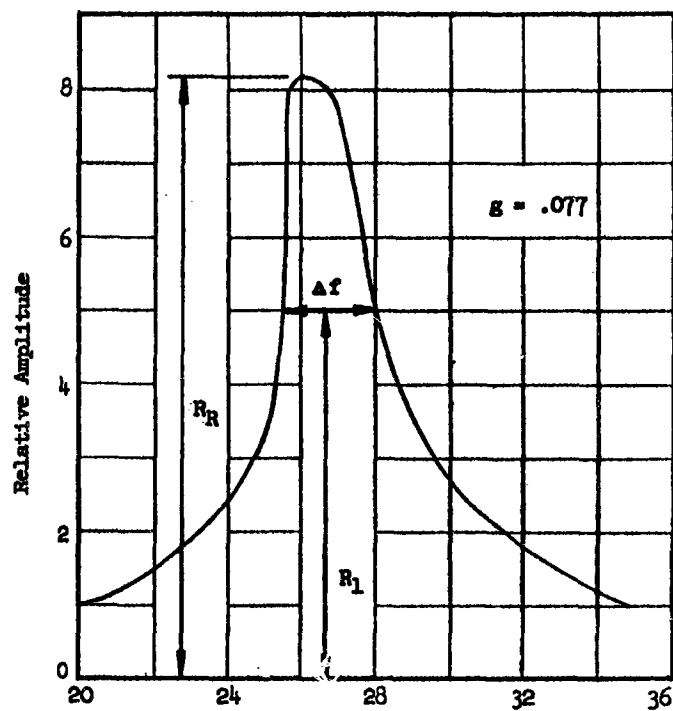


Fig. 4.1.3 FREQUENCY RESPONSE CURVE FOR AIRLOAD SPECIMEN



NOTE:

$$g = \frac{\Delta f / f_n}{\sqrt{\left(\frac{R_R}{R_1}\right)^2 - 1}}$$

Fig. 4.1.4 STRUCTURAL DAMPING COEFFICIENT AIRLOAD SPECIMEN  
 $f_n = 25.8$  CPS

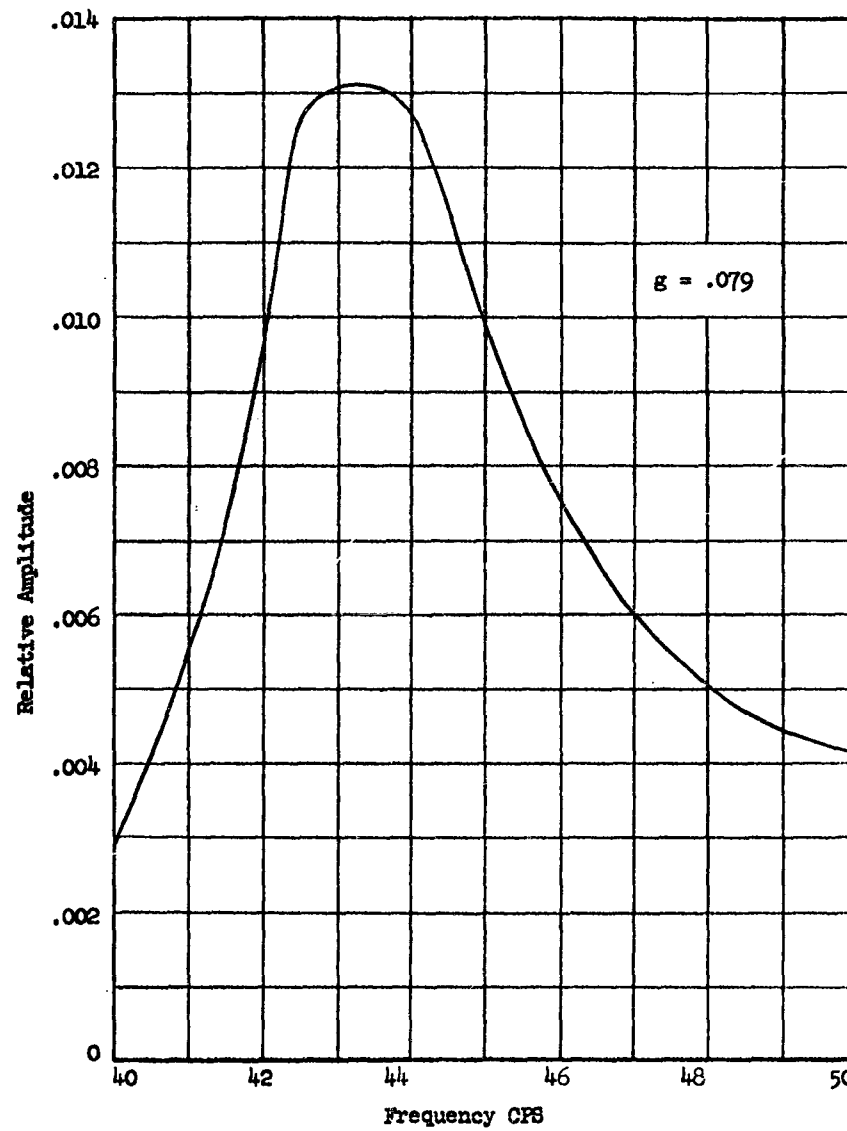


Fig. 4.1.5 STRUCTURAL DAMPING COEFFICIENT AIRLOAD SPECIMEN  $f_n = 43.8$  CPS

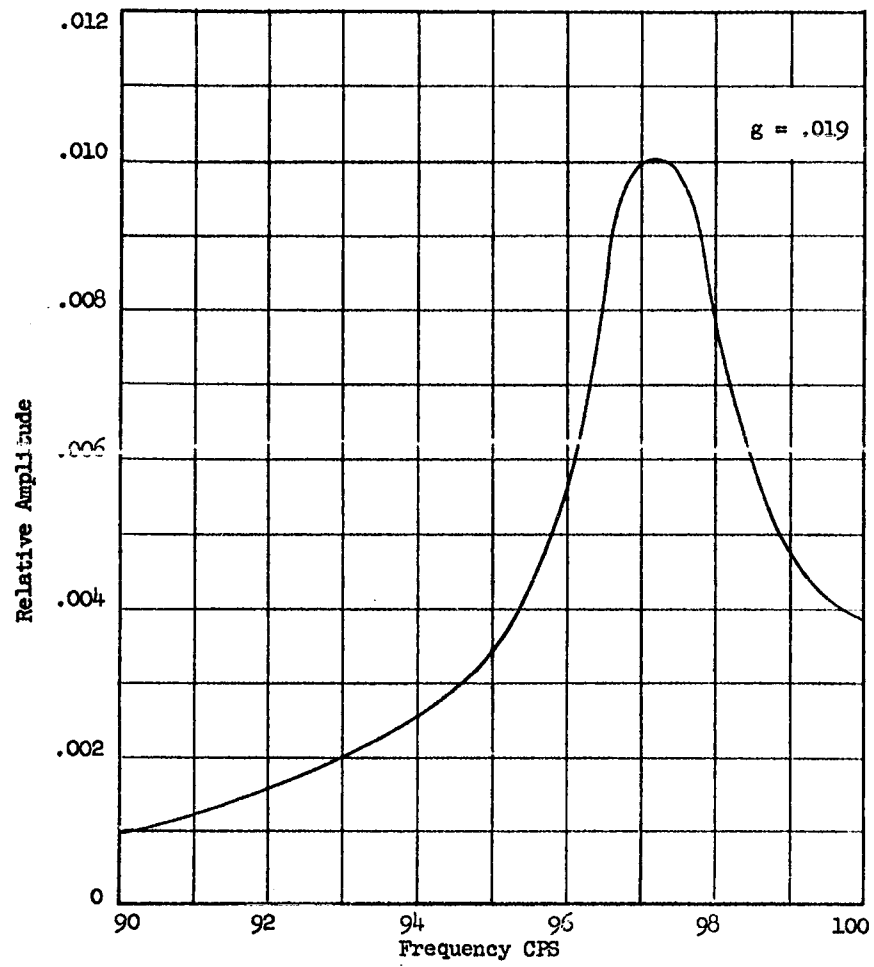


Fig. 4.1.6 STRUCTURAL DAMPING COEFFICIENT AIRLOAD SPECIMEN  $f_n = 97.0$  CPS

Table 4.1.2 MODE SHAPE DATA AT RESONANT FREQUENCIES - 6L								
Frequencies - CPS								
Probe Point	25.8		43.8		103		97	
	Ampl.	Phase	Ampl.	Phase	Ampl.	Phase	Ampl.	Phase
1	.052	0	.0053	0	.0080	0	.0053	0
2	.057	0	.0068	0	.0100	0	.0079	0
3	.040	0	.0042	0	.00049	$\pi/2$	.00057	$\pi/2$
4	.044	0	.0050	0	.0031	0	.0021	0
5	.028	0	.0025	0	.0043	$\pi$	.0027	$\pi$
6	.034	0	.0034	0	.0024	$\pi$	.0014	$\pi$
7	.019	0	.0010	$\pi$	.0051	$\pi$	.0036	$\pi$
8	.022	0	.0014	$\pi$	.0048	$\pi$	.0032	$\pi$
9	.013	0	.00072	$\pi/2$	.0037	$\pi$	.0030	$\pi$
10	.015	0	.00090	$\pi/2$	.0041	$\pi$	.0029	$\pi$
11	.008	0	.00096	$\pi$	.00086	$\pi$	.0013	$\pi$
12	.010	0	.00100	$\pi$	.0012	$\pi$	.0014	$\pi$
15	.011	0	.0013	$\pi$	.00075	0	.00018	$\pi$
16	.005	0	.0015	$\pi$	.0012	0	.00015	$\pi$

Table 4.1.2 Cont. MODE SHAPE DATA AT RESONANT FREQUENCIES - 6L								
Frequencies - CPS								
Probe Point	206		227		250		372	
	Ampl.	Phase	Ampl.	Phase	Ampl.	Phase	Ampl.	Phase
1	.0028	0	.0011	0	.0011	0	.00032	0
2	.0049	0	.0014	0	.00027	$\pi/2$	.00037	0
3	.0019	$\pi$	.00067	$\pi$	.00055	0	.00035	$\pi$
4	.0015	$\pi$	.0010	$\pi$	.00082	$\pi$	.00080	$\pi$
5	.0024	$\pi$	.00063	$\pi$	.00033	0	.00015	$\pi/2$
6	.0035	$\pi$	.0015	$\pi$	.010	$\pi$	.00049	$\pi$
7	.00031	0	.00063	0	.00056	0	.00033	0
8	.0011	$\pi$	.00045	$\pi$	.00057	$\pi$	.00032	0
9	.0016	0	.0010	0	.00054	0	.00012	$\pi/2$
10	.00069	0	.00037	0	.00021	$\pi$	.00027	0
11	.0017	0	.00070	0	.00022	0	.00039	$\pi$
12	.0017	0	.00059	0	.00013	$\pi$	.00020	$\pi$
15	.00025	0	0		.00018	$\pi$	.00010	0
16	.00015	$\pi$	.00010	$\pi$	.00012	$\pi$	.00010	$\pi$

Table 4.1.2 Cont. MODE SHAPE DATA AT RESONANT FREQUENCIES - 6 L

Frequencies CPS								
Probe	418		470					
Point	Ampl.	Phase	Ampl.	Phase				
1	.00066	0	.00015	$\pi$				
2	.00031	$\pi$	.00028	0				
3	.00052	0	.00028	$\pi$				
4	.00047	$\pi$	.00052	$\pi$				
5	.00010	0	.00028	0				
6	.00027	$\pi$	.00016	$\pi/2$				
7	.00010	$\pi$	.00017	$\pi/2$				
8	.00023	0	.00035	0				
9	.00023	$\pi$	.00012	$\pi$				
10	.00026	0	.00012	$\pi$				
11	.00028	$\pi$	.00013	$\pi$				
12	.00013	0	.00015	$\pi$				
15	0		.00015	0				
16	.00022	$\pi$	.00015	0				



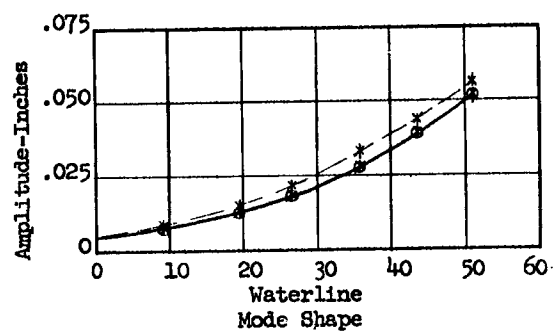
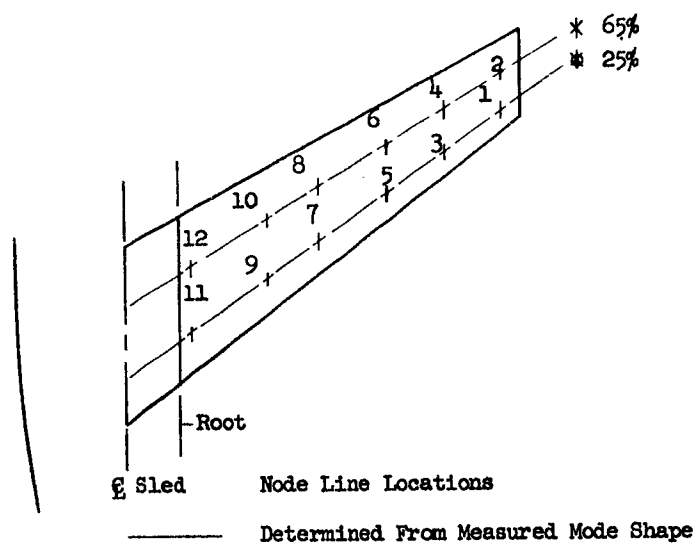
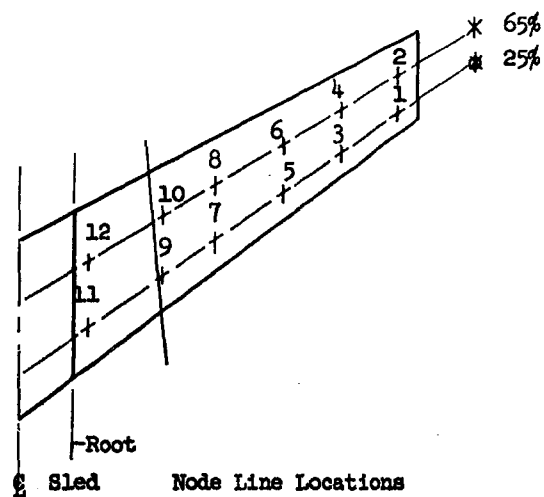


Fig. 4.1.7      FIRST MODE  $f_n = 25.8$  CFS



— Determined from Measured Mode Shape

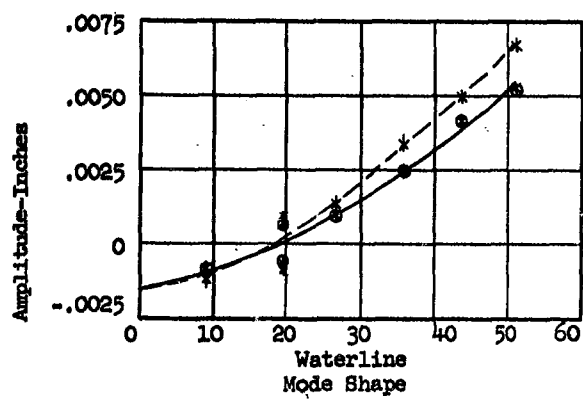
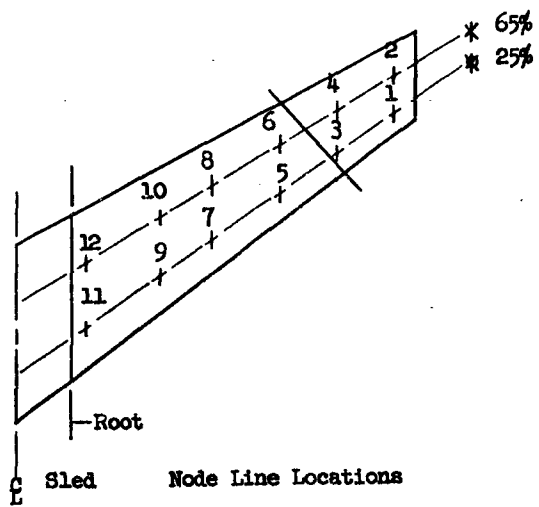


Fig. 4.1.8 SECOND MODE  $f_n = 43.8$  CPS



Sled Node Line Locations  
 — Determined From Measured Mode Shape

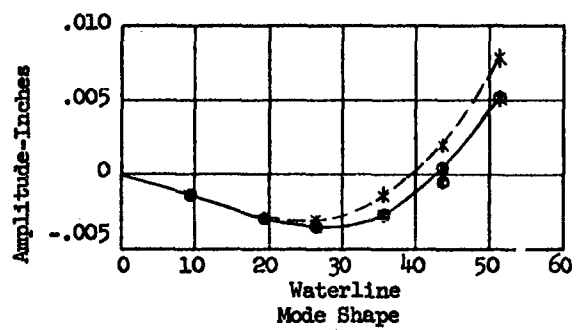
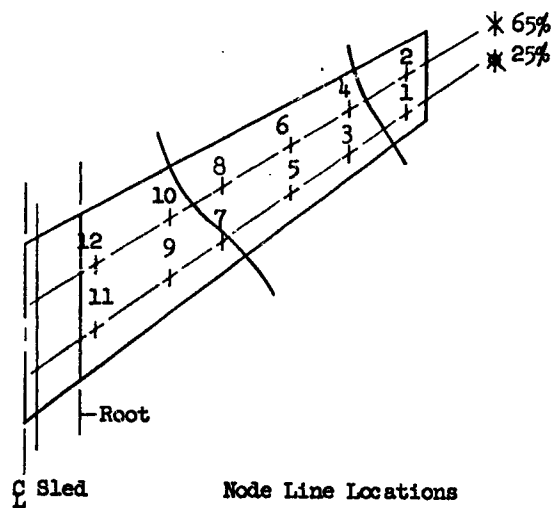


Fig. 4.1.9 THIRD MODE  $f_n = 97.0$  CPS



— Determined from Measured Mode Shape

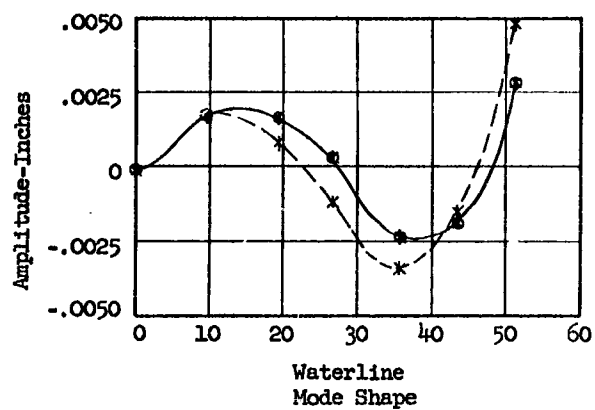


Fig. 4.1.10 FOURTH MODE  $f_n = 206$  CPS

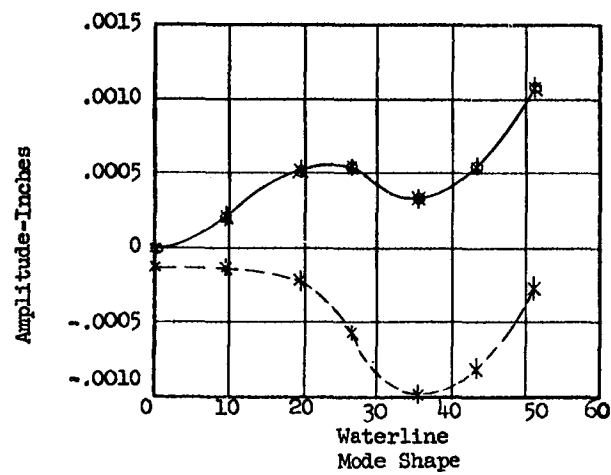
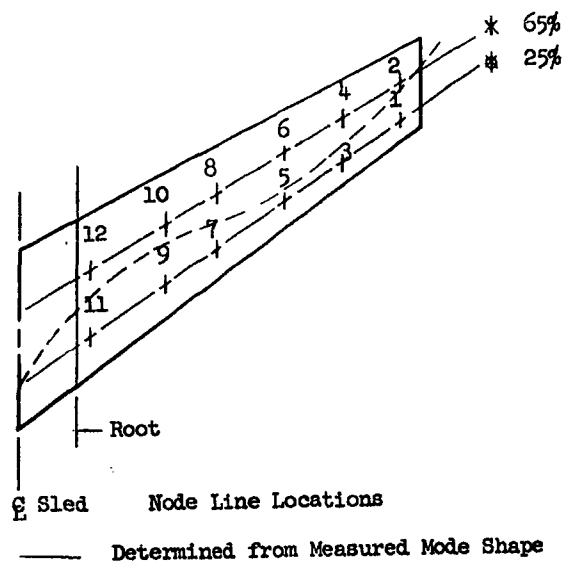


Fig. 4.1.11 FIFTH MODE  $f_n = 250$  CPS

Figures 4.1.4 through 4.1.6. The mode shapes and mode line locations have been summarized in Figures 4.1.7 through 4.1.11.

Since it is impossible to excite pure mode shapes even with several shakers of variable force input, the measured mode shape displacements are undoubtedly contributed to by vibrations of several natural frequencies. The shape of the probe signal was observed for each reading, and in some cases the extraneous frequency contributions were of such a magnitude that the measured mode shapes should not be used for correlation purposes.

It would appear that the resonant frequency observed at 43.8 cps was largely due to the flexibility of the specimen mount and test frame as evidenced by the relatively large displacements at the root.

#### 4.1.2 INFLUENCE COEFFICIENT TEST

##### 1. Description of Test

The elastic behavior of the airload wing and its sled forebody support structure was described at six points along the 25% chordline, and six points along the 65% chordline as was the case for the structural model. The spanwise locations of these points are given in Figure 4.1.2. Deflections were measured at points 13 and 14 to indicate the flexibility of the sled and test stand. The static test set up is shown in Figures 4.1.12 and 4.1.13.

The loads were applied to the specimen through tension pads which were bonded to the compression side of the wing. Tension pads 1 through 8 were 4 inches square. The peak load applied at points 1 - 8 was 800 lbs. with the exception of point 4 where the peak load was 600 lbs. Tension pads 9 through 12 were 5 inches square and the peak load applied at these points was 1200 lbs. The load and unload portions of the load deflection curve were defined at 7 increments of load as indicated in Table 4.1.3. The load was applied by a chain hoist through a linkage shown in Figure 4.1.13 and read on a Dillon force gage having a 1250 lbs. capacity. The estimated accuracy of the load readings is  $\pm 10$  lbs.

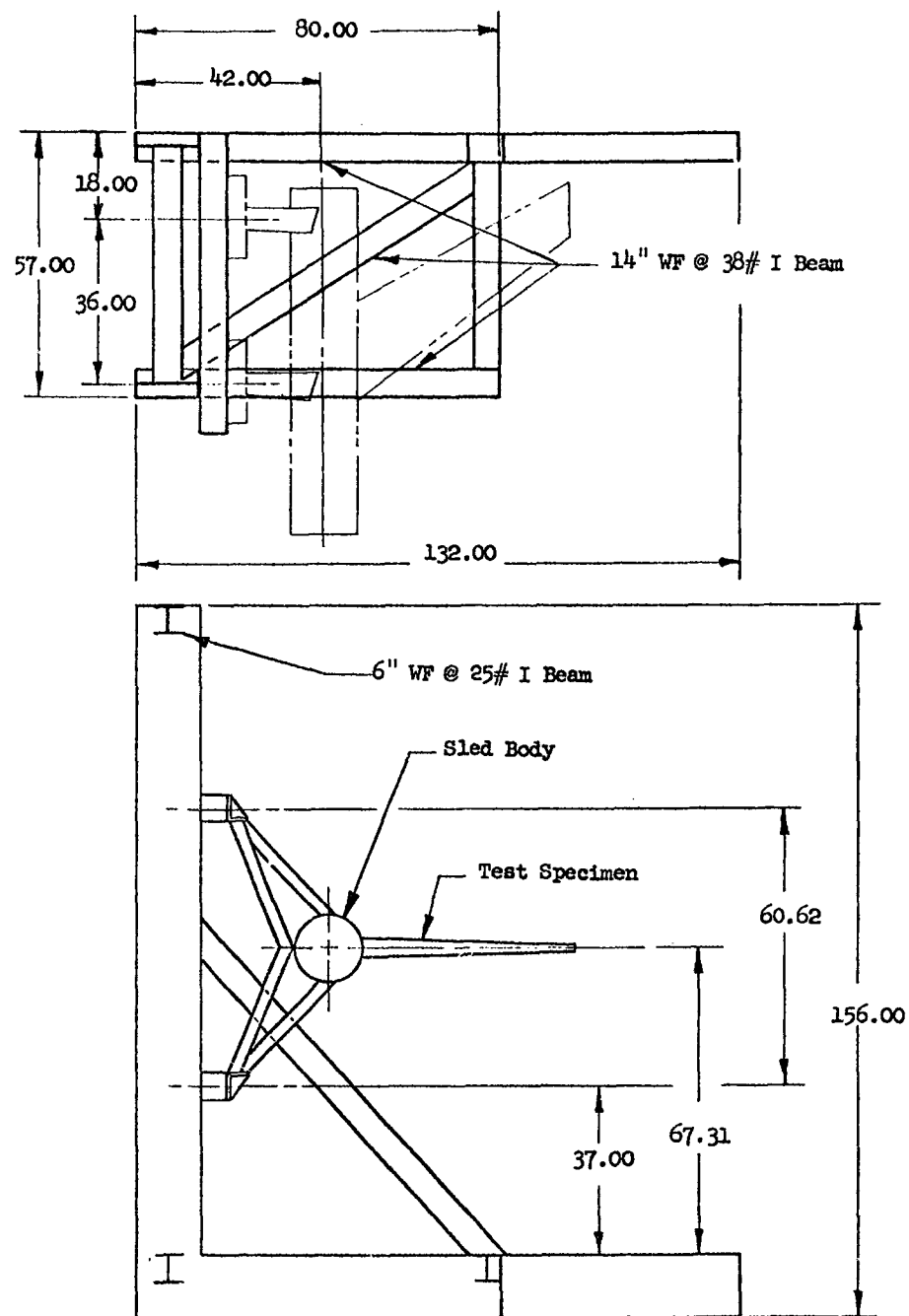


Fig. 4.1.12

TEST FIXTURE



Fig. 4.1.1.13 STATIC TEST SET UP FOR MODEL (6L)



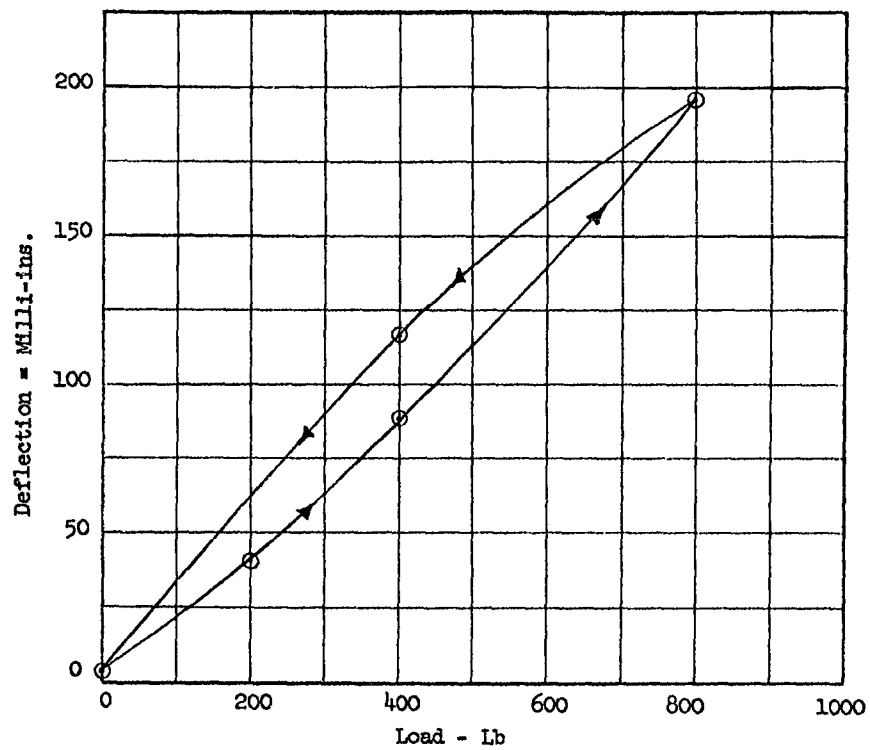


Fig. 4.1.14 LOAD DEFLECTION PLOT SHOWING HYSTERESIS - AIRLOAD SPECIMEN

Note: Load applied at Point 1 and deflection measured at Point 1.

Table 4.1.3 REDUCED LOAD DEFLECTION DATA TAKEN DURING INFLUENCE COEFFICIENT TEST IN. X 10 <sup>-3</sup>														
Defl. Point	Load lbs							Load lbs						
	0	200	400	600	800	400	0	0	200	400	600	800	400	0
1	0	40	88	146	196	116	3	0	47	100	161	221	129	0
2	0	42	91	146	202	119	3	0	51	109	175	241	142	0
3	0	29	63	104	141	84	3	0	34	71	116	156	93	0
4	0	32	67	110	150	89	3	0	36	77	124	169	101	0
5	0	20	43	71	96	59	2	0	23	48	78	107	65	0
6	0	21	45	76	104	63	2	0	23	51	83	113	68	0
7	0	11	25	42	57	35	1	0	13	27	46	62	38	0
8	0	12	27	45	62	38	1	0	13	29	48	66	41	-1
9	0	7	16	28	38	23	0	0	8	18	30	41	25	-1
10	0	9	19	31	42	26	1	0	9	19	32	43	27	-1
11	0	3	9	14	20	12	1	0	5	10	16	21	13	0
12	0	5	10	16	21	13	1	0	4	9	15	21	13	-1
13	0	1	3	5	7	3	0	0	3	5	7	9	5	0
14	0	1	2	3	3	2	0	0	1	2	3	5	2	0
Load Point 1							Load Point 2							

Table 4.1.3 Cont. REDUCED LOAD DEFLECTION DATA TAKEN DURING INFLUENCE COEFFICIENT TEST IN. X 10-3														
Defl. Point	Load lbs							Load lbs						
	0	200	400	600	800	400	0	0	200	400	600	400	0	
1	0	30	62	103	142	84	1	0	35	73	119	84	0	
2	0	30	63	103	143	84	1	0	36	74	122	86	0	
3	0	23	48	78	111	65	1	0	27	55	90	64	0	
4	0	24	50	80	114	68	1	0	28	57	95	67	0	
5	0	17	35	57	80	48	1	0	19	38	64	46	0	
6	0	17	36	59	83	50	1	0	19	40	68	48	0	
7	0	9	20	34	48	29	0	0	11	23	38	28	0	
8	0	11	23	38	53	32	1	0	12	25	41	29	0	
9	0	7	14	24	34	21	0	0	8	16	27	19	1	
10	0	7	15	26	36	22	0	0	8	17	27	20	0	
11	0	4	8	13	18	11	0	0	5	10	15	11	1	
12	0	5	9	15	20	12	0	0	5	9	14	10	0	
13	0	1	3	4	6	3	0	0	2	4	6	4	0	
14	0	1	2	3	3	2	0	0	1	2	3	2	0	
Load Point 3							Load Point 4							

Table 4.1.3 Cont. REDUCED LOAD DEFLECTION DATA TAKEN DURING INFLUENCE COEFFICIENT TEST IN X 10 <sup>-3</sup>																
Defl. Point	Load lbs						Load lbs						Load Point			
	0	200	400	600	800	400	0	400	600	800	400	200	0	200	400	600
1	0	19	41	67	95	56	1	56	81	115	51	26	0	26	68	1
2	0	19	41	67	95	57	1	57	82	116	52	25	0	25	68	1
3	0	15	32	53	76	45	0	45	64	91	40	19	0	19	54	0
4	0	16	34	55	78	47	1	47	66	93	41	19	0	19	55	0
5	0	12	25	41	60	36	0	36	49	69	30	14	0	14	41	1
6	0	11	25	42	61	37	0	37	50	71	31	14	0	14	43	0
7	0	7	16	26	39	23	0	23	30	43	18	9	0	9	26	0
8	0	8	17	29	42	25	0	25	32	45	19	9	0	9	28	0
9	0	5	11	19	28	17	0	17	21	30	13	6	0	6	18	0
10	0	6	12	20	29	18	0	18	22	31	14	6	0	6	20	0
11	0	3	6	11	15	9	0	9	12	17	8	4	0	4	10	0
12	0	4	7	12	17	10	0	10	12	17	7	3	0	3	10	0
13	0	1	3	4	5	3	0	3	5	7	3	1	0	1	3	0
14	0	1	2	2	3	2	1	2	3	4	2	1	0	1	2	0

Table 4.1.3 Cont. REDUCED LOAD DEFLECTION DATA TAKEN DURING INFLUENCE COEFFICIENT TEST IN. X 10 <sup>-3</sup>														
Defl. Point	Load Lbs							Load Lbs						
	0	200	400	600	800	400	0	0	200	400	600	800	400	0
1	0	12	24	38	54	30	1	0	15	29	47	66	38	0
2	0	12	23	37	53	29	1	0	14	29	46	64	36	0
3	0	10	20	32	45	25	1	0	12	25	40	55	31	0
4	0	9	20	32	45	25	0	0	11	23	37	52	30	0
5	0	8	16	25	36	20	0	0	9	20	31	43	24	0
6	0	8	16	26	37	20	0	0	9	18	29	42	24	0
7	0	6	12	19	27	15	0	0	6	13	21	30	17	0
8	0	7	13	20	28	16	0	0	6	14	21	30	17	0
9	0	4	9	14	20	11	0	0	5	10	16	22	13	0
10	0	6	10	15	22	12	0	0	4	10	16	22	13	0
11	0	3	5	8	12	6	0	0	3	6	9	13	7	0
12	0	3	6	10	14	7	0	0	2	6	9	12	7	0
13	0	1	2	3	4	2	0	0	1	2	4	5	2	0
14	0	0	0	1	1	0	0	0	1	1	2	3	1	0
Load Point 7							Load Point 8							

Table 4.1.3 Cont. REDUCED LOAD DEFLECTION DATA TAKEN DURING INFLUENCE COEFFICIENT TEST IN. X 10 <sup>-3</sup>																				
Defl Point	Load Lbs							Load Lbs							Load Lbs					
	0	300	600	900	1200	600		0	300	600	900	1200	600		0	300	600	900	1200	600
1	0	10	21	34	47	28	1	0	15	30	46	65	36	-1	0	-1	0	-1	0	
2	0	10	21	34	48	28	0	0	14	28	43	61	34	-1	-1	-1	-1	-1	-1	
3	0	9	19	29	41	24	0	0	13	26	39	55	31	-1	-1	-1	-1	-1	-1	
4	0	9	18	31	43	25	1	0	11	24	37	52	29	-1	-1	-1	-1	-1	-1	
5	0	8	15	25	34	21	1	0	10	21	32	45	25	-1	-1	-1	-1	-1	-1	
6	0	7	14	24	35	20	0	0	9	19	29	42	23	-1	-1	-1	-1	-1	-1	
7	0	5	11	19	26	16	0	0	7	15	23	33	18	-1	-1	-1	-1	-1	-1	
8	0	6	12	21	29	18	1	0	8	16	23	33	19	-1	-1	-1	-1	-1	-1	
9	0	5	9	15	21	12	0	0	6	12	18	26	14	0	0	0	0	0	0	
10	0	5	10	17	24	15	0	0	6	12	18	25	14	-1	-1	-1	-1	-1	-1	
11	0	3	7	11	15	8	0	0	4	8	12	17	9	-1	-1	-1	-1	-1	-1	
12	0	4	8	13	17	10	0	0	4	8	12	16	9	-1	-1	-1	-1	-1	-1	
13	0	1	2	3	4	2	0	0	2	4	6	8	4	0	0	0	0	0	0	
14	0	0	0	0	0	0	0	0	1	2	3	4	2	0	0	0	0	0	0	
	Load Point 9							Load Point 10							Load Point 10					

Table 4.1.3 Cont. REDUCED LOAD DEFLECTION DATA TAKEN DURING INFLUENCE COEFFICIENT TEST IN. X 10 <sup>-3</sup>														
Defl. Point	Load Lbs						Load Lbs							
	0	300	500	900	1200	600	0	0	300	600	900	1200	600	0
1	0		13	19	25	14	2	0	10	17	25	33	18	0
2	0	7	13	20	26	14	2	0	8	15	22	29	16	0
3	0	6	11	17	22	12	1	0	8	14	21	28	15	0
4	0	7	12	18	23	13	2	0	7	12	18	25	13	0
5	0	5	10	15	20	11	1	0	6	12	18	24	13	0
6	0	6	10	16	20	12	2	0	6	11	16	21	11	0
7	0	5	8	12	16	9	1	0	5	10	15	20	10	0
8	0	5	9	13	18	10	1	0	4	9	13	18	9	-1
9	0	4	7	11	14 <sup>e</sup>	8	1	0	5	9	13	17	9	0
10	0	4	8	12	16	10	1	0	4	7	11	15	8	0
11	0	3	5	9	14	6	1	0	4	7	10	13	7	0
12	0	4	7	11	14	8	1	0	4	6	9	12	7	0
13	0	1	2	3	4	2	0	0	2	3	5	7	3	0
14	0	0	0	0	0	0	0	0	1	1	2	3	2	0
Load Point 11							Load Point 12							

Table 4.1.4 SUMMARY OF INFLUENCE COEFFICIENTS - AIRLOAD SPECIMEN 6L												
Gage Point	Load Point in/lb x 10 <sup>-6</sup>											
	1	2	3	4	5	6	7	8	9	10	11	12
1	245.0	274.0	177.0	197.0	118.0	142.0	67.0	82.4	39.0	54.2	21.2	28.1
2	252.0	296.0	178.0	202.0	118.0	139.0	66.0	79.8	39.9	50.7	21.9	24.6
3	176.0	195.0	139.0	150.0	94.7	113.5	56.2	68.6	34.0	45.8	18.9	23.5
4	188.0	210.0	142.0	158.0	97.5	116.5	56.0	65.0	35.8	43.0	19.7	20.9
5	119.0	134.0	104.0	106.0	75.0	86.0	45.0	53.8	28.1	37.5	16.5	20.1
6	129.0	140.0	102.5	113.0	76.3	88.5	46.1	52.6	29.0	34.7	17.2	17.8
7	71.0	77.4	60.0	63.0	48.7	53.6	33.6	37.4	21.6	27.5	13.3	16.8
8	77.0	82.2	66.2	67.8	52.3	56.2	35.0	37.4	24.3	27.5	15.2	14.9
9	47.2	51.5	42.0	44.4	35.0	37.5	25.0	27.5	17.5	21.6	12.1	14.4
10	52.2	53.8	45.0	45.0	36.0	38.8	27.5	27.4	21.9	20.8	13.3	12.4
11	25.0	26.4	22.0	25.2	18.5	21.1	15.0	16.4	12.5	14.0	10.0	11.0
12	26.7	26.0	24.7	23.8	20.0	21.1	17.2	15.1	15.7	13.4	12.0	9.8



The deflection measurements were made by the same dial gage arrangement used for the structural specimen.

## 2. Results of Test

The load deflection data taken during the test is presented in Table 4.1.3. The influence coefficients were summarized from this data in Table 4.1.4.

The variations from symmetry in this matrix are attributable to load deflection hysteresis which is evident in Figure 4.1.14. Undoubtedly, this hysteresis is due to non-linear slippage in the fasteners and root support as was the case with the structural specimen. If the magnitude of this non-linearity had been foreknown, a different loading arrangement with greater load capacity would have been used.

### 4.1.3 CALIBRATION OF ELASTIC STRAIN GAGES

#### 1. Description of Test

The purpose of this test was to calibrate four elastic torsion bridges and four elastic bending moment bridges. The sign convention relating applied load and bridge output is indicated in Figure 4.1.15. The strain gages which comprise each bridge are identified in Figure 4.1.16 and Table 4.1.5. All of the bridges have been made up from four gages, one in each arm of a four arm bridge. Each of the gages have been mounted on the tension and compression faces of the wing. All of the strain gages used on the airload Model are Baldwin SR-4 Type EBF - 7S + having a gage factor of 2.00.

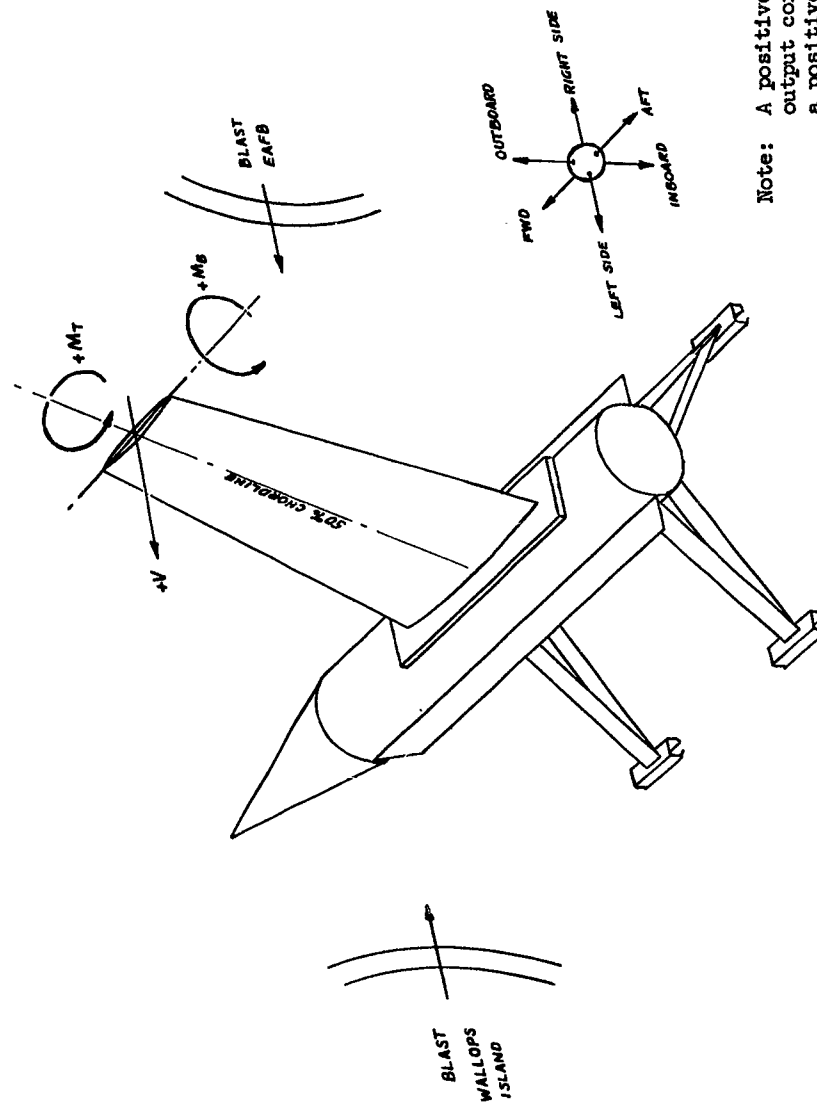
The bridge outputs were recorded for three different load positions whose locations are given in Table 4.1.7. Seven increments of load were applied with a peak load of 3000 lbs. All of the bridges were connected to a Baldwin 20 point switching unit and the strains were read on a Baldwin SR-4 portable strain indicator. Arm AB of each bridge was calibrated with  $22^k$ ,  $22.22^k$ ,  $23.1^k$ ,  $43^k$ ,  $50^k$ , and  $100^k$  resistors, as indicated in Table 4.1.5.

## 2. Results of Test

The load strain data recorded during the test is presented in Table 4.1.6. The sign convention used on the bridge outputs is indicated in Figure 4.1.15.

The load strain data was plotted and analyzed to determine the sensitivity of each bridge to shear, torsion and bending moment. It was apparent that the outputs of the four bending moment bridges were relatively insensitive to shear and torque. The bending moment at a section passing through the bending moment bridge and normal to the 50% chordline has been plotted as a function of indicated strain in Figures 4.1.17 and 4.1.18. It was evident, however, that all four torsional bridges were quite sensitive to both shear and bending moment. As a consequence, it is impractical to plot torsion about the 50% chordline as a function of bridge output without compensating for the effects of shear and bending moment.

The calibration of all eight elastic bridges is given in Figure 4.1.19 with simulated strain plotted as a function of deviation from strain gage resistance.



Note: A positive bridge output corresponds to a positive loading.

FIG. 4.1.15 SIGN CONVENTION FOR LOADING OF WING MODEL

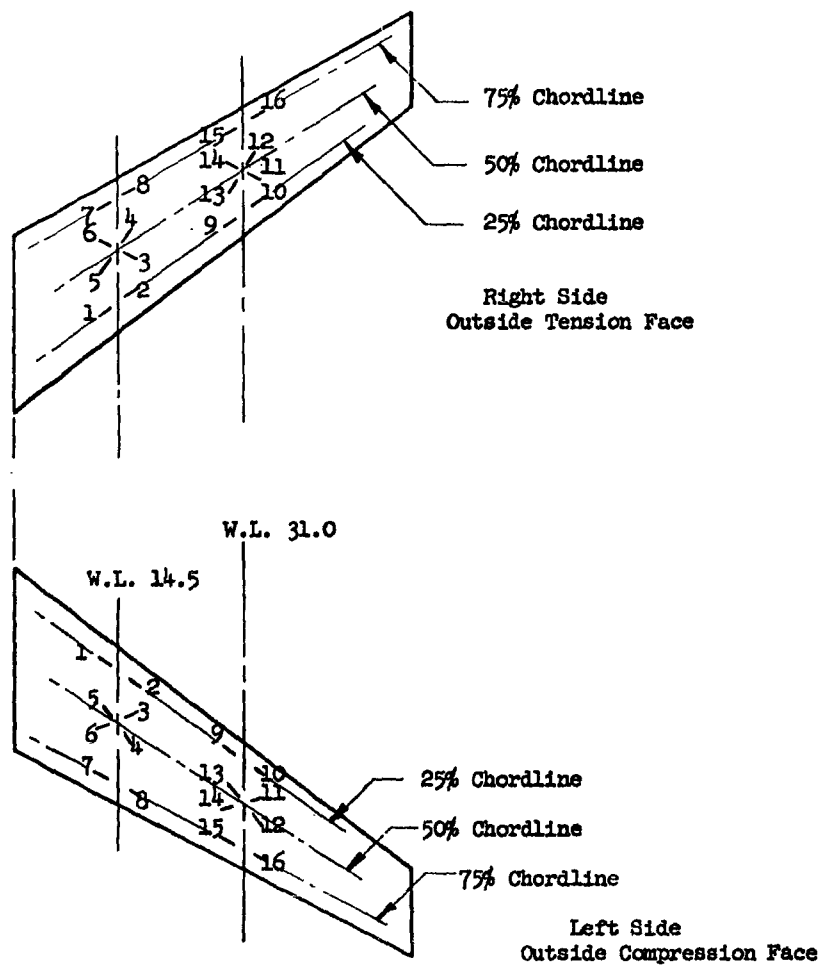


Fig. 4.1.16 AIRLOAD SPECIMEN - STRAIN GAGE LOCATIONS

Table 4.1.5 STRAIN GAGE NUMBER AND LOCATION IN BRIDGE

Bridge Number	Gage No.			
	AD	AB	BC	CD
MAO	16R	16L	15R	15L
Mr'O	10R	10L	9R	9L
MAI	8R	8L	7R	7L
MF'I	2R	2L	1R	1L
TRO	11R	12R	14R	13R
TLO	12R	11L	13L	14L
TRI	3R	4R	6R	5R
TLI	4L	3L	5L	6L

M - Moment

T - Torsion

A - Aft

F - Forward

O - Outboard

I - Inboard

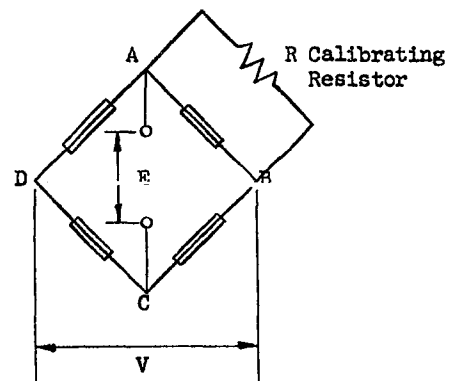


Table 4.1.6 LOAD STRAIN DATA FOR AIRLOAD SPECIMEN

Load Pt. No	Load lbs	Bridge No. Strain ( $\mu$ in/in)							
		MAO	MFO	MAI	MPI	TRO	TLO	TRI	TLI
1	0	0	0	0	0	0	0	0	0
	250	78	93	36	60	-17	-10	-9	-8
	1000	275	369	136	261	-61	-46	-31	-34
	1500	422	561	207	419	-99	-78	-39	-38
	2000	578	760	288	571	-139	-109	-46	-46
	2500	724	954	367	714	-168	-130	-56	-54
	3000	874	1144	442	847	-198	-158	-71	-64
	2000	568	764	295	602	-142	-116	-58	-53
	1000	283	382	150	320	-78	-56	-17	-17
	0	1	4	2	2	0	+2	-3	-5
2	0	0	0	0	0	0	0	0	0
	500	57	93	48	78	-36	-28	-14	-11
	1000	98	173	99	172	-59	-56	-19	-17
	1500	153	263	146	279	-104	-91	-35	-32
	2000	195	343	199	393	-134	-131	-45	-33
	2500	242	426	249	502	-166	-159	-55	-52
	3000	288	503	298	608	-199	-191	-69	-60
	2000	197	330	196	437	-137	-131	-54	-46
	1000	97	161	103	130	-64	-56	-24	-17
	0	13	3	16	5	+3	+1	-4	+1

Table 4.1.6 Cont. LOAD STRAIN DATA FOR AIRLOAD SPECIMEN

Load Pt.No	Load lbs	Bridge No. Strain ( $\mu$ in/in)							
		MAO	MFO	MAI	MFI	TRO	TLO	TRI	TLI
3	0	0	0	0	0	0	0	0	0
	500	154	183	59	116	-33	-32	-18	-17
	1000	279	359	136	253	-70	-65	-34	-32
	1500	420	551	204	407	-118	-105	-51	-46
	2000	558	737	281	556	-166	-150	-60	-53
	2500	730	948	366	709	-212	-182	-77	-70
	3000	880	1132	446	836	-240	-207	-82	-72
	2000	587	757	289	596	-175	-155	-62	-50
	1000	290	385	147	318	-88	-83	-32	-25
	0	15	8	-3	1	+3	-3	-5	+2

Table 4.1.7 BENDING MOMENT ARM - INCHES			
Bridge	Load Point 1	Load Point 2	Load Point 3
MAO	19.44	5.66	19.32
MFO	24.04	10.26	23.92
MAI	38.56	24.78	38.44
MFI	44.18	30.40	44.06
TRO	21.70	7.92	21.58
TLO	21.70	7.92	21.58
TRI	41.36	27.59	41.24
TLI	41.36	27.59	41.24
Torsion Moment Arm			
All Bridges	Load Point 1 0	Load Point 2 0	Load Point 3 -1.38

NOTES:

- 1) Bending moment lever arm is measured parallel to 50% chordline (+ outboard of gage)
- 2) Torsion moment lever arm is measured perpendicular to 50% chordline. (+ forward of gage)



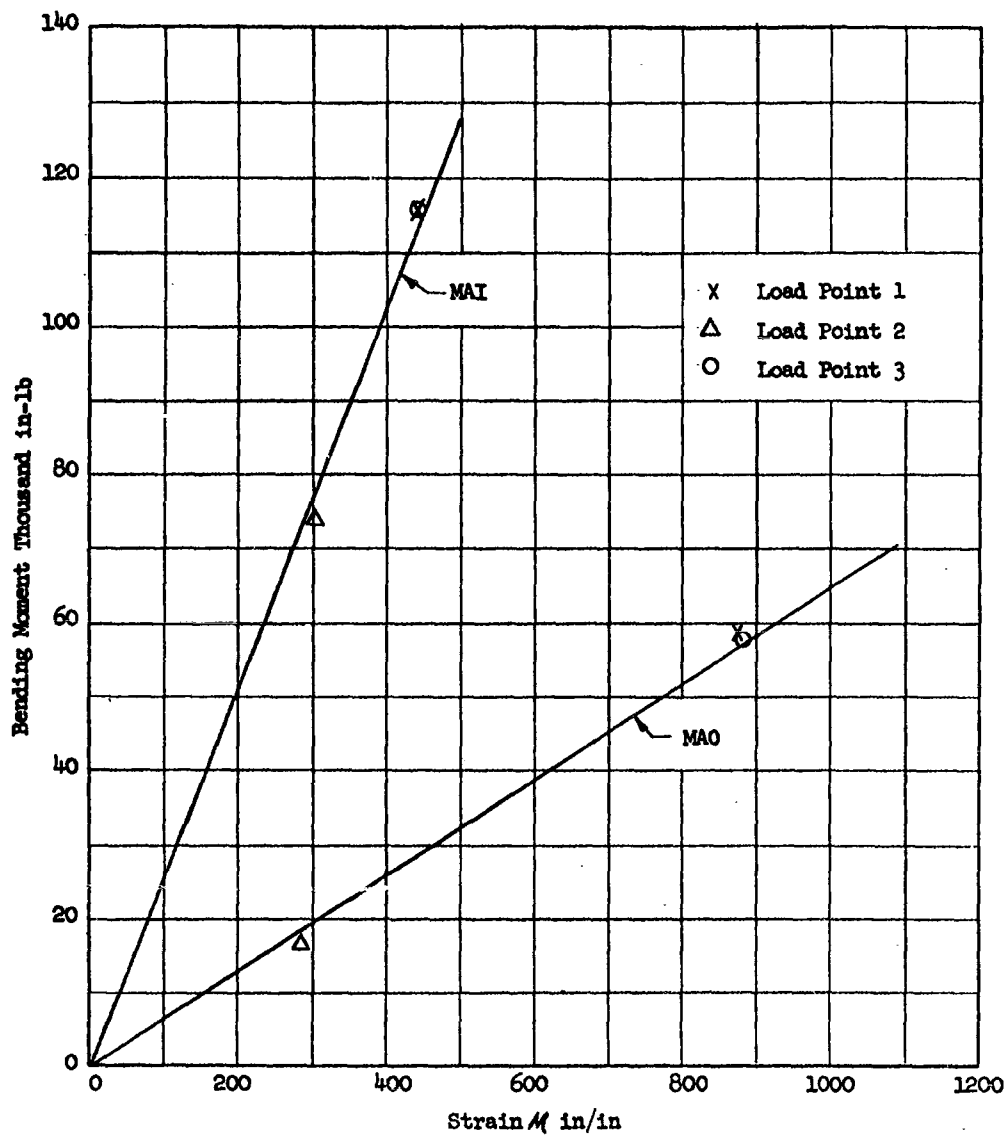


Fig. 4.1.17 BENDING MOMENT AT STRAIN GAGE LOCATION NORMAL TO 50% CHORDLINE VS. BRIDGE OUTPUT

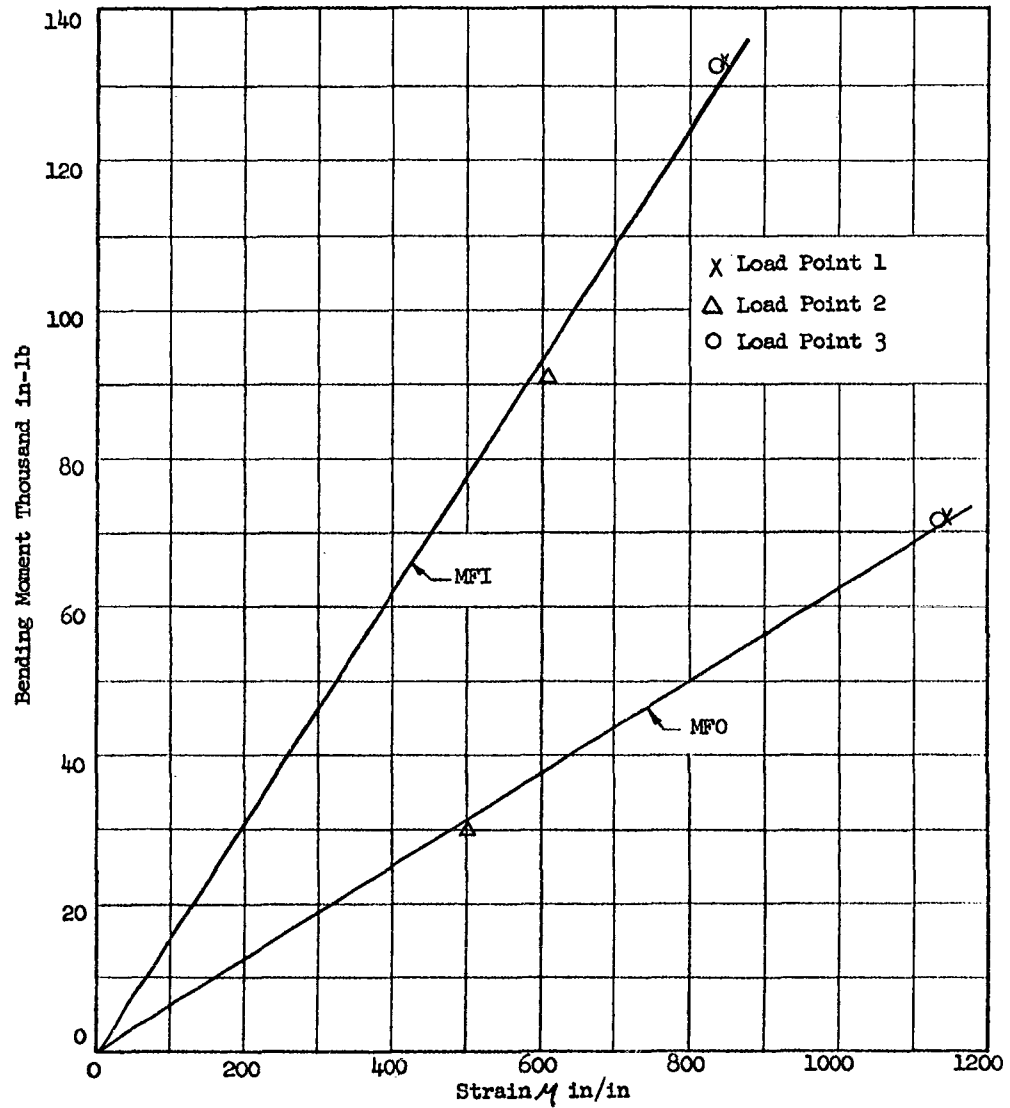


Fig. 4.1.18 BENDING MOMENT AT STRAIN GAGE LOCATION NORMAL TO 50% CHORDLINE VS. BRIDGE OUTPUT

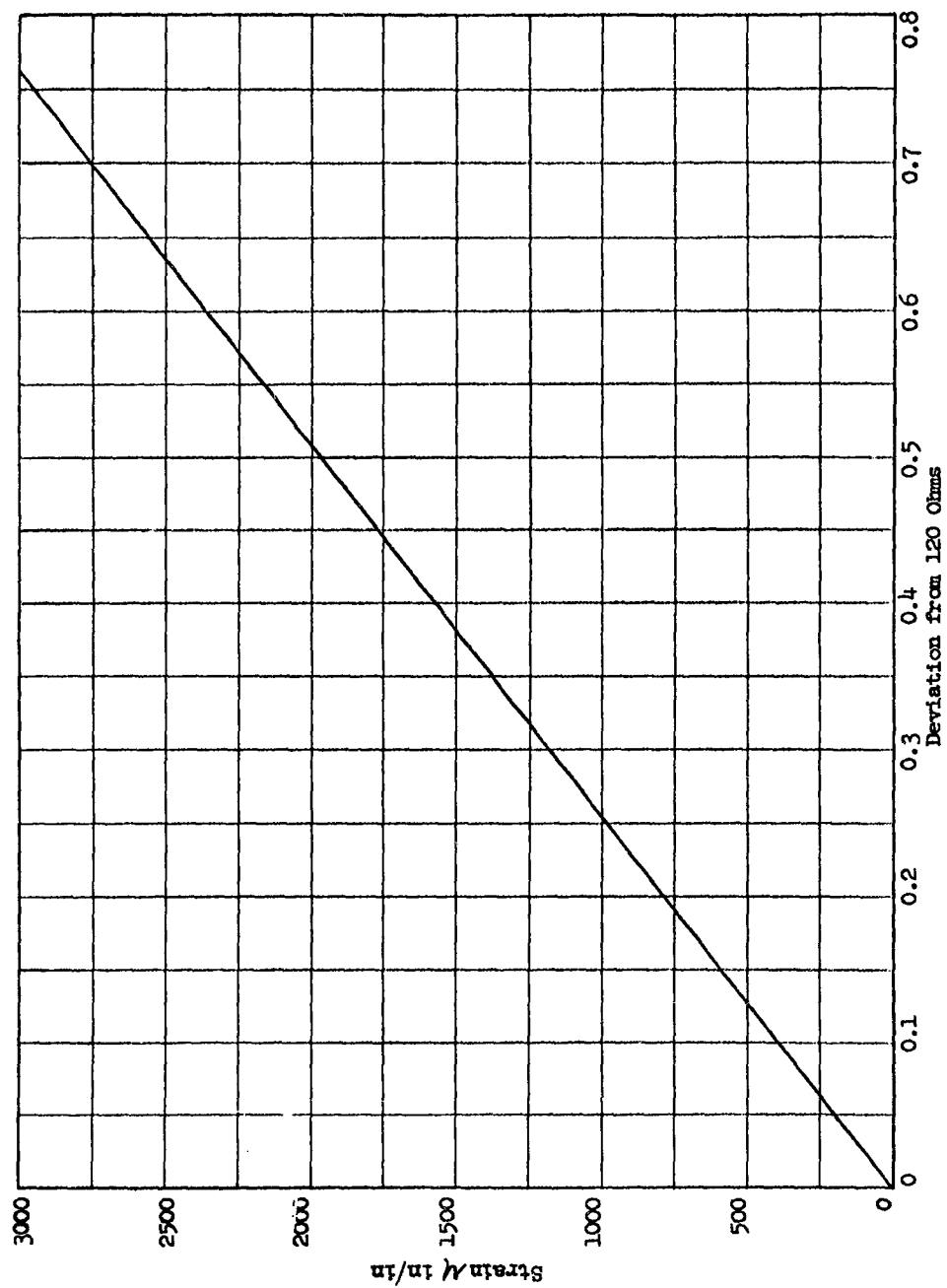


Fig. 4.1.19 INDICATED STRAIN VS. LOAD SIMULATED BY RESISTANCE OF 22.22 $\Omega$ , 23.1 $\Omega$ , 22 $\Omega$ , 43 $\Omega$ , 50 $\Omega$ , AND 100 $\Omega$  OHMS

## 4.2 STRUCTURAL SPECIMEN

### 4.2.1. DYNAMIC TESTS

#### 1. Description of Test

The purpose of the vibration test was to determine the first five or six natural frequencies, mode shapes and node line locations of the structural wing mounted in the sled forebody. For this test, the instrumented specimen was used. Transducer housings, accelerometers, strain gages and all wiring were in place. As a consequence, the mass distribution of this specimen should closely duplicate the specimens tested in the field. In order to measure the vibration characteristics of this specimen, a LPM-25 Per-Mag shaker was attached to the compression skin on the 25% chordline, 3/4" from the tip. The weight of the moving element of this shaker is approximately 0.15 lb. This location was selected because it was not close to any of the anticipated node line locations for the natural frequencies of interest. The shaker was powered by a 100 watt amplifier and frequency oscillator. An MB hand probe suspended from an independent frame was located directly above the shaker. The signal was fed from the probe into an MB vibration meter where the wing displacement was monitored. The shaker and probe arrangement is shown in Fig. 4.2.1. A second hand probe wired to the vibration meter was used to monitor the displacement at any of the 16 locations shown on Fig. 4.2.2. The signals of both probes were fed to a phase scope which determined the relative signs of the displacement signals.

Initially, a frequency survey was made from 0-600 cps with a constant shaker force. From this survey the resonant frequencies were obtained. The mode shapes of each resonant frequency were then measured. Node line locations were obtained by sprinkling iron filings on the tension skin and vibrating at the resonant frequency.

#### 2. Results of Test

The frequency survey data recorded during the test is presented



Fig. 4.2.1 ELECTRODYNAMIC SHAKER AND MONITORING PROBE ARRANGEMENT  
FOR MODEL (6R)

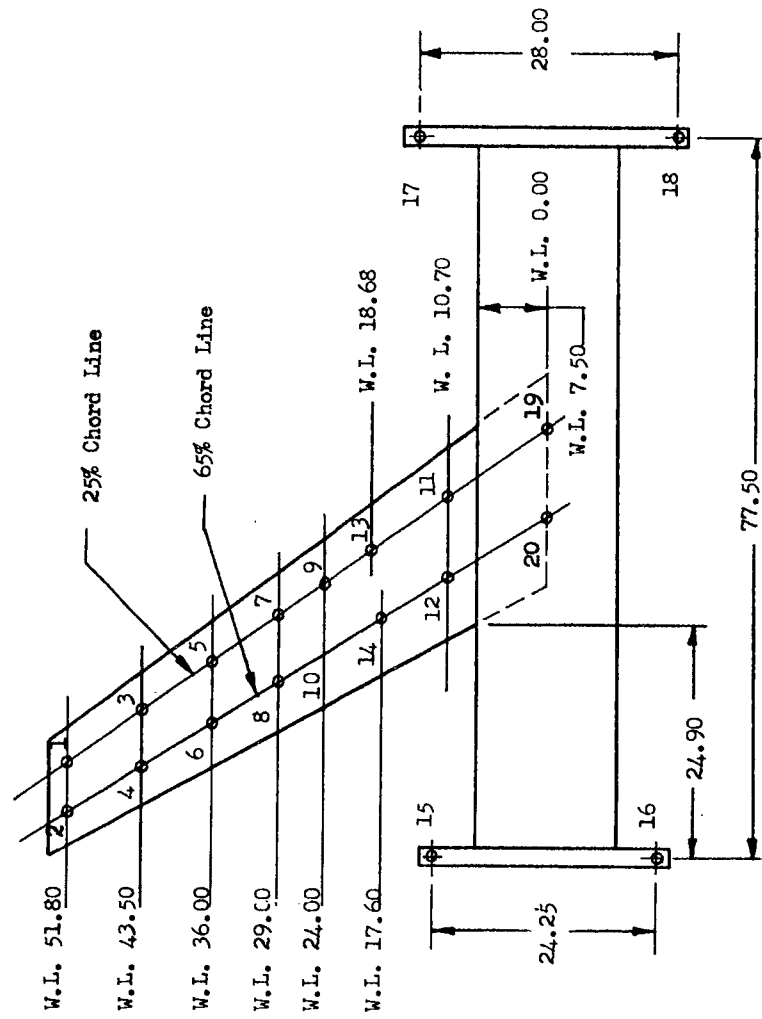


Figure 4.2.2 TENSION PAD LOCATIONS FOR INFLUENCE COEFFICIENT TEST  
AND PROBE POINT LOCATIONS FOR DYNAMIC TESTS  
(STRUCTURAL SPECIMEN)

Table 4.2.1					
FREQUENCY SURVEY DATA					
Freq. (CPS)	Ampl. (in.)	Freq. (CPS)	Ampl. (in.)	Freq. (CPS)	Ampl. (in.)
5	.006	82	.00016	230	.00027
10	.016	83	.000135	235	.00020
15	.0167	84	.00019	240	.00035
16.4	.0188	85	.00026	250	.00028
20	.0212	90	.00050	260	.00043
25	.040	95	.00094	270	.00027
26	.056	100	.0016	*275	.00054
27	.049	105	.0025	290	.00037
28	.052	110	.0049	300	.00025
*29	.074	*112	.0060	310	.000135
30	.052	120	.0035	320	.000115
32	.034	130	.0019	330	.000100
35	.022	140	.0012	340	.00008
40	.012	150	.00070	350	.00012
45	.0074	160	.00035	360	.00016
50	.0049	170	.00015	370	.000205
55	.0034	175	.00025	380	.00029
60	.0026	180	.00053	385	.00050
65	.0016	190	.00200	*390	.00054
70	.0012	*192	.00220	400	.00049
75	.00078	195	.00190	410	.00044
80	.00030	200	.00135	420	.00036
81	.00023	210	.00089	430	.00029

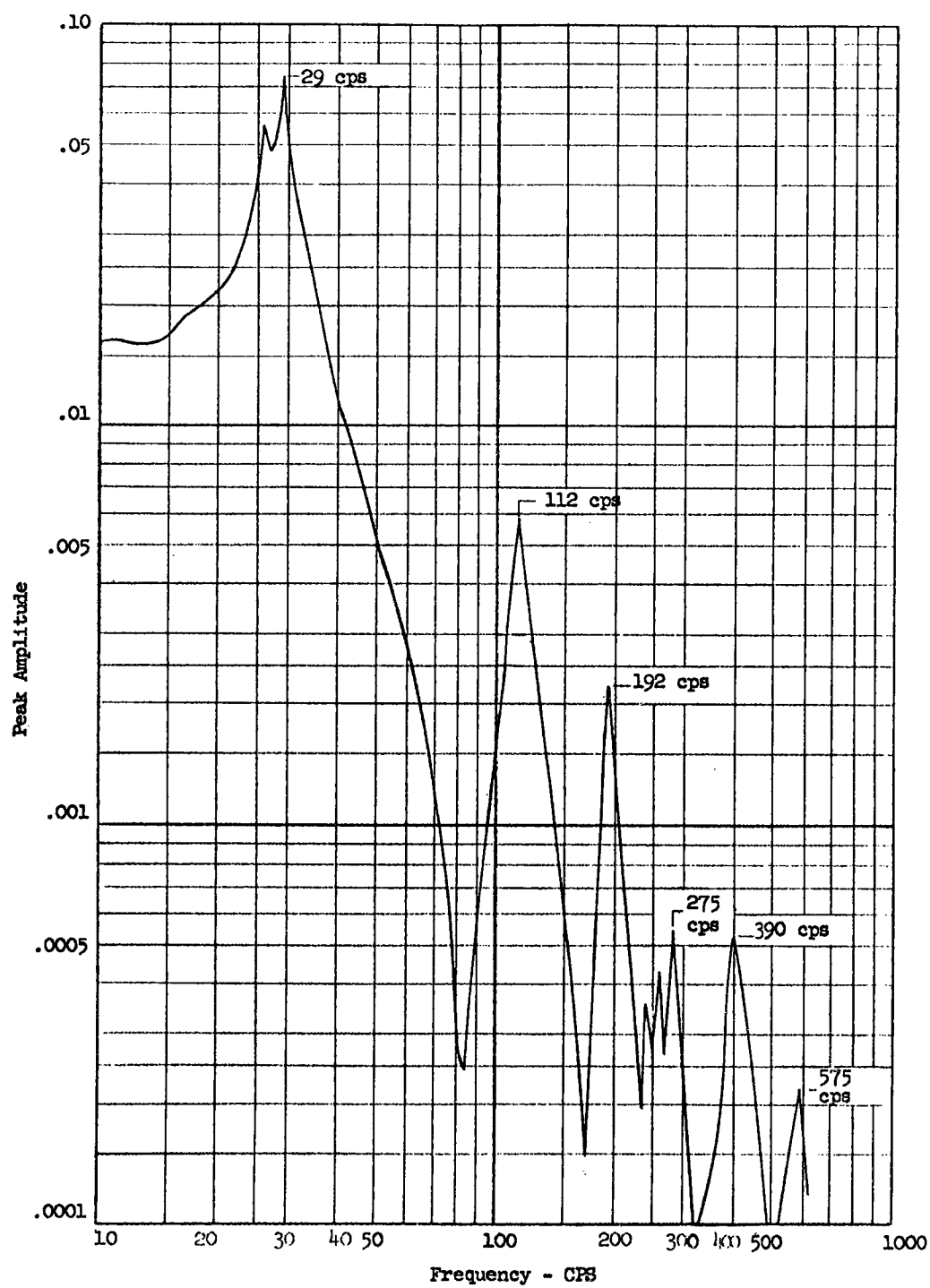


Fig. 4.2.3 FREQUENCY RESPONSE CURVE FOR STRUCTURAL SPECIMEN



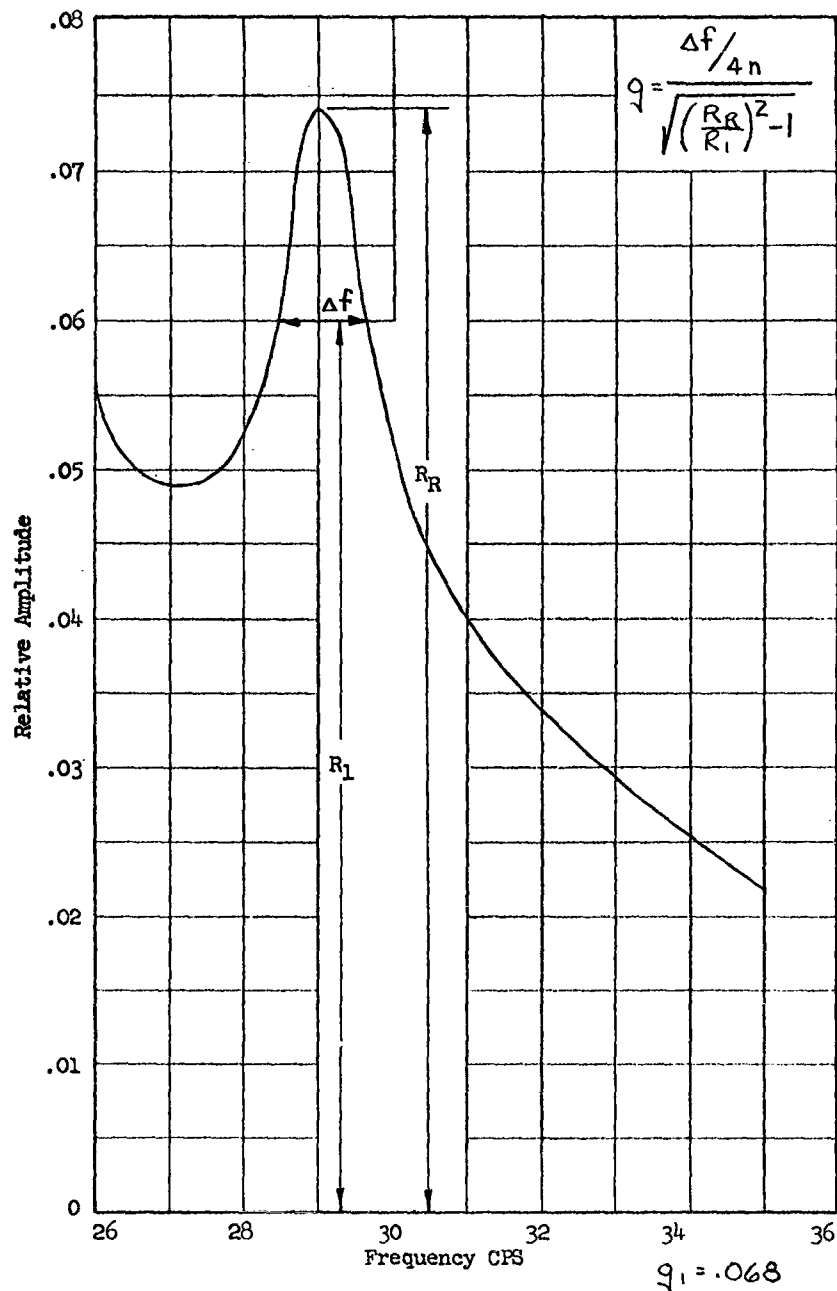


Fig. 4.2.4 STRUCTURAL DAMPING COEFFICIENT-STRUCTURAL SPECIMEN  
 $f_n = 29.0$  cps

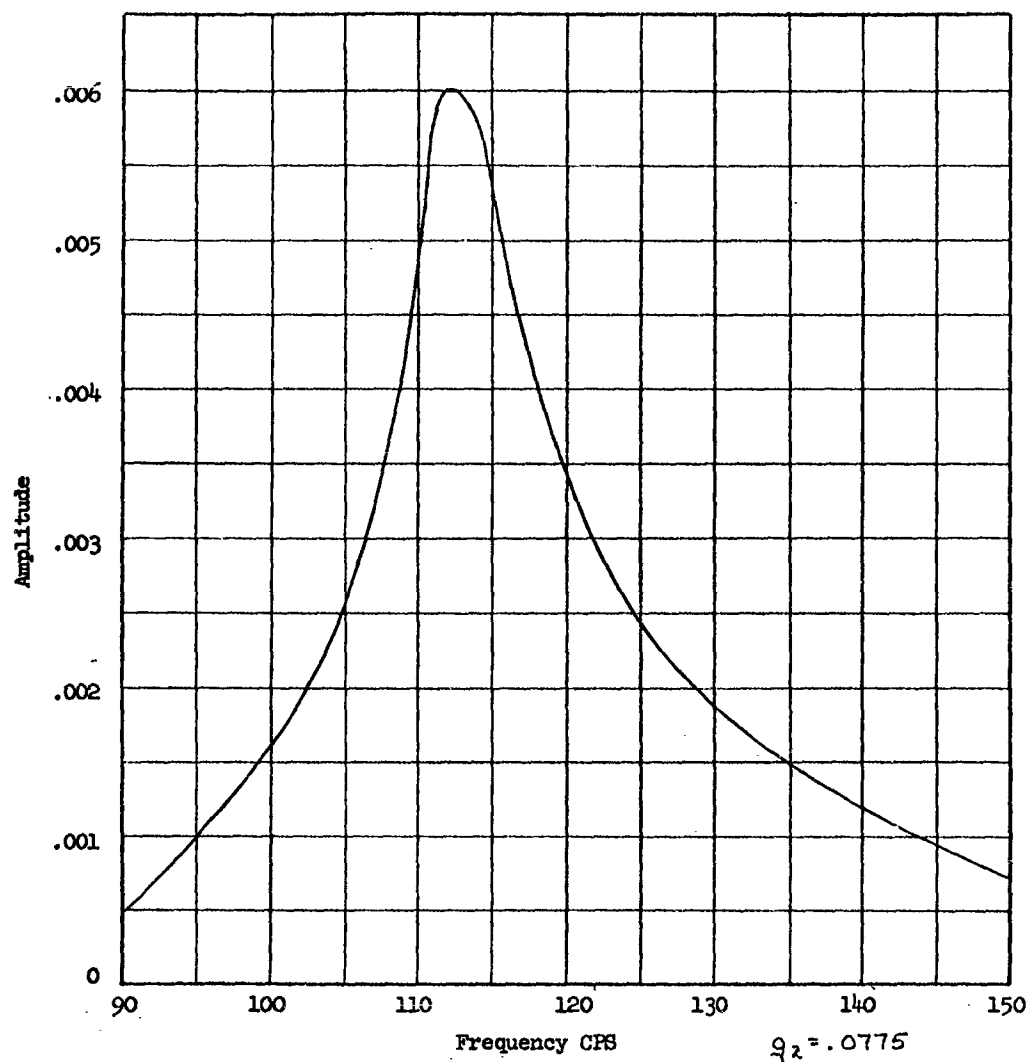


Fig. 4.2:5 STRUCTURAL DAMPING COEFFICIENT-STRUCTURAL SPECIMEN

$f_n = 112$  cps

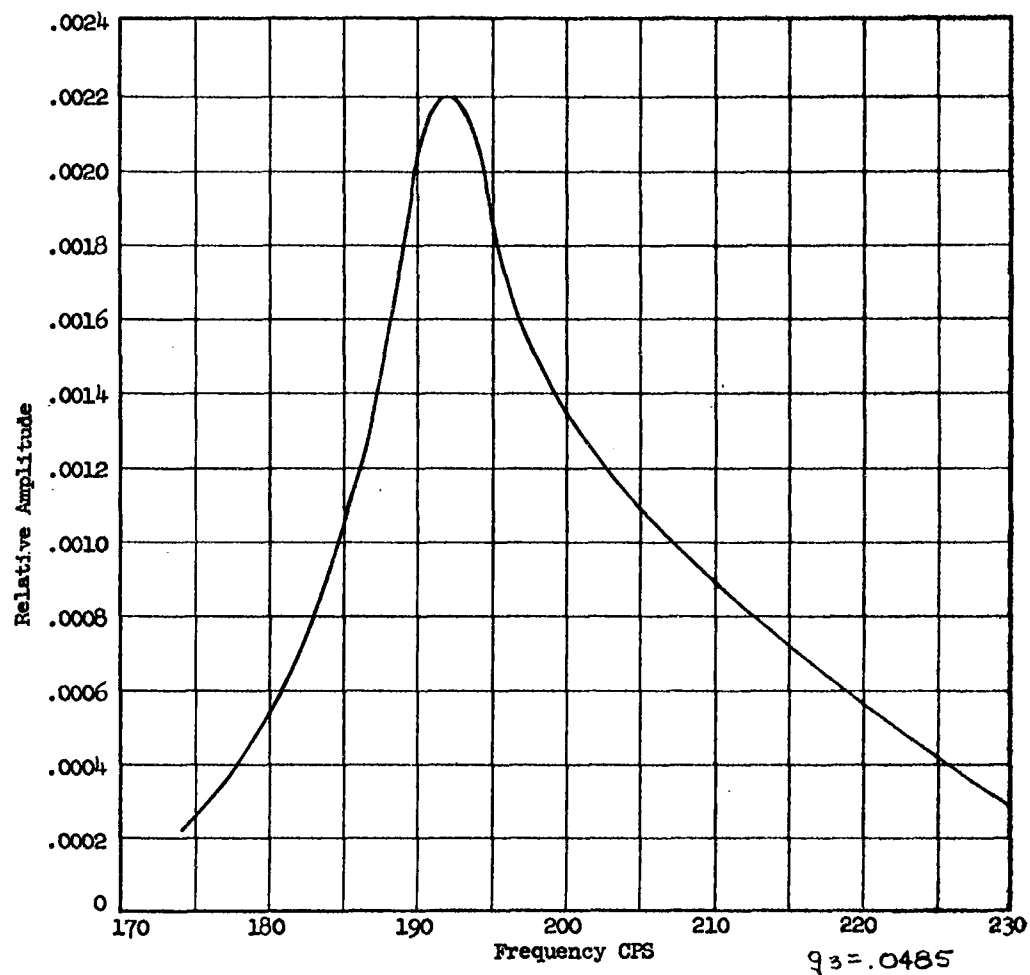


Fig. 4.2.6 STRUCTURAL DAMPING COEFFICIENT-STRUCTURAL SPECIMEN  
 $f_n = 192$  cps

TABLE 4.2.2								
MODE SHAPE DATA AT RESONANT FREQUENCIES-STRUCTURAL SPECIMEN 6R								
Frequency CPS	29.0		112		192		390	
Probe Point	Ampl in	Phase	Ampl in	Phase	Ampl in	Phase	Ampl in	Phase
1	.043	0	.023	0	.014	0	.013	0
2	.049	0	.031	0	.011	0	.016	$\pi$
3	.031	0	.008	$\pi$	.013	0	.010	0
4	.0355	0	.014	0	.008	$\pi$	.012	$\pi$
5	.022	0	.020	$\pi$	.014	0	.010	$\pi$
6	.025	0	.012	$\pi$	.011	$\pi$	.012	$\pi$
7	.016	0	.019	$\pi$	.013	0	.011	$\pi$
8	.018	0	.016	$\pi$	.011	$\pi$	.013	0
9	.013	0	.018	$\pi$	.012	0	.011	$\pi$
10	.013	0	.016	$\pi$	.011	$\pi$	.014	0
11	.018	0	.013	$\pi$	.0135	0	.012	$\pi$
12	.011	0	.013	$\pi$	.014	$\pi$	.016	0
13	.016	0	.019	$\pi$	.015	0	.014	$\pi$
14	.014	0	.015	$\pi$	.012	$\pi$	.014	0
19	.008	0	.007	$\pi$	.001	0	.004	$\pi$
20	.005	0	.008	$\pi$	.002	$\pi$	.001	0

TABLE 4.2.2 (Cont.)								
MODE SHAPE DATA AT RESONANT FREQUENCIES-STRUCTURAL SPECIMEN 6R								
Frequency CPS	575		275					
Probe Point	Ampl in	Phase	Ampl in	Phase				
1	.0009	0	.012	0				
2	.0009	0	.012	0				
3	.0009	$\pi$	.011	$\pi$				
4	.0009	$\pi$	.013	$\pi$				
5	.0009	$\pi$	.012	$\pi$				
6	.0008	0	.015	$\pi$				
7	.0009	$\pi$	.012	0				
8	.0009	0	.013	$\pi$				
9	.0008	$\pi$	.010	0				
10	.0010	$\pi$	.017	0				
11	.0009	0	.012	0				
12	.0009	$\pi$	.014	0				
13	.0010	0	.010	0				
14	.0009	$\pi$	.012	0				
19			.003	0				
20			.006	0				

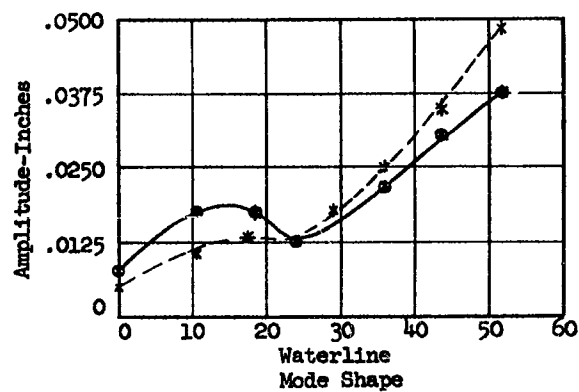
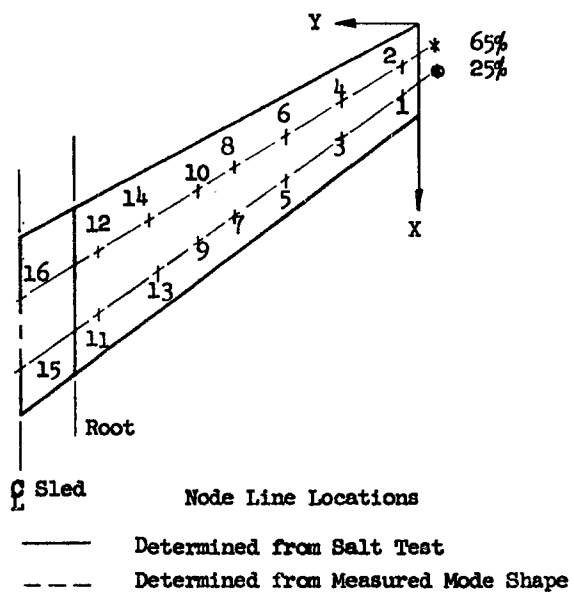


Fig. 4.2.7 FIRST BENDING MODE  $f_n = 29.0$  CPS

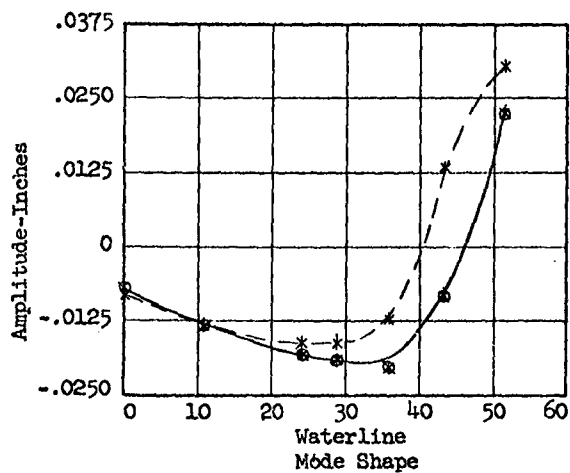
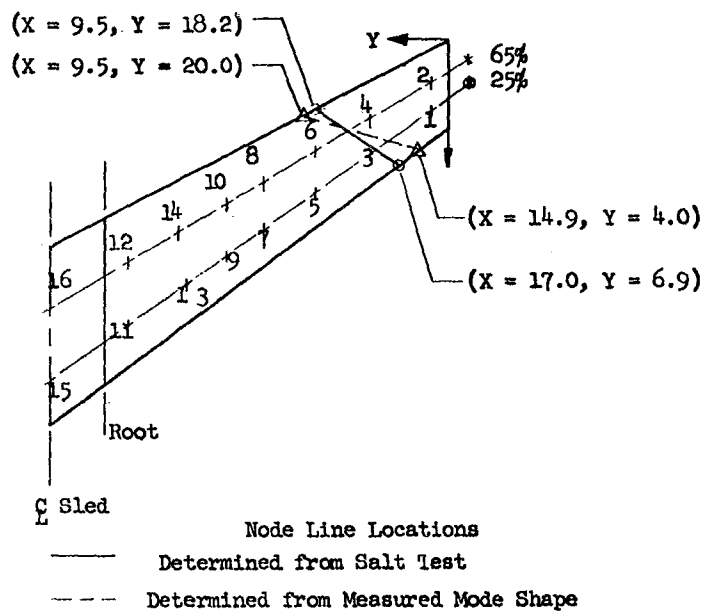
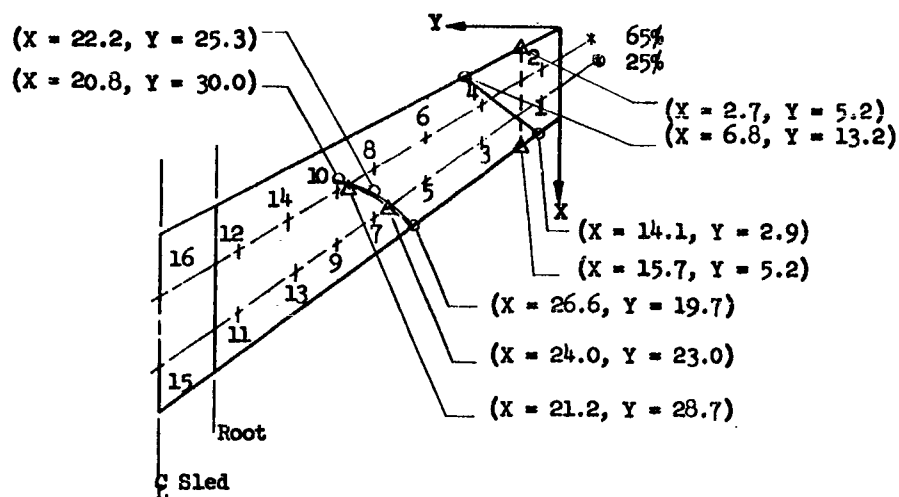


Fig. 4.2.8 SECOND BENDING MODE  $f_n = 112$  CPS



Node Line Locations

--- Determined from Salt Test

--- Determined from Measured Mode Shape

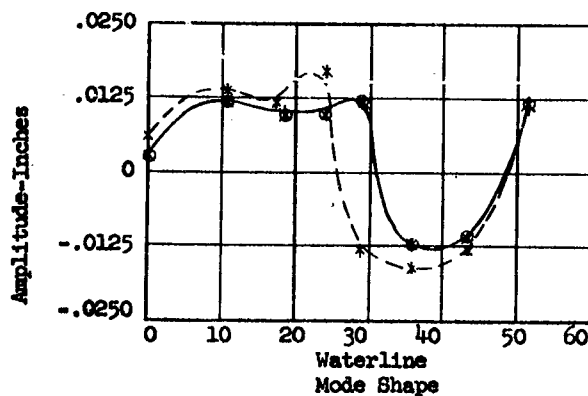


Fig. 4.2.9

THIRD BENDING MODE  $f_n = 275$  CPS



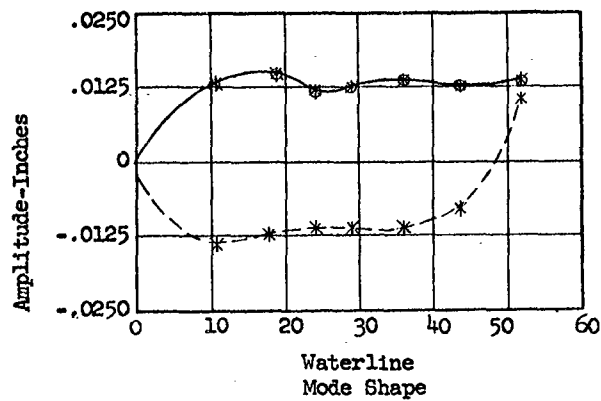
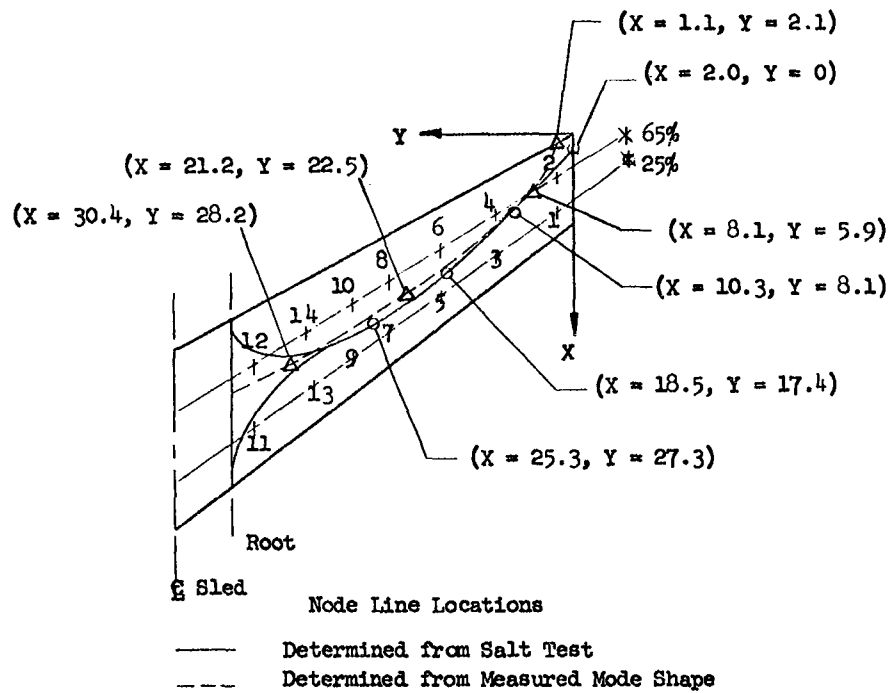


Fig. 4.2.10

FIRST TORSION MODE  $f_n = 192$  CPS

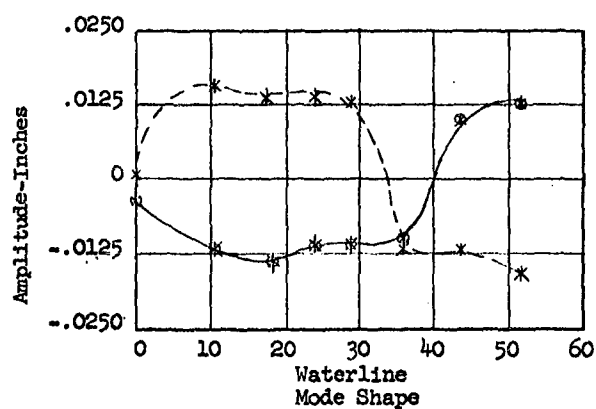
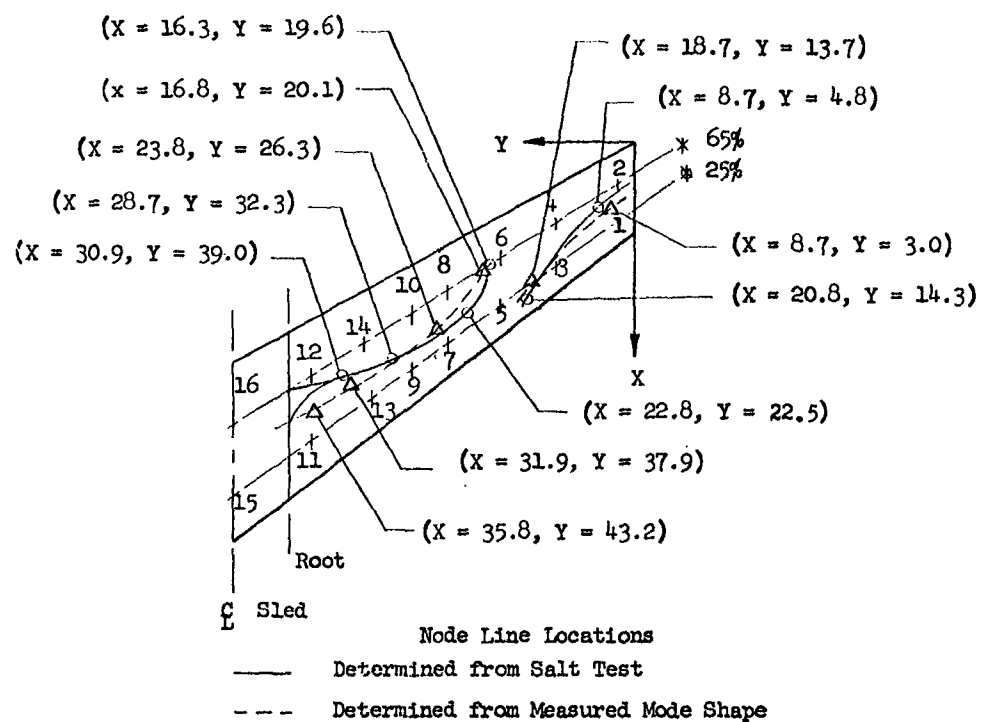


Fig. 4.2.11

SECOND TORSION MODE  $f_n = 390$  CPS



Fig. 4.2.12 NODE LINE LOCATION FOR  $f_n = 29.0$  CPS MODEL (6R)

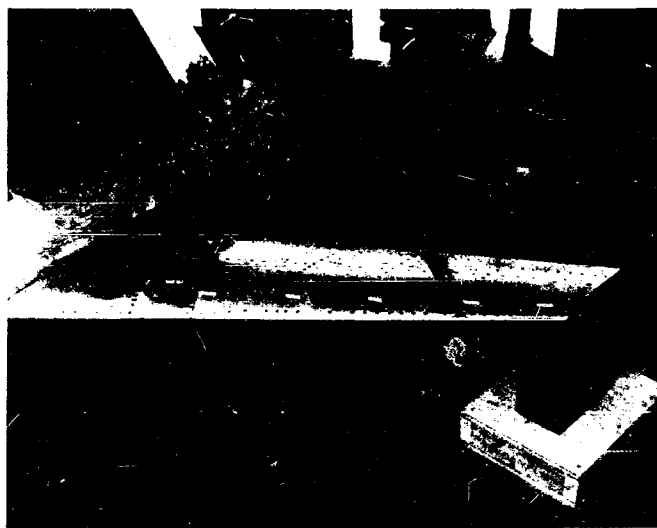


Fig. 4.2.13 NODE LINE LOCATION FOR  $f_n = 11.2$  CPS MODEL (6R)



Fig. 4.2.14 NODE LINE LOCATION FOR  $f_n = 275$  CPS MODEL (6R)

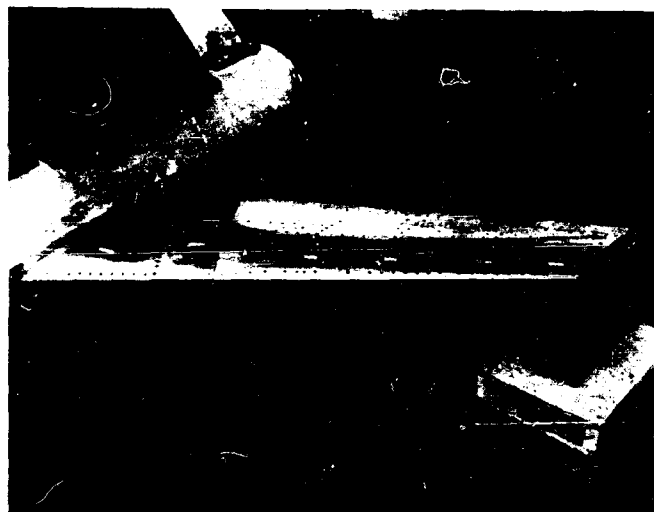


Fig. 4.2.15 NODE LINE LOCATION FOR  $f_n = 192$  CPS MODEL (6R)



Fig. 4.2.16 NODE LINE LOCATION FOR  $f_n = 390$  CPS MODEL (6R)

in Table 4.2.1, and plotted on log-log paper in Figure 4.2.3. The wing displacement at each natural frequency is tabulated in Table 4.2.2. The first three structural damping coefficients were approximated from the response data plotted in Figures 4.2.4 through 4.2.6. The mode shapes and node line locations have been summarized in Figures 4.2.7 through 4.2.11. The odd behavior of the first bending mode shape presented in Figure 4.2.7, in the area of the failure bay, may be attributable to local response of the leading and trailing edge cover plates. As indicated in section 4.1.1, the shape of the probe signal was observed for each reading, and in some cases the extraneous frequency contributions were of such a magnitude that the measured mode shapes should not be used for correlation purposes. Pictures of the node line locations for the first three bending modes, and the first two torsion modes are shown in Figures 4.2.12 through 4.2.16.

#### 4.2.2 STATIC TESTS

##### 4.2.2.1 INFLUENCE COEFFICIENT TEST

###### 1. Description of Test

The purpose of this test was to obtain influence coefficients at a sufficient number of points to adequately describe the elastic behavior of the structural wing and its simulated support. Since a member of this aspect ratio exhibits relatively little chordwise bending, six points along the 25% chordline, and six points along the 65% chordline were chosen as load points, as indicated in Figure 4.2.2. Deflections along any streamwise spanline would be linearly interpolated from the two chordline deflections. It was not practical to locate the load points too close to the breakline. As a consequence, no load was applied at points 13 and 14; however, deflections were measured at these points. In addition, deflections were measured for each load application, at points 15, 16, 17, and 18. Deflections 15 through 18 will help to define the combined flexibility of the sled and test stand. No deflection measurements were made which would have isolated the flexibility of the test stand itself. However, its elastic characteristics could be computed analytically from the information provided in Figure 4.1.12.

The loads were applied to the specimen through tension pads which were bonded to the compression skin directly over the forward and aft main spars. Tension pads 1 through 8 were 3 inches square. The peak load applied at points 1 - 8 was 450 lbs. with the exception of point 2 where the peak load was 400 lbs. Tension pads 9 through 12 were 4 inches square and the peak load applied at these points was 900 lbs. The load and unload portions of the load deflection curve were defined at 7 increments of load as indicated in Table 4.2.3. The load applied by a chain hoist through a linkage shown in Figure 4.2.17 was read on a Dillon force gage. The estimated accuracy of the load readings is  $\pm 10$  lbs.

The deflection measurements were made by dial gages suspended from a frame which is independent of the test stand as shown in Figure 4.2.18. The dial gages are graduated in intervals of .001 inch, however, the readings from gages 15 through 18 were estimated to .0001 inch.

## 2. Results of Test

The load deflection data taken during the test is presented in Table 4.2.3. This information was plotted and straight lines were drawn through the data points. The influence coefficients summarized in Table 4.2.4 are the slopes of the straight lines drawn through the load deflection data. Theoretically, the influence coefficient matrix should be symmetrical about its  $\bar{S}_{ii}$  diagonal. From Table 4.2.4 it is apparent that this symmetry is not too good for those coefficients which were determined on the basis of relatively small deflections. It is believed that the primary cause of this non-symmetry is due to the load deflection hysteresis produced by non-linear slippage in the fasteners and root support. This hysteresis shown in Figure 4.2.19 is evident to some extent in all of the load deflection curves. If sufficient load is not applied at each point to complete this slippage, the shape of the line passed through the data will be a function of the magnitude of the peak load. It is difficult to determine the peak load required to complete slippage at each point. In addition, the peak load is limited by the capacity of the tension pad which it is practicable to use.



Fig. 4.2.17 DILLON FORCE GAGE



Fig. 4.2.18 STATIC TEST SET UP FOR MODEL (6R)



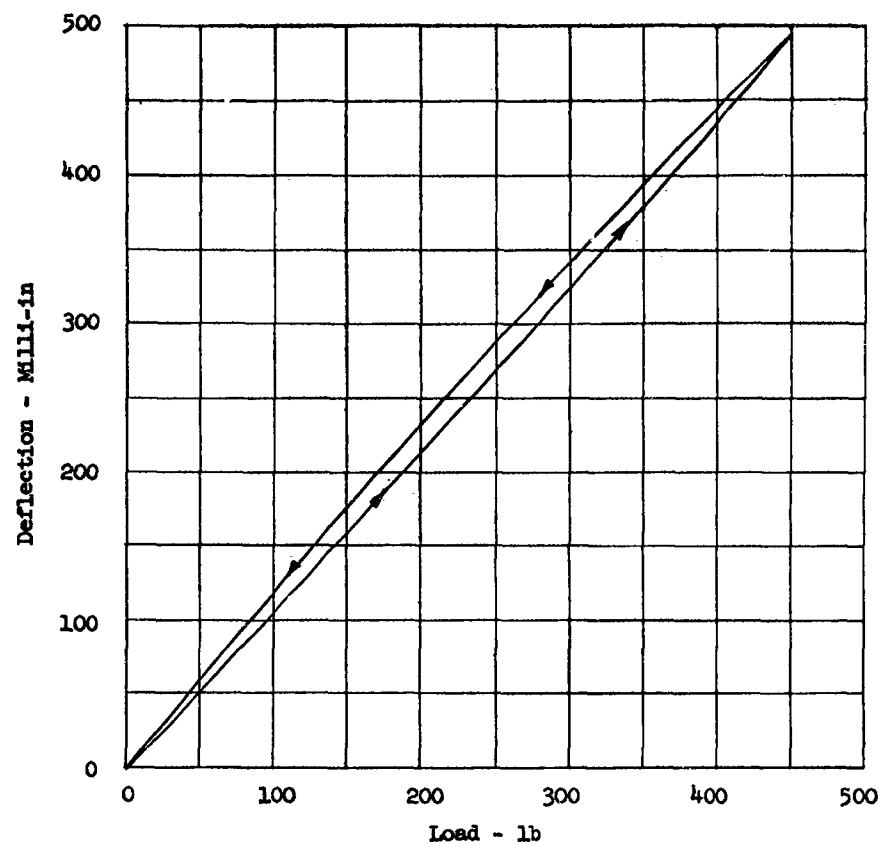


Fig. 4.2.19 LOAD DEFLECTION PLOT SHOWING HYSTERESIS -  
STRUCTURAL SPECIMEN

Note: Load applied at Point 1 and deflection measured  
at Point 1.

TABLE 4.2.3 REDUCED LOAD DEFLECTION DATA TAKEN DURING INFLUENCE COEFFICIENT TEST IN. x 10 <sup>-3</sup>																			
Defl. Point	Load lbs.								Load lbs.										
	0	150	300	450	300	150	0	0	0	150	300	400	300	150	0	0	0	0	0
1	0	155	326	497	341	176	0	0	0	182	363	506	385	192	1	0	0	0	0
2	0	163.5	343.5	521.5	357.5	184.5	0	0	0	202	425	570	434	219	4	0	0	0	0
3	0	102	215	329	226	116	0	0	0	117	246	331	252	126	0	0	0	0	0
4	0	112	235	359	247	128	0	0	0	133	281	377	287	143	1	0	0	0	0
5	0	64	134	207	143	74	0	0	0	72	152	205	157	79	0	0	0	0	0
6	0	72	153	236	162	84	0	0	0	86	181	243	186	93	1	0	0	0	0
7	0	37	80	123	86	44	0	0	0	42	89	121	93	48	0	0	0	0	0
8	0	44	94	144	100	52	0	0	0	51	109	147	112	57	0	0	0	0	0
9	0	23	49	75	52	52	0	0	0	24	53	73	56	29	0	0	0	0	0
10	0	29	61	93	65	34	0	0	0	33	71	95	73	39	0	0	0	0	0
11	0	2.8	5.8	8.3	6.0	2.8	0	0	0	2.5	5.5	8	6.8	2.2	0	0	0	0	0
12	0	3.5	7.8	10.0	7.5	3.7	0	0	0	3.0	7.6	10.3	7.5	5.2	0	0	0	0	0
13	0			4.3			2	0	0			37			3	0	0	0	0
14	0			47.5			1	0	0			44			0	0	0	0	0
15	0	.9	2.3	3.8	2.7	1.4	0	0	0	1.1	2.1	3	2.2	1.1	0	0	0	0	0
16	0	.3	.8	1.3	1.0	.5	0	0	0	.6	1.0	1.3	1	.6	0	0	0	0	0
17	0			8.7			.4	0	0			7.6			.1	0	0	0	0
18	0			2.9			.9	0	0			1.1			.2	0	0	0	0
Load Point 1								Load Point 2											

TABLE 4.2.3 Cont. REDUCED LOAD DEFLECTION DATA TAKEN DURING INFLUENCE COEFFICIENT TEST IN. X 10<sup>-3</sup>

Defl. Point	Load 1lb.										Load 1lb.										
	0	150	300	450	300	150	0	0	150	300	450	300	150	0	0	150	300	450	300	150	0
1	0	6	219	331	225	116	4	0	131	272	401	275	139	2							
2	0	110	230	341	233	119	2	0	141	294	435	298	150	1							
3	0	77	161	243	167	86	4	0	91	192	282	194	99	1							
4	0	82	171	253	173	89	2	0	105	219	324	222	113	2							
5	0	51	107	159	110	57	2	0	59	123	184	126	65	1							
6	0	57	118	175	121	62	1	0	71	147	219	150	77	1							
7	0	31	65	97	68	35	1	0	35	74	110	76	39	0							
8	0	36	74	109	76	38	0	0	43	91	135	93	47	0							
9	0	20	40	60	43	22	1	0	21	46	68	48	25	0							
10	0	24	49	72	51	27	1	0	28	59	83	60	32	0							
11	0	2.8	5.3	8.8	5.5	3.3	.3	0	2.4	5.1	8.1	5.7	3.1	-.5							
12	0	4.3	6.3	9.8	7.3	4	0	0	3.1	6.1	9.9	6.9	3.3	-1.1							
13	0			32			1	0			29			-.3							
14	0			34.5			-1	0			38.5			0							
15	0	1.4	2	4.1	2.3	1.4	0	0	1.1	2.3	3.7	2.2	1.1	-.2							
16	0	.4	.8		.9	.4	-.1	0	.5	1	1.4	.9	.5	0							
17	0			7.8			.2	0			7			3							
18	0			2.4			.3	0			1.5			0							
Load Point 3										Load Point 4											

TABLE 4.2.3 Cont. REDUCED LOAD DEFLECTION DATA TAKEN DURING INFLUENCE COEFFICIENT TEST IN X 10 <sup>-3</sup>																
Defl. Point	Load lbs.								Load lbs.							
	0	150	300	450	300	150	0	0	0	150	300	450	300	150	0	0
1	0	63	133	203	40	70	0	0	0	83	168	251	171	87	0	0
2	0	65	137	210	144	72	0	0	0	83	177	265	181	93	0	0
3	0	49	102	156	108	54	0	0	0	61	123	187	127	65	-1	0
4	0	49	105	161	111	55	0	0	0	68	135	206	141	72	0	0
5	0	34	73	114	78	40	0	0	0	41	86	128	89	45	0	0
6	0	36	77	120	82	41	-1	0	0	50	103	153	105	54	1	0
7	0	22	46	73	50	26	0	0	0	26	53	80	56	29	0	0
8	0	24	51	80	55	27	-1	0	0	33	66	100	69	35	0	0
9	0	14	30	47	33	17	0	0	0	16	33	51	37	19	0	0
10	0	16	34	54	37	19	-1	0	0	22	43	66	46	24	1	0
11	0	1.8	4.2	7.2	5	2.5	-0.3	0	0	2.5	4.3	7.0	6.7	3.8	0	0
12	0	2	4.5	8.3	5.1	2.6	-1	0	0	2.1	5.1	8.7	7.3	4.3	-0.2	0
13	0			2.6			1	0	0			25			0	0
14	0			27.5			.5	0	0			27			-4	0
15	0	1.2	2.4	3.1	2.2	1.2	.1	0	0	.6	1.5	2.8	1.8	.8	-0.2	0
16	0	.3	.6	1	.6	.2	-0.1	0	0	0	.4	.8	.5	0	-0.3	0
17	0			7.3			0	0	0			6.9			.2	0
18	0			2.5			0	0	0			2.2			.2	0
Load Point 5								Load Point 6								

TABLE 4.2.3 Cont. REDUCED LOAD DEFLECTION DATA TAKEN DURING INFLUENCE COEFFICIENT TEST IN $\times 10^{-3}$																			
Defl. Point	Load lbs.											Load lbs.							
	0	150	300	450	300	150	0	0	150	300	450	300	450	300	150	0	150	300	450
1	0	39	78	122	84	43	-1	0	53	109	162	111	55	-1					
2	0	40	79	124	85	44	0	0	57	115	171	117	59	0					
3	0	30	61	96	66	34	-1	0	42	83	124	86	43	0					
4	0	30	62	97	67	34	-1	0	44	90	134	92	46	0					
5	0	23	46	72	50	26	-1	0	30	60	91	63	31	-1					
6	0	23	47	73	51	26	-1	0	34	69	104	71	36	0					
7	0	16	32	51	36	18	-1	0	20	40	61	42	22	0					
8	0	17	34	43	36	19	0	0	25	50	75	51	26	1					
9	0	11	21	35	24	12	-1	0	14	26	40	28	15	0					
10	0	13	24	38	27	14	-1	0	18	34	52	36	19	0					
11	0	2.4	3.5	6.6	5	2.4	-8	0	2.4	3.3	6.4	4.9	2.6	0					
12	0	3	3.5	6.4	5.3	2.8	-7	0	3.2	4.3	7.4	5.6	3.2	1					
13	0			21			0	0			22			0					
14	0			20.5			0	0			27			0					
15	0	.6	1.5	2.7	1.5	1	-3	0	1	1.7	2.8	1.8	.7	-3					
16	0	.3	.5	1.3	.7	.5	-1	0	.4	.9	1.2	.8	.4	0					
17	0			7.4			0	0			.7			.1					
18	0			2.9			0	0			2.6			0					
Load Point 7										Load Point 8									

TABLE 4.2.3 Cont. REDUCED LOAD DEFLECTION DATA TAKEN DURING INFLUENCE COEFFICIENT TEST IN X 10 <sup>-3</sup>																	
Defl. Point	Load lbs.						Load lbs.						Load lbs.				
	0	300	600	900	600	300	0	300	600	900	600	300	0	300	600	900	600
1	0	49	102.5	158.5	110.5	56.5	1	0	67	212	147	73	0	0	67	212	147
2	0	48	103	158	109	57	1	0	71	222	154	77	1	0	71	222	154
3	0	40	84	129	90	48	1	0	54	168	116	59	1	0	54	168	116
4	0	39	83	127	89	46	1	0	57	179	124	64	1	0	57	179	124
5	0	30	65	100	71	37	1	0	40	127	89	44	1	0	40	127	89
6	0	30	64	100	70	36.5	.5	0	45	143	99	50	2	0	45	143	99
7	0	22	49	76	54.5	28	0	0	28	89	64	32	2	0	28	89	64
8	0	22.2	47.2	74.2	52.2	27.2	.2	0	33	107	76	38	2	0	33	107	76
9	0	16.7	36.7	56.7	41.2	21.7	.7	0	19	61	44	25	1	0	19	61	44
10	0	16	35.5	55	40.5	21.5	.5	0	27	88	64	35	4	0	27	88	64
11	0	3.3	8.3	13.1	9.8	5.7	0	0	2.7	11.4	8.5	4.4	-1	0	2.7	11.4	8.5
12	0	3.2	8.2	12.7	15.3	6	0	0	3.9	14	10	4.7	0	0	3.9	14	10
13	0			36.9			1.5	0		38			0	0		38	
14	0			35			1	0		49			0	0		49	
15	0	1.8	3.7	5.5	3.6	2	.1	0	1.6	5.5	3.6	1.8	0	0	1.6	5.5	3.6
16	0	.8	1.4	2	1.4	.8	0	0	.8	2	1.2	.7	.1	0	.8	2	1.2
17	0			14.2			.1	0		13			.1	0		13	
18	0			5.8			.2	0		5.3			.5	0		5.3	
Load Point 9						Load Point 10						Load Point 10					

TABLE 4.2.3 Cont. REDUCED LOAD DEFLECTION DATA TAKEN DURING INFLUENCE COEFFICIENT TEST IN $\times 10^{-3}$																				
Defl. Point	Load lbs.										Load lbs.									
	0	300	600	900	600	300	0	0	0	300	600	900	600	300	0	0	0	300	600	900
1	0	9	17.8	27	18.8	10.2	.7	0	0	10	21.5	32.5	22.5	10.5	-5	0	0	10	22.5	32.5
2	0	8.5	17.2	25.8	18.1	10	1	0	0	10	21	32	22	10	-1	0	0	10	22	32
3	0	7.5	15.3	23.5	17.4	10	1	0	0	8.5	18.5	27.5	19.5	9.8	-5	0	0	8.5	19.5	27.5
4	0	7	13.7	21	15	8.9	.8	0	0	8.5	18	27	18.5	9	0	0	0	8.5	18.5	27
5	0	6.7	12.7	20	15	9.8	.8	0	0	6.5	15	22	16	8	-5	0	0	6.5	16	22
6	0	6	11.3	18	13.5	8.8	.5	0	0	7	15	22.7	16	8.6	0	0	0	7	16	22.7
7	0	5.7	10	17	13.4	9	1	0	0	5.5	12	18.3	13.5	7.5	0	0	0	5.5	13.5	18.3
8	0	5.5	9.2	15.2	11.9	8.4	1	0	0	5.5	12	18	12.5	7	-5	0	0	5.5	12.5	18
9	0	5.5	8.8	15.2	12.3	8.9	1	0	0	5	10.5	15.5	11.5	7	.5	0	0	5	11.5	15.5
10	0	4.5	7	12.7	11.2	8.5	1	0	0	4.7	10.5	16	12	7.5	0	0	0	4.7	12	16
11	0	2.9	4.3	8.3	7.1	6.8	.4	0	0	2.7	5	7.4	6.4	.4	.7	0	0	2.7	6.4	7.4
12	0	2.5	3.5	7.3	6.3	5.9	.5	0	0	3.1	6.6	9.6	7.8	.5	.8	0	0	3.1	7.8	9.6
13	0			6.5			-5.5	0	0			12.5			0	0	0			12.5
14	0			9			-9	0	0			13			.5	0	0			13
15	0	1.5	2.7	4.3	2.8	1.5	0	0	0	1.3	2.5	4.1	2.7	1.3	0	0	0	1.3	2.7	4.1
16	0	.7	1.3	2	1.5	.9	1	0	0	.4	1	1.8	1	.4	-1	0	0	.4	1	1.8
17	0			12.7			0	0	0			11.2			.1	0	0			11.2
18	0			6.5			.3	0	0			4.1			1.2	0	0			4.1
Load Point 11										Load Point 12										

TABLE 4.2.4 SUMMARY OF INFLUENCE COEFFICIENTS-STRUCTURAL MODEL 6 R												
Gage Point	Load Point $in/lb \times 10^{-6}$											
	1	2	3	4	5	6	7	8	9	10	11	12
1	1106	1250	738	891	451	562	271	365	176	236	30.0	36.1
2	1160	1425	766	974	467	594	276	382	176	247	28.1	35.6
3	722	825	540	634	347	415	214	280	145	187	26.7	30.5
4	799	942	571	725	358	460	216	302	142	199	23.4	30.0
5	453	512	354	411	253	284	160	204	111	142	22.2	24.5
6	525	608	400	494	267	340	162	234	111	159	20.0	25.2
7	267	303	220	249	162	178	113	136	84.5	99	18.9	20.4
8	320	368	249	304	178	225	118	167	82.2	118	16.3	20.0
9	171	182	138	153	114	113	76	89	64.5	69	16.9	17.8
10	207	237	164	198	120	147	84.5	117	61.1	95.5	13.6	18.2
11	19.3	20	18.2	18.2	16.0	17.8	14.7	14.4	14.7	12.7	9.1	8.2
12	24.0	26	22.7	22.0	18.9	19.6	14.0	16.7	14.1	15.6	8.1	10.7



#### 4.2.2.2 CALIBRATION OF ELASTIC STRAIN GAGES

1. The purpose of this test was to calibrate two elastic torsion bridges and one elastic bending moment bridge. These bridges are identified as  $T_1$ ,  $T_2$ , and  $M_2$  in Figure 4.2.20 a and b and Figure 4.2.21. Torsion bridges,  $T_1$  and  $T_2$  are made with one gage in each arm of a four arm bridge. These gages are all mounted to the inside face of the tension skin inboard and outboard of the break station. The bending moment bridge is also made up with one gage in each arm of a four arm bridge. As shown in Table 4.2.5 two gages are mounted on the inside face of the tension skin, and two gages are mounted on the compression skin just inside of the forward and aft spars. All of the strain gages used on the structural model are Baldwin SR-4 type EBF-7D + having a gage factor of  $2.05 \pm 1\%$ .

The strain was recorded for the bending moment bridge during the influence coefficient test with loads applied at points 1, 2, 3, and 4. The torsion bridge strains were recorded during the same test with loads applied at points 1 through 4, 7 and 8. All of the bridges were connected to a Baldwin 20 point switching unit and the strains were read on a Baldwin SR-4 portable strain indicator. The estimated accuracy of the strain readings is  $\pm 10$  micro in/in. Arm AB of each bridge was calibrated with  $20^K$ ,  $40^K$ ,  $100^K$ ,  $350^K$ , and  $700^K$  resistors.

#### 2. Results of Test

The load strain data recorded during the test is presented in Table 4.2.6. To determine the bending moment for bridge  $M_2$  the lever arm is measured from the load point parallel to the 50% chordline to a line passing through the strain gages, and perpendicular to the 50% chordline. To determine the torsional moment for bridge  $T_1$ , and  $T_2$ , the lever arm is measured from the load point perpendicular to the 50% chordline. The lever arms are summarized in Table 4.2.7. The moment strain relationship for bridge  $M_2$  is given in Figure 4.2.22. It is apparent that the output of this bridge is relatively insensitive to shear and torque. On the other hand it was found that the torsion bridge is quite sensitive to both shear and moment. However, even

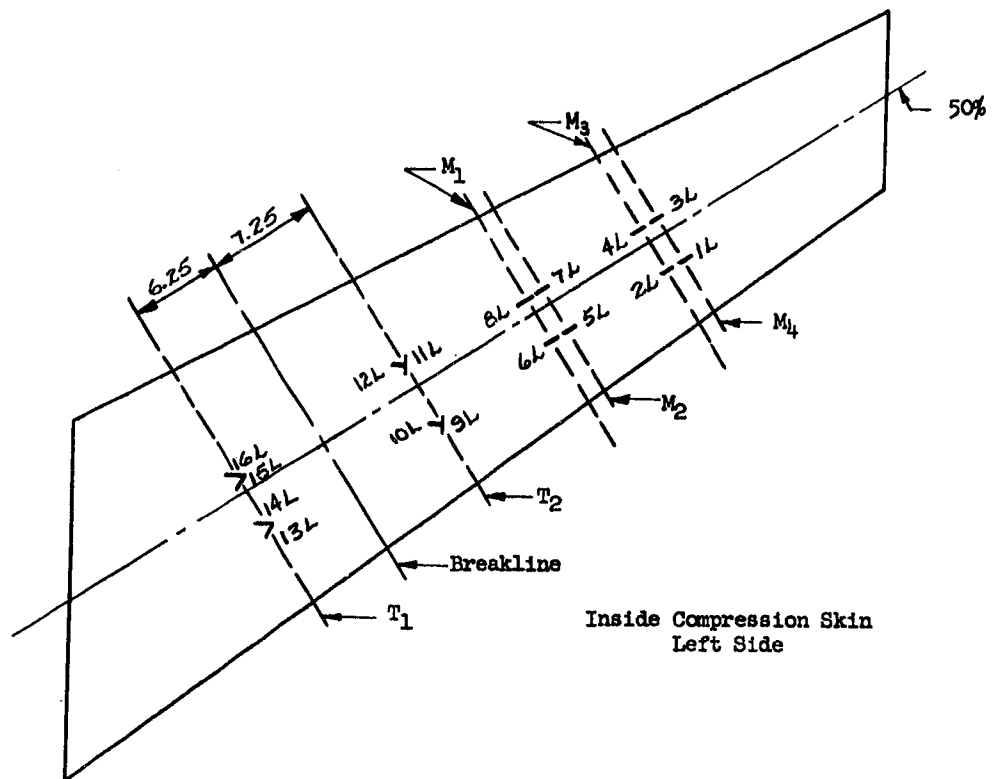


Fig. 4.2.20(a) PLAN VIEW LOCATION OF STRAIN GAGES

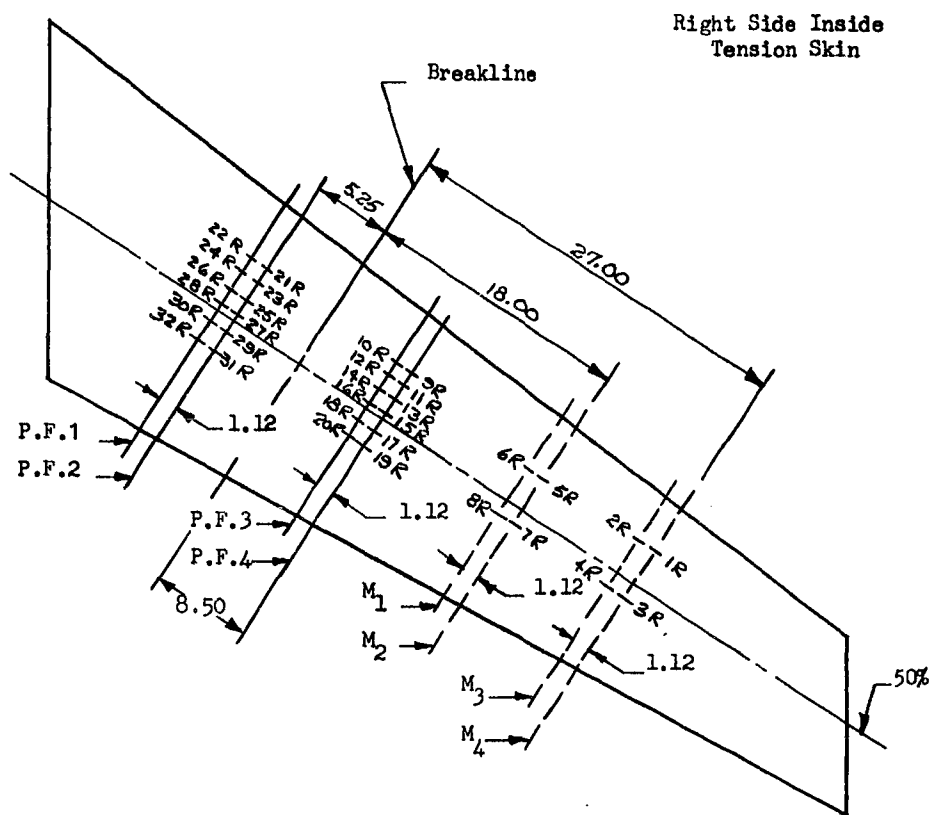
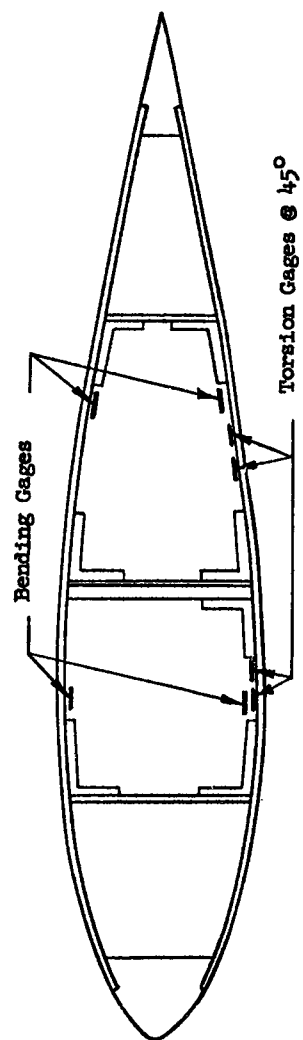
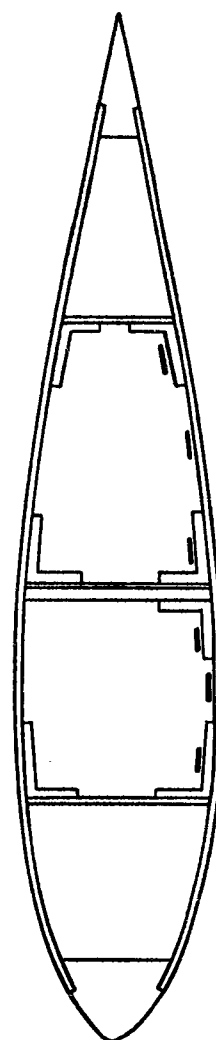


Figure 4.2.20 (b) PLAN VIEW LOCATION OF STRAIN GAGES



TYPICAL LOCATION OF ELASTIC, BENDING AND TORSION STRAIN GAGES



TYPICAL LOCATION OF POSTFAILURE BENDING MOMENT GAGES

Fig. 4.2.21

Table 4.2.5 STRAIN GAGE NUMBER AND LOCATION IN BRIDGE				
Bridge No.	Gage No.			
	AD	AB	BC	CD
M <sub>1</sub>				
M <sub>2</sub>	5 <sub>R</sub>	7 <sub>L</sub>	7 <sub>R</sub>	5 <sub>L</sub>
M <sub>3</sub>				
M <sub>4</sub>				
T <sub>1</sub>	13 <sub>L</sub>	16 <sub>L</sub>	15 <sub>L</sub>	14 <sub>L</sub>
T <sub>2</sub>	9 <sub>L</sub>	12 <sub>L</sub>	11 <sub>L</sub>	10 <sub>L</sub>

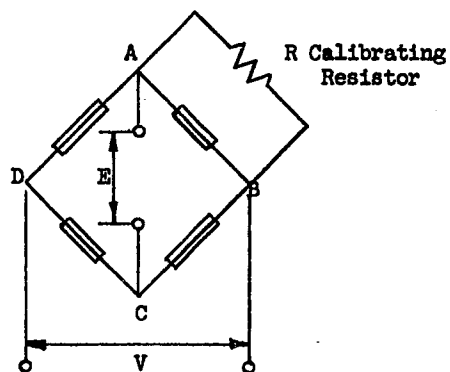


Table 4.2.6 LOAD STRAIN DATA				
Bridge No. Strain $\mu$ in/in				
Load Point	Load-lbs	$M_2$	$T_2$	$T_1$
1	0	0	0	0
	150	281	8	47
	300	568	17	95
	450	86	27	145
	300	592	17	97
	150	29	7	46
	0	0	2	1
2	0	0	0	0
	150	344	-34	27
	300	703	-67	57
	400	929	-9	7
	300	708	-69	5
	150	357	-38	2
	0	8	-4	2
3	0	0	0	0
	150			
	300	313	16	87
	450	464	28	127
	300	305	2	85
	150	149	9	45
	0	3	0	0

Table 4.2.6 LOAD STRAIN DATA				
Bridge No. Strain $\mu$ in/in				
Load Point	Load	M <sub>2</sub>	T <sub>2</sub>	T <sub>1</sub>
4	0	0	0	0
	150	220	41	18
	300	447	76	39
	450	646	110	60
	300	440	75	35
	150	220	38	15
	0	2	4	1
7	0	0	0	0
	150	2	8	30
	300	2	13	66
	450	3	20	97
	300	3	12	66
	150	2	8	32
	0	92	1	0
8	0	0	0	0
	150	20	42	3
	300	40	84	3
	450	60	123	7
	300	40	80	5
	150	20	39	2
	0	8	1	1

Table 4.2.7 SUMMARY OF BENDING & TORSION LEVER ARMS						
BENDING MOMENT ARM - INCHES						
Bridge	Load Point 1	Load Point 2	Load Point 3	Load Point 4	Load Point 7	Load Point 8
M <sub>1</sub>	22.89	25.60	12.77	15.88		
M <sub>2</sub>	21.77	24.48	11.65	14.76		
M <sub>3</sub>	13.89	16.60	3.77	6.88		
M <sub>4</sub>	12.77	15.48	2.65	5.76		
T <sub>1</sub>	46.02	48.73	35.90	39.01	18.29	22.10
T <sub>2</sub>	32.52	35.23	22.40	25.51	4.79	7.60
Torsion Moment Arm						
All Bridges	+2.62	-1.53	+2.98	-1.80	+3.62	-2.20



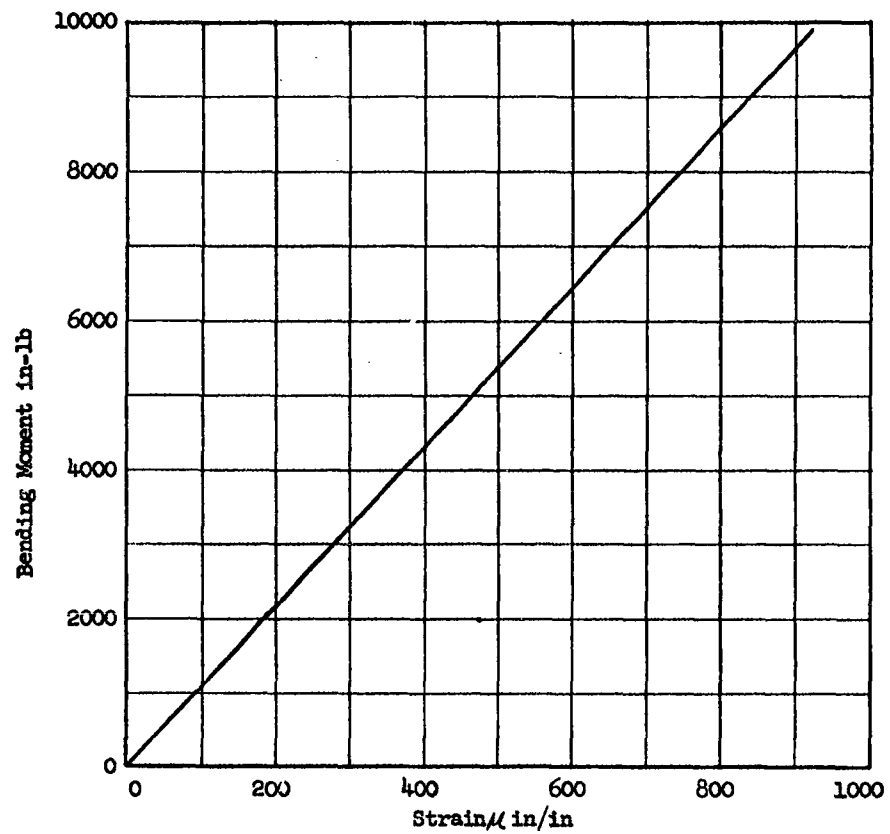


Fig. 4.2.22 BENDING MOMENT - STRAIN RELATIONSHIP FOR ELASTIC BRIDGE  $M_2$   
MADE UP OF STRAIN GAGES 5R, 7R, 5L, 7L

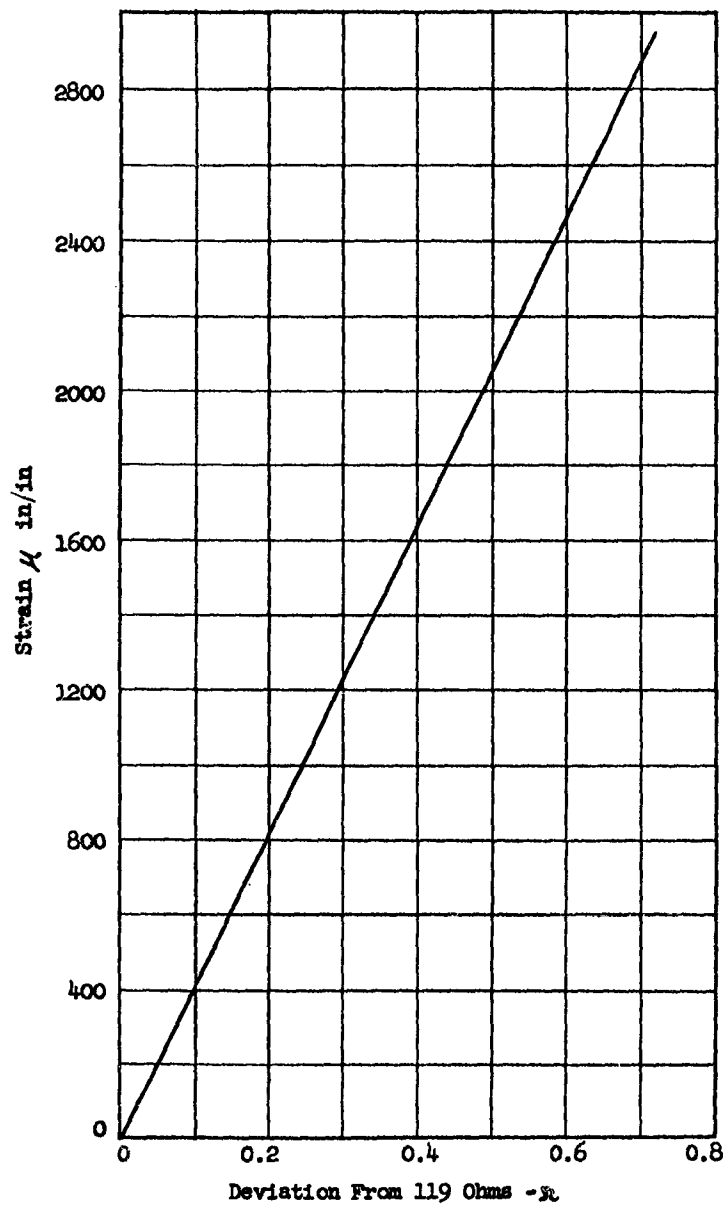


Fig. 4.2.23 INDICATED STRAIN FOR BRIDGES  $M_1$ ,  $T_1$ , AND  $T_2$  VS. LOAD  
SIMULATED BY RESISTANCES OF 20k, 40k, 100k, 350k  
AND 700k OHMS

when the sensitivity to shear and moment is considered, it was not possible to obtain a linear relationship between bridge output and the sum of the weighted moment, shear and torsion for loads applied at points 1 - 4, 7 and 8. The calibration of all three elastic bridges is given in Figure 4.2.23 with simulated strain plotted as a function of deviation from strain gage resistance.

#### 4.2.3 DESTRUCTION TESTS

##### 4.2.3.1 POSTFAILURE MOMENT ROTATION TEST

###### 1. Description of Test

The purpose of this test was to determine the applied moment rotation characteristics of the structural specimen in the postfailure region up to a peak angle of rotation of at least 50 degrees.

A single point load was applied at the centroid of the wing planform outboard of the breakline. This location was chosen in order to approximate the ratio of bending moment to shear which would exist for a blast induced airload applied in the field tests. The load was applied by a 6 ton capacity chain hoist. The hoist can be moved along a beam which was aligned parallel to and directly under the 50% chordline. The destruction test set up is shown in Figure 4.2.24.

In the postfailure region the applied load was always kept perpendicular to the wing outboard of the breakline. The load was distributed to the wing by a heavy aluminum clamp which was contoured and glued to the tension skin of the specimen. The static weight of the clamp and the structure outboard of the failure station produced an initial bending moment of 1350 in/lb at the breakline. A tension link which was calibrated from 0 - 8000 lbs. was used to determine the magnitude of the load applied to the wing. It is estimated that the maximum error in determining the load from the strain recorded on the tension link is  $\pm 50$  lbs.

The primary means for measuring the rotation of the breakline was a dial gage frame which is shown in Figure 4.2.25. The two vertical posts of the dial gage frame which protrudes through a slot in the tension



Fig. 4.2.24 DESTRUCTION TEST SET UP FOR MODEL (6R)



Fig. 4.2.25 DIAL GAGE FRAME FOR MEASURING POST-ELASTIC  
ROTATION OF MODEL (6R)

skin were bolted to the 1/4 inch thick web of the center spar. Both of the dial gages used to measure the angular rotation were placed above the tension skin, 8.00 inch apart. As a result of this arrangement, the vertical dial gage posts were unaffected by the compression skin buckle in the postfailure region of deformation. In addition, the heavy web of the center spar was relatively unaffected by the local buckling of structural elements in the failure bay. The estimated accuracy of the computed angle of rotation as measured from the dial gage readings is  $\pm 5$  minutes up to a hinge angle of 40 degrees. At this point, the top dial gage could no longer be used and subsequent deflections were scaled. The estimated accuracy of the computed angle of rotation after 40 degrees is  $\pm 10$  minutes.

A secondary means for measuring the angle of rotation was provided in the event trouble developed with the dial gage frame readings. This method consisted of approximating the slope, inboard and outboard of the breakline by measuring vertical deflections. The displacement of the root was determined by four dial gages located at the ends of the sled forebody as shown in Fig. 4.2.24. One dial gage was located just inboard of the failure bay, and a second gage, outboard of the failure bay. A three foot steel scale was suspended from the trailing edge, 3/4 inch inboard of the tip. The deflection of the metal rule was read by means of a transit level to the nearest 1/32 inch.

To insure that the dial gage frame and load cell were functioning properly, two cycles of loading were applied and released, having a peak value of approximately 5000 lb. The corresponding values of rotation were determined from the dial gage readings and compared with values of rotation which were analytically estimated. The two values were found to be in good agreement.

## 2. Results of Test

Initial application of the 5000 lb. check out loads produced some plastic buckling of the .025" thick leading and trailing edge cover plates in the failure bay. As a consequence, there was a small permanent set when

this load was released. Following this check out run the load was gradually increased, giving rise to larger plastic deformation of the leading and trailing edge cover plates. At a peak load of 6920 lbs., a wrinkling mode of failure developed across the compression skin as shown in Figure 4.2.26. The measured length of the buckle was 2.65 inches. The appearance of the failure mode was identical to that observed on the failure bay model which was tested at MIT. The peak bending moment at the breakline was found to be 140800 in-lb., as compared with 136000 in-lb for the failure bay model. It should be noted that the failure bay model previously tested at MIT did not have the leading and trailing edge cover plates, as did the specimen tested at AAI. Upon precipitation of failure, the load dropped off to 4450 lb. and the angle of rotation increased 1.44 degrees. At an angle of 8.86 degrees and a load of 1540 lb., the leading edge cover plate tore along the forward spar. At an angle of 13.14 degrees and a load of 1175 lb., a 3 inch crack developed along the inboard clamped edge of the compression buckle. At an angle of 18.04 degrees and a load of 400 lb. a crack developed all the way across the crown of the compression skin buckle. At an angle of 14.35 degrees and zero load the 3 inch crack along the inboard clamped edge of the compression buckle was extended all the way across the compression skin. At an angle of 20.77 degrees and a load of 1230 lb., there appeared to be some binding of the leading and trailing edge cover plates. At an angle of 31.58 degrees and a load of 1010 lbs., the compression buckle collapsed as shown in Figure 4.2.27 and 4.2.28. At an angle of 49 degrees and a load of 1140 lbs., a crack developed all of the way across the tension skin. From 44.3 degrees out to 59.6 degrees there was considerable internal cracking of structural members observed audibly, at every recorded increment of loading. The appearance of the internal structure with the tension skin removed is shown in Figures 4.2.29 and 4.2.30. The load, adjusted bending moment, and angular rotation as reduced from the data recorded during the test is presented in Table 4.2.8 and plotted in Figure 4.2.31. The elastic rotation of the failure bay between the dial

gage posts has been subtracted from the total rotation, and the bending moment at the breakline has been corrected for the effect of the mass outboard of the breakline. It did not appear practical to deform the specimen beyond 60 degrees due to the geometry of the test stand and chain hoist; however, no appreciable binding was evidenced at the peak recorded angle of rotation of 59.6 degrees.

The results from the secondary method of measuring angular deflections were used to spot-check rotations computed from the dial gage frame data. Good agreement was obtained between the two methods. The results from the secondary method are less accurate, and, as a consequence, are not included in this report.

#### 4.2.3.2 CALIBRATION OF POSTFAILURE STRAIN GAGE BRIDGES

##### 1. Description of Test

The second objective of the destruction test was to provide sufficient information to construct two bending moment bridges which would have a linear output in the postfailure as well as the elastic region of response. It was intended that these two bridges (one of which should be outboard of the failure bay and one inboard of the failure bay) should be made up of any combination of the twenty-four gages labeled 9R through 32R. All of the postfailure gages used on the structural model are Baldwin SR-4 Type EBF-7D having a gage factor of  $2.05 \pm 1\%$ . Each of the 24 postfailure strain gages was connected into one arm of a four arm bridge having 120 ohm resistors in the other three arms. All of the bridges were connected to either a Baldwin 20 or 12 point switching unit and the strains from each of the 24 bridges were read on a Baldwin SR-4 portable strain indicator. The arm containing the strain gage was calibrated with  $20^K$  and  $40^K$  resistors.

##### 2. Results of Test

The strain measurements recorded for each postfailure strain gage are presented in Table 4.2.8.

By comparing the strain measurements of the primary gage with its corresponding back up gage, there appears to be good consistency in the behavior of the two sets of gages. Some drift was observed in the SR-4 strain indicator during the course of the test which may have been as much as 100 micro inches per inch of indicated strain.

The indicated strain was plotted as a function of load for each of the 24 gages. Workable combinations of the six gages at each of four stations were selected by careful inspection of the characteristics of each gage in the postfailure region. Approximately twelve such combinations were investigated by weighting the individual gages to obtain the best linear load vs. combined strain throughout the elastic and plastic regions of deformation.

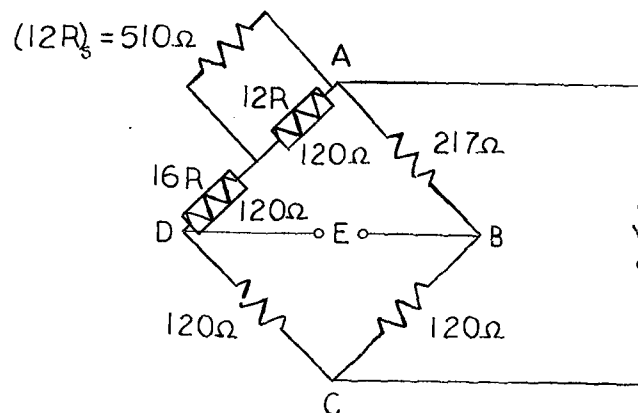
The four best combinations of strain gages have been plotted in Figures 4.2.32 through 4.2.35. The outboard postelastic bridge which was finally selected for field use was constructed from strain gages 12R and 16R. The corresponding back up gages chosen were, 11R for 12R and 15R for 16R. The inboard postelastic bridge was constructed from strain gages 21R and 29R, with gages 22R and 30R acting as the corresponding back up gages. In order to limit the strain output of a particular gage in proportion to the weighting factors indicated in Figure 4.2.33 and 4.2.34, a shunt resistor is placed in parallel with the strain gage. The construction of the two postelastic strain gage bridges, and the calculations to determine the weighing resistors is presented in the following discussion.

#### Postelastic Bending Moment Bridge 12R and 16R

Primary Gage	Back up Gage	Desired Weighting Factor
12R	11R	0.647
16R	15R	1.000



### Construction of Bridge



Strain output for bridge 12R, 16R is:

$$\epsilon_o = \frac{1}{G.F.} \left( \frac{\Delta(16R) + \left( \frac{(12R)_s}{(12R)_s + 12R} \right)^2 \Delta(12R)}{R_{AD}} \right)$$

Where G.F. = 2.05

Since  $\Delta(16R)$  and  $\Delta(12R)$  remains the same for a given strain when the individual gages are combined into a single bridge, the weighting factors are as follows:

$$K_{16} = 1.000$$

$$K_{12} = \left( \frac{(12R)_s}{(12R)_s + 12R} \right)^2 = \left( \frac{510}{510 + 120} \right)^2$$

$$K_{12} = 0.655$$

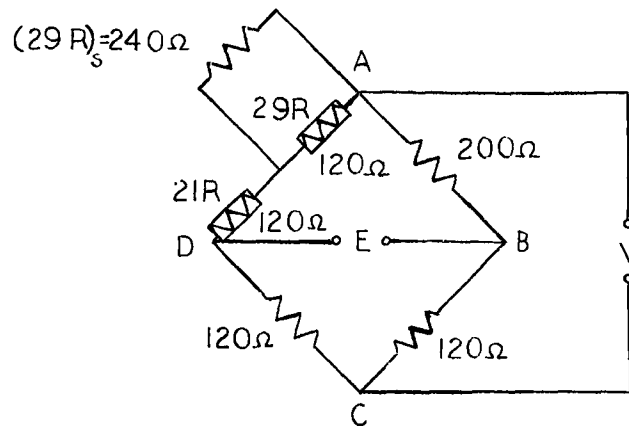
Total resistance of arm AD and AB

$$R_{AD} = 120 + \frac{510 \times 120}{510 + 120} = 217\Omega$$

# Postelastic Bending Moment Bridge 21R and 29R

Primary Gage	Back Up Gage	Desired Weighting Factor
21R	22R	1.000
29R	30R	0.452

## Construction of Bridge



Strain output for bridge 21R, 29R is:

$$\epsilon_o = \frac{1}{G.F.} \left( \frac{\Delta(21R) + \left( \frac{(29R)_s}{(29R)_s + 29R} \right)^2 \Delta(29R)}{R_{AD}} \right)$$

The weighting factors are as follows:

$$K_{21} = 1.00$$

$$K_{29} = \left( \frac{(29R)_s}{(29R)_s + 29R} \right)^2 = \left( \frac{240}{240 + 120} \right)^2$$

$$K_{29} = 0.444$$

Total Resistance of Arm AD and AB

$$R_{AD} = 120 + \frac{240 \times 120}{240 + 120} = 200\Omega$$

TABLE 4.2.8					
LOAD, MOMENT, ROTATION & STRAIN					
RUN #	1	2	3	4	5
Applied Load lbs.	0	1920	3900	4910	0
Moment @ Breakline in-lb	1350	40040	79940	100290	1350
Rotation @ Breakline Deg.	0	.317	.668	.82	.061
Strain in/in					
Gage No.					
9R	0	505	985	1145	-85
10R	↑	540	1050	1280	-20
11R		500	1020	1300	+100
12R		550	1150	1360	-30
13R		490	890	990	-50
14R		600	1110	1260	- 10
15R		560	1075	1280	+ 10
16R		500	1075	1300	+ 10
17R		640	1180	1540	+130
18R		530	1200	1460	0
19R		355	605	715	- 20
20R		410	750	920	- 10
21R		685	1345	1670	+105
22R		640	1390	1700	+120
23R		850	1760	2150	- 30
24R		835	1665	2065	- 5
25R		840	1710	2110	+ 70
26R		880	1770	2200	+120
27R		660	1410	1750	+65
28R		780	1590	2000	+80
29R		910	1630	2040	+20
30R		840	1610	1930	-30
31R	↓	805	1660	1960	-65
32R	0	900	1870	2180	-70

TABLE 4.2.8					
LOAD, MOMENT, ROTATION & STRAIN					
RUN #	6	7	8	9	10
Applied Load lbs.	2680	5140	5650	6120	6660
Moment @ Breakline in-lb	55,350	104,920	115,200	124,670	135,550
Rotation @ Breakline Deg	.404	.798	.848	.956	1.085
Strain in/in					
Gage No.					
9R	655	1245			1445
10R	770	1440			1730
11R	880	1530			1920
12R	830	1600			1990
13R	625	1105			1395
14R	760	1380			1670
15R	770	1380			1660
16R	740	1370			1690
17R	1000	1750			2170
18R	760	1540			1930
19R	450	770			890
20R	505	975			1165
21R	1030	1860			2290
22R	1110	1990			2490
23R	1150	2260			2885
24R	1195	2265			2835
25R	1250	2325			2945
26R	1190	2330			2910
27R	1025	1940			2390
28R	1180	2220			2775
29R	1295	2305			2915
30R	1125	2095			2605
31R	1115	2105			2515
32R	1280	2390			2950

TABLE 4.2.8					
LOAD, MOMENT, ROTATION & STRAIN					
RUN #	11	12	13	14	15
Applied Load lbs.	6920	4450	2150	0	2220
Moment @ Breakline in-lb	140,790	91,020	44,670	1350	46080
Rotation @ Breakline Deg	1.18	2.622	2.013	1.254	1.819
Strain in/in					
Gage No.					
9R		825		-375	
10R		1040		-160	
11R		1640		450	
12R		1820		330	
13R		880		- 25	
14R		1050		-130	
15R		1120		- 90	
16R		1120		-120	
17R		1660		330	
18R		1350		-160	
19R		630		- 30	
20R		895		15	
21R		1200		-220	
22R		1350		- 20	
23R		2175		- 10	
24R		2185		135	
25R		2195		185	
26R		2000		- 50	
27R		1915		175	
28R		2055		145	
29R		2615		565	
30R		2235		185	
31R		1935		-195	
32R		2260		40	

TABLE 4.2.8					
LOAD, MOMENT, ROTATION & STRAIN					
RUN #	16	17	18	19	20
Applied Load lbs.	4680	3600	2710	2190	1200
Moment @ Breakline in-lb	95650	73890	55960	45480	25530
Rotation @ Breakline Deg	2.750	3.689	4.669	5.751	5.020
Strain in/in					
Gage No.					
9R	715			235	
10R	970			500	
11R	1660			1240	
12R	1730			1270	
13R	925			375	
14R	1070			400	
15R	1060			460	
16R	1050			440	
17R	1670			1190	
18R	1260			720	
19R	650			330	
20R	835			415	
21R	1130			150	
22R	1330			400	
23R	2110			1600	
24R	2135			1645	
25R	2155			1415	
26R	1900			900	
27R	1845			1165	
28R	1955			1005	
29R	2625			2205	
30R	2185			1665	
31R	1835			565	
32R	2200			950	

TABLE 4.2.8					
LOAD, MOMENT, ROTATION & STRAIN					
RUN #	21	22	23	24	25
Applied Load lb.	0	1010	2050	1540	1400
Moment @ Breakline in-lb	1350	21690	42,650	32,360	29,540
Rotation @ Breakline Deg	3.488	4.588	5.963	8.865	10,342
Strain in/in					
Gage No.					
9R	-385		195		
10R	-180		440		
11R	510		1215		
12R	380		1310		
13R	- 85		405		
14R	-160		420		
15R	-150		425		
16R	-170		410		
17R	420		1210		
18R	-140		590		
19R	- 80		340		
20R	-155		365		
21R	-340		80		
22R	-170		350		
23R	240		1590		
24R	345		1595		
25R	335		1390		
26R	- 80		840		
27R	155		1145		
28R	75		955		
29R	755		2215		
30R	315		1655		
31R	-395		485		
32R	- 90		920		

TABLE 4.2.8					
LOAD, MOMENT, ROTATION & STRAIN					
RUN #	26	27	28	29	30
Applied Load lb.	1175	610	0	625	1175
Moment @ Breakline in-lb	24,990	13,610	1332	13,920	24,990
Rotation @ Breakline Deg	13.141	11.274	9.039	11.274	13.393
Strain in/in					
Gage No.					
9R	85		-315		110
10R	350		- 35		365
11R	1155		675		1175
12R	1110		570		1060
13R	45		-125		95
14R	0		-220		75
15R	- 5		-250		-15
16R	- 25		-260		-25
17R	1130		640		1210
18R	530		- 80		690
19R	160		-120		180
20R	115		-235		125
21R	-270		-410		-270
22R	- 20		-180		-120
23R	1810		670		1860
24R	1795		755		1765
25R	855		360		840
26R	200		- 80		380
27R	720		30		760
28R	320		- 85		315
29R	2295		1145		2335
30R	1585		535		1620
31R	-400		-625		-375
32R	130		-430		60



TABLE 4.2.8					
LOAD, MOMENT, ROTATION & STRAIN					
RUN #	31	32	33	34	35
Applied Load lbs.	1120	1000	490	0	500
Moment @ Breakline in-lb	23,870	21,420	11,160	1308	11,370
Rotation @ Breakline Deg	15.568	19.677	18.035	14.351	16.77
Strain in/in					
Gage No.					
9R		30		-305	
10R		490		35	
11R		1255		685	
12R		1320		680	
13R		- 60		-185	
14R		-190		-270	
15R		-180		-345	
16R		-240		-360	
17R		1250		695	
18R		580		60	
19R		135		-145	
20R		50		-260	
21R		-425		-585	
22R		- 90		-325	
23R		1960		830	
24R		1885		875	
25R		315		150	
26R		-230		-210	
27R		570		- 70	
28R		65		-175	
29R		2585		1305	
30R		1650		635	
31R		-555		-775	
32R		-120		-550	

TABLE 4.2.8					
LOAD, MOMENT, ROTATION & STRAIN					
RUN #	36	37	38	39	40
Applied Load lbs.	1230	1250	1360	1170	1000
Moment @ Breakline in-lb	26,050	26,410	28,610	24,760	21,320
Rotation @ Breakline Deg	20.769	24.917	26.807	28.688	29.989
Strain in/in					
Gage No.					
9R	15				
10R	365				
11R	1115				
12R	1290				
13R	- 95				
14R	-150				
15R	-225				
16R	-240				
17R	1140				
18R	650				
19R	100				
20R	45				
21R	-415				
22R	- 80				
23R	2010				
24R	1895				
25R	230				
26R	190				
27R	495				
28R	5				
29R	2475				
30R	1645				
31R	595				
32R	160				

TABLE 4.2.8					
LOAD, MOMENT, ROTATION & STRAIN					
RUN #	41	42	43	44	45
Applied Load lbs.	1010	500	0	400	850
Moment @ Breakline in-lb	21,500	11,250	1217	9240	18275
Rotation @ Breakline Deg	31.575	29.471	25.587	29.116	31.813
Strain in/in					
Gage No.					
9R	25		-295		
10R	365		55		
11R	1185		835		
12R	1330		790		
13R	-225		-275		
14R	-380		-370		
15R	-395		-495		
16R	-460		-525		
17R	1260		830		
18R	760		250		
19R	60		-200		
20R	-35		-360		
21R	-495		-715		
22R	-140		-484		
23R	2110		1060		
24R	1985		1065		
25R	-270		-190		
26R	-680		-510		
27R	160		-320		
28R	-430		-465		
29R	2535		1525		
30R	1640		745		
31R	-785		-955		
32R	-300		-670		

TABLE 4.2.8					
LOAD, MOMENT, ROTATION & STRAIN					
RUN #	46	47	48	49	50
Applied Load lbs.	1100	1080	1100	1100	1200
Moment @ Breakline in-lb	23290	22850	23210	23175	25150
Rotation @ Breakline Deg	33.753	36.585	39.054	41.624	44.307
Strain in/in					
Gage No.					
9R	20			65	
10R	485			630	
11R	1255			1450	
12R	1485			1615	
13R	-225			-285	
14R	-410			-490	
15R	-415			-505	
16R	-495			-565	
17R	1290			1500	
18R	710			740	
19R	50			90	
20R	- 50			0	
21R	-475			-450	
22R	35			65	
23R	2170			2200	
24R	2065			2145	
25R	-290			-470	
26R	-1010			-1100	
27R	140			75	
28R	-435			-625	
29R	2705			2905 <sup>1</sup>	
30R	1685			1725	
31R	-775			-845	
32R	-130			-270	

TABLE 4.2.8					
LOAD, MOMENT, ROTATION & STRAIN					
RUN #	51	52	53	54	55
Applied Load lbs.	910	1200	1140	1140	740
Moment @ Breakline in-lb	19300	25090	23880	23860	15800
Rotation @ Breakline Deg	44.307	47.475	47.475	49.00	49.00
Strain in/in					
Gage No.					
9R					
10R					
11R					
12R					
13R					
14R					
15R					
16R					
17R					
18R					
19R					
20R					
21R					
22R					
23R					
24R					
25R					
26R					
27R					
28R					
29R					
30R					
31R					
32R					

TABLE 4.2.8					
LOAD, MOMENT, ROTATION & STRAIN					
RUN #	56	57	58	59	60
Applied Load lbs.	1030	930	910	870	0
Moment @ Breakline in-lb	21550	19540	19,020	18,210	810
Rotation @ Breakline Deg	53.85	53.85	59.6	59.6	53.15
Strain in/in					
Gage No.					
9R					
10R					
11R					
12R					
13R					
14R					
15R					
16R					
17R					
18R					
19R					
20R					
21R					
22R					
23R					
24R					
25R					
26R					
27R					
28R					
29R					
30R					
31R					
32R					



Fig. 4.2.26 INITIAL FAILURE OF MODEL (6R)

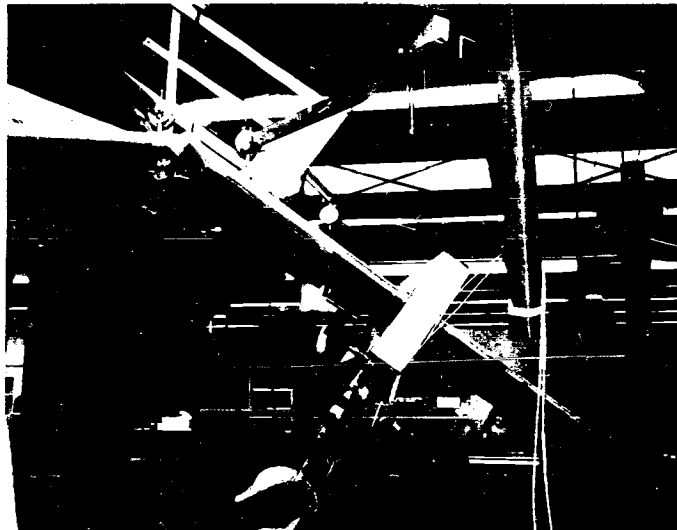


Fig. 4.2.27 BROKEN (6R) MODEL



Fig. 4.2.28 COLLAPSED COMPRESSION BUCKLE OF (6R) MODEL





Fig. 4.2.29 DEFORMED INTERNAL STRUCTURE OF MODEL (6R)



Fig. 4.2.30 DEFORMED INTERNAL STRUCTURE OF MODEL (6R)

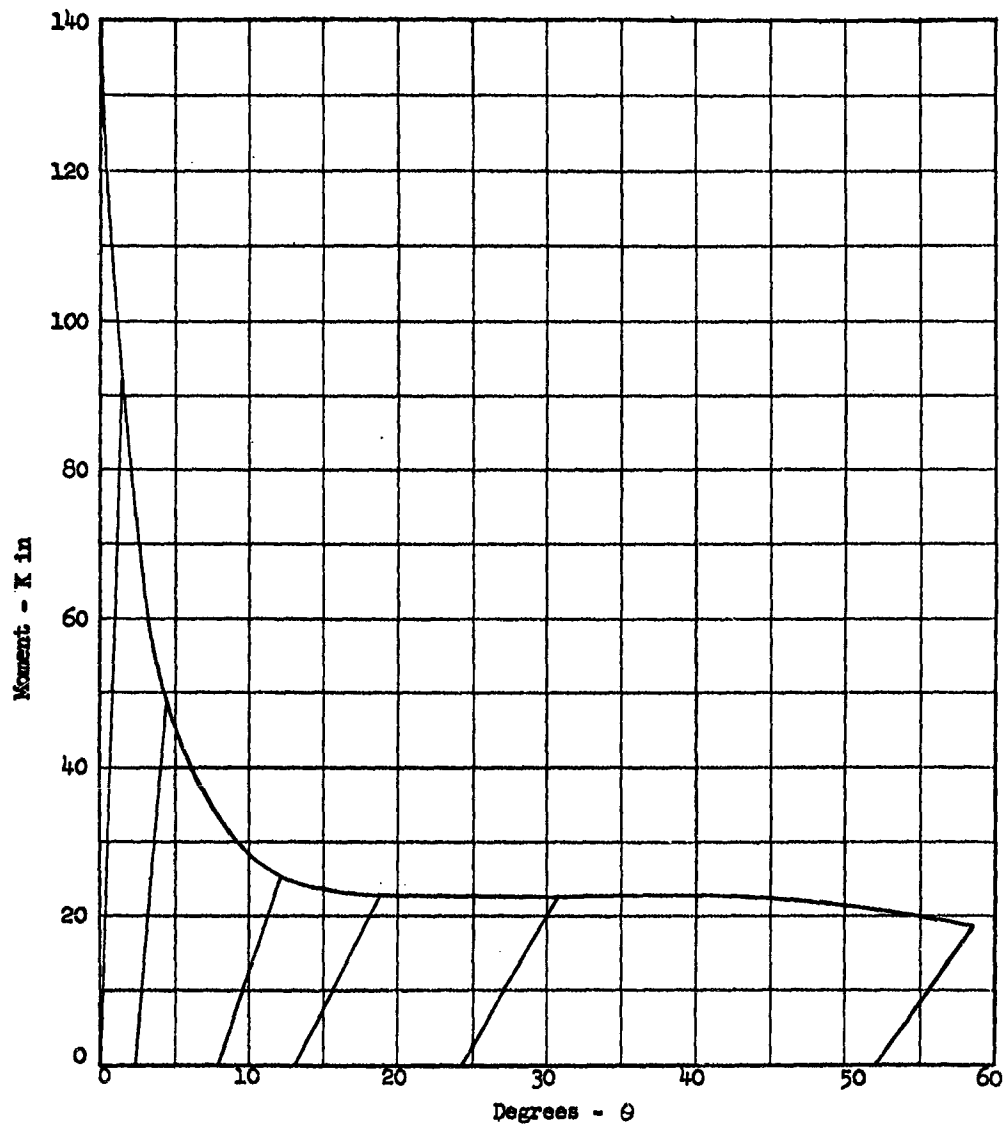


Fig. 4.2.31 POSTFAILURE MOMENT ROTATION CURVE AT THE BREAKLINE

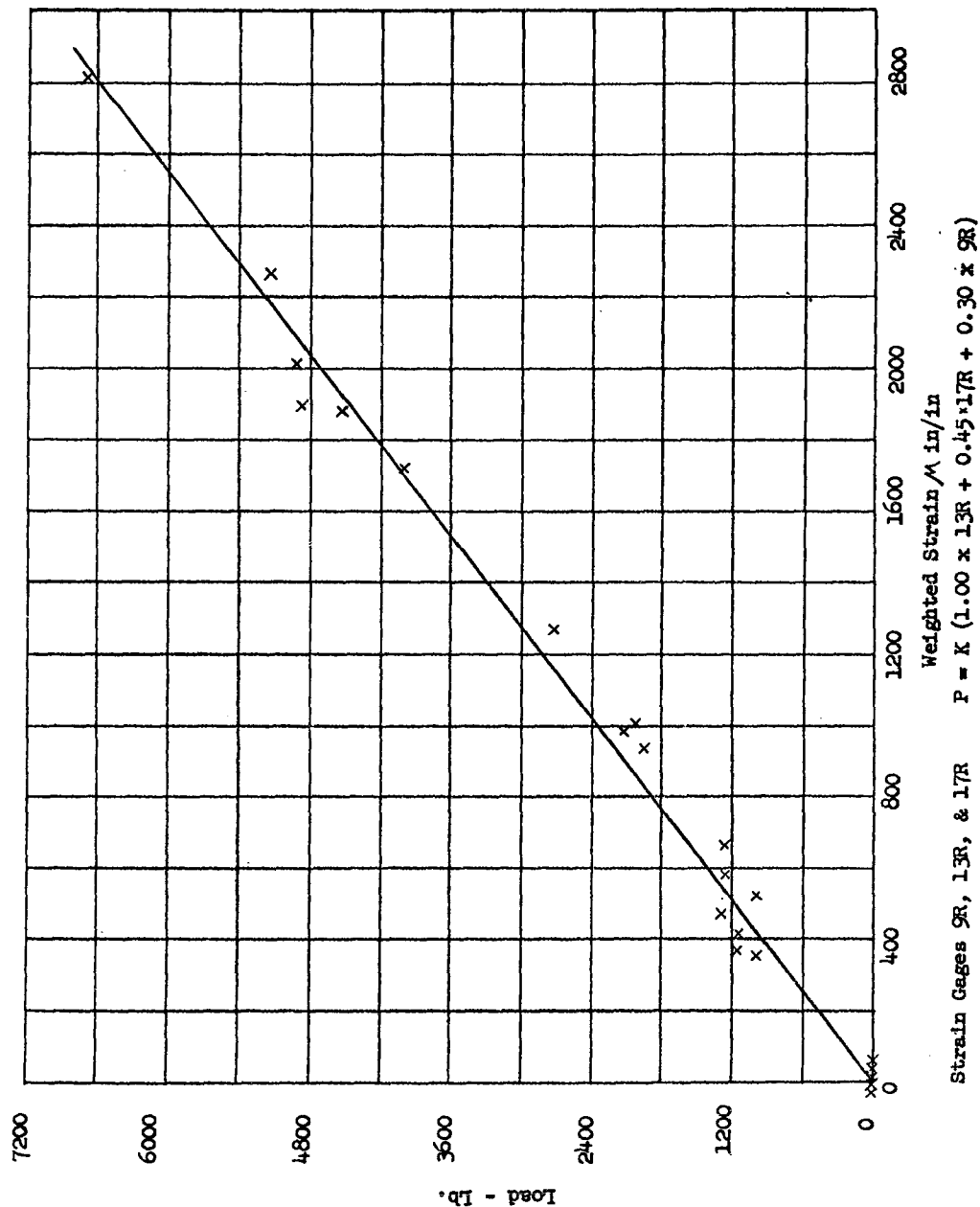


Fig. 4.2.32 POSTFAILURE BENDING MOMENT BRIDGE NO. 1



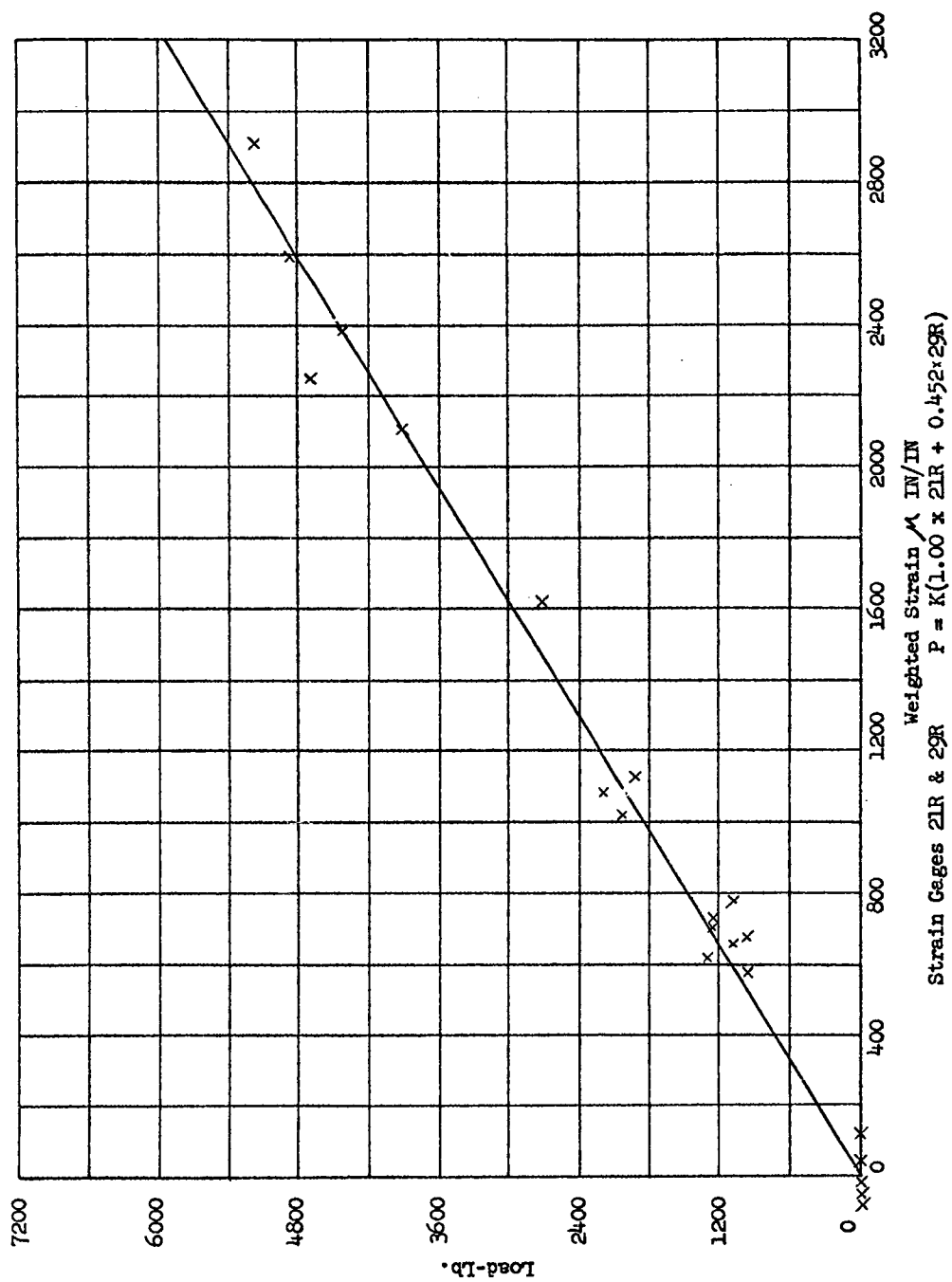


Fig. 4.2.34 POSTFAILURE BENDING MOMENT BRIDGE NO.3

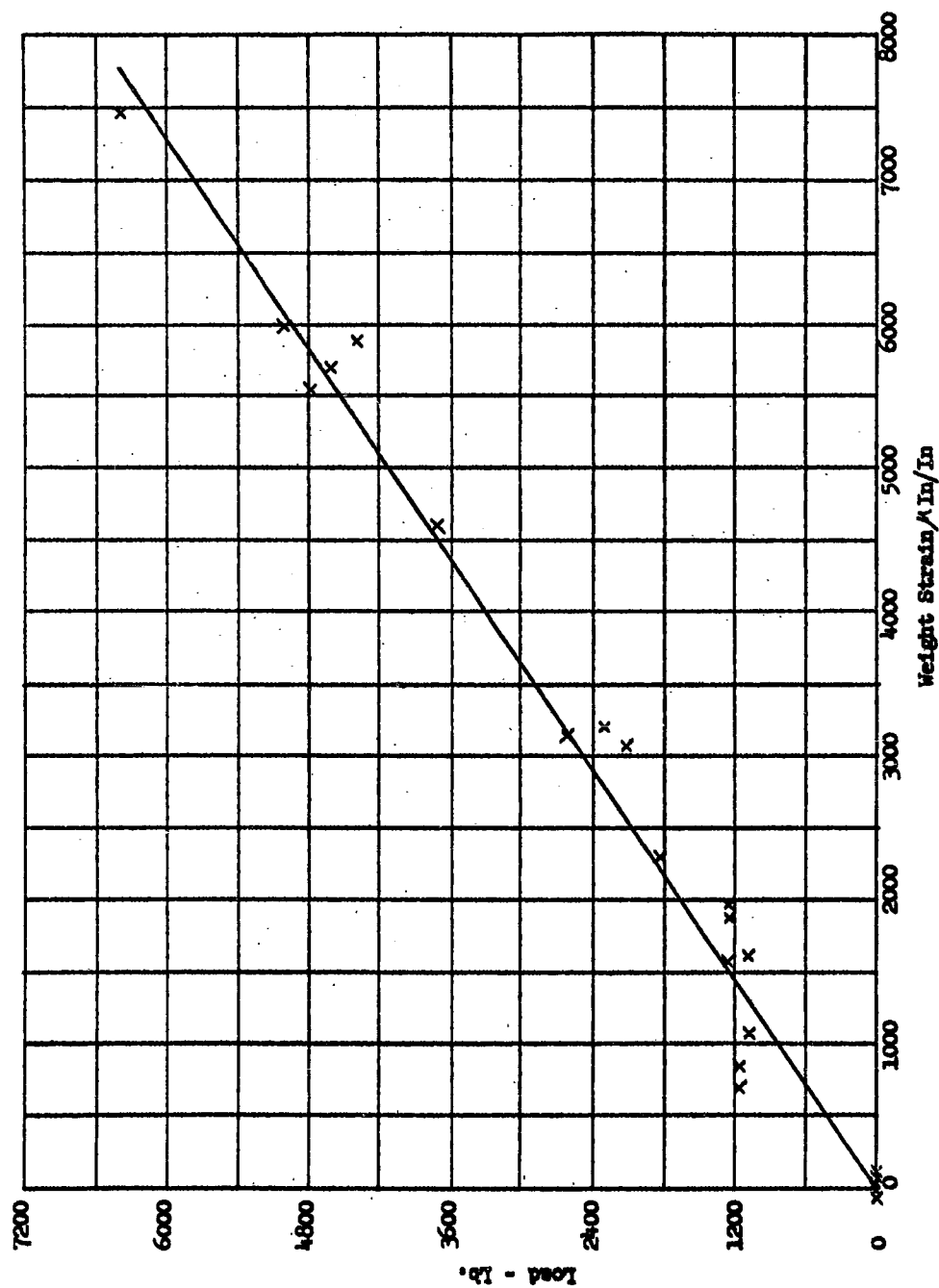


Fig. 4.2.35 POSTFAILURE BENDING MOMENT BRIDGE NO. 4

## 5.0 SLED INSTRUMENTATION

### 5.1 DESCRIPTION OF INSTRUMENTATION

#### 5.1.1 LOCATION AND TYPES OF TRANSDUCERS

Instrumentation of the (6L) and (6R) specimens include linear accelerometers, pressure transducers and strain gages which are located as shown in Fig. 5.1.1. The number of recorded instrumentation channels for model (6L) include (2) acceleration, (19) differential pressure, (18) absolute pressure, (2) elastic bending moment, and (2) elastic torsion. For the (6R) model, the same number of acceleration and pressure channels were used along with (4) elastic bending moment, (2) elastic torsion, and (2) postfailure bending moment channels.

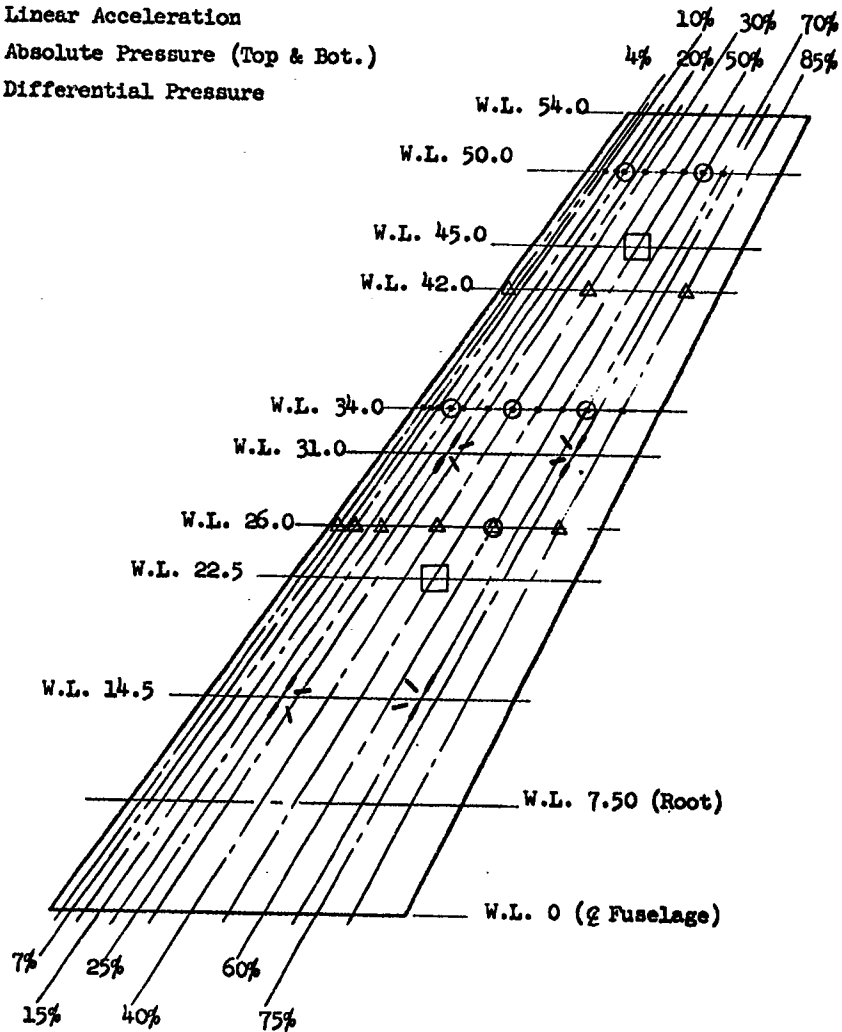
The accelerometers used were CEC Type 4-202-0001 + 1000g, made by Consolidated Electrodynamics Corporation. Each of the two accelerometers shown in Fig. 5.1.1 require one recording channel. Their sensitive axes are aligned to measure accelerations perpendicular to the wing surface.

The pressure transducers used are NASA Model TP49 and BRL Miniature Piezoelectric gages. Their locations are shown in Fig. 5.1.1. All of the gages are arranged in absolute or differential pairs. One absolute gage measures pressure on one side of the wing, and its mate measures pressure on the opposite side of the wing, each requiring a separate recording channel. A differential pair consists of two gages located on opposite sides of the wing and connected electrically to indicate the difference of gage measurements. The differential pair of gages require only one recording channel. Toward the leading and trailing edges, where the wing thickness is too small for two transducers, a NASA differential gage of double ended construction permits use of a single gage to obtain differential pressure measurements. These particular types of gages require a single recording channel.

The strain gages used on the solid (6L) specimen are type EBF-7S + manufactured by Baldwin Lima Hamilton. Those used on the structural (6R) specimen are Type EBF-7D +.

### Legend

- ⊙ BRL Miniature Piezoelectric Gage
- |< Strain (Top & Bot.)
- Linear Acceleration
- △ Absolute Pressure (Top & Bot.)
- Differential Pressure



Note: Bending Moment and Torque Measurements were made with Strain Gage Bridges at Top and Bottom Surfaces.

Fig. 5.1.1 INSTRUMENTATION INSTALLATION - AIRLOAD SPECIMEN



The (32) strain gages on the (6L) specimen were arranged to measure elastic bending moment and torsion at the inboard and outboard stations shown in Figure 5.1.1. The outboard and inboard bending moment bridge is constructed of four active gages, two on the tension side, and two on the compression side, all measuring stress along the chordwise direction. A back-up bridge of identical construction was located at each of these stations. The outboard and inboard torsion bridge is also constructed of four active gages on the compression faces, each measuring strain at an angle of 45 degrees to the chordwise direction. Back-up bridges were also located at each of these stations.

Thirty-four (34) of the strain gages shown on the lab model (6R) Figure 4.2.20 were selected for use on the field model. The outboard and inboard torsion bridges were constructed of four active gages on the compression side, each measuring strain at an angle of 45 degrees to the chordwise direction. No back-ups were used for these bridges. There were two primary elastic bending moment bridges each constructed of four active gages, (2) on the compression side and (2) on the tension side, all measuring strain in a chordwise direction. A back-up bridge of identical construction was located at each of these stations to account for a total of (16) elastic bending moment strain gages.

The postfailure moment bridges, located outboard and inboard of the failure bay on the tension side of the wing, require (10) active strain gages. These (10) gages were selected from the (24) postfailure gages on the laboratory specimen as shown in Figure 4.2.20. Four, one active arm bridges were constructed from the (10) gages, such that their combined weighted outputs would give a linear relationship between bending moment and indicated strain in the post-elastic as well as elastic regions of deformation. The first bridge consists of gages 13, 17, and 9 with respective weighting factors of 1.00, 0.45 and 0.308. The second bridge consists of gages 16 and 12 with respective weighting factors of 1.00 and 0.655. The third bridge consists of gages 21 and 29 with weighting factors of 1.00 and 0.444. The fourth bridge consists of gages 30, 32 and 26 with weighting factors of 1.00, 1.00

and 0.610. The strain gages were weighted by applying the appropriate shunt resistors across the gages. For temperature compensation an additional (10) strain gages were used as dummy resistors to complete the bridges.

#### 5.1.2 RECORDING EQUIPMENT

The original recording equipment installed in the sled was a CEC 20 Kc carrier system. This consisted of a type 5-119 Recording Oscillograph, employing series 7-300 galvanometers, and eight four channel type 1-127 Carrier Amplifiers. Recording speed used was 100 inches per second. Spot width is given by the manufacturer as 0.010 inch static and 0.005 inch dynamic, corresponding to 100 microseconds static and 50 microseconds dynamic uncertainty in time measurement. Assuming that a reading accuracy of 100 microseconds can be achieved, total resolution is on the order of 200 microseconds. In addition to the oscillograph, a 14 channel Leach magnetic tape recorder was used.

The thirty-two channels of CEC-127 carrier amplifiers were used along with seven Statham CA3-11 amplifiers for pressure and acceleration recording. The CEC 20 Kc carrier amplifiers have a flat frequency response ( $\pm 1\%$ ) to 3000 cps and the Statham 10 KC carrier amplifiers have a flat frequency response ( $\pm 5\%$ ) to 2000 cps. Both have a non-linearity of  $\pm 1\%$ . A total of thirty-seven pressure channels and two acceleration channels were required.

The amplifier outputs were fed to galvanometers in the CEC 5-119 recording oscillograph and voltage controlled oscillators in the Leach MTR-1200 Magnetic Tape Recorder. Available galvanometers include 31 type 7-361 flat ( $\pm 5\%$ ) to 5000 cps, 2 type 7-326 flat ( $\pm 5\%$ ) to 3000 cps, 10 type 7-343 flat ( $\pm 5\%$ ) to 200 cps and 2 type 7-341 flat ( $\pm 5\%$ ) to 60 cps, all having a non-linearity of  $\pm 1\%$ . To complete the total of required recorder channels for pressure transducers a Leach Magnetic Tape Recorder, Model MTR-1200 was used. This is a fourteen channel unit using wide band FM subcarrier oscillators type AR105. With a 54 KC center frequency the frequency response is flat (0.5 db, 6%) to an upper limit of ten KC.

### 5.1.3 PHOTOGRAPHIC COVERAGE

Primary photographic data was provided by three sledborne high speed motion picture cameras. In addition to the sledborne cameras, secondary information was furnished by ground mounted high speed motion picture cameras.

A Fairchild HS-101 camera was mounted in the forward camera compartment of the rocket sled vehicle and focused on the leading edge of the wing specimen. Two Fairchild HS-100 cameras were mounted aft of the wing specimen on top of the sled instrumentation compartment and were focused on the trailing edge of the wing. (See Figure 5.1.2) The HS-100 and the HS-101 have picture frame rates of approximately 1000 pictures per second which provide approximately four seconds of running time with a one hundred feet capacity film magazine. The sledborne cameras were controlled through a time delay squib circuit which started the two centerline cameras one second before shock arrival and stopped them after six seconds. The outboard camera was actuated prior to shut off of the other two cameras and ran for four seconds.

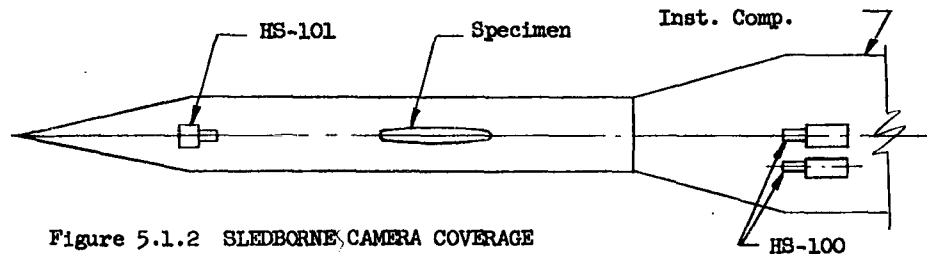


Figure 5.1.2 SLEDBORNE CAMERA COVERAGE

This arrangement provided sledborne camera coverage from before the event point until after the sled had entered the waterbrake area. Therefore, the specimen damage resulting from the blast and any damage due to braking accelerations was recorded, and the latter can be factored out of the test results.

It had been anticipated that quantitative data relating specimen deflection to time could be obtained from the sledborne cameras. However, it was impossible to obtain quantitative data of sufficient accuracy to satisfy

the requirements of the theoretical correlation program. There were four primary problems existing with the sledborne cameras which contributed to data inaccuracies. (1) The wide angle lenses required to provide complete coverage of the specimen characteristically provided pictures distorted at the edges of the frame. (2) The camera frame rate was not sufficiently high to eliminate all distortion due to motion. (3) The track environment introduced considerable vibratory motion into the cameras. This motion was very difficult to distinguish from specimen motion with only the horizon as a fixed reference. (4) The sledborne timing receiver was not completely reliable, and in many cases no timing signal was recorded on the films. It should be noted that the accuracy requirements of the Ballistic Research Laboratories were not quite as stringent as those for the ASD theoretical correlation and for this reason the films of the F-84 specimens were considered useable.

In addition to the sledborne cameras, high speed cameras similar to the Fairchild's were ground mounted beside the sled track to cover areas of interest during the tests. A typical arrangement is shown in Figure 5.1.3.

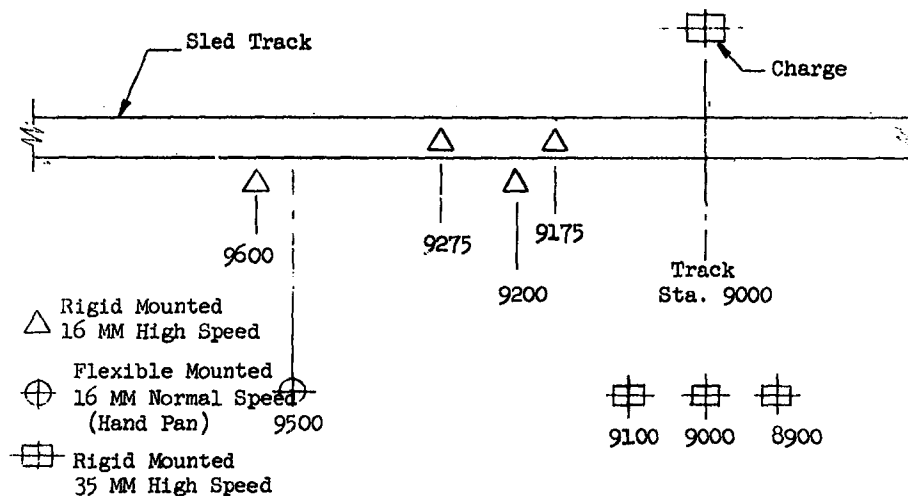


Figure 5.1.3 GROUND MOUNTED CAMERA COVERAGE

Additional photographic coverage was provided as required, such as pre run and post run motion and still pictures and documentary films.

#### 5.1.4 TIME CORRELATION

Several binary time coding systems are extensively used at the AFFTC to provide a method of correlation of data from different recording equipment. The binary coding is a mathematical scheme for representing numbers as powers of two. The system used on the sled tests was the parset time coding which is a seventeen digit register showing time in seconds, minutes and hours. The system recycles every twenty-four hours and is periodically synchronized with WWV. The second and minute register contain six digits each, and the hour register contains five digits. The code is superimposed on precision pulses of 10 and 100 PPS. The seventeen digit code is preceded and followed by a key pulse. Therefore, nineteen of the 100 PPS pulses are coded to form the complete time register. The code is presented every second, and the indicated time is for the leading edge of the key pulse that precedes the time code. Any time within the one second interval must be added to the indicated time. Since the parset time code was recorded simultaneously on all recorders utilized during the tests including cameras, the binary system provided a reference for correlation of the data from all recorders.

### 5.2 SYSTEM RESPONSE CHARACTERISTICS

#### 5.2.1 ACCELEROMETERS

The accelerometers made by CEC, have the type number 4-202-0001  $\pm 1000$  G. Four were used having a range of  $\pm 1000g$ . They have a nominal  $\pm 20$  millivolt sensitivity for the full range of  $\pm 1000$  g and are calibrated to 10 microvolts, for 5 volt excitation. Nominal bridge impedance is 350  $\pm 10\%$  ohms. Frequency response is flat within  $\pm 5\%$  to 1400 cps (using natural frequency of 4100 cps and damping of 0.85 of critical) according to calibration data of the unit with the lowest response. For the four units tested, response within  $\pm 5$  percent extended to 1400, 2300, 2400, and 3000 cps respectively.

Combined linearity and hysteresis of these units is listed by the manufacturer as  $\pm 0.75\%$  of full range output, as measured from the best straight line through the calibration points. Measured values for the four units are well below this ( $\pm 0.25\%$ ).

#### 5.2.2 STRAIN GAGES

The strain gages used are Baldwin Lima Hamilton Type EBF-7S+, and Type EBF-7D+. Both have a nominal resistance of  $120 \pm 0.5$  ohms and a nominal gage factor of 2. The frequency response limit of the gages is very high. There is a theoretical upper limit to the frequency response of the gage which is a function of the gage length. For a quarter inch gage length on steel this is on the order of one megacycle for a ten percent drop in output. According to "Strain Gage Techniques" by Murray and Stein, some errors in reading are to be expected when the wave length of the strain vibrations being measured becomes less than twenty times the gage length. For a quarter inch gage length, on steel this is on the order of 40 kilocycles. The frequency response of most measurement systems considered here is on the order of 10 kilocycles and becomes the controlling factor.

#### 5.2.3 PRESSURE TRANSDUCERS

##### 5.2.3.1 SELECTION CRITERIA

The pressure transducers used, the NASA Model TP 49 and the BRL Miniature Piezoelectric Gage, were selected to fit a set of criteria which eliminated the majority of gages available. A primary consideration is the physical size of the wing which is limited by the track's ability to support the blast load on the wing model. For the model dimensions chosen, a limit of one-half inch thickness is required for the transducer. High frequency response is also required, the original requirement calling for a flat response ( $\pm 5\%$ ) up to 7000 cps. Low frequency response to D.C. is preferred. A fifty PSIG range is required, with an overall accuracy of 2 percent. Insensitivity to shock and vibration effects encountered during the sled run and blast are required. Also, low sensitivity to temperature effects is required.

At the time a pressure transducer was being selected, seven types of gages were available. These types are piezoelectric, strain, variable reluctance, variable capacitance, differential transformer, potentiometer, and electrokinetic. A large amount of information is contained in TN4713, "A compilation of Manufacturer's Data on Commercially Available Pressure Gages", U. S. Naval Ordnance Laboratory. The last three types are not acceptable because of size and frequency response limitations. The first four types have characteristics approaching those required for this program but no commercially available gage fulfilled all of the necessary requirements. The piezoelectric gages do not have response to zero frequency and require relatively expensive amplifiers. No strain gage transducer small enough for the program was available. Also, some failures of small transducers of this type in blast tests at Aberdeen discouraged further efforts along this line. Only one variable capacitance transducer was commercially available, at a cost considerably higher than that of other gage systems. Information contained in University of Dayton Memorandum No. 132 by J. C. Wurst indicated that this gage did not meet the frequency response requirement, despite the manufacturer's claim. Variable reluctance 49TP transducers developed by NASA at Langley combine favorable characteristics of size, cost, and insensitivity to extraneous inputs. Also, they are designed to operate with a CEC carrier system, which was being used on the sled by Aberdeen Proving Ground. The chief shortcoming of this transducer is its upper limit of frequency response. A later decision to eliminate the heavy CEC carrier system and replace it with Statham strain gage amplifiers presented additional difficulties. A miniature piezoelectric transducer developed by Aberdeen Proving Ground was included later gaining better high frequency response at the chosen locations at the expense of a loss of low frequency information.

#### 5.2.3.2 SHOCK TUBE TESTS

An investigation was made of the NASA pressure transducers to determine what improvements could be made to increase the upper limit of frequency response. The transducer has a resonant frequency of about 4500 cps

at which the peak rises to about five times the flat response value. This is caused by the acoustic characteristics of the inlet hole and internal volume within the transducer. It was decided to test the transducer in the University of Dayton shock tube with varied inlet conditions. This was done in twelve tests, with various dimensions of inlet and various acoustical filters. It was found that a flat frequency response ( $\pm 10\%$ ) could be achieved up to 1800 cps, corresponding to a 3 db point of 3600 cps. This was accompanied by a reduction in resonant peak from five to about two and a reduction in "ringing" at 4000 cps. A CEC carrier system was used in these tests and transient response data was processed by a digital computer to obtain frequency response data.

Following the actual testing at the University of Dayton, a meeting was held at M.I.T. to review the original frequency response requirements for the pressure transducer and to discuss methods for improvement of the existing system. The original requirement called for a rise time of 85 microseconds. The system, however, using a CEC oscillograph, was limited to a time resolution of 200 microseconds and would not allow measurement of diffraction loading. Accurate measurement of vortex loading requires a rise time of 200 microseconds and this was chosen to establish the frequency response requirement. The new requirement was chosen to provide a flat frequency response ( $\pm 5\%$ ) to an upper limit of 3000 cps.

Results of the shock tube tests were discussed and it was decided that the pressure transducer and its installation were as good as the "state of the art" permits. Additional improvements in the frequency response characteristics, in order to meet the 3000 cps requirement, could best be accomplished by electrical filtering techniques.



### 5.3 ESTIMATED ACCURACY

#### 5.3.1 ACCELERATION

The accelerometers can be used with the CEC Amplifier and CEC Galvanometer, the Statham Amplifier and CEC Galvanometer, or the Statham Amplifier and Leach Tape Recorder.

Errors in the calibration procedure and those inherent in the equipment used, contribute to the total error of the acceleration measurement system. Since no test equipment is used to provide a direct acceleration input, the recording system must be calibrated indirectly, by the use of shunt resistors. The calibration procedure requires the use of shunt resistors on the order of 10K ohms. For the 350 ohm bridge used, 1% resistors result in a calibration error of  $\pm 1.0\%$ . Non-linearity and hysteresis in the accelerometers is specified by the manufacturer as  $\pm 0.75\%$ .

The associated electronic equipment has the following characteristics. The CEC amplifier has a non-linearity of  $\pm 1\%$  and a frequency response of  $\pm 1\%$  from 0 to 3 KC (within 3 db 0 to 20 KC). The CEC galvanometer type 7-361 has a non-linearity of  $\pm 1\%$  and a frequency response (flat  $\pm 5\%$ ) 0 to 5 KC or (flat  $\pm 3$  db) 0 to 14 KC. The Statham Amplifier CA3-11 has a linearity error of approximately 1%. Its published ratings are 0.25% non-linearity and hysteresis and 0.5% gain stability. Thermal coefficient of sensitivity is listed as 0.02% per degree F. The Statham CA 3-11 has a frequency response (flat  $\pm 5\%$ ) from 0 to 2000 cps or (flat  $\pm 3$  db) from 0 to 5.7 KC. The Leach Wide Band FM VCO type AR 105 has a non-linearity of  $\pm 2\%$ . Its frequency response, with 54 KC center frequency, (flat 0.5 db) is from 0 to 10 KC or (flat 3 db) is from 0 to 28.5 KC.

The following estimate of accelerometer error accounts for errors from accelerometer to reduced data. For the combination including accelerometer, resistance calibration, CEC Amplifier, CEC Galvanometer, data reading (estimated at 0.5 percent) and scale factor accounting for excitation differences between accelerometer calibration and resistance calibration

(estimated at 5%); linearity error (R.M.S.) is 5.4 percent. Additional errors evidenced by the change in reference level (zero shift) of the recording are not accounted for here.

#### 5.3.2. PRESSURE

##### 5.3.2.1 DIFFERENTIAL

Either the NASA variable reluctance or the BRL piezoelectric transducers can be used to make differential measurements. The NASA transducers were used with the same electronic equipment as was used with the accelerometers.

The following estimates of NASA gage pressure measurement error account for errors from transducer to recorder. No calibration error is included.

Linearity error (R.M.S.) for the first combination, including a differential pair of NASA transducers, CEC amplifier, and CEC galvanometer, is two percent. Linearity error for the second combination, including Statham amplifier and CEC galvanometer, is two percent. Linearity error for the third combination, including Statham amplifier and Leach tape recorder is 2.25 percent.

No estimate is made here of accuracy of the BRL piezoelectric transducer since temperature effects caused large zero shifts and resulted in too many losses of records. It would be expected because of the good linearity of these gages, that errors should be less than those given for the NASA gages; however, it is expected that temperature effects would enter this consideration and no information is available on these characteristics of the BRL transducer.

##### 5.3.2.2 ABSOLUTE

Either the NASA variable reluctance or the BRL piezoelectric transducers can be used to make absolute measurement. The NASA transducers were used with the same electronic equipment as was used with the accelerometers.

The following estimates of NASA gage pressure measurement error account for errors from transducer to recorder. No calibration error is included. Linearity error (R.M.S.) for the first combination, including a single NASA transducer, CEC amplifier, and CEC galvanometer, is 1.7 percent. Linearity error for the second combination, including accelerometer, Statham amplifier, and CEC galvanometer is 1.7 percent. Linearity error for the third combination, including accelerometer, Statham amplifier, and Leach tape recorder, is two percent.

No estimate is made here of the accuracy of the BRL piezoelectric transducer.

#### 5.3.3 TORSION AND BENDING MOMENT

The strain gage bridges for measurement of bending of the 6L specimen are used with CEC galvanometers, without an amplifier. Calibration of the bridges is performed using a load cell accurate to five units out of 700 and readings of strain output and load cell input are accurate to two out of 400. Calibration error (R.M.S.) resulting is one percent. Error in the galvanometer is one percent and oscillograph reading error of 0.020 inch out of two inches is one percent. Oscillograph record calibration is made using a shunt resistor whose tolerance is one percent. The R.M.S. combination of these four errors is two percent.

The strain gages have a fifty strain unit deviation over the temperature range from 100°F to 250°F and are used over a range of 3000 strain units; giving approximately two percent temperature error. When four of these gages are combined into a four arm bridge their temperature error is negligible compared to the linearity error if temperature effects are the same on all four arms. If transient heating raises tension side temperature one hundred degrees over compression side temperature, an error of one percent results for the strain-resistance relation, appearing as a zero shift.

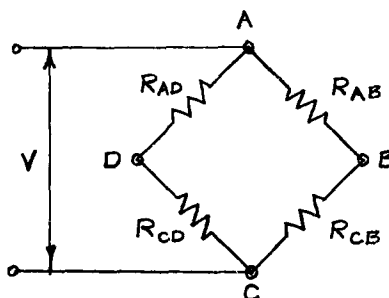
The strain gage bridges for measurement of torsion of the 6L specimen are arranged electrically in a way similar to that of the bending

bridges. The mechanical arrangement differs, however, since torsion gages are mounted on one side of the specimen while half the bending gages are on one side and half are on the other.

The same considerations apply to both the bending and torsion bridges in determining errors arising in calibration and recording. Temperature induced error, however, is less for torsion bridges since all torsion gages are mounted on one side only. Even though a temperature difference may exist between the two sides of the model, reasonably uniform temperatures on either side should result in an error which is negligible compared to the linearity error.

The method of estimating errors due to temperature effects is now indicated.

Bridge output when disturbed from balance by change in resistance of at least one arm:



$$\frac{e_o}{V} = \frac{1}{4} \left[ \frac{\Delta R_{CD}}{R_{CD}} + \frac{\Delta R_{AB}}{R_{AB}} - \frac{\Delta R_{AD}}{R_{AD}} - \frac{\Delta R_{CB}}{R_{CB}} \right]$$

where:  $e_o$  = bridge output voltage (volts)

$V$  = bridge excitation voltage (volts)

$R_{AB} = R_{CB} = R_{CD} = R_{AD}$  = strain gage resistance (ohms)

$\Delta R_{AB}$  = change in strain gage resistance (ohms)

Temperature Error:

$$\text{Let } \frac{\Delta R_{CD}}{R_{CD}} = \gamma_1, \quad \frac{\Delta R_{AB}}{R_{AB}} = \gamma_2, \quad \frac{\Delta R_{AD}}{R_{AD}} = \gamma_3, \quad \frac{\Delta R_{CB}}{R_{CB}} = \gamma_4$$

where  $\gamma$  is a function of temperature.

$$\text{Then } \frac{e_o}{V} = \frac{1}{4} [\gamma_1 + \gamma_2 - \gamma_3 - \gamma_4]$$

Temperature Error:

$$\frac{d \frac{e_o}{V}}{dT} = \frac{\partial \frac{e_o}{V}}{\partial \gamma_1} \frac{d\gamma_1}{dT} + \frac{\partial \frac{e_o}{V}}{\partial \gamma_2} \frac{d\gamma_2}{dT} + \frac{\partial \frac{e_o}{V}}{\partial \gamma_3} \frac{d\gamma_3}{dT} + \frac{\partial \frac{e_o}{V}}{\partial \gamma_4} \frac{d\gamma_4}{dT}$$

$$\frac{\partial \frac{e_o}{V}}{\partial \gamma_1} = \frac{1}{4} \frac{\partial \frac{e_o}{V}}{\partial \gamma_2} = \frac{1}{4}, \quad \frac{\partial \frac{e_o}{V}}{\partial \gamma_3} = -\frac{1}{4}, \quad \frac{\partial \frac{e_o}{V}}{\partial \gamma_4} = -\frac{1}{4}$$

For a temperature error of 2% in arms AB and CD, relative to arms AD and CB

$$\frac{d\gamma_1}{dT} = \frac{d\gamma_2}{dT} = \frac{2}{100}, \quad \frac{d\gamma_3}{dT} = \frac{d\gamma_4}{dT} = 0$$

$$\frac{d \frac{e_o}{V}}{dT} = \frac{1}{4} \frac{2}{100} + \frac{1}{4} \frac{2}{100}$$

$$\frac{d \frac{e_o}{V}}{dT} = \frac{1}{100}$$

#### 5.3.4 SLED VELOCITY ERROR

Sled velocity is determined from records of time of arrival of the sled at accurately known stations along the track. Space interval marks are obtained from electromagnetic pickups which are located sixty feet apart along the track and time for each interval can be obtained from the channel which records time signals transmitted from the blockhouse. This information allows computation of an average velocity for each interval.

Errors in determination of instantaneous velocity arise from two sources; those which appear in computation of average velocity and those which result from using average velocity over the interval, to approximate instantaneous velocity.

The errors which appear in the average velocity computation arise in reading the oscillograph record and in the computation accuracy. It is assumed that an oscillograph reading error of 0.020 inch is made in assigning values to both distance and time intervals, corresponding to 0.27 ft. distance error and 0.00031 sec. time error for a chart interval of 4.5 inches. This affects the velocity computation in the following manner:

$$v = \frac{D}{T}$$

$$\frac{dv}{dR} = \frac{\partial V}{\partial D} \frac{dD}{dR} + \frac{\partial V}{\partial T} \frac{dT}{dR}$$

V = average velocity in interval (ft/sec)

D = interval distance (feet)

T = time (seconds)

R = chart interval

$$\frac{\partial V}{\partial D} = \frac{1}{T} \frac{1}{\text{sec}} , \quad \frac{\partial V}{\partial T} = - \frac{D}{T^2} \frac{\text{ft}}{\text{sec}^2}$$

$$\frac{\partial V}{\partial D} = \frac{850}{60} \frac{1}{\text{sec}} , \quad \frac{\partial V}{\partial T} = - \frac{(60)(850)(850)}{(60)(60)} \frac{\text{ft}}{\text{sec}^2}$$

$$\frac{dD}{dR} = \frac{.020}{4.5} (60) \frac{\text{ft}}{\text{interval}}, \quad \frac{dT}{dR} = \frac{.020}{4.5} \frac{60}{850} \frac{\text{sec}}{\text{interval}}$$

$$\frac{dD}{dR} = 0.2665 \frac{\text{ft}}{\text{interval}}, \quad \frac{dT}{dR} = 0.00031 \frac{\text{sec}}{\text{interval}}$$

Thus error in velocity computation due to reading inaccuracies is:

$$\frac{dV}{dR} = \frac{850}{60} (0.2665) - \frac{(60)(850)(850)}{(60)(60)} (0.00031)$$

$$\frac{dV}{dR} = 3.78 - 3.73$$

$$\frac{dV}{dR} = 0.05 \text{ ft/sec error in interval due to reading error}$$

Computational error acquired in slide rule calculation of velocity is assumed to be three units out of 850; that is, three feet per second.

The errors which result from using average velocity over the interval to approximate instantaneous velocity can be determined with sufficient accuracy as follows:

Since actual velocity varies relatively smoothly, increasing during the start of the run, and decreasing during the end, it may be assumed that average velocity is equal to instantaneous velocity at the center of the interval and maximum error occurs at the end of the interval. The magnitude of the error is half the difference between the average velocity of the interval and the average velocity of the preceding or succeeding interval. Results of the Number 24 test run reveal no such difference between intervals around blast time indicating that velocity was constant at that time and error due to instantaneous velocity change can be assumed to be negligible.

Examination of the magnitudes of the errors as discussed and of the results themselves indicates that the predominant error is that due to computation inaccuracies; i.e., a slide rule error of 3 feet per second.

## 6.0 FIELD TEST PROGRAM .

AAI - Aircraft Armaments, Inc., installed the rocket sled on the high speed track at Edwards Air Force Base and provided personnel and materials to operate and maintain the sled and support the field test program through its conclusion.

### 6.1 TEST OBJECTIVES.

The objectives of the field test program were to provide experimental data on blast induced airloads on airfoils and elastic and post-failure structural responses of the airfoils. The data will be used for correlation with theoretical prediction methods and later refinement of the theoretical methods. The analytical techniques developed as a result of the data generated in the test program will be utilized in aircraft design to determine vulnerability of current and future aircraft to nuclear blast. In addition, the data accumulated in the JANAF Test Program will be evaluated to determine the feasibility of conducting a similar but more extensive program, Project "BIG SEA".

### 6.2 GENERAL DESCRIPTION

A field test program was conducted in two phases. Phase I tests were conducted at the high speed sled track, AFFTC, Edwards Air Force Base, California. Phase II tests were conducted at the shock tube facility, NASA Wallops Station, Wallops Island, Virginia.

#### 6.2.1 PHASE I - EDWARDS AIR FORCE BASE SLED TESTS

The Phase I test program utilized the rocket sled, designed and manufactured under the subject contract, as the carrier for the airfoil specimens. Tests were conducted on swept wing specimens of two different planforms. All tests conducted under BRL direction utilized an F-84 horizontal stabilizer as the test specimen. In the tests conducted under AAI direction for ASD, a tapered swept wing specimen was used, similar to a miniature B-52 or B47 wing. Both specimen types were instrumented with pressure transducers, accelerometers and strain gages.



In each test an airfoil specimen was mounted on the rocket propelled sled which also contained the specimen data recording equipment. The sled was propelled through a test area at .8 Mach velocity. An HE charge was detonated by the sled in the test area at a predetermined slant range to provide the desired orientation of vehicle and blast wave at the blast wave-specimen intercept point. The effects of the angle of attack induced by the blast wave as functions of acceleration, pressure and strain on the airfoil specimen were measured and recorded through the specimen instrumentation system and sled mounted high speed motion picture cameras. Data on blast wave characteristics such as shock arrival time, shock velocity and wave form were measured and recorded through a series of piezoelectric pressure transducers placed at points of interest in the blast field. The following figures illustrate the sled vehicle with the two different test specimens mounted (Figures 6.2.1.1 - BRL Specimen, 6.2.1.2 - ASD Specimen); Part of the Recording Equipment Mounted in the Sled (Figure 6.2.1.3); The H.E. Charge and Blast Line Instrumentation (Figure 6.2.1.4); and a Typical Test Showing the Sled Vehicle Entering the Blast Area (Figure 6.2.1.5).

Data relating sled position to time was provided by Edwards Air Force Base Space - Time System. This system consists of a series of magnetic pickups spaced at equal intervals along the sled track. A permanent magnet attached to one of the sled slippers passes over the pickups as the sled moves down the track creating a voltage pulse which is recorded on an oscillograph. A binary time code was recorded by all recording equipment simultaneously. The time code provided a reference for correlation of data from different recorders.

The HE charge weights and distances from the track were varied during the program in order to obtain airload data both at small and at relatively large induced angles of attack and for both long and short overpressure durations. A schedule of the run conditions for the Phase I field test program is shown in Table 6.2.1.

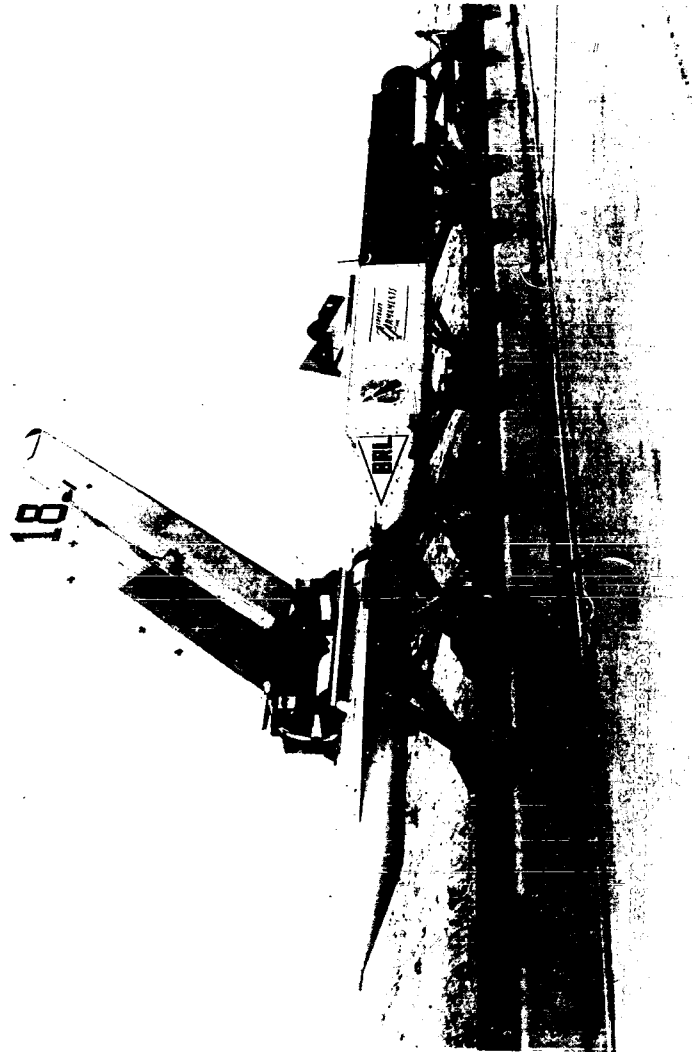


Fig. 6.2.1.1 BRL SPECIMEN



Fig. 6.2.1.2 ASD SPECIMEN

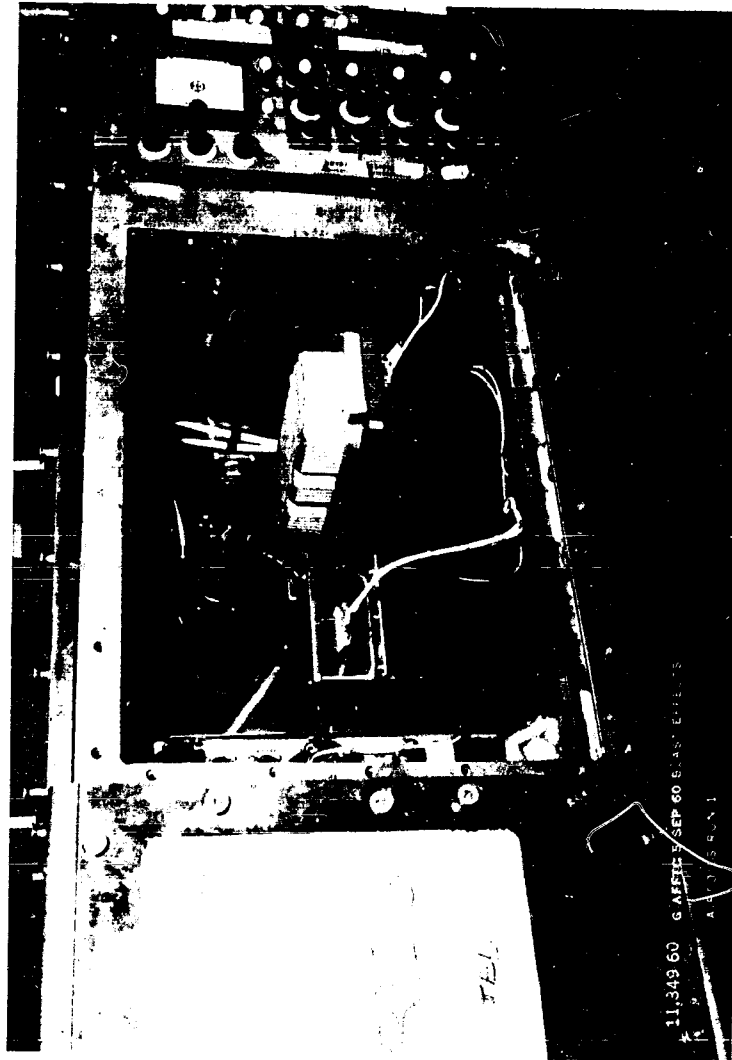


Fig. 6.2.1.3 PART OF THE RECORDING EQUIPMENT MOUNTED IN THE SLED



Fig. 6.2.1.4 THE H.E. CHARGE AND BLAST LINE INSTRUMENTATION



Fig. 6.2.1.5 TYPICAL TEST SHOWING THE SLED VEHICLE ENTERING THE BLAST AREA

Table 6.2.1 RUN CONDITIONS FOR PHASE I FIELD TEST PROGRAM

TEST NO.	CHARGE WEIGHT (POUNDS)	CHARGE DISTANCE (FEET)	OVERPRESSURE (PSI)		DURATION (MSEC)	SLED VELOCITY (MACH NO.)	WING SPECIMEN
			$\bar{p}$	$\bar{p}'$			
1	20	50	3.37	7.4	7.7	0.8	F-84
2	50	60	4.3	9.9	10.0	0.8	F-84
3	200	80	5.4	12.7	14.5	0.8	F-84
4	50	35	11.4	30.2	7.1	0.8	F-84
5	2500	220	4.4	9.9	36.9	0.0	F-84
6	200	80	5.4	12.7	14.5	0.8	F-84
7	10000	350	4.1	9.3	57.6	0.8	F-84
8	200	80	5.4	12.7	14.5	0.8	F-84
9	30000	600	3.1	6.8	91.1	0.0	F-84
10	50	35	11.4	30.2	7.1	0.8	F-84
11	--	--	--	--	--	0.8	F-84
12	2500	250	3.4	7.5	38.7	0.8	F-84
13	30000	600	3.1	6.8	91.1	0.8	F-84
14	200	47	16.2	46.5	9.9	0.8	F-84
15	30000	600	3.1	6.8	91.1	0.8	F-84

Table 6.2.1 RUN CONDITIONS FOR PHASE I FIELD TEST PROGRAM (continued)						
TEST NO.	CHARGE WEIGHT (POUNDS)	CHARGE DISTANCE (FEET)	OVERPRESSURE (PSI)		DURATION (MSEC)	SLED VELOCITY (MACH NO.)
			$\dot{L}$	$r$		
16	30000	600	3.1	6.8	91.1	0.8
17	2500	160	7.4	18.0	30.6	0.8
18	--	--	--	--	--	0.8
19	2500	220	4.4	9.9	36.9	0.0
20	2500	220	4.4	9.9	36.9	0.8
21	BRL	Jeep	Test			
22	BRL	Jeep	Test			
23	BRL	Jeep	Test			
24	200	53	12.4	33.4	11.0	0.8
25	--	--	--	--	--	0.8
26	200	53	12.4	33.4	11.0	0.8
						6L
						6L
						6L



#### 6.2.1.1 GROUP RESPONSIBILITIES

AAI - Aircraft Armaments, Inc. personnel were responsible for direction of the ASD portion of the test program. In addition, the AAI personnel were responsible for maintaining the sled vehicle at the test site and furnishing assistance to the BRL group during conduct of the portion of the program under BRL cognizance.

BRL-Personnel from the Ballistics Research Laboratories, Aberdeen Proving Ground, Aberdeen, Maryland, supplied technical direction for the tests conducted on the F-84 horizontal stabilizers. BRL representatives were also responsible for measuring and recording blast field data and supervising placement and detonation of the HE charges. At the conclusion of the F-84 tests, the BRL field personnel furnished assistance to AAI during tests conducted on the ASD 6L model.

EAFB - AFFTC, Edwards Air Force Base, California, furnished operational personnel, facilities and equipment necessary to the test program.

#### 6.2.1.2 DETAIL DISCUSSION OF TESTS

As indicated in Table 6.2.1, the first twenty (20) sled tests were conducted on F-84 horizontal stabilizers and were under the technical direction of the Terminal Ballistics Branch of the Ballistics Research Laboratories, Aberdeen Proving Ground, Maryland. The last three (3) tests were conducted on the 6L specimen for the Structures Branch of the Flight Dynamics Laboratory, Aeronautical Systems Division, Wright-Patterson Air Force Base, Ohio and were under the technical direction of AAI. Tests 21, 22 and 23 were conducted by another branch of the Ballistics Research Laboratories and have no bearing on the research tests conducted on airfoils. In addition to the tests shown in Table 6.2.1, four checkout runs were conducted at the beginning of the program. A discussion of the test program is presented below.

All field test personnel arrived at Edwards Air Force Base on 22 August 1960. All test equipment was located and work areas were

established. Installation of instrumentation in the test vehicle was started on 25 August 1960.

Instrumentation installation was completed and the first check out sled run was conducted on 6 September 1960. No specimen was installed for this test and no HE charge was detonated. The purpose of the test was to establish the velocity profile of the basic vehicle in order to make accurate performance calculations for future tests. The run also provided a means of evaluating the effects of sled environment on the instrumentation components. During this test three of the shock mounts on the CEC amplifiers failed. There had been concern that some of the instrumentation packages might be adversely affected by the severe shock and vibration environment of a sled. This experience increased this concern, therefore components of an alternate system utilizing a Statham CA3-11 strain gage amplifier and Leach magnetic tape recorder were also placed aboard the sled for subsequent check out runs. Three more check out runs were made which showed the CEC amplifiers to be completely inadequate to withstand the sled environment. Additional problems were also encountered with the inverters that supplied power to the CEC amplifiers. The CEC equipment had to be abandoned and an instrumentation system was improvised around the use of the Statham amplifiers. There were some undesirable aspects of this system such as low frequency response and partial incompatibility of the pressure transducer and amplifier, but BRL felt that the system would yield data suitable for their purposes.

At the conclusion of the series of check out runs, the following instrumentation components were available or would be available for use in the sled test program.

Quantity

1	CEC Type 5-119 Recording Oscillograph
32	CA3-11 Statham 10 Kc Carrier Amplifiers
8	CA3-20 Statham 10 Kc Carrier Amplifiers
3	Leach MTR-1200 Magnetic Tape Recorders

After evaluation of the results of the check out runs it was decided to replace the CEC amplifiers and the inverters with the Statham amplifiers and to utilize the Leach machine to record the data. It should be noted here that once the decision was made to substitute the Statham CA3-11 amplifiers for the CEC amplifiers it was mandatory that the untested Leach recorder be used since the CA3-11 amplifiers did not have sufficient power output to drive the galvanometers in the CEC oscillograph. Furthermore, no other recorders or amplifiers were available which met the program requirements. It was also decided to continue to record strain and acceleration data on the CEC 50 channel oscillograph, due to the limited quantity of tape recorders and amplifiers available.

Two of the CA3-20 amplifiers, which provided sufficient output power to drive the oscillograph galvanometers, were required to amplify the output signals from the specimen accelerometers. The strain gage output signals required no amplification and were wired directly to the oscillograph galvanometers. Of the useable amplifiers six CA3-20's and thirty-two CA3-11's were available for pressure data. The quantity of amplifiers available exactly equalled the number required, leaving no spares.

Since BRL was interested in pressure distribution over the airfoil only as secondary data, it was agreed at this time to move the tests on the ASD 6L and 6R specimens to the end of the schedule and to proceed at once with the BRL tests. This arrangement provided time during the BRL runs to debug the pressure instrumentation system and allowed time for the components on order to be delivered. Since ASD considered the pressure data of primary importance, the new schedule was the only

practical arrangement possible.

All mechanical aspects of the test program were satisfactory at the conclusion of the checkout tests and an instrumentation system which provided marginal possibilities for success had been agreed on. The necessary sled modifications were made for the instrumentation, and the first data run was made on 22 September 1960. A twenty (20) pound TNT charge was detonated fifty (50) feet from the centerline of the track at Station 9000 as the test vehicle passed at 0.8 Mach velocity. The strain, acceleration, specimen deflection and over pressure of the specimen resulting from the blast wave were recorded by the sledborne instrumentation. Blast field data were recorded by the BRL blast line instrumentation. The test was considered satisfactory although only a limited amount of specimen pressure data were recorded.

Runs 2 and 3 were conducted using charge weights of fifty (50) pounds and two hundred (200) pounds at distances of sixty (60) and eighty (80) feet respectively. These tests, like test number 1, provided specimen data in the elastic region at relatively small angles of attack ( $12^{\circ}$  to  $18^{\circ}$ ).

Run Number 4 was the first test in which an attempt was made to structurally fail the test specimen to obtain data in the post elastic region. A fifty (50) pound charge of TNT was detonated thirty-five (35) feet from the track centerline as the sled passed Station 9000. The following data were recorded:

- 10 channels of specimen strain
- 2 channels of specimen acceleration
- 10 channels of specimen pressure
- 1 channel of sled acceleration
- parset timing on all recorders
- 3 high speed motion pictures

The specimen failure induced by the blast wave consisted of compression skin buckling at approximately midspan. There was no visible indication of internal structural damage.

Tests 5 and 6 were conducted the week of 16 October 1960. Test number 5 was a static test. In this test the sled vehicle was placed at track Station 9000 and a two thousand five hundred (2500) pound charge of TNT was detonated two hundred twenty (220) feet from the track centerline. After the test, it was found that the sledborne oscillograph and cammeras had not operated. Therefore, the specimen data were lost. The reason for the failure was determined to be a power failure. The power furnished from the block house was not sufficient to energize the squib circuitry which started the recording equipment. No data were recorded by the blast field instrumentation either; failure of this equipment was also attributed to loss of power.

Run number 6, a dynamic test, was also conducted during the same week. A two hundred (200) pound charge of TNT, located eighty (80) feet from the track centerline at Station 9000 was detonated as the sled passed. All systems functioned as programmed and the following data were recorded:

- 9 channels of strain
- 2 channels of acceleration
- 7 channels of pressure
- 3 high speed motion pictures
- parset timing

Test number 7 was conducted on 25 October 1960. Ten thousand (10000) pounds of TNT located three hundred fifty (350) feet from the sled track was utilized to provide the blast conditions of the test. The following data were recorded:

- 7 channels of strain
- 2 channels of acceleration
- 5 channels of pressure
- 3 high speed motion pictures
- parset timing

The test specimen and the BRL reaction mount were extensively damaged, which was not expected. It was necessary to rebuild the specimen reaction mount before any more tests could be conducted.

A test, number 8, utilizing two hundred (200) pounds of TNT for the blast was conducted during the week of 30 October 1960. This test replaced a previously scheduled two thousand five hundred (2500) pound "kill" shot. The schedule change was necessary in order to continue testing with a light duty specimen mount while a stronger mount was being fabricated. Several problems were encountered in the test due to instrumentation component failures and only the following data were recorded:

- 6 channels of strain
- 1 channel of acceleration
- 3 channels of pressure
- parset timing was erratic

Two sled tests were conducted during the week of 27 November 1960. A static test employing thirty thousand (30000) pounds of TNT was conducted on 29 November 1960, and a dynamic test, designed to fail the wing specimen, was conducted on 30 November 1960. The instrumentation functioned satisfactorily during the static test. The Leach tape recorder and the range timing did not operate during the dynamic test. The instrumentation recorder assignments for the two runs follows:

- CEC Oscillograph
  - 4 channels pressure
  - 4 channels strain
  - 1 channel acceleration
  - parset timing
- Leach Tape Recorder
  - 11 channels pressure
  - parset timing

Runs number 11 and 12 were conducted on 6 December 1960. The same test conditions existed for both runs since the two thousand five hundred (2500) pound TNT charge failed to detonate during run 11. Run 12 was conducted during the afternoon of 6 December. All systems functioned as programmed. During the week of 11 December 1960 tests numbers 13 and 14 were conducted. Both tests were dynamic. In test number 13 thirty

thousand (30000) pounds of TNT were detonated six hundred (600) feet from track Station 9000 as the test vehicle passed. All systems functioned satisfactorily. The following data were recorded:

- 7 channels of strain
- 2 channels of acceleration
- 12 channels of pressure
- 3 high speed motion pictures
- parset timing

Run number 14 was a specimen destruction test. The F-84 wing specimen failed at midspan all pressure transducers above the break were damaged - five beyond repair. The instrumentation wiring was burned badly by hot gasses, when an igniter connector blew out of the front of the rocket motor. Consequently, no data were recorded.

Tests number 15 and 16 were conducted during the weeks of 18 and 25 December 1960 respectively. In both tests thirty thousand (30000) pounds of TNT were detonated at a slant range of six hundred (600) feet as the test vehicle passed Station 9000. All instrumentation functioned as programmed. The following data were recorded:

Run 15

- 3 channels of strain
- 11 channels of pressure
- 3 high speed motion pictures
- parset timing

Run 16

- 7 channels of strain
- 14 channels of pressure
- 3 high speed motion pictures
- parset timing

Test number 17 was conducted on 5 January 1961. This test was designed to fail the wing specimen. A two thousand five hundred (2500) pound TNT charge was detonated one hundred sixty (160) feet from the test

vehicle as it passed the test area. The BRL reaction mount failed which resulted in destruction of both the specimen and mount and damage to the test vehicle and sled track. All instrumentation functioned and the following data were recorded:

- 5 channels of strain
- 1 channel of acceleration
- 9 channels of pressure
- 3 high speed motion pictures
- parset timing

Tests number 18, 19, and 20 were conducted on 20, 21, and 28 January 1961 respectively. Charge size and distance were the same for the three tests, two thousand five hundred (2500) pounds of TNT at two hundred twenty (220) feet distance. Tests 18 and 20 were dynamic tests. Test 19 was static. Run number 18 was unsuccessful due to the fact that the charge failed to detonate. The detonation failure was traced to a defective safety switch in the detonation circuit. Test 19 was performed as scheduled. However, no data were recorded on the oscillograph or cameras for two reasons: 1) the charge was detonated 1.5 seconds early and 2) the squibs which started the recording equipment were not energized. Nine (9) channels of pressure data were recorded on the Leach Tape recorder. Test 20, the final BRL test, was conducted on 28 January 1961. An unexpected failure of the specimen occurred. All instrumentation functioned as programmed. The following data were recorded:

- 7 channels of strain
- 8 channels of pressure
- 3 high speed motion pictures
- parset timing

During the month of February 1961 installation of the instrumentation system to be used in the tests on the ASD specimens was completed. The system utilized three (3) Leach tape recorders in conjunction with the CEC 50 channel oscillograph. The Leach recorder offered several features which made it preferable to the CEC oscillograph. These were:



1) greater flexibility afforded by playback, 2) high frequency response, 3) construction suited to sled environment. In addition, this recorder was being considered for use on the planned "BIG SEA" program and these tests afforded an opportunity to operationally test its performance. The CEC oscillograph was retained in the system to record accelerations and strains.

Experience with the instrumentation during the BRL test series had revealed several deficiencies and led to concern as to whether data of sufficient quality could be obtained to satisfy the ASD requirements. In the BRL test series the pressure data taken at the specimen was used as back up information, but in the ASD problem the time variation of pressure at various points on the wing specimen was of primary concern, therefore, the requirements for the instrumentation was much more exacting. In preparing for the ASD tests it was decided to make a number of controlled experiments to determine the characteristics of the principal components that comprised a pressure channel. Experimentation was begun on run 20, the last of the BRL dynamic runs. In this run four pressure channels using TP-49 NASA transducers and two channels using BRL piezoelectric transducers were carefully calibrated and subjected to special tests.

During the calibration of the NASA transducer channels two problems were encountered. First, it was difficult to balance the Statham CA3-11 amplifiers. This problem was eventually overcome by use of a capacitance trimmer in the bridge and although the balancing of each channel took time, it was considered a satisfactory solution of the problem. The second problem was nonlinearity of the calibration curve. This characteristic was most pronounced at the lower and higher pressures with fairly good linearity through the middle ranges. It was decided that pressure calibration of each channel before and after the test run would be necessary and the number of resistors used in electrical calibration should be increased to four. Furthermore, the resistors used in the electrical calibration should be selected to suit the particular transducer in each channel.

Attempts to calibrate the BRL piezoelectric transducer channels revealed problems that could not be overcome with the equipment that was available. When the pressure gage was subjected to a step change in the pressure level, the generated pressure signal would quickly decay to the original value. A decay time for this type of test in the order of 20 milliseconds was obtained whereas decay times of not less than 2 seconds were needed. The need for a solid state amplifier with a very high input impedance (100 megohms or more) was indicated but no instrument of this type could be found. The applications for a pressure channel with such a short decay time as 20 milliseconds would be very limited in the ASD problem, therefore, the value of this type of transducer in the ASD program was minimal.

The records obtained from the four channels using NASA transducers contained several unexplained instances of noise of rather large amplitude. Several possible sources of the noise such as electrical connectors, the tape recorder, and the acceleration response of the transducer was suspected. The records obtained from the BRL transducers were very noisy and a peculiar shake was obtained in the pressure signal. This experience further detracted from the value of this transducer in the ASD program.

The experience of run 20 indicated that a substantial improvement in the performance of the instrumentation was necessary before data of suitable quality for the ASD program could be obtained. Two dynamic runs therefore were scheduled for the purpose of exploring the capability of the system to provide satisfactory aerodynamic and structural data. Run 24 was made on 3 March 1961. Twelve channels of wing pressure were taken using NASA transducers and four channels using the BRL piezoelectric units. Ten of the twelve channels using NASA gages showed repeated calibrations to  $\pm 1/2$  psi or better which was considered very good. The other two channels were acceptable. The BRL transducers were not calibrated because no set up was available to accomplish this test, therefore, the laboratory calibration values were used. All pressures were recorded on Leach tape recorders and strains

and accelerations were recorded on the CEC oscillograph. Some of the pressure transducers were sealed off at the wing so that only noise signals could be recorded.

Analysis of the recorded results obtained from run 24 yielded the following: The noise in the electrical calibration signal on the NASA channels was equivalent to  $\pm 1.4$  psi. This was the envelope of the noise and was roughly equal to the 3 percent WOW and Flutter signal quoted for the Leach tape recorder. This condition apparently sets the lower limit to the measurement accuracy that can be expected in the pressure channels. The noise in the pressure signal during sled motion was equal to  $\pm 2.4$  psi. This signal was apparently introduced by the track vibration but the component through which it was introduced was not known. At blast arrival the channels with the covered gages showed a signal equal to 15 to 24 psi. This signal when compared to the reflected shock overpressure of 34.5 psig as computed by BRL from the blast line instrumentation was a very large signal and obviously too much to be tolerated. The open gages showed this large signal at blast arrival plus an overshoot and oscillation due apparently to under-critical damping. This large signal shortly after blast arrival was common to all channels, including the parset timing. They correlated in time and since the tape recorder was the only instrument common to all channels it was suspected of contributing a significant portion of the noise. The signal on the channels using the BRL piezoelectric transducers had the appearance of accelerometer signals. They also showed the large signals that were evident on the closed NASA gage channels. The strain and accelerometer signals were not reliable after shock arrival and no useable data was obtained.

Run 25 was also accomplished on 3 March 1961. This test was planned to determine the affect of the pressures from the moving sled on the blast line instrumentation. No charge was detonated during this test. The run demonstrated that the blast line gages were not affected by the sled pressures at least until the wing was adjacent to the blast line probes. This condition is acceptable, therefore no problem is created by the sled pressures.

Run 26 was made on 21 March 1961. This run was made to further check the noise that was generated in the Leach tape recorder and define the problem of shock isolation that appeared to be present. Accelerations in excess of 100 g's were measured on accelerometers placed in the sled adjacent to the recorders. All traces recorded on the tape recorders showed large signals as the sled entered the blast.

#### 6.2.1.3 CONCLUSIONS

It should be emphasized that none of the instrumentation systems tried in the field tests were considered optimum. In the interests of economy and expediency it was necessary in most instances to use equipment available from Government supply. All organizations realized from the inception that any system assembled in this way had only a marginal probability of withstanding the sled environment and yielding the desired data. The results obtained from the controlled experiments during runs 20 and 24 indicated that the instrumentation system was completely inadequate for the exacting requirements of the ASD programs, therefore, no attempt was made to collect data on the ASD specimens.

The need for extensive testing and modification of the instrumentation system was apparent. The principal areas requiring attention were:

1. Qualitative and quantitative testing to determine the tape recorder axis most sensitive to shock and vibration and the effects of random shock and vibration excitation on recorder noise levels,
2. Design and development of a shock and vibration isolation system for the recording equipment,
3. Procurement of new amplifiers or extensive modification of the available amplifiers and design and fabrication of additional circuitry to provide components compatible with the pressure transducers. The alternative solution was procurement of a completely new pressure measuring system.

No funds were available to make any of the required revisions. Further, representatives from NASA had offered the facilities of their large diameter shock tube at Wallops Island, Virginia, for performance of limited blast tests. Since the specimen carrier was fixed during the shock tube experiment, the vibration and acceleration environment associated with the rocket sled was eliminated. Therefore, it was possible to utilize the CEC amplifiers in the pressure instrumentation system. The problem with compatibility of components was eliminated. Although there were several severe limitations imposed on the experiments by the shock tube facility, it was decided to move the field program to Wallops Island until the problems with the instrumentation system on the sled program could be solved.

#### 6.2.2 PHASE II - WALLOPS STATION SHOCK TUBE TESTS

As a result of the problems with the sled borne instrumentation encountered during the rocket sled test program conducted at Edwards Air Force Base, California, it was decided to take advantage of the NASA offer of their shock tube facility at Wallops Island, Virginia Station. The NASA operates the shock tube facility to conduct aerodynamic research on airfoil models which are subjected simultaneously to subsonic airflow up to velocities of .7 Mach and blast induced gusts. The tests are conducted by directing the flow from an open ended shock tube 80 feet long and 10 feet in diameter over the externally mounted model. The duration of the flow is approximately 100 milliseconds. During this time a blast wave is directed from the side into the flow and over the model. The blast gust deflects the shock tube flow, subsequently, providing the desired angle of attack to the test specimen.

Six tests were conducted at the NASA facility. The 6L specimen was mounted in the forward section of the rocket sled which had been used in the Edwards Air Force Base Program. The sled forebody was then rigidly mounted in front of the shock tube muzzle.

The wing specimen provided for the tests was instrumented to provide thirty-seven (37) data channels of pressure information, four (4) channels of strain information and two (2) channels of acceleration data. Thirty (30) channels of pressure data from NASA 49TP pressure transducers, were recorded on the CEC 5-119 fifty (50) channel recording oscillograph. Excitation voltage and signal amplification was provided by eight (8) four (4) channel CEC Type 1-127 carrier amplifiers. Seven (7) channels of pressure data from BRL Piezo electric pressure transducers, were recorded through the high impedance equipment in the BRL instrumentation trailer. Data from the strain gages was recorded on the fifty (50) channel oscillograph without signal amplification. Wing acceleration data were recorded on the fifty (50) channel oscillograph. Excitation and signal amplification was provided by Statham model CA3-20 strain gage amplifiers.

The airfoil pressure transducers, accelerometers and strain gages measured the transient aerodynamic effects induced by the blast wave. The data signals were amplified by the CEC carrier amplifiers originally used on the sled test program. The 50 channel CEC oscillograph, also from the sled test program, was utilized to record the specimen data. The amplifiers and oscillograph were housed in a building approximately 300 feet from the test specimen.

Both BRL and NASA furnished personnel and equipment to measure and record blast field data. A timing signal and appropriate sync pulses were recorded by all recording equipment simultaneously to provide a means of correlation of data from different recorders.

Figure 6.2.2.1 illustrates Test Set Up at the Test Facility. Figures 6.2.2.2, 6.2.2.3, 6.2.2.4 and 6.2.2.5 are photographs which show the airfoil specimen mounted in front of the shock tube. Figure 6.2.2.6 shows part of the specimen instrumentation components mounted in the instrumentation shelter.

Two high speed motion picture cameras were used to record wing deflection during the tests. One of the cameras was mounted in the forward camera compartment in the sled forebody and one camera was mounted on the



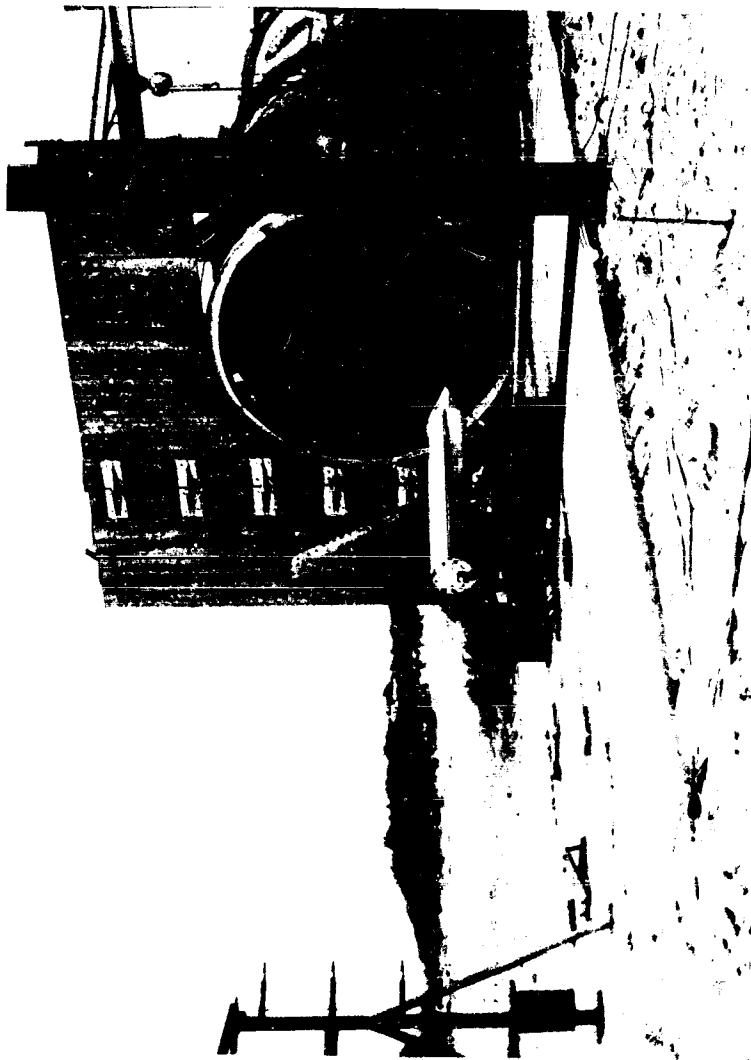


Fig. 6.2.2.2 RAKE INSTALLATION - WALLOPS ISLAND SHOCK TUBE



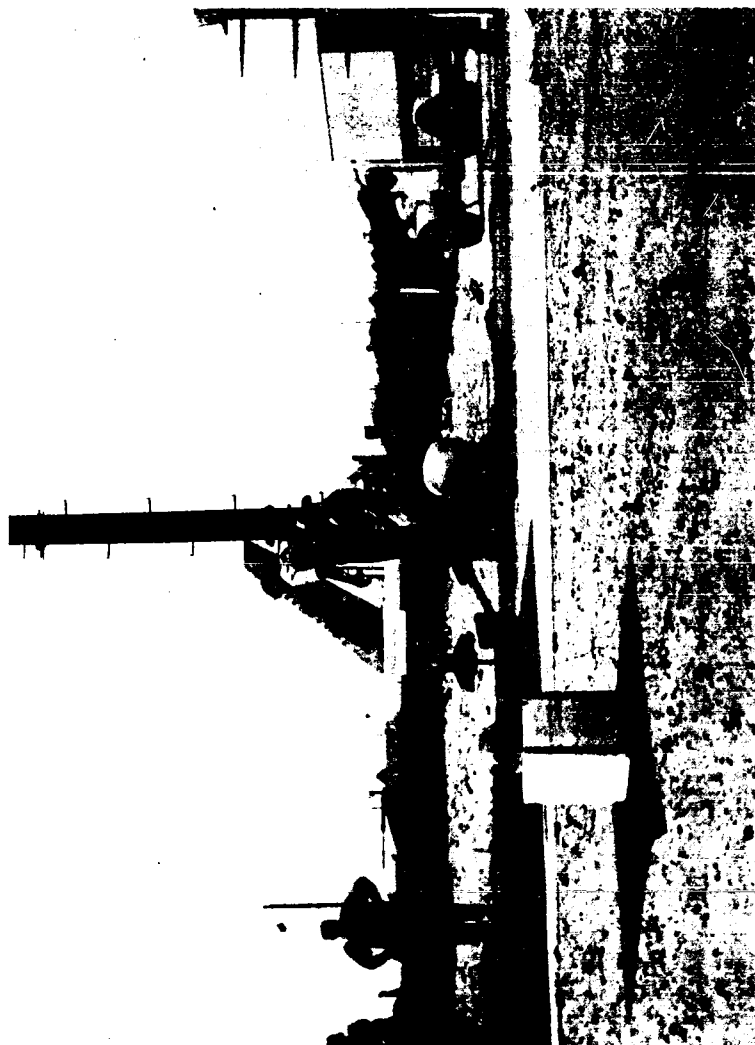


Fig. 6.2.2.3 EXPLOSIVE EMPLACEMENT - WALLOPS ISLAND SHOCK TUBE

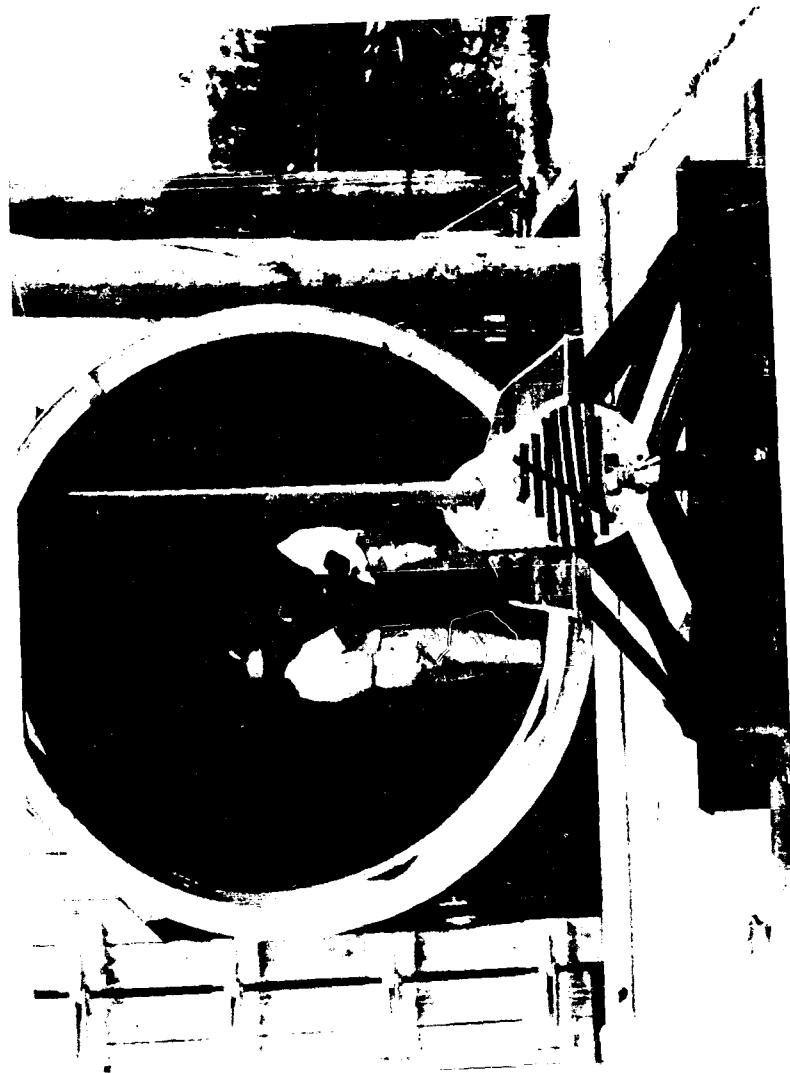


Fig. 6.2.2.4 SHOCK TUBE DIAPHRAGM BEFORE TEST - WALLOPS ISLAND SHOCK TUBE

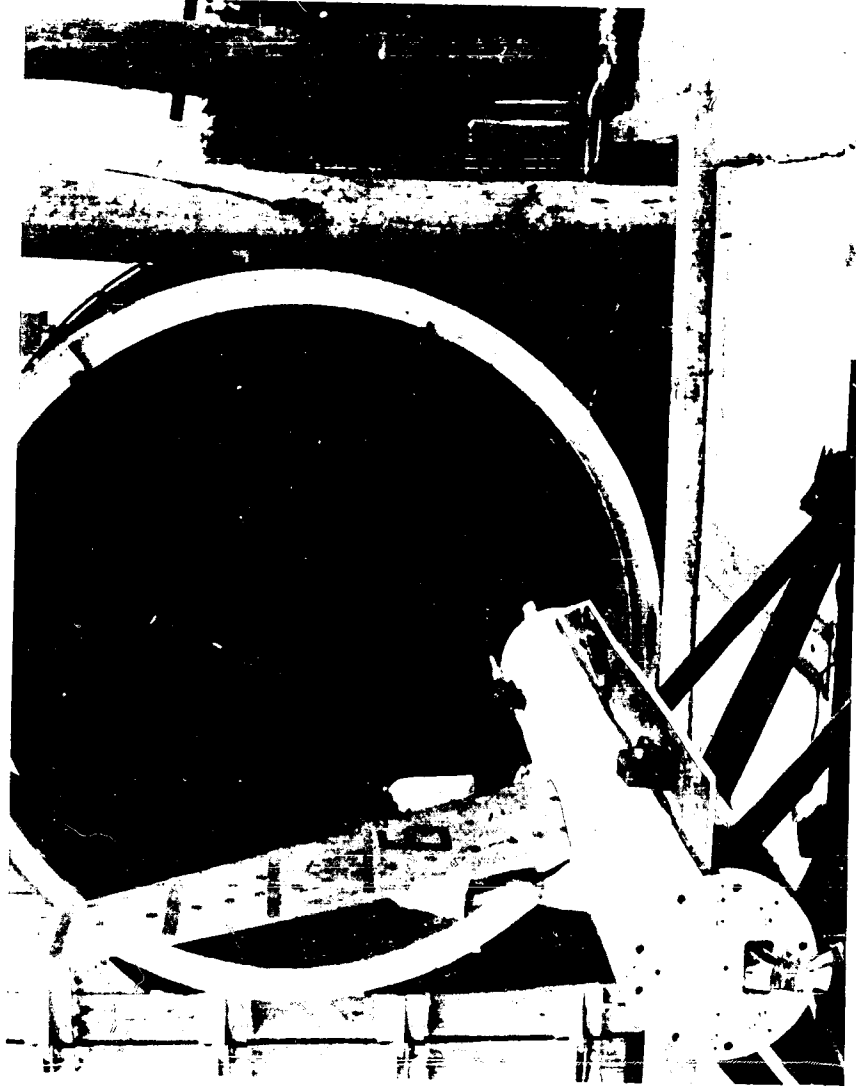


Fig. 6.2.2.5 SHOCK TUBE DIAPHRAGM AFTER TEST - WALLOPS ISLAND SHOCK TUBE

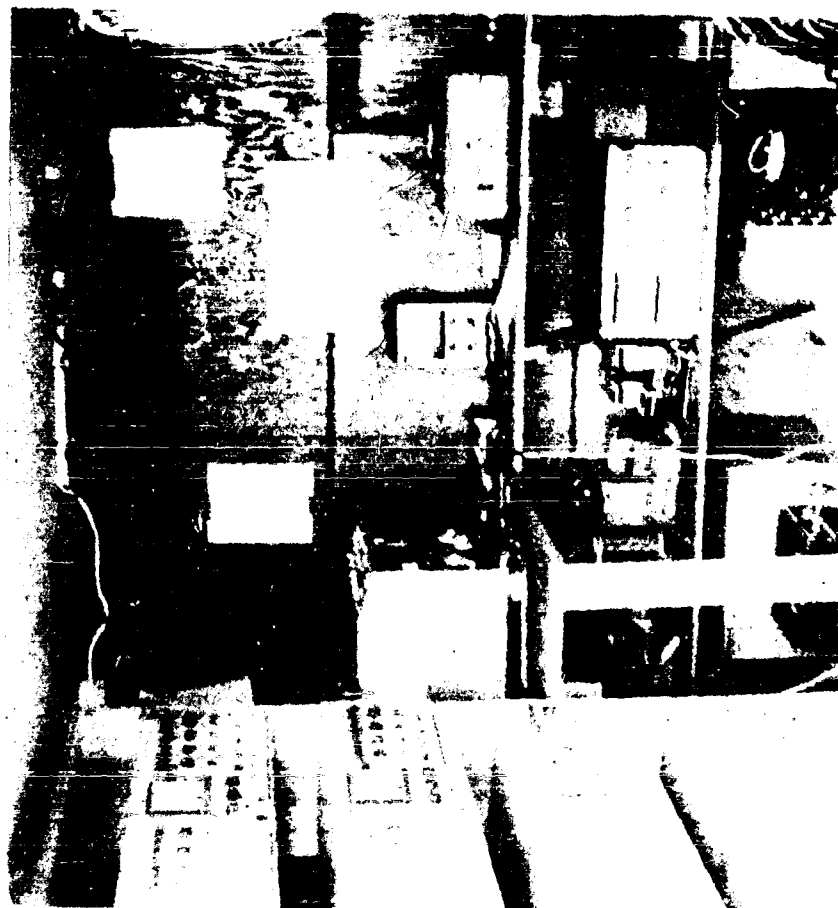


Fig. 6.2.2.6 SPECIMEN INSTRUMENTATION COMPONENTS - WALLOPS ISLAND SHOCK TUBE

field pressure rake aft of the wing specimen. The cameras were focused on the leading and trailing edges of the wing. Leading and trailing edge deflection vs. time was obtained from the films. The pertinent test conditions of the six tests conducted at the Wallops Island Facility are shown in Table 6.2.2.

Table 6.2.2 WALLOPS ISLAND TEST CONDITIONS						
Test No.	Charge Wt. (lbs)	Charge * Distance (Ft.)	Explosive	$\alpha_1$	P(psi)	t (msec)
1	17.49	70.0 x 3.3	Pentolite	8°	2.17	9.14
2	17.44	35.4 x 3.0	Pentolite	20°	6.30	6.4
3	640.0	98.5 x 2.7	HBX-1	30°	10.6	19.3
4	17.83	27.0 x 0	Pentolite	30°	10.6	5.41
5	640.0	130.0 x 3.0	HBX-1	20°	5.45	23.0
6	640.0	258.0 x 3.4	HBX-1	8°	2.17	31.2

\* Note: The first number is perpendicular distance from specimen, the second number is off set distance forward of the 50% chord of the specimen.

#### 6.2.2.1 DETAIL DISCUSSION OF TESTS

Field test personnel arrived at the NASA Wallops Station, Virginia test facility on 31 May 1961. The wing specimen, mounted in the rocket sled forebody, was installed in front of the shock tube and the instrumentation system was installed and checked out. Installation of the test specimen and instrumentation was completed on 23 June 1961. After installation operations were completed AAI test personnel returned to the AAI plant for a five week period to allow NASA personnel time to make flow field and blast field measurements. The NASA and ERL personnel recorded flow and blast field data throughout the series of six tests conducted at the shock tube facility.

Field test personnel returned to the Wallops Island test site on 31 July 1961. All instrumentation circuits were connected and calibrated. The first test was conducted on 10 August 1961. In test No. 1, 17.49 pounds of Pentolite were located seventy (70) feet to the left of the specimen and three and three tenths (3.3) feet forward of the fifty (50) percent specimen chord and detonated. The blast produced an  $8^{\circ}$  specimen angle of attack ( $\alpha_1$ ). The following specimen data were recorded:

- 27 channels of pressure
- 4 channels of strain
- 2 channels of acceleration
- 3 high speed motion pictures
- timing

Tests numbers 2, 3, and 4 were conducted during the week of 14 August 1961. In test No. 2, 17.44 pounds of Pentolite, located thirty-five and four tenths (35.4) feet to the left and three (3) feet forward of the wing specimen, was detonated to provide an induced angle of attack ( $\alpha_1$ ) of  $20^{\circ}$ . The following specimen data were recorded:

- 28 channels of pressure
- 4 channels of strain
- 2 channels of acceleration
- 3 high speed motion pictures
- timing

In test number 3, six hundred forty (640) pounds of HBX-1 located ninety eight and one half feet to the left and two and seven tenths feet forward of the specimen were detonated to induce a specimen angle of attack ( $\alpha_1$ ) of  $30^{\circ}$ . The following specimen data were recorded:

- 28 channels of pressure
- 4 channels of strain
- 2 channels of acceleration
- 3 high speed motion pictures
- timing

Test number 4 utilized 17.83 pounds of Pentolite which were detonated twenty-seven (27.0) feet to the left of the test specimen. The blast wave resulting from the detonation deflected the air flow from the shock tube to provide a specimen angle of attack ( $\alpha_1$ ) of  $30^\circ$ . The following specimen data were recorded:

- 30 channels of pressure
- 4 channels of strain
- 2 channels of acceleration
- 3 high speed motion pictures
- timing

Tests number 5 and 6, the final tests in the series, were conducted during the week of 21 August 1961. In both tests the blast wave was generated by detonation of six hundred forty (640) pounds of HBX-1. The charge was located one hundred thirty (130.0) feet to the left and three (3.0) feet forward of the wing specimen in test number 5. In test number 6, the charge was located two hundred fifty-eight (258.0) feet to the left and three and four tenths (3.4) feet forward of the test specimen. Detonation of the charges resulted in specimen induced angles of attack ( $\alpha_1$ ) of  $20^\circ$  and  $8^\circ$  respectively. The following specimen data were recorded:

Test number 5

- 34 channels of pressure
- 4 channels of strain
- 2 channels of acceleration
- 3 high speed motion pictures
- timing

Test number 6

- 31 channels of pressure
- 4 channels of strain
- 2 channels of acceleration
- 3 high speed motion pictures
- timing

The test equipment was dismantled and shipped, and the field test personnel returned to AAI on 29 August 1961.

The reduced data from the Wallops Island Test Program are published in Volume II of this report. The data from run number 6 was not reduced since it was of such poor quality that it was determined to be useless for correlation purposes.

#### 6.2.2.2 CONCLUSIONS

Several significant problems and/or limitations were inherent with the Wallops Island facility.

1. The short duration of the shock tube flow did not provide the desired duration of steady state aerodynamic data.
2. The flow duration and the structures in the shock tube area limited the tests to charge weights of 640 pounds or less.
3. The velocity of the shock tube flow was limited to 0.7 Mach which was less than desired.
4. Since the charge is located to the left of the test specimen at the NASA facility, it was impractical to conduct destruction tests on the 6R structural models which were designed for failure from a charge located to the right of the specimen. Although it would have been possible to build a structure to suspend the specimen upside down which would have provided the proper orientation between the charge and specimen, sufficient inaccuracies would have been introduced into the data due to aerodynamic interference effects between the supporting structure and the specimen to make the information unuseable for theoretical correlation purposes.

#### 6.2.3 RECOMMENDATIONS

The experience gained in conducting the field test program at the Edwards Air Force Base Rocket Sled Track and at the NASA Shock Tube Facility indicate the need for several improvements in the test equipment before further tests are conducted.

The shock tube testing technique provides for a much broader choice in selection of test apparatus, especially instrumentation components,



by eliminating the severe environmental conditions of the rocket sled technique. However, it is felt that the limitations of the shock tube facility imposed on a test program of the size and scope of the anticipated "BIG SEA" program eliminates the shock tube technique as a method of testing. It was successfully proven during the Phase I tests at Edwards Air Force Base that all the mechanical problems prevalent in a test program of this magnitude can be solved. The only problems, preventing successful achievement of the project objectives, remain in the area of instrumentation. For these reasons the following recommendations are made:

1. Utilize the rocket sled testing technique for experimental data acquisition during the "BIG SEA" program.
2. Develop instrumentation components that can withstand the severe conditions of the sled environment and will measure the parameters of interest to the accuracy required in the "BIG SEA" program.
3. Include the dynamic testing of the 6R specimens in the "BIG SEA" program.
4. Utilize the leach tape recorder as the "BIG SEA" recorder instrument but design and install a shock and vibration mount to protect the recorder from the sled vibrations.

## 7.0 SUMMARY

### 7.1 SLED

The sled operated satisfactorily through the entire series of dynamic and static tests requiring only nominal maintenance. Its actual performance substantiated the theoretical predictions outlined in this report, the peak velocity being very nearly the figure predicted. No structural faults were encountered and the sled appears sound and ready for modification and installation of equipment for the project BIG SEA program.

### 7.2 TEST SPECIMENS

Three 6R structural specimens and one (1) 6L airloads specimen were manufactured during the program. The 6L specimen was instrumented and used in three dynamic runs at Edwards Air Force Base and six shock tube tests at the NASA Wallops Island facility. The 6R specimen could not be tested at the Wallops Island site because the specimen is asymmetrical in design and the blast loading originated from the wrong side of the sled. Both specimens were statically and dynamically tested in the laboratory to determine their structural characteristics. The 6R specimens could be factored into plans for the "BIG SEA" program and experimental data obtained there. ASD will consider this possibility.

### 7.3 INSTRUMENTATION

The field program was seriously hampered by the inadequacy of the instrumentation. The initial concern was with the pressure transducer, but with the beginning of the field program the associated electronics became the problem and the limiting factor in the system performance. The NASA pressure transducer proved to be rugged and reliable and performed as the pre-field tests indicated it would. This unit had performance characteristics sufficient for the JANAF program but will be inadequate for the contemplated "BIG SEA" program.

For the measurement of specimen pressures it was originally planned to use a complete CEC instrumentation system which included the pressure transducer, amplifier, inverter, and recorder. The pressure transducer,

inverter, and amplifier were completely inadequate to withstand the sled vibration environment and had to be abandoned. AAI supplied NASA pressure transducers, and Statham amplifiers were substituted for the CEC equipment. The CEC oscillograph was retained in the system but was augmented by the addition of Leach tape recorders. This improvised system was adequate for the BRL tests but was found to be completely inadequate for the exacting requirements of the ASD program. After three check out runs to test the instrumentation problems the ASD test program was moved to the NASA Wallops Island shock tube. The instrumentation installation at this facility was stationary and the system reverted to the CEC equipment originally planned for use in the sled.

The Leach tape recorder was the only instrument in the pressure measurement system that should be considered for use in the "BIG SEA" program. This unit also was suspected of introducing considerable amounts of noise, especially at the on-set of the blast, but it is believed that its performance can be made acceptable by use of a suitable shock and vibration mount.

Except for the recorder problems, the instruments used in the acceleration and strain channels performed satisfactorily and similar instruments selected to suit the "BIG SEA" problem should be quite adequate for that program. The Leach tape recorders, after it is shock mounted, should afford an adequate means of recording the data.

The cameras on the program performed adequately and a similar installation should be adequate for the "BIG SEA" program. Except for the recorder, an entirely new instrumentation system must be acquired to measure "BIG SEA" specimen pressures. The NASA pressure transducer proved to be a reliable instrument, but its performance is too limited for use in the "BIG SEA" program. A pressure transducer with a much higher frequency response will be needed with special limitations placed on its thermal and acceleration characteristics. The associated electronics must be compatible with the transducer and recorder and be capable of withstanding the severe sled environment.

#### 7.4 TEST DATA

The data taken on the F-84 specimens will be processed by BRL and the results published in reports planned for this purpose. The blast line data on the tests made at the Wallops Island test facility was taken by BRL and will be processed and published by that agency. NASA measured supplemental data on the jet flow from the shock tube and will publish that data in a separate report. The specimen data from the Wallops Island tests was taken by AAI. This data is being processed and will be published, together with an analysis, as Volume II of this report. The value of this data has not yet been assessed but preliminary indications are that adequate data was obtained on five (5) of the six (6) Wallops Island tests.

#### 7.5 "BIG SEA" PROBLEMS

The information acquired during the program relating to the feasibility of adapting these test methods to the contemplated "BIG SEA" program can be summarized as follows:

1. The sled proved itself to be sound, easy to maintain and operate, and completely suitable for adaptation to the "BIG SEA" program. Some minor modifications to the motor section to accept other type motors will be necessary. Also some very minor changes to the camera installation are contemplated.
2. The strain and acceleration data can be taken by instruments similar to those used on this program. The Leach taper recorder should be used to record the strain and acceleration data.
3. The Leach tape recorder should be adequate for use in the "BIG SEA" program. A shock and vibration mount should be provided to isolate these units from the sled vibration environment. Some testing to determine the requirements for this mount should be planned.
4. The cameras used on the program performed satisfactorily and are adequate for the "BIG SEA" program. Some additional protection to completely shield the cameras from the blast has been suggested.

5. A new pressure transducer and associated electronics must be acquired to measure specimen pressures in the "BIG SEA" program. A few candidate transducers have been offered that promise a satisfactory solution. A program of testing to evaluate the merits of these candidate units is advised. A satisfactory solution to this problem would remove all major uncertainties and the "BIG SEA" program could be planned with good prospects of success.

## APPENDIX A JANAF Post-Failure Response Program and Results

### A.1 INTRODUCTION

The JANAF program involves the use of sled-mounted wing models exposed to HE blasts. Two types of models are involved: aerodynamic and structural. The aerodynamic models are intended to be essentially rigid in order to obtain aerodynamic data which are contaminated as little as possible by structural response.

The structural models are intended to yield both aerodynamic and structural data. In two of the three structural runs, it is intended that post-failure deformation take place. In order to design the models so that the deformation will be neither too small nor excessive, it is necessary to make preshot estimates of the deformations. These estimates can be made intelligently only by using post-failure structural response methods such as described in WADC TR 56-150, Pt 5. These methods cannot feasibly be employed without recourse to a computer. The 1103A Univac Scientific digital computer at ASD has been used for this purpose.

The response program which is described in the following is essentially a minimal program intended for use in design studies for the JANAF program. As such, it can be used to obtain rough response estimates, but should not be considered adequate for final correlation work.

### A.2 THE COMPUTER PROGRAM

The JANAF post-failure structural response program employs the matrix-inversion method of WADC TR 56-150, Pt. 5. The program can handle up to ten normal modes and fifty mass points. The mass points are also the points at which aerodynamic loads are applied.

The mode shapes and frequencies for the JANAF structural model were supplied by AAI. A preliminary estimate of the post-failure structural characteristic curve for the model, Figure A.1, was furnished by Mr. D'Amato of MIT.

Aerodynamic data were supplied by Drs. Witmer and Ruetenik of MIT. These data and their usage in the computer program will be described qualitatively, because the aerodynamics employed are believed to represent a substantial departure from any previous work.

Three curves, shown in Figure A.2 are involved in determining the aerodynamic forces. The first, Figure A.2a is a curve of  $\frac{C_n(\alpha, s)}{\alpha}$  vs. "s", where  $C_n(\alpha, s)$  is the two-dimensional normal force coefficient as a function of angle of attack,  $\alpha$ , and distance traveled in chord lengths, "s". This curve is based upon the results of shock-tube tests at MIT. Initially, at  $s=0$ , the normal force coefficient is given approximately by  $\frac{C_n(\alpha, 0)}{\alpha} = \frac{4}{M'}$ , where  $M'$  is the Mach number based on conditions behind the shock. A linear decay was assumed from  $s=0$  to  $s=1$ .

For  $s > 1$ , a curve is given for each of several values of angle of attack. The curve labelled  $\alpha = 0$  is the potential flow result (indicial sinking function) applicable to very small angles of attack. The other curves show the effect of transient stalling. The computer program utilizes the information on Figure 2a in the following way. Each of the curves has been fitted with an analytical expression. The computer program uses these expressions to calculate  $\frac{C_n(\alpha, s)}{\alpha}$  and, by linear interpolation between the two curves which bracket the actual angle of attack,  $\frac{C_n(\alpha, s)}{\alpha}$ . The lower of these values is then chosen. In this way, the potential flow curve is utilized until transient stalling for the given angle of attack occurs. The normal force then follows a stall pattern which is dependent upon the variation of the angle of attack with time. This method is not a truly unsteady method; neither is it a quasi-steady method. Actually, it contains elements of both methods, and might therefore be termed a quasi-unsteady method. The method should give good results as long as the rapid angle of attack variations of the lifting surface occur near zero time. In the limiting case in which the only angle of attack variation occurs at zero time (i.e., in the shock tube), the method gives the correct results.

This procedure results in the two-dimensional normal force coefficient. Three-dimensional and sweepback effects are accounted for using Figures A.2b and A.2c. Figure A.2b shows the variation of the steady-state ratio of three-dimensional to two-dimensional normal force coefficient. This curve applied, then, for large values of "s". A transition factor, Figure A.2c, was estimated by Drs. Witmer and Ruetenik of MIT to permit transition from two-dimensional to three-dimensional conditions. At  $s=0$ , conditions are truly two-dimensional, and it has been assumed that two-dimensional conditions persist until  $s=1$ . Three-dimensional conditions are assumed to exist for  $s > 16$ . A linear transition from two- to three-dimensional conditions is assumed between  $s=1$  and  $s=16$ .

Strip theory was employed in order to determine the force acting at each aerodynamic point. The parameter "s" was based on the local chord and the total velocity immediately behind the shock front. The angle of attack at each station was defined in terms of the local relative velocities in each of three orthogonal directions, the sweep angle of break, and the hinge angle  $\delta^{\wedge}$ . Included in the local velocities were the sled forward speed, the material velocity due to the blast, and the rotational velocity about the hinge line. Thus, no aerodynamics due to model motion were included.

Finally, the local sweep angle of the surface relative to the total velocity is altered by the break. This was accounted for by multiplying  $\frac{C_N}{C_n}(\alpha, \infty)$  (Figure 2b) by  $\frac{\cos \Lambda_e}{\cos \Lambda}$ , where  $\Lambda$  is the sweep angle of the undamaged wing and  $\Lambda_e$  is the effective local sweep angle of the broken wing.

### A.3 RESULTS

Following writing and debugging of the computer program, a static post-failure test was conducted by Mr. D'Amato at MIT on a two-dimensional model of the failure bay of the JANAF structural model. Mr. D'Amato informed Avidyne personnel on November 2, 1960, of the results of that test.



Mr. D'Amato's original estimate of the shape of the post-failure structural-characteristic curve had been borne out by the static test, so that the post-failure curve already included in the computer program would suffice for response studies. The failure moment found by Mr. D'Amato was 136,000 lbs.

For the conditions of the scheduled runs, the responses were as follows:

<u>Run</u>	<u>Peak Angle of Attack</u>	<u>Charge Weight</u>	<u>Max <math>\delta</math> or Max Bending Moment</u>
A	5°	20#	+31000 in.lbs., - 40000 in.lbs.
B	30°	20#	5.0°
C	30°	12000#	44.6°

For run A, an elastic response is desired. The computed response is elastic, and the largest positive bending moment is 23% of the failure bending moment. A somewhat higher bending moment might be desirable, depending upon details of the instrumentation and recording system and upon the aerodynamic problems which might be encountered in going to a higher angle of attack. If a slightly higher angle of attack were used, the peak bending moment would be roughly proportional to the angle of attack.

It is interesting to note that the negative peak bending moment is greater in magnitude than the positive peak bending moment. This is due to the fact that the short duration of the material velocity in run A causes the negative phase to phase in with the elastic oscillation in such a way as to enhance the negative peak bending moment considerably.

For run B, a small amount of post-failure deformation is desired. The computed deformation of 5° is reasonable, but a slightly larger deformation of, say, 10° would be preferable.

For run C, a deformation of between 40° and 50° is desired. The computed response obviously satisfies this requirement.

The possibility of using a weaker model in order to increase the deformation in run B was considered. To this end, the critical bending moment in the computer program was reduced to 100,000 in.lbs., with the shape of the post-failure structural characteristic curve unchanged. For the weaker structure, the deformations for runs B and C were computed to be  $5.6^\circ$  and  $48.3^\circ$ , respectively. It is clear from this result that the deformation resulting in run B cannot reasonably be increased by lowering the critical bending moment, or, equivalently, by increasing the peak angle of attack. This behavior is due to the fact that the material velocity duration is so short that the energy in the forcing function has largely expended by the time the structure breaks. Apparently, the only feasible way of increasing the deformation is to provide a longer forcing duration by increasing the charge size. This increase in charge size is not desired by Dr. Witmer, however, since such action would jeopardize the high decay-rate information which is being sought. The conclusion is, therefore, that the present structural model design must be considered satisfactory.

It is interesting also to note the small influence of break strength on the computed deformation for run C. This is due to the strength of the aerodynamic restoring forces produced by the sweptback break. These forces are becoming so large by the time  $\gamma$  reaches  $40^\circ$  or so that a considerably larger input (or, equivalently, a considerably smaller break strength) is required in order to increase the deformation even a small amount.

It is rather unfortunate that, in both the post-failure runs, the maximum deformation is comparatively insensitive to changes in break strength (and, similarly, to the shape of the post-failure curve) and magnitude and time-history of the aerodynamic input. Because of this fact, comparison of the maximum computed deformation with the maximum experimental deformation does not offer a stringent test of either the structural theories or the transient aerodynamic theories involved in the calculation of the response. For example, the break strength or the estimation of transient

stalling effects could be considerably in error without substantially affecting the computed peak deformation. The necessity for good experimental time-histories of aerodynamic loads, bending moments, and displacements for purposes of correlation becomes of paramount importance on the basis of the above considerations.

#### A.4 CONCLUSIONS

In summary, two conclusions have been reached:

- (1) The JANAF structural model as currently designed is acceptable.
- (2) The maximum deformation of the structural model does not offer a stringent test for the theories for the particular cases being studied; good time-histories are, accordingly, of utmost importance.

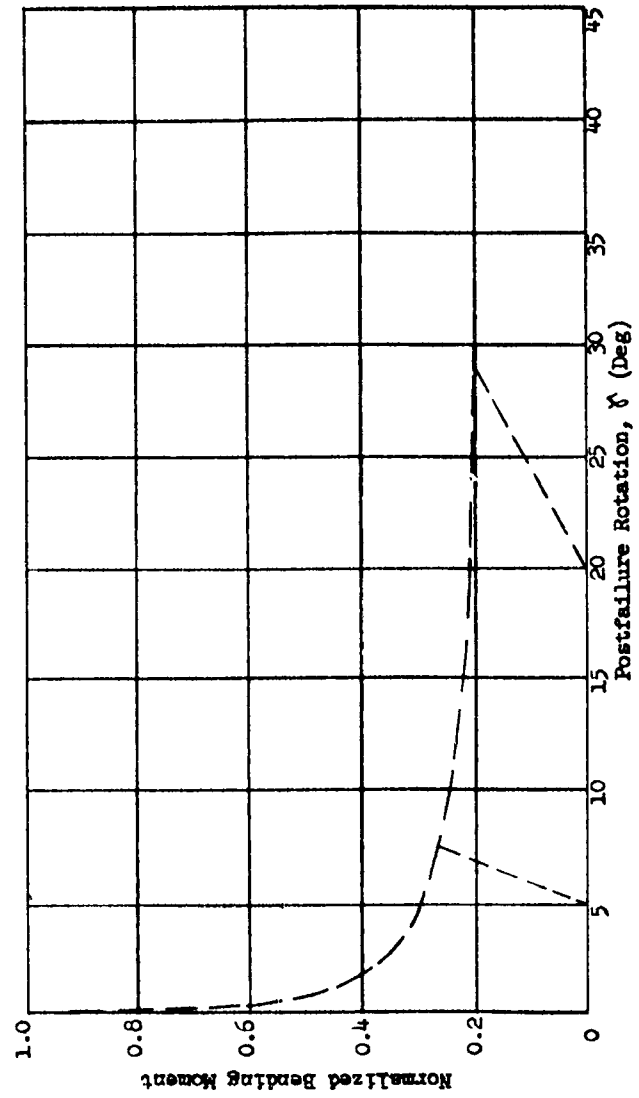


Figure A.1 PRELIMINARY STATIC POSTFAILURE CURVES FOR  
STRUCTURAL MODEL DESIGN JANAF PROGRAM

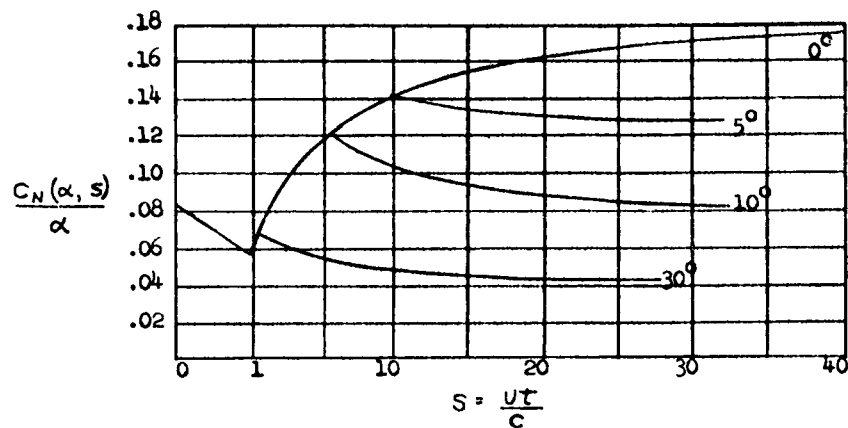


Figure A.2a

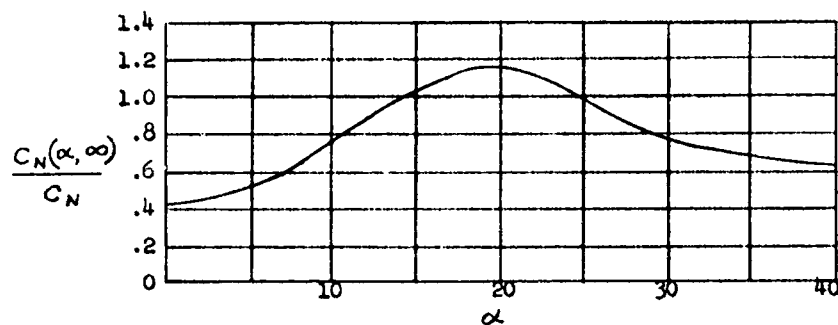


Figure A.2b

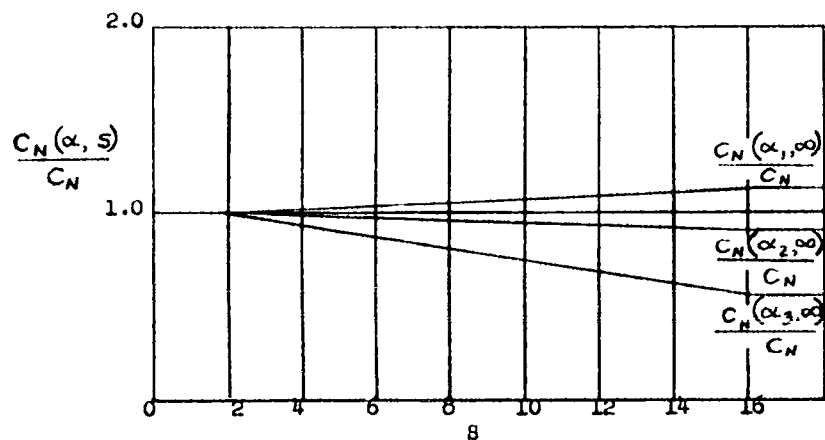


Figure A.2c

Figure A.2 AERODYNAMIC PROCEDURES

#### REFERENCES

1. Benjamin, R. J., Frassinelli, G. J., Gran, W. M., Hobbs, N. P., Ruetenik, J. R., Witmer, E. A., (Unclassified Title) Study to Plan a Program to Determine High Blast-Induced Airloads and Structural Response of Lifting Surfaces, Cook Research Laboratories, Avidyne Research, Massachusetts Institute of Technology, WADD TR 60-117 Vol. I & II, December 1959, Confidential.
2. D'Amato, R., Destruction Tests of Aircraft Structural Components, Part I - Description of Static-Test Techniques and Presentation of Postfailure Structural Characteristics of Some Complex Built-Up Structures, WADC TR 54-385, Part I, June 1, 1955.
3. Crisone, E. S., Ayrazian, M., Wetmore, K. R., Destruction Tests of Aircraft Structural Components, Part II - Development of a Single - Channel Bending Moment Measurement Method Applicable to a Complex Built-Up Structure for Both the Elastic and the Post-Buckling Regime of Structural Response, WADC TR 54-385, Part II, September 1, 1955.
4. Di'Amato, R., Static Postfailure Characteristics of Multiweb Beams, WADC TR 59-112, February 1959.
5. Witmer, E. A. (Unclassified Title) The Prediction of Lethality Envelopes for Aircraft in Flight, Part I - General Considerations, WADC TR 56-150, Part I, June 1958, Confidential FRD.
6. Criscione, E. S. and Hobbs, N. P., (Unclassified Title) The Prediction of Lethality Envelopes for Aircraft in Flight - Part 2 - Detailed Theoretical Analysis, WADC TR 56-150, Part 2, October 1958, Confidential.
7. Crisone, E. S. Hobbs, N. P., and Witmer, E. A., (Unclassified Title) The Prediction of Lethality Envelopes for Aircraft in Flight Part 3 - Correlation of Prediction with Field-Test Results on F-80 Drone Aircraft, WADC TR 56-150, Part 3, January 1959, Secret.

8. Ayrazian, M., and Crisone, E. S., (Unclassified Title) The Prediction of Lethality Envelopes for Aircraft in Flight, Part 4 - Correlation of Predictions with Field-Test Results on F-86D and F-80 Ground Mounted Horizontal Stabilizers, WADC TR 56-150, Part 4, July 1958, Secret.
9. Hobbs, N. P., (Unclassified Title) The Prediction of Lethality Envelopes for Aircraft in Flight, Part 5 - Simplified Prediction Methods, WADC TR 56-150, Part 5, June 1958, Confidential - FRD.
10. Gerard, G., and Becker, H., Handbook of Structural Stability, NACA TN 3781 1957.
11. Miller, J., Stress Strain and Elongation Graphs for Alclad Aluminum - Alloy 24S-T Sheet, NACA TN 1512 1948.
12. Miller, J., Stress Strain and Elongation Graphs for Aluminum-Alloy 75S-T6 Sheet NACA TN 2085 1950.
13. Semonian, J., and Peterson, J., An Analysis of the Stability and Ultimate Compressive Strength of Short Sheet-Stringer Panels with Special Reference to the Influence of the Riveted Connection Between Sheet and Stringer. NACA Report 1255, 1956.
14. Schuette, E., McCulloch, J., Charts for the Minimum - Weight Design of Multiweb Wings in Bending. NACA TN 1323 1947.
15. Semonian, J. W., and Anderson, R. A., An Analysis of the Stability and Ultimate Bending Strength of Multiweb Beams with Formed-Channel Webs, NACA TN 3232, August 1954.
16. Norris, C. H., Structural Design for Dynamic Loads, McGraw-Hill Book Co., Inc., New York, 1954
17. Bisplinghoff, R., Ashley, H., and Holfman, R., Aeroelasticity, Addison-Wesley Publishing Co., Inc., Cambridge, Mass., 1955.
18. Myklestad, N. O., Fundamentals of Vibration Analysis, McGraw-Hill Book Co., Inc., New York, 1956.

19. Scanlan, R. H., and Rosenbaum, R., Aircraft Vibration and Flutter, The Macmillan Co., New York, 1960.
20. MIL-HDBK-5, Strength of Metal Aircraft Elements, Armed Forces Supply Support Center, Washington 25, D. C., March 1959.
21. Alcoa Structural Handbook, Aluminum Company of America, 1955.
22. Roark, R. J., Formulas for Stress and Strain, 3rd Edition, McGraw-Hill Book Co., Inc., New York, 1954.
23. Bruhn, E. F., Analysis and Design of Airplane Structures, Tri-State Offset Co., Ohio, 1952.
24. Den Hartog, Mechanical Vibrations, Fourth Edition, McGraw-Hill Book Co., Inc., 1956.
25. Ames Research Staff, Equations, Tables, and Charts for Compressible Flow, NACA Report 1135, 1953
26. Glasstone, S., The Effects of Nuclear Weapons, U.S. AEC, 1957
27. Brode, H. L., Point Source Explosion in Air, The Rand Corporation, RM-1824, December 1956.
28. Brode, H. L., Numerical Solutions of Spherical Blast Waves, Journal of Applied Physics, Vol. 26, 1955, pg. 766.
29. Goodman, H. J., Computed Free-Air Blast Data on Bare Spherical Pentolite, BRL Report No. 1092, February 1960.
30. Joint Services Sled Program. (Data Sheet).
31. USS "T-1" Steel Handbook, United States Steel Corporation.
32. D'Amato, R., Theoretical and Experimental Postfailure Characteristics of Critical Bay of Structural Response of Model 6R of JANAF Blast Loads Sled Test Program. Viscoelastic and Structures Research Laboratory, Massachusetts Institute of Technology, November, 1960.